

**DESIGN AND OPTIMIZATION OF A PERMANENT MAGNET  
LINEAR RELUCTANCE MOTOR FOR RECIPROCATING  
ELECTRO-MECHANICAL SYSTEMS**

by

Steven Andrew Evans, BEng(Hons), AMIEE

A Doctoral Thesis

Submitted in partial fulfilment of the requirements  
for the award of


Doctor of Philosophy of the Loughborough University

November 1996

LOUGHBOROUGH UNIVERSITY

Department of Electronic and Electrical Engineering

© by Steven Andrew Evans 1996

 Loughborough UNIVERSITY	
Date	May 97
Class	
Acc No	040129882

99100111

This thesis describes the design, analysis and optimization of a linear motor for use in reciprocating electro-mechanical systems. A review of various types of limited range linear motion motors was undertaken and the most suitable design identified was that of the permanent magnet linear reluctance motor. These machines are rapidly replacing conventional electrical, mechanical and hydraulic systems in a wide range of applications, such as Stirling cycle cryogenic coolers, artificial heart devices and aircraft flight surface actuators. They take the form of a bi-directional moving-iron or variable air-gap device in which a soft-iron armature, positioned on the central axis of two opposing ring magnets, moves when a current is fed through a solenoidal coil situated between the magnets. An optimum design should possess a linear coil current/armature displacement characteristic, produce the maximum possible force on the armature and have a fast dynamic response. An essential requirement is a restoring axial stiffness, to ensure that the armature returns to its central position in the absence of any coil current. Due to the complex geometry of the device, and the non-linear magnetic materials involved, a finite element approach was used in studying the internal magnetic conditions. Following this, various dimensional changes were made to the magnetic circuit of the typical motor investigated, and different magnetic materials were employed to improve the static characteristics. A mathematical model that includes the drive system has been developed, employing tensor techniques, to accurately predict the dynamic performance. A factorial design approach has been used to identify the dimensions of the motor most significant in affecting the device performance, and an optimum design has been identified. Simulated and finite element results are compared with the experimental performance of various prototype motors, to illustrate the effectiveness of the modelling technique.

## ACKNOWLEDGEMENTS

---

I am indebted to the Department of Electronic and Electrical Engineering of Loughborough University for the research studentship. I would like to express my gratitude to my Director of Research, Prof. Ivor R. Smith for his constructive comments and advice in the writing of this thesis. His enthusiasm, dedication and expertise was an inspiration. My thanks also for the part-time research assistantship awarded during my final year of study which helped me greatly.

Thanks must also go to my Supervisor, Mr. J. Gordon Kettleborough for his suggestions and guidance in the writing of this thesis and for his initial recommendation for the part-time research assistantship.

Thanks also to Dr. Keith Gregory for the generous use of his plotting routine software and for the many helpful discussions we had during the early years of the research. I am also grateful to Mr. S. K. Jim from Coercive Systems Ltd., Rochester, Kent, UK for the hardware support and to Mr. Dave Michelson from the mechanical workshop for manufacturing the prototype motors.

I must also congratulate the Applied Electromagnetics Research Centre at the University of Bath, UK for developing an excellent finite element software package, *MEGA*, which was vital for the successful completion of the research. Thanks must also go to my many colleagues in the Electrical Power Research Group and friends who helped make my stay enjoyable in particular Susanne, Yi, Bob, Kirk, Malcolm, Ebrahim, Derrick, Gitau, Bill, Lynn, Sheila and Margaret.

I am also grateful to my mum, Doreen and my late dad, Bruce, who both helped me in the early years of my education. Especially, to my late dad who gave me the initial inspiration to become an Electrical Engineer.

*To my Mum Doreen,  
and to the memory of my Dad Bruce.*

## TABLE OF CONTENTS

---

	Page
Abstract .....	i
Certificate of Originality .....	ii
Acknowledgements .....	iii
Dedication .....	iv
Table of Contents .....	v
List of Principal Symbols .....	xi
<b>CHAPTER 1 INTRODUCTION .....</b>	<b>1</b>
1.1 Thesis Objective .....	1
1.2 Thesis Organisation .....	2
<b>CHAPTER 2 LIMITED LINEAR MOTION ELECTRICAL</b>	
<b>MACHINES .....</b>	<b>5</b>
2.1 Introduction to Linear Motors .....	5
2.2 Moving-Coil Linear Motors .....	6
2.3 Moving-Iron Linear Motors .....	6
2.3.1 Fundamental types of Variable Air-gap Linear Motor ..	7
2.4 Requirements of the Linear Motor .....	7
2.5 Applications of the Linear Motor .....	8
2.6 Linear Motor Design Analysis .....	8
2.6.1 Linear Synchronous Motors .....	9
2.6.2 Linear DC Motors .....	10
2.6.3 Linear Stepper Motors .....	11
2.6.4 Linear Reluctance Motors .....	12
2.6.5 Linear Solenoids .....	14
2.6.6 Limited Angle Torque Motors .....	15
2.7 Comparison of Linear Motor Performance .....	16
2.8 Conclusions .....	19

**CHAPTER 3 PERMANENT MAGNET LINEAR RELUCTANCE**

<b>MOTOR</b> .....	26
3.1 Principle of Operation .....	26
3.2 Selection of Materials .....	28
3.2.1 Magnetic Material .....	29
3.2.2 Permanent Magnet Material .....	30
3.2.3 Coil Material and Assembly .....	33
3.3 General Design Arrangement .....	34
3.3.1 Mechanical Arrangement .....	34
3.3.2 Coil Arrangement .....	35
3.4 Optimum Design .....	36
3.5 Conclusions .....	37
<b>CHAPTER 4 FINITE ELEMENT ANALYSIS AND MODELLING</b> .....	
4.1 Numerical Methods in Electrical Engineering .....	47
4.2 Representation of the Magnetic Field in the Linear Motor .....	48
4.2.1 Time Invariant Magnetic Field .....	48
4.2.2 Time Variant Magnetic Field .....	50
4.3 Axi-symmetric Formulation .....	51
4.4 Electromagnetic Finite Element Analysis Software .....	52
4.5 Modelling of Magnetic Material Properties .....	53
4.6 Permanent Magnet Representation .....	55
4.7 Pre-Processing Operations .....	56
4.7.1 Problem Geometry and Mesh Construction .....	56
4.7.2 Distant Boundaries and Boundary Conditions .....	57
4.7.3 Modelling of Excitation Sources .....	58
4.8 Post-Processing Operations .....	58
4.8.1 Equipotential Plots .....	59
4.8.2 Flux Linkage Computation .....	59
4.8.2.1 Flux Linkage Computation from a Static Field Solution .....	60

4.8.2.2	Flux Linkage Computation from a Transient Field Solution . . . . .	60
4.8.3	Force Computation . . . . .	61
4.8.3.1	The Virtual Work Principle . . . . .	61
4.8.3.2	Finite Element Implementation of the Virtual Work Principle . . . . .	62
4.8.3.3	Maxwell Stress Tensor Method . . . . .	63
4.8.3.4	Comparison of Methods . . . . .	64
4.9	Conclusions . . . . .	65

## **CHAPTER 5 STATIC ANALYSIS OF THE LINEAR RELUCTANCE**

<b>MOTOR</b> . . . . .	<b>72</b>
5.1 Magnetic Field Solution . . . . .	72
5.1.1 Magnetic Flux Distribution with the coil unexcited . . . .	72
5.1.2 Magnetic Flux Distribution with the coil excited . . . . .	74
5.2 Force Characteristic . . . . .	74
5.2.1 Linear Analysis Results . . . . .	74
5.2.2 Non-linear Analysis Results . . . . .	75
5.3 Flux Linkage Characteristic . . . . .	77
5.3.1 DC Inductance Bridge . . . . .	77
5.4 Conclusions . . . . .	78

## **CHAPTER 6 DYNAMIC ANALYSIS OF THE LINEAR**

<b>RELUCTANCE MOTOR</b> . . . . .	<b>91</b>
6.1 Dynamic Simulation Analysis Software . . . . .	91
6.2 Mathematical Model . . . . .	92
6.2.1 Motor Differential Equations . . . . .	92
6.2.1.1 Electrical Circuit Equation . . . . .	92
6.2.1.2 Mechanical Motion Equation . . . . .	93
6.2.1.3 Differential Equations in State-Variable Form . . . . .	93
6.2.2 Non-Linear Characteristics . . . . .	94



6.2.2.1	Flux Linkage Characteristic Bicubic Spline Approximation . . . . .	95
6.2.2.2	Force Characteristic Bicubic Spline Approximation . . . . .	96
6.2.2.3	Magnetic Stiffness Characteristic Cubic Spline Approximation . . . . .	97
6.2.3	Other Motor Parameters . . . . .	97
6.2.4	Numerical Integration . . . . .	98
6.2.4.1	Electrical Circuit Equation . . . . .	99
6.2.4.2	Mechanical Motion Equation . . . . .	100
6.3	Computer Implementation . . . . .	101
6.4	Simulated and Experimental Results . . . . .	102
6.5	Controlling the Current in the Linear Motor Coil . . . . .	103
6.5.1	Principle of Operation . . . . .	104
6.5.1.1	Tolerance Band Control . . . . .	104
6.5.2	Modelling of the Switch-Mode Inverter Circuit . . . . .	105
6.5.2.1	Positive Current Flow Sign Convention . . . . .	106
6.5.2.2	Modelling of the Semiconductor Switches and Diodes . . . . .	106
6.5.2.3	Voltage Equation Assembly . . . . .	106
6.5.2.4	Branch/Mesh Transformation . . . . .	109
6.6	Computer Implementation . . . . .	110
6.7	Simulated and Experimental Results . . . . .	112
6.8	Conclusions . . . . .	113

**CHAPTER 7 RE-FORMATION OF THE LINEAR RELUCTANCE**

<b>MOTOR I</b> . . . . .	142
7.1 Initial Geometric Parameter Modifications . . . . .	142
7.1.1 Re-positioning the Permanent Magnets . . . . .	142
7.1.2 Chamfering of the Stator End-Rings . . . . .	143
7.1.3 Armature Diameter . . . . .	144
7.1.4 Armature Centre-Section Length . . . . .	149

7.1.5 Armature Centre-Section Diameter . . . . .	150
7.2 Second Prototype Linear Reluctance Motor . . . . .	151
7.2.1 Stator and Armature Dimensions . . . . .	151
7.2.2 Determination of the Magnetization Curves . . . . .	153
7.2.3 Static Force Characteristic . . . . .	154
7.2.4 Static Flux Linkage Characteristic . . . . .	156
7.2.4.1 Theoretical Method . . . . .	157
7.2.4.2 Experimental Measurement Method . . . . .	158
7.2.5 Simulated and Experimental Results . . . . .	159
7.3 Conclusions . . . . .	161
<b>CHAPTER 8 RE-FORMATION OF THE LINEAR RELUCTANCE</b>	
<b>MOTOR II</b> . . . . .	198
8.1 Further Geometric Parameter Modifications . . . . .	198
8.1.1 Hollow Armatures . . . . .	198
8.1.2 Comparison of Hollow and Solid Armatures . . . . .	202
8.1.3 Air-gap Length . . . . .	203
8.1.4 Radially Magnetized Permanent Magnets . . . . .	203
8.1.5 Stator Yoke Pole-Shoe Length . . . . .	204
8.2 Maximising the Armature Displacement . . . . .	205
8.3 Magnetic Material Study . . . . .	206
8.4 Conclusions . . . . .	209
<b>CHAPTER 9 OPTIMIZATION OF THE LINEAR RELUCTANCE</b>	
<b>MOTOR</b> . . . . .	232
9.1 Determination of Optimization Procedure . . . . .	232
9.2 Factorial Design Studies . . . . .	233
9.2.1 The 2 <sup>n</sup> Factorial . . . . .	233
9.2.2 Armature Variable Parameters . . . . .	234
9.2.3 The Armature Factorial Design Study . . . . .	235
9.2.3.1 Analysis of the Response Models . . . . .	237

9.2.3.2	Analysis of the Coefficients of the Response Models .....	241
9.2.3.3	Variation of Parameter Limit Settings .....	244
9.2.4	The Stator Factorial Design Study .....	246
9.2.4.1	Analysis of the Response Models .....	248
9.2.4.2	Analysis of the Coefficients of the Response Models .....	249
9.2.5	Determining the Optimum Design .....	250
9.3	Optimum Design .....	251
9.3.1	Comparison of Optimized, Improved and Original Designs .....	251
9.4	Conclusions .....	253
<b>CHAPTER 10</b>	<b>CONCLUSIONS AND FURTHER WORK .....</b>	<b>275</b>
10.1	Conclusions .....	275
10.2	Further Work .....	277
References	.....	279
Bibliography	.....	292
<b>APPENDICES</b>	.....	<b>293</b>
A	Initial Specification of the Linear Motor .....	293
B	Specification of the Optimum Linear Motor .....	294

## LIST OF PRINCIPAL SYMBOLS

---

$A$	Magnetic vector potential	
$A$	Pole-face area	$m^2$
$A_c$	Copper wire conductor cross-sectional area	$m^2$
$a$	acceleration	$m/s^2$
$B$	Flux density vector	T
$B_{bb}$	Branch back-emf matrix	V
$B_{mm}$	Mesh back-emf matrix	V
$B$	Coil back-emf coefficient	Vs/m
$B_a$	Air-gap flux density	T
$B_r$	Permanent magnet remanent flux density	T
$C_m^b$	Branch/mesh transformation tensor	
$C_m^b$	Mesh/branch transformation tensor	
$D$	Displacement current density vector	$A/mm^2$
$d_a$	Stator bore diameter	m
$d_c$	Enamelled copper wire diameter	m
$d_i$	Inner coil diameter	m
$d_o$	Outer coil diameter	m
$d_w$	Window depth	m
$E_b$	Branch source voltage vector	V
$E_m$	Mesh source voltage vector	V
$E, e$	Coil induced emf	V
$F$	Total armature force	N
$F_{accel}$	Acceleration force	N
$F_{coil}$	Coil force	N
$F_{load}$	Load force	N
$F_{mag}$	Magnetic stiffness force	N
$F_r$	Friction force	N
$f$	Excitation frequency	Hz
$f_r$	Resonant frequency	Hz
$H$	Magnetic field strength vector	A/m

---

$H_a$	Air-gap magnetizing force	A/m
$H_c$	Permanent magnet coercive force	A/m
$h$	Integration step interval	s
$I^b$	Branch current vector	A
$I^m$	Mesh current vector	A
$I, i$	Coil current	A
$I_{actual}$	Actual coil current	A
$I_{demand}$	Demand coil current	A
$I_{error}$	Coil Current error	A
$I_{+limit}$	Upper tolerance band control limit	A
$I_{-limit}$	Lower tolerance band control limit	A
$J$	Coil current density vector	A/mm <sup>2</sup>
$k_{cf}$	Fluxmeter correction factor	
$k_d$	Viscous damping coefficient	Ns/m
$k_i$	DC motor constant	N/A
$k_s$	Magnetic stiffness	N/m
$k_{sf}$	Space factor	
$L_{bb}$	Branch incremental inductance matrix	H
$L_{mm}$	Mesh incremental inductance matrix	H
$L$	Coil inductance	H
$l$	Permanent magnet length	m
$l_a$	Air-gap length	m
$l_c$	Copper wire conductor length	m
$l_p$	Pole-face overlap length	m
$l_w$	Window length	m
$M$	Armature mass	kg
$N$	Number of coil turns	
$N_e$	Number of exciting coil turns	
$N_s$	Number of search coil turns	
$P$	Permeance	Wb/A
$R_{bb}$	Branch resistance matrix	Ω
$R_{mm}$	Mesh resistance matrix	Ω

$R$	Coil resistance	$\Omega$
$S$	Reluctance	A/Wb
$T$	Maxwell stress tensor	
$V_b$	Branch voltage vector	V
$V_m$	Mesh voltage vector	V
$V$	Coil voltage	V
$V_{dc}$	Source DC voltage	V
$V_{in}$	Linear operational amplifier input voltage	V
$V_m$	Permanent magnet volume	m <sup>3</sup>
$v$	Armature velocity	m/s
$W$	Magnetic stored energy	J
$x^b$	Branch armature displacement vector	m
$x^m$	Mesh armature displacement vector	m
$x$	Armature displacement	m
$\lambda$	Coil flux linkage	Wb
$\mu$	Permeability	H/m
$\mu_0$	Permeability of air	H/m
$\mu_m$	Absolute permeability of permanent magnet	H/m
$\mu_{mr}$	Relative permeability of permanent magnet	
$\mu_r$	Relative permeability	
$\rho_c$	Resistivity of copper	$\Omega\text{m}$
$\sigma$	Electrical conductivity	mho/m
$\tau_e$	Electrical time constant	s
$\tau_m$	Mechanical time constant	s
$\phi$	Flux	Wb
$\phi_c$	Control flux	Wb
$\phi_p$	Polarizing flux	Wb

*All other symbols are defined as they appear.*

**INTRODUCTION**

Although by definition, rotary electric motors produce rotary motion, there are nevertheless numerous situations where this is subsequently translated to linear motion, such as machine tools and conveyor systems, or short-stroke reciprocating motion, such as vibrators, compressors or actuator systems. When a rotary motor is used for a short-stroke application, lead or worm screws, gears or other mechanisms are required to convert the rotary motion into linear motion, which adds unwanted complexity and reduces reliability. Various other sources can be used to provide the motion, such as a fluid power source in a hydraulic or pneumatic actuator, but these are mechanically complex, have an appreciable mass, suffer from fluid leakage through seals, and require stringent maintenance.

Producing linear motion directly from a linear motor eliminates the problems mentioned above, and results in a more robust, reliable, quieter and less expensive drive system. In the past, conventional linear solenoids employing mechanical springs have been used, but with the rapid progress in recent years in permanent magnet technology, through the development of high energy rare-earth magnets, a range of high performance linear motors and actuators have become available. These provide an attractive alternative to solenoids and pilot oil-operated devices, and are already used in applications such as Stirling cycle cryogenic coolers, artificial heart devices and aircraft flight surface actuators. One typical device is the permanent magnet linear reluctance motor studied in this thesis.

### **1.1 Thesis Objective**

The objective of this thesis is to undertake research leading to the design and development of a small high performance permanent magnet linear reluctance motor for use in reciprocating electromechanical systems. The motor needs to produce a bi-directional linear output, with the armature returning to its central position in the

absence of excitation current. The force developed needs to be as high as possible, to produce a motor with a high force/volume ratio, and to be linear over the working range of the armature stroke. It also needs to have a good dynamic response. In later chapters, design and optimization considerations are undertaken by using finite element analysis and, by mathematically modelling the motor and its associated dc-to-dc converter, the dynamic response is analyzed.

## 1.2 Thesis Organisation

Chapter 2 outlines the two basic types of limited linear motion electrical machine: the moving-coil and the moving-iron devices, and also presents the fundamental types of variable air-gap linear motor. An overview is given of the requirements and applications for the motor under development, and detailed considerations are made of various candidate motor designs for these applications. The preferred design is determined as the permanent magnet linear reluctance motor, and reasons for its selection are advanced.

Chapter 3 describes in detail the principle of operation of the permanent magnet linear reluctance motor, from which a prototype design is evolved. The selection of appropriate materials for the magnetic circuit and the permanent magnets, and the reasons for their preference, are all discussed. Mechanical design aspects and an optimum design are described.

Chapter 4 introduces the finite element method, the numerical technique used as a tool in the optimization of the linear motor. The equations that represent the magnetic field produced by the motor are developed, and an electromagnetic finite element analysis software package is selected for the modelling process. Modelling of both the magnetic material properties and the permanent magnets is explained. The chapter also describes the pre-processing operations involved, including mesh construction, specifying boundary conditions and excitation sources. Post-processing operations to provide meaningful data from the field solutions are outlined, including equipotential plots, flux linkage and force computations.



The prototype linear motor is modelled and investigated in chapter 5, using the processes described in chapter 4. The static magnetic flux distribution, force and flux linkage characteristics are obtained and compared with experimental results to assess the accuracy of the modelling technique. Conclusions are drawn as to possible design improvements.

Chapter 6 evaluates the dynamic behaviour of the motor, using a mathematical model in the form of a set of first-order differential equations that can be solved using numerical techniques. Two models are developed; the first consisting of the motor in isolation, and the second when a full-bridge dc-to-dc converter is connected at the input terminals, to provide four-quadrant operation with a tolerance band current control scheme. An experimental assessment of the motor is presented, and compared with simulated results to illustrate the effectiveness of the dynamic modelling method.

Chapter 7 improves the static and dynamic characteristics of the motor presented in chapters 5 and 6, by modifying various dimensions of the magnetic circuit. A parametric study is undertaken, by varying the geometric parameters individually, to improve both the static and dynamic performance. The study aims to increase the force acting on the armature, and improve the magnetic stiffness, dynamic performance and linearity. A second prototype motor was designed and manufactured, which allowed further comparisons between theoretical and experimental characteristics.

Chapter 8 continues with modification to the motor magnetic circuit, to further improve its static and dynamic performance. The use of alternative magnetic materials is also considered.

Optimization of the improved design, resulting from chapters 7 and 8, is presented in chapter 9. This is achieved by factorial design, which identifies the geometric parameters most significant in affecting the motor performance, and from this information an optimum design is developed. Two factorial design studies are carried out, an armature parameter study followed by a stator parameter study. The static and

dynamic performances of the optimum design are then compared with those of both the original prototype and the improved design. A detailed specification of the optimum design concludes the work.

Conclusions and suggestions for further work are given in Chapter 10.

**LIMITED LINEAR MOTION ELECTRICAL MACHINES**

Electrical machines are electromechanical devices that contain both electrical and mechanical systems, and a medium in which the two can interact. In practice, the interaction takes place through an electromagnetic field that is common to both systems, with energy being transferred from one system to another as a consequence of this process.

**2.1 INTRODUCTION TO LINEAR MOTORS**

The most common form of electrical machine is the rotary motor, with the various types available including the dc motor, the induction motor and the synchronous motor. These devices are used when the need exists for electrical energy to be converted to rotational mechanical energy, and a corresponding range of linear machines exists for when the need is to produce a linear output.

Just as in a rotary motor, in which an electromagnetic torque is developed to produce rotational motion, the electromagnetic force generated in a linear motor produces linear movement. This can either be over an extended distance, as in transportation and conveyor systems, electromagnetic levitation and launchers [1], or a relatively short displacement, as in short-stroke oscillatory vibrators or shakers [2]. Almost every rotary motor has its analogous linear machine; and linear induction motors, synchronous motors, reluctance motors and pulse motors are all in use.

Linear motors have been designed and developed by applying two fundamental operating principles. The first of these relies on the interaction between a current-carrying conductor and a magnetic field in close proximity, and the second on the alignment of magnetomotive forces. There are two categories of linear motor which exploit these principles; one is the moving-coil design that uses the first principle for the generation of motion and the other is the moving-iron design based on the second

principle. Both types of motor are described below, although emphasis is given to the design and development of novel short-stroke linear motors, often referred to as linear actuators.

## **2.2 MOVING-COIL LINEAR MOTORS**

In moving-coil linear motors, such as electrodynamic oscillators and loudspeakers, magnetic forces arise from electric charges in motion, with a magnetic (Lorentz) force [3] being produced on a conductor which is located in a magnetic field. The magnetic field is usually supplied by a permanent magnet, as shown in Fig. 2.1, and the force produced is directly proportional to the current in the conductor.

An important feature of these devices is that the very light moving member, which consists of a wound coil on a light plastic or paper former, produces a very fast response. In addition, there are no radial forces between the moving assembly and the stator if the coil is not aligned correctly in the concentric position, due to the absence of magnetic material on the moving assembly. This enables the guidance of the moving assembly to be either mechanically lightweight or air cushioned.

## **2.3 MOVING-IRON LINEAR MOTORS**

The moving-iron linear motor shown in Fig. 2.2 has an iron armature and is often referred to as a variable air-gap device, with the force being produced by changes in the magnetic energy stored in the coupling field located in the air-gap. These devices often have both a constant and a controllable source of mmf. The constant source, commonly called the polarizing mmf, is usually provided by one or more permanent magnets and the controllable source, usually known as the control mmf, by a controlled current passing through a coil. Adding or subtracting the two mmfs produces the net force on the armature and hence the motion. The two types of variable air-gap linear motor [4] in common use are described below.

### **2.3.1 Fundamental types of Variable Air-gap Linear Motor**

One form of variable air-gap device, usually used for servo valves, has a configuration in which the moving-iron armature moves in a direction parallel to the polarizing field, as shown in Fig. 2.3. In the other arrangement, used for pen motors and similar devices, the moving-iron moves in a direction perpendicular to the polarizing field, as shown in Fig. 2.4. Although the principles of operation of both types are the same, the output characteristics are very different. Devices whose armatures move in a direction parallel to the polarizing field produce large forces but only over a very limited displacement, whereas those where the armature moves perpendicular to the polarizing field provides a large armature displacement but only a small force. Both types can be designed to move in either direction from the stable rest position, and are able to produce oscillating motion. The radial force existing between the moving-iron and the stator is however a disadvantage and necessitates stiff linear bearings to support the armature.

## **2.4 REQUIREMENTS OF THE LINEAR MOTOR**

This thesis investigates the design of a linear motor, in an attempt to produce a relatively large force over a short stroke length. The motor armature is required to return to its central position in the absence of a control mmf, and to produce the largest possible force for given overall external dimensions. In addition, the requirements for a fast dynamic response and a linear movement over the normal operating range necessitates the force against armature displacement characteristic being linear for the complete range of exciting currents, as shown in Fig. 2.5.

A simple mechanical design is preferred, to reduce manufacturing costs and to enable the motor to be used in applications in the aircraft or automotive industries where reliability is important. The motivation behind the research programme was to develop a short-stroke linear motor that could satisfy all of the above requirements. Appendix A gives a full specification for the linear motor under development.

## 2.5 APPLICATIONS OF THE LINEAR MOTOR

One possible use for a linear motor is to drive the main control valves in primary actuators on board aircraft [5], to control the main flight surfaces such as elevators, ailerons, rudders and spoilers. The control needs to be fast, reliable and continuous and with a high resolution, and is vital for the safe operation of the aircraft. In this application, the motor is required to produce a large output force over a relatively short stroke length. Linear motors are also used in other applications such as driving Stirling cycle cryogenic cooling engines for satellite sensors for high resolution imaging [6], infra-red vision systems and space power systems. Here again they have many advantages over conventional solenoids, oil-operated proportional hydraulic valves and servo valves [7]. In all these applications, the load on the valve provides a centralising force [5, 8] that increases with the armature displacement. The review of linear motor principles that follows attempts to determine the most useful design for this application.

## 2.6 LINEAR MOTOR DESIGN ANALYSIS

Initially, all existing types of linear motor were considered as candidates for the specification proposed in appendix A. However, since the moving-coil linear motor generates both a small force and a small displacement, it was soon rejected. The motor has therefore to be of the moving-iron type, with a symmetrical design to provide the required bi-directional operation about a stable central position. To achieve a long armature stroke length, it must move in a direction perpendicular to the polarizing mmf. Motors in which the armature moves in a direction parallel to the polarizing mmf are very restricted, with the maximum armature displacement being dictated by the length of the air-gaps and typically being less than 2 mm. Although in theory, linear induction, synchronous, dc and stepper motors can all be designed in flat or tubular forms to provide a short-stroke reciprocating movement; linear induction machines were regarded as unsuitable for the present application due to their poor performance at small armature displacements. The detailed appraisal below is restricted to the various forms of motor capable of meeting the specification.

### 2.6.1 Linear Synchronous Motors

There are three basic forms of linear synchronous motor; flat single-sided, double-sided and tubular. Each can be either field or permanent magnet excited, and the choice of motor is dependent on the application. Flat single-sided and double-sided motors are commonly used for ground transportation, where the stator is the track along which the moving member travels. The motors can be either heteropolar or homopolar, with the former having the field winding on the moving member and the three-phase armature winding on the stator, and the latter usually having both windings on the moving member.

For applications requiring a short-stroke reciprocating motion, the tubular linear synchronous motor shown in Fig. 2.6 is used. The field excitation is provided by cylindrical shell type permanent magnets on the moving member, and the polyphase armature windings on the stator core are formed into circular coils. The armature coils are supplied from a static inverter, with the switching pattern of the semiconductor switches governed by signals fed back from a suitable position sensor. The system can be controlled so that its performance is similar to that of a dc motor, and in fact it is often referred to as a brushless linear dc motor [9, 10].

The permanent magnets are made from a rare-earth material with a very high energy product and a high coercivity that enables small sized magnets to be used and the rotor mass to be reduced. The position sensor commonly comprises a number of Hall-effect sensors mounted on the stator teeth. If an armature coil is energised with a fixed dc current, and the moving member is moved throughout its complete stroke length, a trapezoidal force characteristic is produced. The semiconductor switches supplying the armature are gated when the force is a maximum and constant, with this position being sensed by the Hall-effect devices. All phases of the three-phase armature are supplied for the one-third pole pitch during which the force is constant, and switching of the phases produces a constant force function over two pole pitches.

Fast and inexpensive integrated circuits provide in a single package all the inverter functions and processing that are needed, which makes the drive system attractive for the present application. Applications for linear synchronous motors vary from traction [9] to artificial heart pump drives [11].

### **2.6.2 Linear DC Motors**

The principle of operation of the linear dc motor is identical to that of its rotary counterpart and, as with the linear synchronous motor, heteropolar and homopolar versions are available in either flat or tubular arrangements. The major disadvantage of all dc motors is the mechanical commutator and brushes, which necessitate regular maintenance. In addition, carbon deposits from the brushes prevent their use in clean environments and drastically reduces their reliability. However, the iron-cored two-pole tubular linear motor [12, 13], shown in Fig. 2.7, does not use a mechanical commutator or brushes and is suitable for short-stroke reciprocating applications. Its two main components are a field winding located in a stator core and a circular cross-section moving armature wound with a single layer winding. Fig. 2.7 shows that the direction of this winding is reversed at its centre, which results in a dc motor with neither mechanical commutator nor brushes. Flexible wires supply the moving armature and these need to be replaced regularly, reducing the reliability of the device.

Current supplied to the field winding sets up the main field flux, as shown in Fig. 2.7. Under each pole-shoe, the radial component of the flux cuts at right angles the current flowing in the armature winding, and gives rise to an axial force on the armature. Since the output force is dependent on both the field current and the armature current, a very high force can be produced by injecting a high current into the armature winding. One advantage of this motor is its capability for controlling the force/displacement characteristic by use of a graded armature winding [12]. To produce a bi-directional displacement, the current in either the field or the armature windings must be reversed, and to obtain a motor capable of moving over extended displacements shorter pole-shoes can be fitted. Long pole-shoes, as shown in Fig. 2.7, are used only in short-stroke applications, as large displacements would otherwise



cause a reduction in the output force. When the armature winding moves to a position where both directions of current flow are present under the same pole-shoe, the forces produced oppose each other. The field excitation could be replaced by a permanent magnet excitation source, and the mechanical commutator could be replaced with an electronic commutator to make linear dc motors more attractive.

### **2.6.3 Linear Stepper Motors**

Linear stepper motors, also known as linear pulse motors, are incremental motion devices. The input is a series of pulses, each one of which results in an incremental movement dependant on the slot pitch in both variable-reluctance and hybrid permanent-magnet machines [2]. Both flat single-sided and double-sided motors are available [14, 15] for use when a long stroke length is required. For short-stroke applications, a tubular structure is preferred, as this usually results in a smaller sized motor for a given rating compared to a flat type. Another advantage of the tubular construction is the absence of the attractive force across the air-gap that exists in all flat single-sided linear motors.

Generally speaking, tubular linear stepper motors comprise two circular coil windings separated by a circular ring permanent magnet in a soft iron stator core, as shown in Fig 2.8 for a typical two-phase four-pole arrangement. The permanent magnet establishes the polarizing mmf, whereas the two coils provide the control mmf. The stator teeth and those on the moving member are slightly offset. The advantages of this configuration are the simple circular shape of the permanent magnets and the small outer diameter. A major disadvantage, however, is the force imbalance due to the magnetic flux path being longer through the outer poles than through the inner poles, resulting in a reduction of the pull-in force and a larger positional error [16].

A recent important development in linear stepper motor design [16] has eliminated this imbalance and has also increased, by a factor of three, the output force from the device. The new arrangement employs a moving member in the form of a flat shaped permanent magnet, sandwiched between two soft iron pieces to form the circular

cross-section structure shown in Fig. 2.9. The new design is fundamentally different in that the magnetic path for the permanent magnet is circumferential, unlike the axial arrangement of the conventional design, and the flux paths are of equal reluctance. Furthermore, as the permanent magnet is physically much larger than in a conventional motor, the rare-earth permanent magnet material can be replaced by a relatively inexpensive material such as Alnico.

Linear stepper motors have many advantages over other forms of linear motors, since they are mechanically very simple and are therefore very rugged. Incremental steps, as small as 0.1 mm, enable precise positional control to be achieved, and closed-loop operation is unnecessary. They do, however, suffer from overshoot when a step response is demanded and the motor may even experience oscillations. Linear stepper motors are typically used in applications such as aircraft control systems [2], artificial heart devices [17] and control rod drives for nuclear reactors [18].

#### **2.6.4 Linear Reluctance Motors**

Like many other forms of linear motor, variable reluctance devices can either be flat [19, 20] or tubular [7, 22], with the main problem with a flat construction again being the force of attraction across the air-gap. However, with all linear oscillating motors the varying magnetic flux in the iron circuit produces eddy currents that impair the dynamic performance, and with a flat construction the iron circuit can easily be laminated. Although this is more difficult with a tubular construction, it has the advantages of a smaller size for a given rating and the elimination of the attraction force across the air-gap by correct alignment of the moving member in the stator bore.

Due to these advantages, the tubular construction is adopted for the majority of applications and, for reasons of physical size and reliability, they usually contain few components. This keeps the design simple and provides a rugged, reliable and compact device which is ideal for the application presently under investigation. The permanent magnets that provide the polarizing mmf are made from a rare-earth material with a high flux density, a high coercive force and a large energy product

[21], to provide high air-gap flux densities and large forces. A single excitation coil normally provides the control mmf.

The two basic linear reluctance motor designs differ only in the location of the permanent magnets. One design has the magnets positioned on the moving member, while in the other they are on the stator and separated by the coil. The coil itself must obviously be located on the stator, and a typical design is shown in Fig. 2.10. Here the permanent magnets are also located on the stator, which is preferred for manufacturing convenience as a moving-magnet plunger consists of a series of separate components that have to be assembled in a specific order. As a consequence the plunger is less solid than that in the alternative design, where it consists of a single iron rod. Secondly, the brittle nature of rare-earth materials discourages their use on the moving member, which may experience considerable mechanical shock and stress during normal operation.

The principle of linear reluctance motor operation is similar to that of the limited angle torque motor examined in section 2.6.6, and limited angle torque motors are in fact simply rotary versions of the motors considered here. Linear reluctance motors operate [7, 22] by balancing the two forces acting on a moving member positioned on the central axis of two opposing permanent ring magnets, as shown in Fig. 2.10. Exciting the coil located between the two ring magnets disturbs the symmetrical distribution of the polarizing flux in the magnetic circuit of the device. The control mmf produced increases the level of flux at one end of the motor and reduces it at the other, and causes the moving member to move, until the force produced by the energised coil is counter-balanced by the restraining or reluctance force (also known as the magnetic stiffness) due to the permanent magnets and any external load. The reluctance force is caused by the unsymmetrical flux paths and the differing reluctances produced when the moving member is displaced, and it acts as a spring force tending to restore the displacement to zero. Linear reluctance motors are used in various applications, one example being artificial heart actuators [23].

### 2.6.5 Linear Solenoids

Conventional linear electromagnetic solenoids are usually of the flat-faced plunger type. Their design allows only one direction of movement from the stable position, and because the plunger moves in a direction parallel to the main magnetic path large forces are produced over very limited plunger displacements, (see section 2.3.1). An attractive force is generated over an air-gap and, because of this, the force is small when the air-gap is large and vice versa. The force-displacement characteristic follows an inverse square law [24], which creates problems when accurate and fast control of the plunger position is required [5]. These can, however, be overcome by modifying the design of the magnetic circuit, and conical-faced plungers, tapered plungers and cylindrical-faced plungers [24] have all been used to modify and improve the characteristic. In one method, a triangular rim on the stator pole-face is used to produce a smoother force characteristic [25] and in another, a truncated cone shaped plunger and a tapered stator pole-face are used [26] to produce the same effect.

The application under consideration requires bi-directional movement from a stable position, unlike the uni-directional movement obtained from the designs so far discussed in this section. There are, however, bi-directional cylindrical solenoid actuators that eliminate the problem of the inverse square force-displacement characteristic, by including permanent magnets in their design as shown for a typical device in Fig. 2.11 [27, 28]. The position of the plunger located within the two mechanical springs is controlled by using a ring shaped permanent magnet to generate a polarizing mmf, with a coil on either side of the magnet supplying the control mmf. The permanent magnet attracts the plunger to one of the pole-faces, depending on its initial position, and it is held there because the force exerted by the permanent magnet is greater than that of the compressed spring  $S_1$ . The mmf of the exciting coil  $C_1$  reduces the effective flux of the magnet, so decreasing the holding force to less than that produced by the spring. A resultant force then moves the plunger to the other stable position. When the current in coil  $C_1$  is removed the plunger remains in its new position until coil  $C_2$  is excited, because the force produced by the permanent magnet holding the plunger stationary is greater than that produced by the compressed spring.

Since the design of Fig. 2.11 has a stable position at the centre of the plunger stroke, to which the plunger reverts if too little current is fed to the coil, the second prime requirement of the design is achieved. Another design [29] eliminates the need for mechanical springs, by incorporating the permanent magnet on the plunger. The excited coils then simply either repel or attract the permanent magnet to one of three stable positions. Both designs provide a fast dynamic response over a relatively long stroke length, and by using rare-earth permanent magnets high forces can be generated.

### **2.6.6 Limited Angle Torque Motors**

The use of rotary motors to convert rotational motion into limited linear motion was mentioned in chapter 1, the main problem being the lack of suitable gearing to convert multiple revolutions into a short linear stroke. This has been investigated [5], but the excessive gear wear and the limited acceleration achieved made the method unacceptable, even though torque amplification was obtained.

It is possible to convert a limited rotational movement into a limited linear movement by means of a coupling assembly consisting of a ball and socket arrangement directly connected to the motor and load shafts respectively. This arrangement achieves a limited linear motion, without the problems of backlash and shaft speed ripple associated with gearing [30]. The limited rotational movement can be provided by a type of Laws' relay [31, 32], a limited motion high torque rotary actuator [30, 33] frequently called a limited angle torque motor [5, 34]. Two configurations are possible, the first having permanent magnets located on the moving-iron rotor and excitation coils on the stator core, and the second having both magnets and coils on the stator. In the version shown in Fig. 2.12, the rotor typically moves through an angle of  $\pm 10^\circ$  from its central stable position, which could be converted into approximately  $\pm 2$  mm of linear movement using the coupling arrangement described above.

The principle of operation of a limited angle torque motor is well documented [34]. The permanent magnets in Fig. 2.12 establish magnetic fields in the air-gaps between the stator and the rotor blade, and if the rotor is moved from the central stable position the magnetic asymmetry gives rise to a reluctance torque that tends to restore the magnetic circuit symmetry and centralise the rotor.

When the coils are excited, the flux from one of the permanent magnets is increased and that from the other is reduced. The fluxes crossing the air-gaps are therefore unequal and the rotor moves until the torque generated by the excited coil is equal and opposite to the reluctance torque. A new stable position of the rotor is then achieved and a new torque balance established, and for a limited movement the displacement is proportional to the coil current. The main advantage of limited angle torque motors is their high torque/size ratio, and they are used frequently in process control and aerospace applications.

## **2.7 COMPARISON OF LINEAR MOTOR PERFORMANCE**

The proportionality between rotor displacement and coil current of a limited angle torque motor is retained until the rotor moves to a position where the overlap of any one pole approaches zero. In practice this is prevented by locating mechanical pins in the stator to limit the rotor displacement. The characteristic will also become non-linear if the flux produced by the coils exceeds that of the magnets, but this will not occur in a properly designed and controlled motor. The small size of the moving-iron rotor blade results in a fast dynamic response, and the added capability of a centrally stable position of the rotor makes these motors very attractive. Their high power/weight ratio is important in applications where weight is to be minimised, e.g., in aircraft actuators.

Limited angle torque motors have, however, a major problem in their rotary to linear conversion arrangement. The direct coupling assembly limits the maximum linear travel to approximately  $\pm 2$  mm, and although a longer coupling would produce a larger travel, this would be at the expense of mechanical rigidity. The use of complex

moving mechanisms is impractical, due to wear and reliability, and their use would result in a less rugged and compact final product. Due to these factors the limited angle torque motor was rejected for the present application.

The inverse square force-displacement profile of linear solenoids without permanent magnets is extremely difficult to control under fast dynamic conditions, while devices with permanent magnets exhibit a bistable operation. In the designs discussed in section 2.6.5, two, and possibly three, stable positions exist, which makes them unsuitable for the present application where a central equilibrium position is needed when the coil current is removed. The use of the mechanical springs required in one of the designs would inevitably reduce reliability. However, the two bistable solenoid actuators provide a fast high-performance bistable and long stroke operation, and as such the designs are innovative. Permanent magnet linear motors [35], developed by the same designer as the bistable solenoid actuators described above, also have a bistable action. Unfortunately they are complex in their construction, with the coil on the moving member creating many problems, and the use of up to eight permanent magnets make them expensive to manufacture and mechanically complex.

Linear dc motors require a mechanical commutator, and designs employing this were immediately rejected. The linear motor described in section 2.6.2 does not require a mechanical commutator, but the use of flexible wires to supply the moving armature winding is a disadvantage. Another disadvantage is the excessive heat dissipated in the armature winding, which is difficult to remove. Although the force/displacement profile can be controlled to a certain degree by using graded armature windings, this is insufficient to overcome the several disadvantages. A better solution is to use electronic commutation with permanent magnet field excitation.

Linear stepper motors are incremental motion devices and as such are inappropriate for the continuous movement required in the present application, although they do produce positional control even in an open-loop mode. Employing the motor design of section 2.6.3, with its interior permanent magnet mover, will give an increased output force without any imbalance to reduce the pull-in force. A significant

disadvantage of these devices is the high manufacturing cost, due to the need to machine the teeth to a very high tolerance.

A linear synchronous motor supplied through a variable frequency inverter, with the armature currents controlled by signals from rotor position sensors, has ideal control characteristics. It is termed a brushless linear dc motor drive, and has a very good dynamic performance. The small size of the rare-earth magnets used on the rotor results in a compact low mass rotor, with a force/mass ratio several times higher than that of a conventional linear dc motor. Adopting permanent magnet excitation on the rotor reduces the overall heat loss, and the armature windings on the stator can be externally cooled very easily (in contrast to the linear dc motor with the armature windings are on the rotor). The brushless dc drive system is therefore suitable for the present application, provided it is controlled so that when the armature current is removed the rotor returns to its central position.

The last machine to be examined is the linear reluctance motor. This requires very few components, and the simple, rugged and very reliable design is easy, quick and cheap to manufacture. It is also relatively small in size, and since it can be made even more compact if diaphragm spring bearings are used instead of linear bearings, it appears very suitable for the present application. The single coil can be controlled using an H-bridge chopper circuit, with both current and position feedback to produce a very precise positional drive system. Alternatively when used in open-loop it can be a very effective oscillating motor. When properly designed it will produce a strong centralising force when the excitation current is removed, but the large mass required to produce the large magnetic return force causes a poor dynamic response. Nevertheless, it is preferred to the brushless linear dc motor, due to its single excitation coil (rather than a three-phase winding) and the correspondingly simplified control electronics, and therefore was chosen as the most suitable device for the present application.



## **2.8 CONCLUSIONS**

This chapter has introduced the two basic types of limited linear motion electrical machine and presented the two fundamental types of variable air-gap linear motor. An outline of the requirements and applications of the motor under development was also explained. A detailed design analysis of numerous candidate designs suitable for the applications led to the conclusion that the most appropriate choice is the permanent magnet linear reluctance motor.

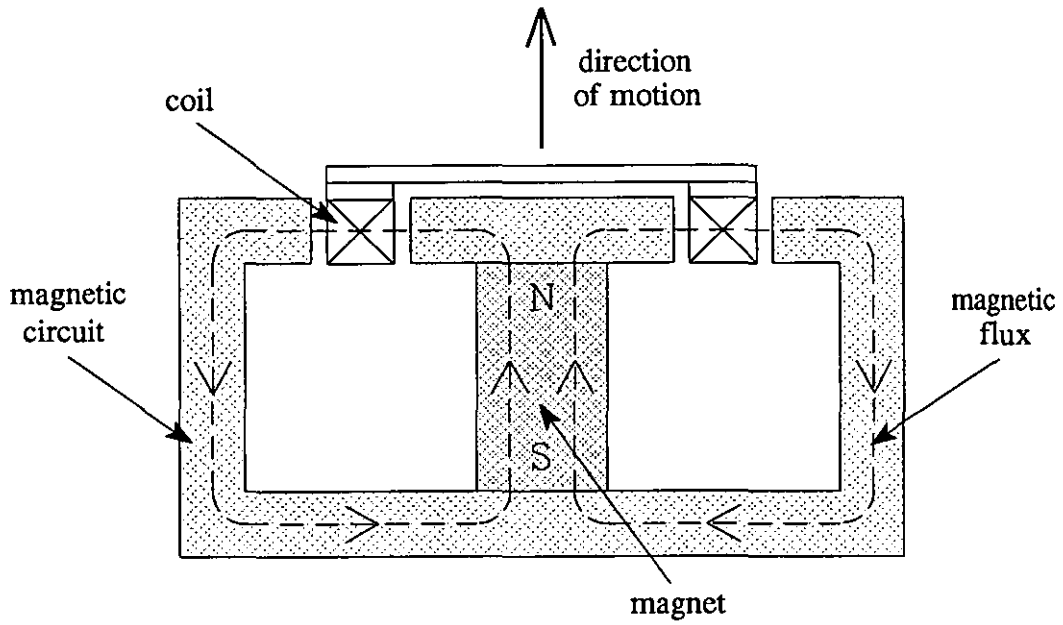


Fig. 2.1 Moving-coil linear motor cross-section

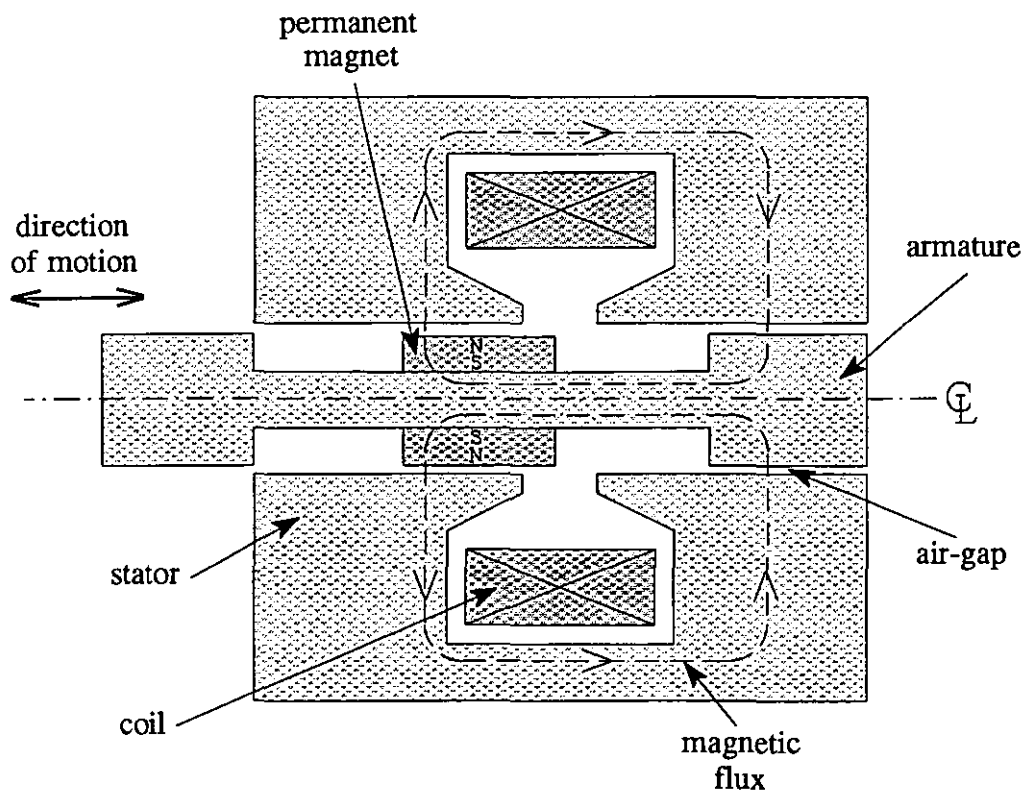


Fig. 2.2 Moving-iron linear motor cross-section

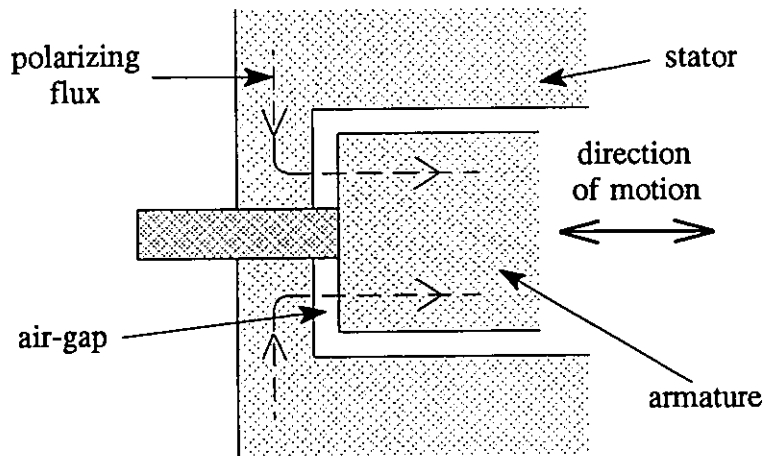


Fig. 2.3 Armature motion parallel to the polarizing field

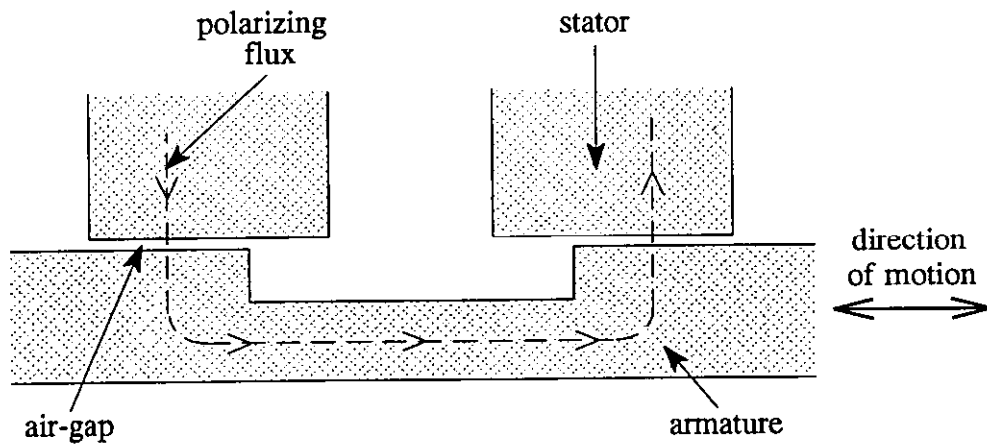


Fig. 2.4 Armature motion perpendicular to the polarizing field

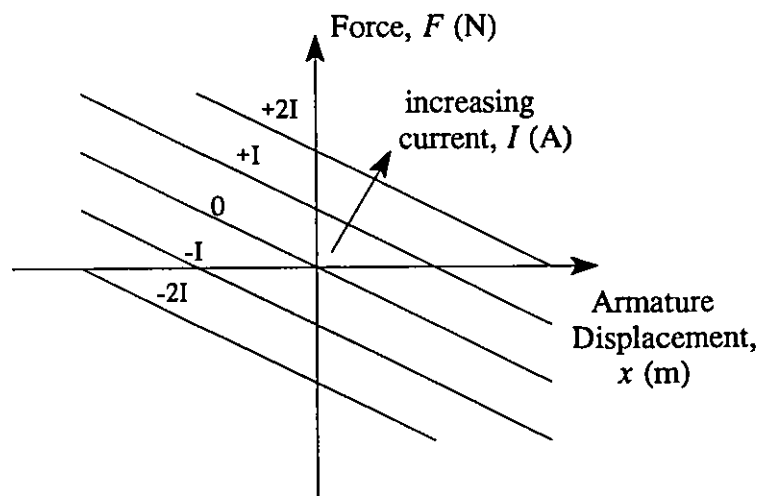


Fig. 2.5 Ideal force/armature displacement characteristic for various currents

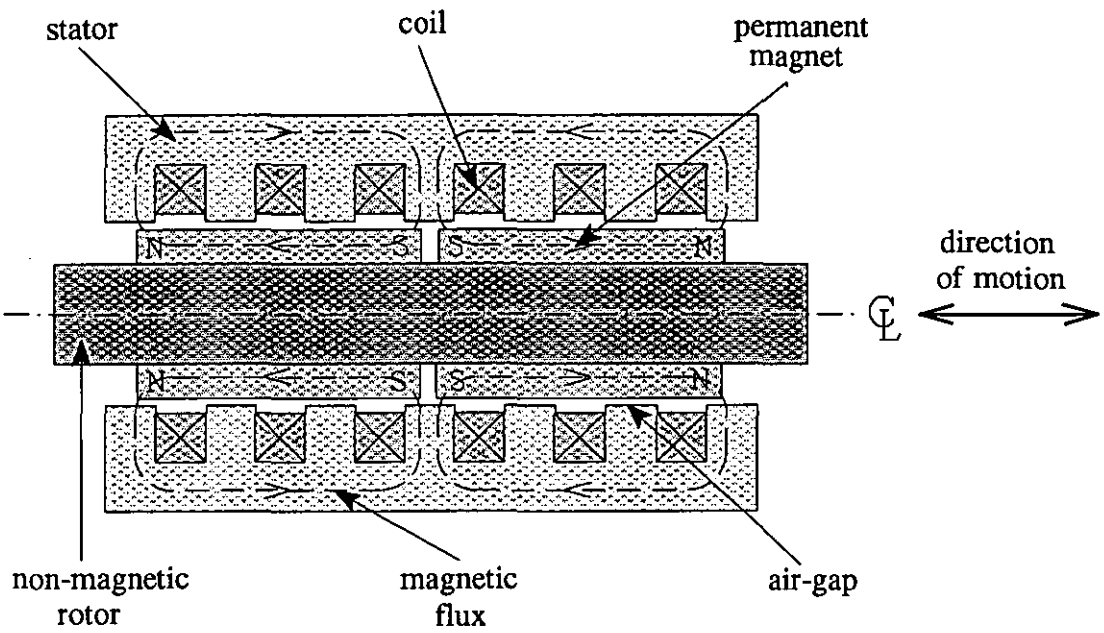


Fig. 2.6 Tubular linear synchronous motor cross-section

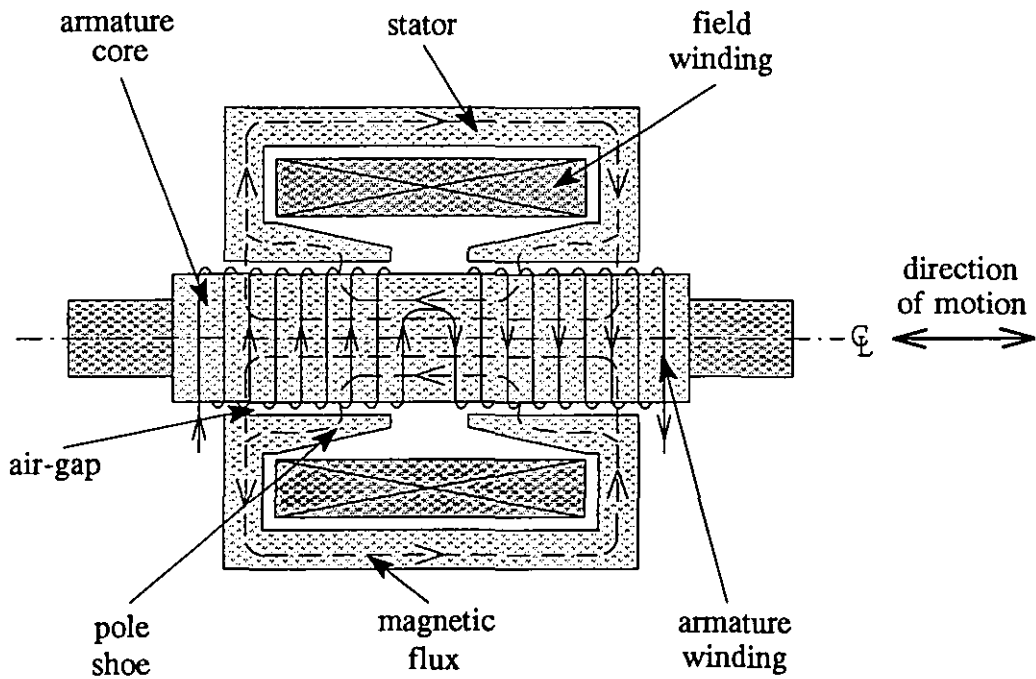


Fig. 2.7 Linear dc motor cross-section

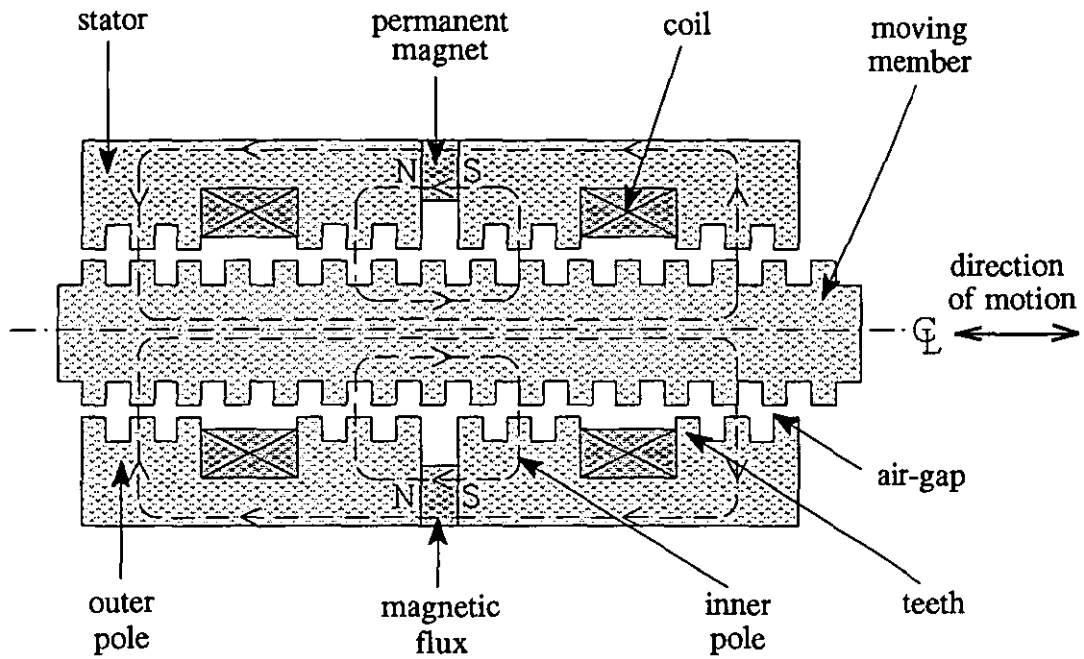


Fig. 2.8 Conventional linear stepper motor cross-section

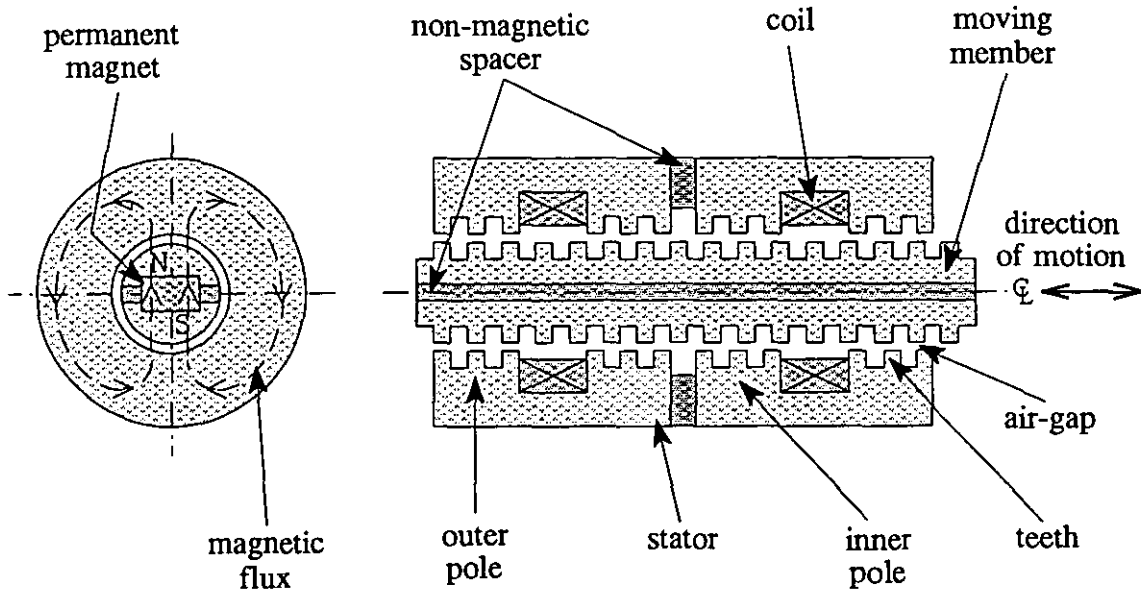


Fig. 2.9 Improved linear stepper motor with interior permanent magnet mover cross-section

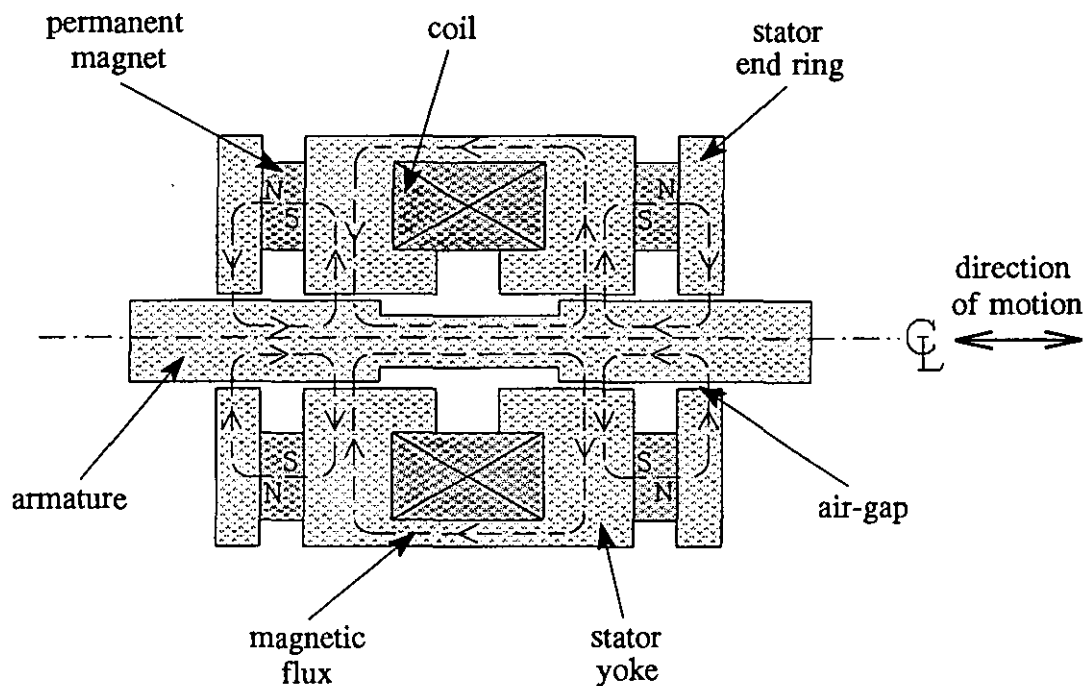


Fig. 2.10 Linear reluctance motor cross-section

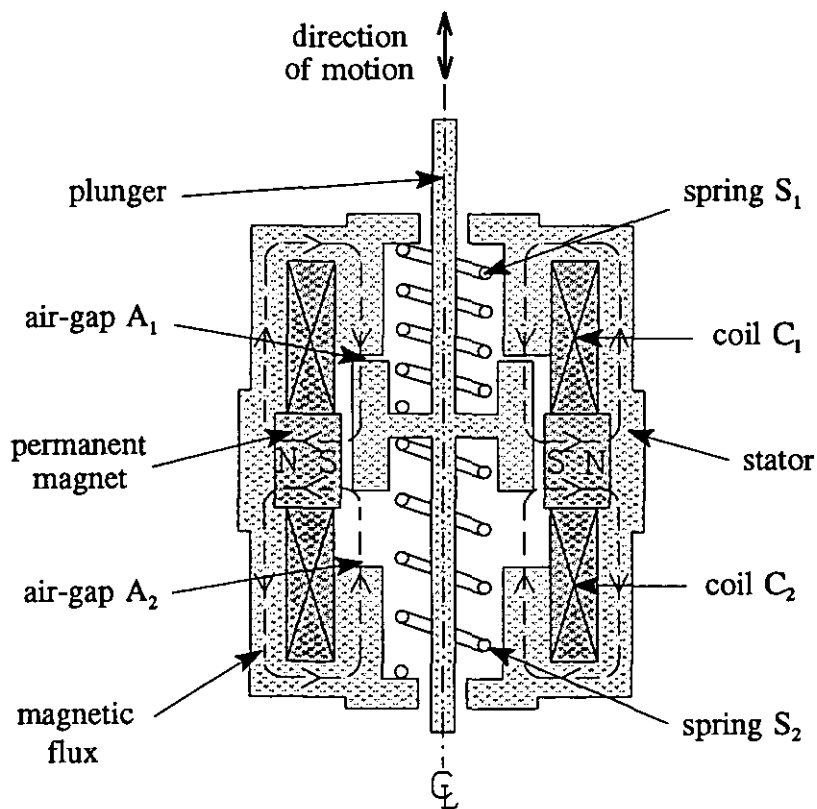
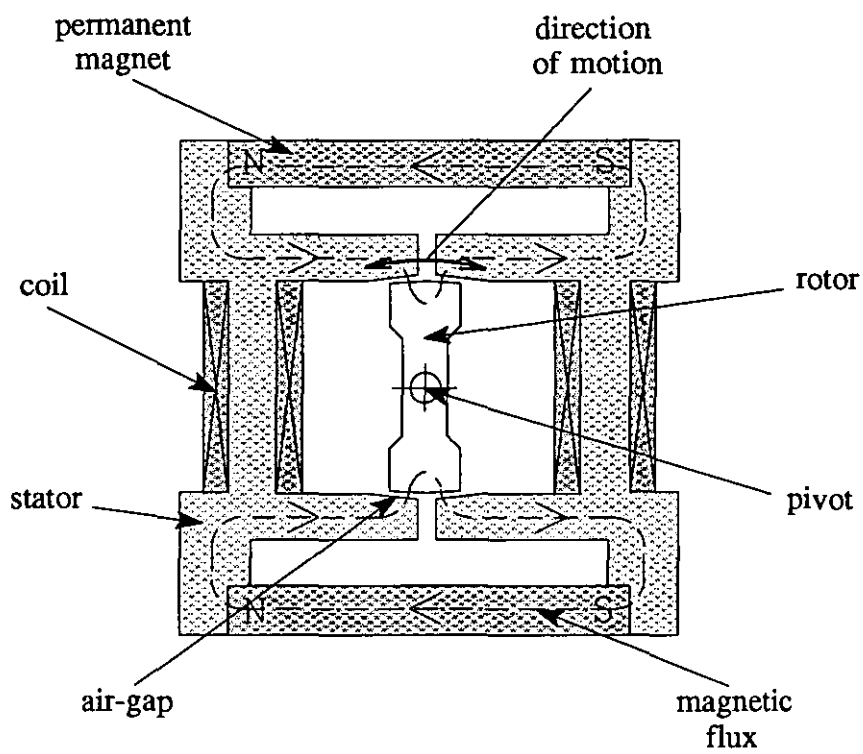


Fig. 2.11 Bistable solenoid actuator with two springs cross-section



**Fig. 2.12** *Limited angle torque motor cross-section*

**PERMANENT MAGNET LINEAR RELUCTANCE MOTOR**

This chapter considers in detail the principle of operation of the permanent magnet linear reluctance motor, from which a prototype design is evolved. The selection of appropriate materials for the magnetic circuit and the permanent magnets and the reasons for their preference are all discussed. Mechanical design aspects and an optimum design are also described.

### 3.1 PRINCIPLE OF OPERATION

The permanent magnets provide the driving force or magnetomotive force  $mmf$ , in the magnetic circuit and produce the polarizing flux  $\phi_p$ . The armature, which moves perpendicular to the flux, has a constant air-gap length  $l_a$  but a variable pole-face area  $A$ . The device will therefore have a relatively long armature stroke but a low value of force  $F$  [4]. The device operates on the flux alignment principle, with the forces produced in the air-gap tending to align the armature and the stator poles in a way that maximises the air-gap flux by minimising the reluctance  $S$  of the magnetic circuit. Fig. 3.1 shows the armature aligned with the stator poles, with a polarizing flux  $\phi_p$  crossing the air-gap of length  $l_a$  and area  $A = \pi d_a l_p$ , (where  $d_a$  is the stator bore diameter, referenced from the centre of the air-gap, and  $l_p$  the length of overlap of the stator and armature pole-faces). The magnetic circuit reluctance is:

$$S = \frac{mmf}{\phi_p} \quad (3.1)$$

Assuming that the magnetic material is infinitely permeable the air-gap  $mmf$  is:

$$mmf = H_a l_a \quad (3.2)$$

where  $H_a$  is the air-gap magnetizing force. The polarizing flux is:

$$\phi_p = B_a A \quad (3.3)$$

where  $B_a$  is the air-gap flux density. Substituting equations (3.2) and (3.3) into



equation (3.1) gives:

$$S = \frac{H_a l_a}{B_a A} \quad (3.4)$$

and substituting  $B_a = \mu_0 H_a$  and  $A = \pi d_a l_p$  into equation (3.4) gives:

$$S = \frac{l_a}{\mu_0 \pi d_a l_p} \quad (3.5)$$

In equation (3.5), both  $l_a$  and  $d_a$  are constant and the air-gap reluctance  $S$  is inversely proportional to the length of the overlap  $l_p$  (or the pole-face overlap area  $A$ ). To minimise the air-gap reluctance this should be as large as possible, which corresponds to the aligned position shown in Fig. 3.1 and clearly maximises the flux crossing the air-gap. If the armature is moved from its aligned position to a new position, as shown in Fig. 3.2, the reluctance increases due to the overlap length  $l_p$  being reduced. Under these conditions a net force  $F$  acts on the armature, tending to align it with the stator pole-face to maximise the flux  $\phi_p$  crossing the air-gap, and hence minimising the reluctance.

Fig. 3.3 shows two magnetic circuits arranged to produce opposing restoring forces. Each circuit has a reduced length of overlap  $l_p$ , and both exert a force on the armature attempting to increase the overlap areas. However, since these forces  $F_1$  and  $F_2$  are equal and opposite, the armature will assume a stable equilibrium position at the central position of the two circuits. Any armature deviation from this position will cause a force imbalance, tending to centralise the armature. The stator and the armature pole-faces in Fig. 3.3 are short, which produces a short armature stroke.

If the stator pole-face is lengthened, as in Fig. 3.4, and the armature configuration is as shown, the resulting increased pole-face overlap allows a greater movement of the armature before the overlap approaches zero. In practice this will not be achieved, due to the large centralising force tending to return it to the central equilibrium position. The centralising force is, in effect, a magnetic spring type return force, that eliminates the use of mechanical springs in the linear motor and is known also as a reluctance force. In the typical characteristic of Fig. 3.5, the force  $F$  on the armature

is zero in the central stable position and very large at large displacements from this position. The characteristic commonly defines the magnetic stiffness of the device, with the force  $F$  obeying the relationship [4]:

$$F = \frac{1}{2} m m f^2 \frac{dP}{dx} \quad (3.6)$$

where  $P = (1/S)$  is the permeance of the magnetic circuit. If the polarizing flux is produced by two ring-shaped permanent magnets, and the armature is positioned on their central axis, the arrangement shown in Fig. 3.6 is obtained. An exciting coil located between the two permanent magnets produces the control flux. When no current flows through this coil, the armature is at its central stable equilibrium position.

When a current is applied to the exciting coil, the control flux  $\phi_c$  that is established disturbs the symmetrical distribution of the polarizing flux. Fig. 3.7 shows the flux paths that are established when a current flows through the coil. Use of the corkscrew rule shows that the magnetic flux produced by the coil current is in the direction shown in the figure. This flux unbalances the reluctance forces acting on the armature, which moves to a new position to restore equal reluctance paths in each magnetic circuit, when the force produced by the excited coil  $F_{coil}$  equals the magnetic centralising force  $F_{mag}$  if the armature shaft is unloaded. This situation is shown in Fig. 3.8, with equilibrium occurring at a displacement  $x'$  when the magnetic energy stored in the air-gap is minimised. If external load is present, the force produced by the excited coil will equal the sum of the centralising force and the external load.

### 3.2 SELECTION OF MATERIALS

The choice of magnetic material for the motor is important, as it has to resist corrosion and withstand arduous environmental and climatic conditions. It must also have a high saturation flux density, to produce a small motor with a high air-gap flux density and a very high output force. The choice of permanent magnet material is also important, since a small motor needs correspondingly small permanent magnets, which must be sufficiently strong to produce the required high air-gap flux density.

### 3.2.1 Magnetic Material

Generally speaking, magnetic materials are required to have a high permeability and a low hysteresis loss, which implies a very narrow hysteresis loop and the lowest possible coercivity [36]. Normal hot-rolled transformer and dynamo silicon-steels suffer from relatively low permeabilities and high hysteresis loss. Commercially available nickel-iron alloys have superior characteristics at low field strengths and flux densities below 0.8 T, when compared with silicon-iron. Three typical alloys, Permalloy A, Radiometal and Rhometal, are compared with 4% silicon-iron and dynamo iron in Table 3.1 [36].

Magnetic Material	Chemical % by weight			$\rho$	$\mu_{ri}$	$\mu_{rm}$	$B_{sat}$	$w_h$
	Ni	Fe	Si					
Permalloy A	78.5	21.5		16	12 000	90 000	1.08	5
Radiometal	50.0	50.0		45	2 000	25 000	1.60	22
Rhometal	36.0	64.0		85	1 800	7 000	0.90	45
4% Silicon-Iron		96.0	4.0	55	500	9 000	1.95	35
Dynamo Iron		100.0		14	250	5 000	2.12	70

- $\rho$  resistivity ( $\mu\Omega\cdot\text{cm}$ )  
 $\mu_{ri}$  initial relative permeability  
 $\mu_{rm}$  maximum relative permeability  
 $B_{sat}$  flux density saturation point (T)  
 $w_h$  hysteresis loss at  $B_{max} = 0.5$  T ( $\text{J}/\text{m}^3/\text{Hz}$ )

**Table 3.1** *Magnetic Material Properties*

The table shows clearly the higher permeability and lower hysteresis loss of the nickel-iron alloys, although this is at the expense of a lower saturation level. Thus, Permalloy A, which has an exceptionally high relative permeability  $\mu_r$  of 90 000, saturates at only 1.08 T. The superior material properties are achieved by heat

treatment with rapid cooling. The advantages of these alloys is that they can be saturated by a relatively small applied field, and it was on this basis that it was decided to use a nickel-iron alloy for the magnetic circuit of the linear motor.

Using a material to its maximum potential with a high saturation level leads to a motor that produces the same force on the armature as a physically larger motor using a material with a lower saturation level. Fig. 3.9 shows the saturation level for the complete range of nickel-iron alloys. It is evident that an alloy of 27% nickel and 73% iron is to be avoided, since it is non-ferromagnetic at room temperature. The material with the highest saturation point is Radiometal, which comprises 50% nickel and 50% iron and has a saturation level of 1.6 T. To ensure that the motor has a good dynamic performance, the material must have a high electrical resistivity to suppress the detrimental effects of eddy currents. Fig. 3.10 shows the electrical resistivity for various alloys, with the highest resistivity clearly associated with alloys containing about 35% nickel. However, materials containing between 25% and 50% nickel still merit consideration. The mean magnetization curves for these alloys and dynamo iron are shown in Fig. 3.11.

The magnetic material chosen for the linear motor was Radiometal 4550. Although it is inferior to Permalloy A, in terms of maximum initial and relative permeability, electrical resistivity and hysteresis loss, the deciding factor in its favour was that it has the highest saturation level of all the nickel-iron alloys. Applications where Radiometal is already used include the cores of precision instrument transformers, galvanometers and special uses in sound reproduction and communication engineering [36].

### 3.2.2 Permanent Magnet Material

In many ways, the requirements of the permanent magnet material are opposite to those of the materials used in the magnetic circuit. They should exhibit a high coercivity and a high remanent flux density, and the hysteresis loop should be as large as possible [37]. In choosing a material for the present application, the quality of a

permanent magnet was judged on its demagnetization curve, which is the part of the hysteresis loop that lies in the second quadrant between the remanent flux density and the coercive force. An important parameter when choosing a permanent magnet material is the point on the demagnetization curve where the  $BH$  product is a maximum, at which the volume of magnetic material required will be a minimum.

Magnet technology over recent years has progressed rapidly due to the introduction of rare-earth materials [37], which have a high coercive force, a high flux density and a large energy product. Three groups (or generations) of rare-earth permanent magnets are identified, based on their chemical composition, and these groups illustrate the historical development of these magnets. The first, developed in the early 1970's, comprises the "1-5" magnets, within which the most widely used material is sintered samarium cobalt ( $\text{SmCo}_5$ ) [38]. The second comprises the "2-17" magnets, which are again based on  $\text{SmCo}$ , and have been in use since about 1980, a typical material being  $\text{Sm}_2(\text{Co,Fe})_{17}$ . They have a better performance than the first generation and are rapidly replacing them in applications where the third generation of magnets cannot be employed. This latest permanent magnets, commercially available since 1983, comprise the "2-14-1" material neodymium-iron-boron  $\text{Nd}_2\text{Fe}_{14}\text{B}$ . They are superior to the best of the first generation, and neodymium is more plentiful than samarium and the supply of iron appears almost endless.

All the rare earth materials have significant advantages over existing types of permanent magnet material, such as Ferrite and Alnico, and their properties are compared in Table 3.2 [21]. The obvious improvements have resulted in magnets becoming smaller in size and lighter in weight, which has allowed the development of more compact motors. This is of major importance in the present work, and will lead to a linear motor capable of a large output force from a physically small package. In general, compact motor designs benefit considerably from the use of materials such as sintered  $\text{SmCo}_5$  and  $\text{NdFeB}$ , which produce devices with high air-gap magnetic fields and high power/volume and power/weight ratios. One major feature of rare-earth magnets is the linear demagnetization curve, which greatly simplifies the modelling of such magnets and aids accurate motor design prediction. The machine

Magnet Material	$B_r$	$H_c$	$BH_{max}$	$T_{max}$	$\rho$
Ferrite	0.40	295	2.9	250	4.9
Alnico	1.24	50	4.0	500	7.3
SmCo <sub>5</sub>	1.01	750	18.5	350	8.4
NdFeB	1.35	1020	36.0	180	7.5

- $B_r$  remanent flux density (T)  
 $H_c$  coercive force (kA/m)  
 $BH_{max}$  maximum energy product (MG-Oe)  
 $T_{max}$  maximum operating temperature (°C)  
 $\rho$  density (g/cm<sup>3</sup>)

**Table 3.2** Permanent Magnet Material Properties

designer is freed from the need to fit complicated mathematical functions to the non-linear demagnetization characteristics that are an inherent property of some Ferrites and all Alnico alloys.

The most recent material to be developed, NdFeB, enables the same design techniques and manufacturing methods to be followed as SmCo<sub>5</sub>, but has a slightly superior performance. From the demagnetization curves for both materials, given in Fig. 3.12, it is clear that NdFeB shows a dramatic improvement over other types of magnets, with a remanent flux density that is superior to Alnico 5-7. In general, NdFeB is preferred to SmCo because it has a higher energy product, higher coercivity and greater remanent flux density [21]. A high coercive force avoids the need for very small air-gaps, which aids production and reduces labour time and costs and also provides a magnet that is less susceptible to demagnetization.

There are however problems with NdFeB magnets. The alloy is subject to corrosion at room temperature, especially in relatively humid atmospheres [39-44], and if untreated turns into a block of oxidised magnetic powder. As a result the surface of

the magnet needs to be coated, and nickel plating, aluminium ion-plating [40] and epoxy resin coating having all been shown to offer good protection [41, 43, 44]. Another method of avoiding corrosion is to add small quantities of dysprosium (an expensive heavy rare earth material) or cobalt [37] to the material of the magnet, none of which has any significant effect on the important properties.

When considering a number of physical and mechanical properties such as wear resistance, hardness, temperature resistance and electrical conductivity, a double coating of Chromium (topcoat) and Nickel (undercoat) has recently shown to be desirable, and is only slightly inferior to epoxy coatings in terms of its protective value [43, 44]. The addition of vanadium, dysprosium or cobalt [39], whilst reducing corrosion, also reduces the deterioration of the magnetic properties at high temperatures. This instability at high temperatures is another problem with NdFeB, since the Curie temperature of only 320 °C means that designers are faced with the problem of keeping the operating temperature below about 180 °C. SmCo<sub>5</sub> is capable of being used up to a temperature of approximately 350 °C and in this respect it is the superior choice. Finally, the mechanical properties of NdFeB, in terms of tensile and compressive strength, are better than that of SmCo, which is very brittle and prone to chipping and cracking.

The permanent magnet material chosen for use in the linear reluctance motor was NdFeB, for the reasons outlined above. Although rare-earth alloys are expensive, their use is necessary to produce an optimum motor design. Mass production of the motor would obviously enable the cost of individual magnets to be reduced dramatically.

### **3.2.3 Coil Material and Assembly**

Copper was chosen for the coil because it is soft, ductile and a good conductor. A number of turns of copper wire were helically wound to form a single layer, with several layers constituting the completed coil. The coil cross-section is rectangular and that of the wire is circular. The coil was wound on a specially prepared insulated bobbin, with a turn of insulation tape between each layer because of the relatively

large inter-layer voltages. Enamel insulated wire was used, because of the high temperatures expected when the motor is operated continuously.

### **3.3 GENERAL DESIGN ARRANGEMENT**

The linear reluctance motor was designed for ease of manufacture and assembly, with each component arranged to be slotted easily into the motor housing.

#### **3.3.1 Mechanical Arrangement**

Fig. 3.13 shows an exploded view of the motor. All the magnetic circuit components are manufactured to a fixed outer diameter of 46.0 mm, and that of the permanent magnets is 40.0 mm. The 57.0 mm total length of the magnetic circuit is divided into three sections; the two end sections consisting of a stator end ring and a permanent magnet, each 5.0 mm long, and the stator yoke of 10.0 mm long along the outer diameter and 15.0 mm along the inner diameter, (or stator bore), to produce the extended stator pole-shoes. The centre section contains the 17.0 mm long stator back iron and the exciting coil. The coil leads are brought out through a slot in one of the stator yokes, and although only one slot is required, another is provided in the other yoke to maintain the symmetry of the magnetic circuit. The armature is of the same material as the stator and the outer diameter is 9.51 mm. The narrow centre-section has a diameter of 7.0 mm and is 21.0 mm long. The air-gap length is 0.305 mm.

The motor is housed in an aluminium structure, and linear bearings support the armature. The most expensive parts are the permanent magnets and the linear bearings, although the bearings could be replaced by diaphragm springs that are stiff in the radial direction, to keep the armature concentric with the stator bore, and free in the axial direction to allow movement of the armature. Such an arrangement would reduce considerably the final cost and also the physical size and mass of the device. Fig. 3.14 shows a photograph of the initial motor design showing the housing, stator magnetic circuit and armature. Figs. 3.15(a) and (b) are two diagrams of the prototype motor, showing the main dimensions of both the stator and the armature.



### 3.3.2 Coil Arrangement

The window area in the stator, where the coil is located, is defined by the dimensions of the stator magnetic circuit. At the preliminary design stage, no knowledge of the coil ampere-turns needed to produce a specific armature displacement was known, and the coil was therefore manufactured to fill completely the window area. The coil length was made slightly smaller than the available window length to allow for any bulging of the coil sides. A further allowance was made for an insulating layer of plastic sheet around the inside of the coil bore and the sides of the coil. The diameter of the enamelled wire  $d_c$  used was 0.40 mm and a current density  $J$  of 3 A/mm<sup>2</sup> would allow a dc current  $I$  of 0.38 A to flow, since:

$$I = JA_c = J \left[ \frac{\pi d_c^2}{4} \right] \quad (3.7)$$

where  $A_c$  is the cross-sectional area of the circular copper conductor. The resulting coil had 25 turns per layer and 23 layers, with the 575 turns producing an *mmf* of 218.5 AT at a current of 0.38 A.

The space factor  $k_{sf}$  of the coil is the ratio of the total cross-sectional area of copper to the total cross-sectional area of the window, or:

$$k_{sf} = \frac{N \pi d_c^2}{4 l_w d_w} \quad (3.8)$$

where  $l_w$  and  $d_w$  are respectively the length and depth of the window and  $N$  is the number of coil turns. The figure obtained for  $k_{sf}$  of 0.48 is typical of that expected when enamelled copper wire and inter-layer insulation are used, and was adopted in all later designs to predict the number of turns that could be located in any given window area. In general, a high space factor is desirable, since the size of a coil to satisfy any given requirements varies inversely as the space factor [24]. The resistance  $R$  of the coil was calculated from:

$$R = \frac{\rho_c l_c}{A_c} \quad (3.9)$$

where  $\rho_c$  is the resistivity of copper and  $l_c$  is the total length of the wire copper conductor given by:

$$l_c = N\pi \left[ \frac{d_o + d_i}{2} \right] \quad (3.10)$$

where  $d_o$  and  $d_i$  are the inner and outer diameters of the coil respectively. Substituting  $A_c = (\pi d_c^2/4)$  and equation (3.10) into equation (3.9), and rearranging, gives:

$$R = \frac{2\rho_c N(d_o + d_i)}{d_c^2} \quad (3.11)$$

The resistance was calculated to be 7.67  $\Omega$  which compared closely with the measured resistance of 7.7  $\Omega$ , and is used in the mathematical modelling of later chapters.

### 3.4 OPTIMUM DESIGN

Due to the complex geometry of the linear motor and the non-linear and hysteretic properties of magnetic materials, the mathematical modelling is very demanding. The motor design involves solving the underlying Maxwell's Equations that govern its behaviour, with numerical methods being the most commonly used techniques. Their use enables numerous comparisons between alternative designs to be produced quickly, and enables dimensional changes to be made and different magnetic materials to be investigated and an optimum design established.

Since the motor utilises permanent magnets, optimization is critical, particularly when an expensive material such as NdFeB, is involved. The use of numerical techniques enables this to be achieved and in the next chapter appropriate methods are investigated for modelling the motor, solving the model to obtain the magnetic field and acquiring meaningful data from the solution to aid in the design optimization.

### **3.5 CONCLUSIONS**

This chapter has described in detail the principle of operation of the permanent magnet linear reluctance motor, from which a prototype device has been designed and developed. Appropriate materials have been chosen for the magnetic circuit and the permanent magnets.

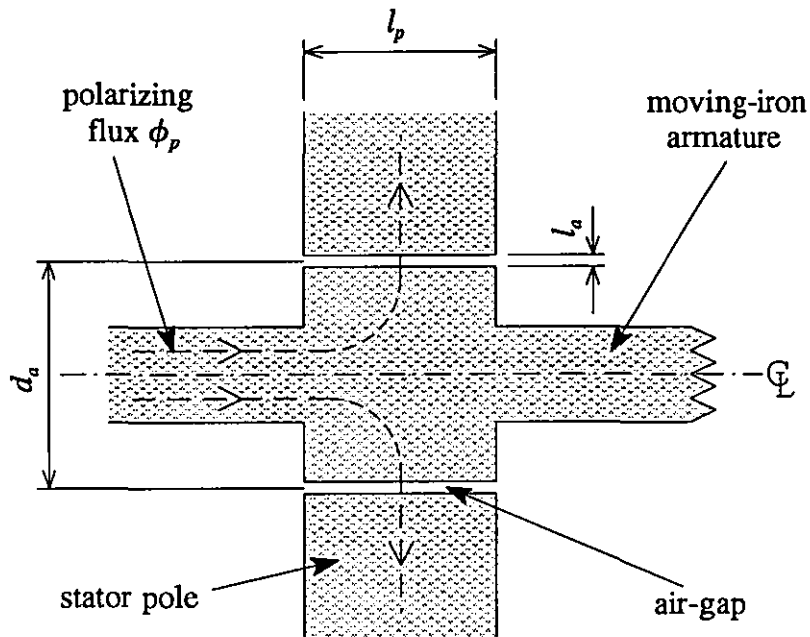


Fig. 3.1 Single stator pole with aligned armature

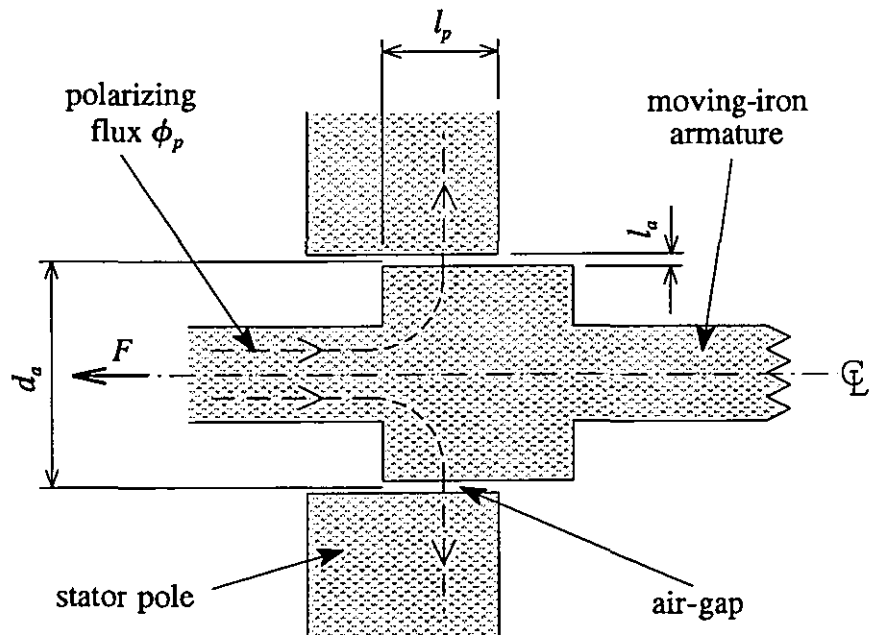


Fig. 3.2 Single stator pole with misaligned armature

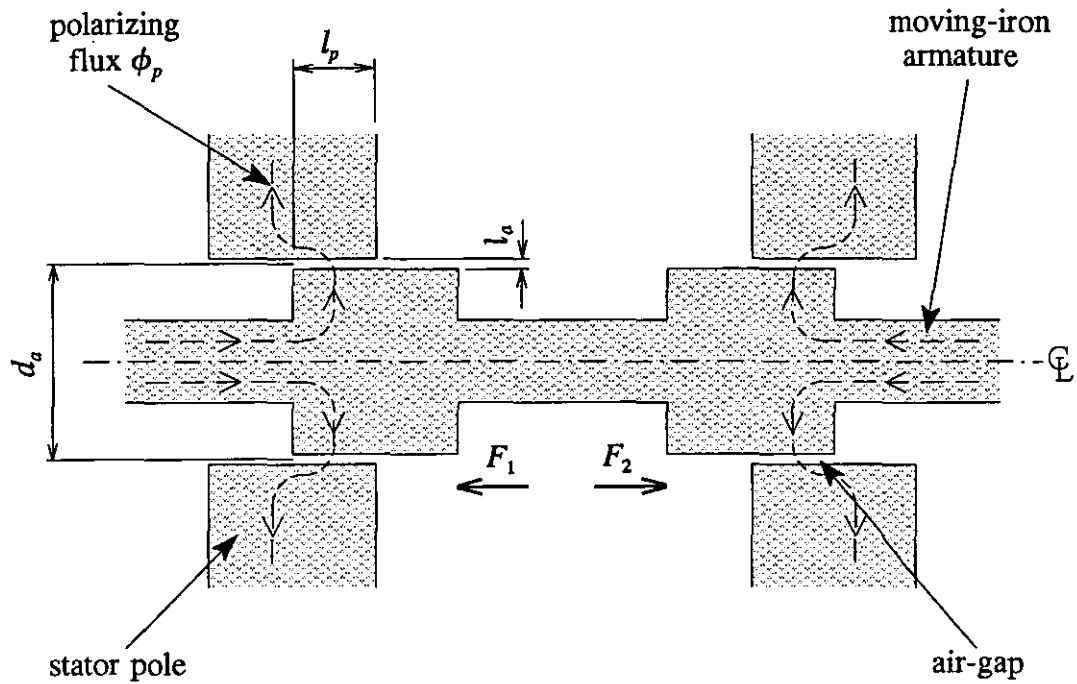


Fig. 3.3 Double stator pole arrangement producing a short armature stroke length

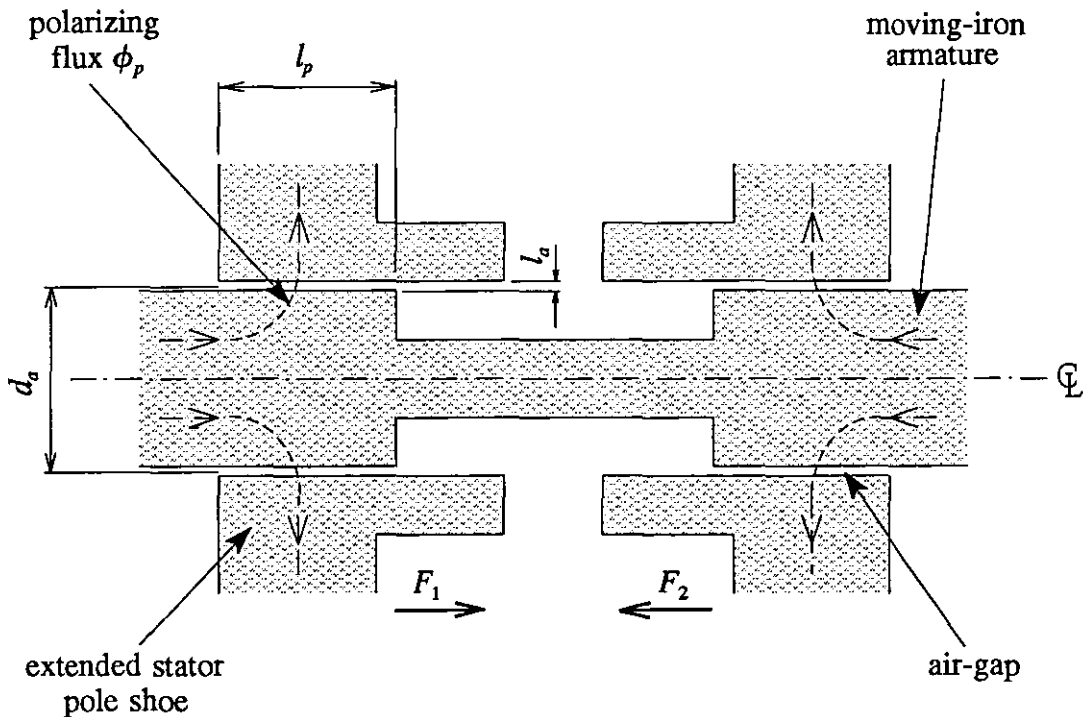


Fig. 3.4 Double stator pole arrangement producing a long armature stroke length

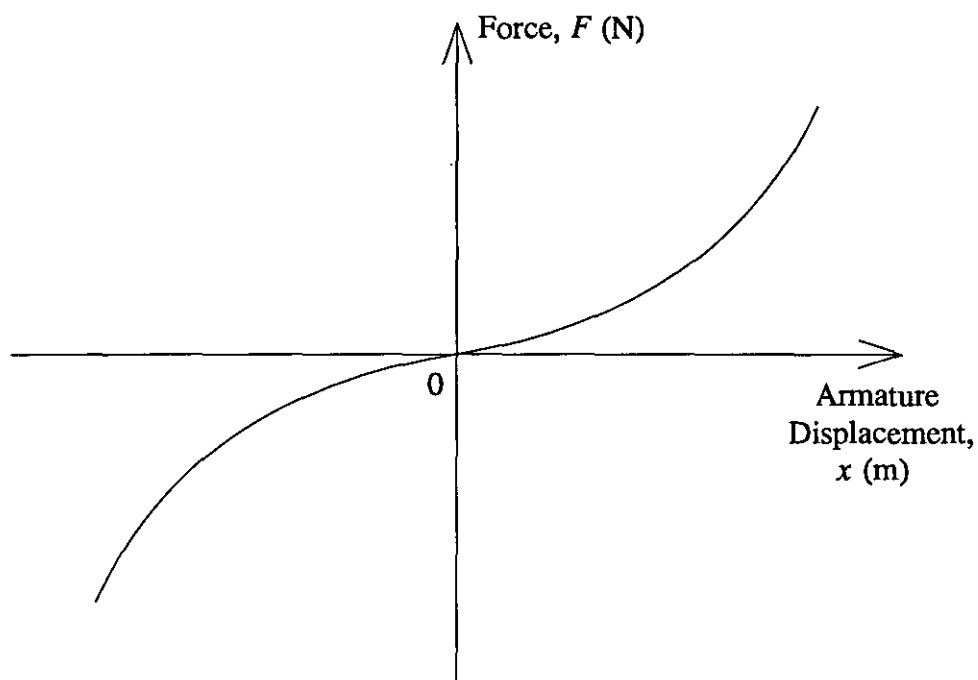


Fig. 3.5 Magnetic stiffness characteristic

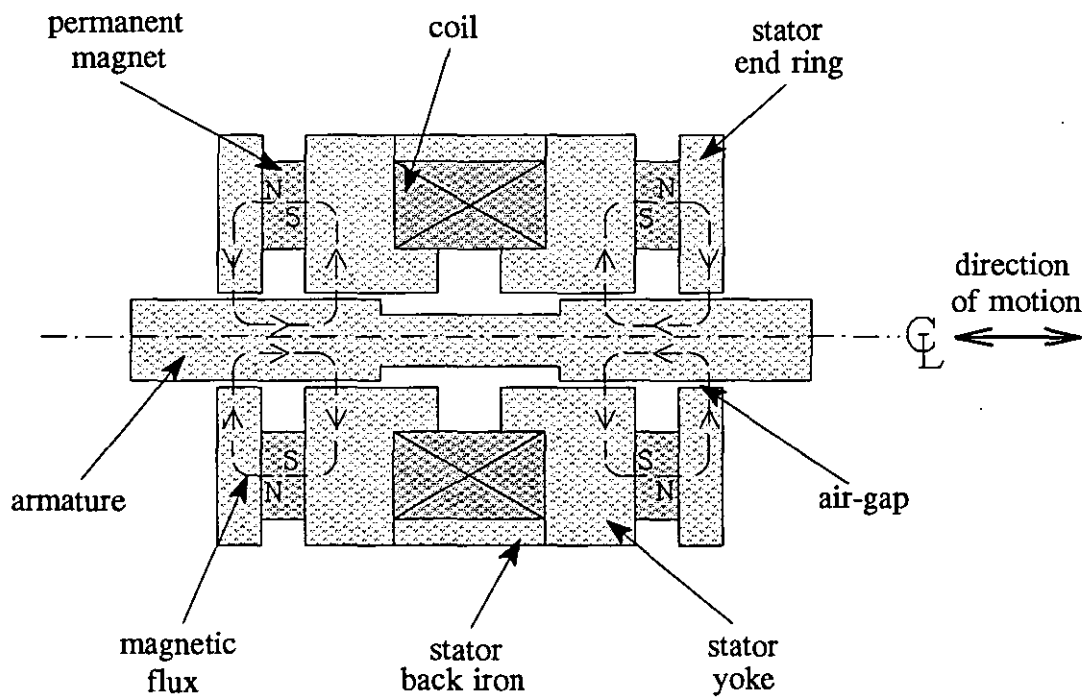


Fig. 3.6 Linear reluctance motor with unexcited coil

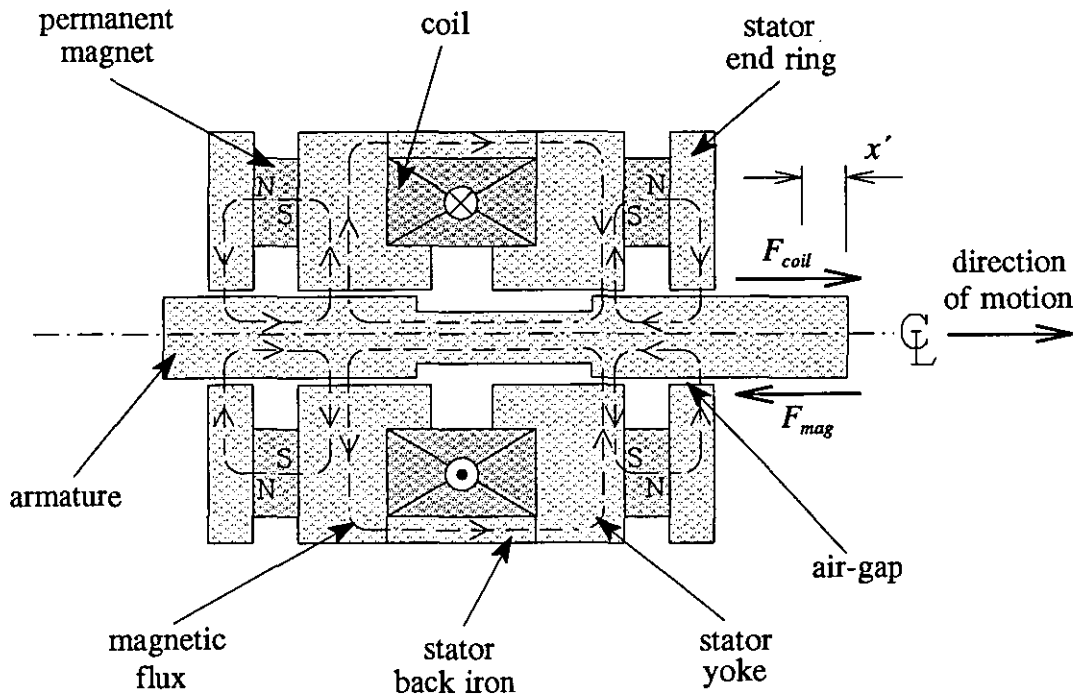


Fig. 3.7 Linear reluctance motor with excited coil

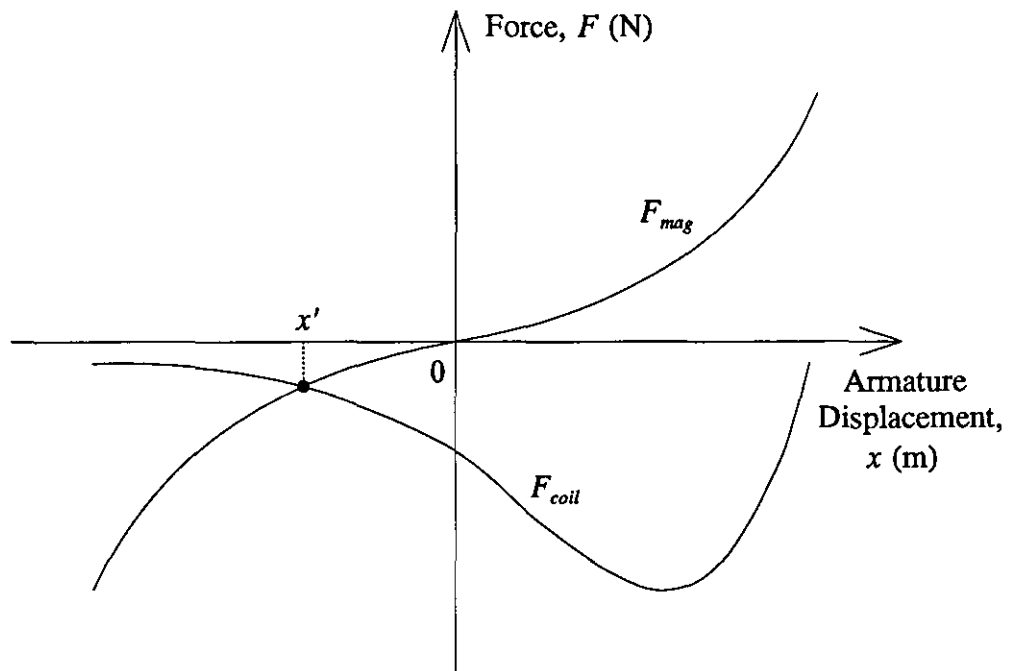


Fig. 3.8 Magnetic stiffness and coil force characteristic

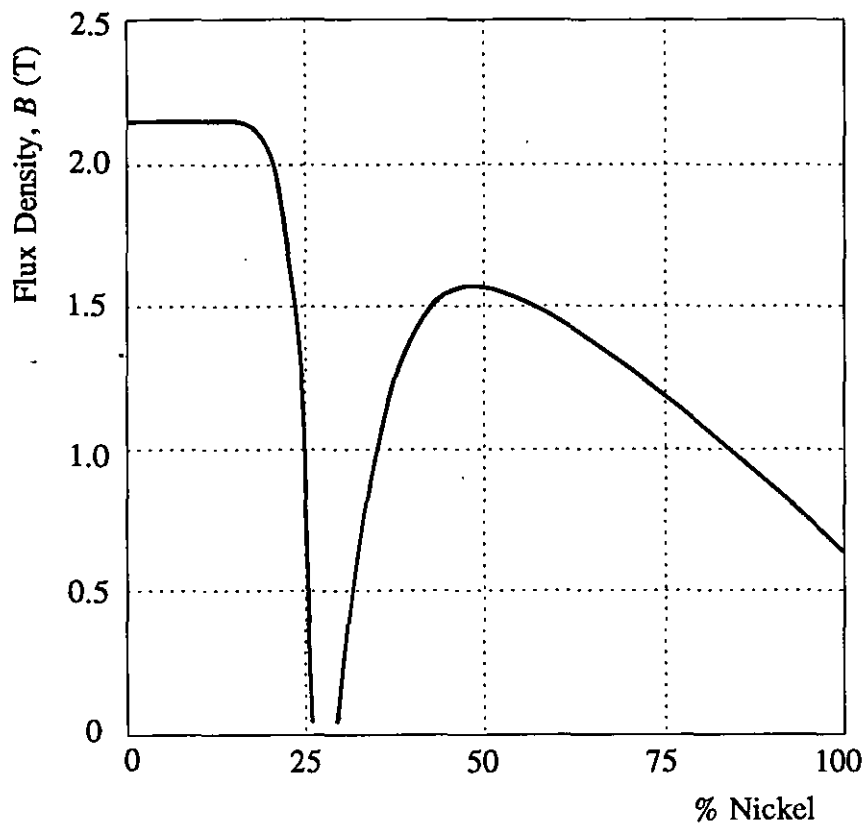


Fig. 3.9 Saturation value of nickel-iron alloys

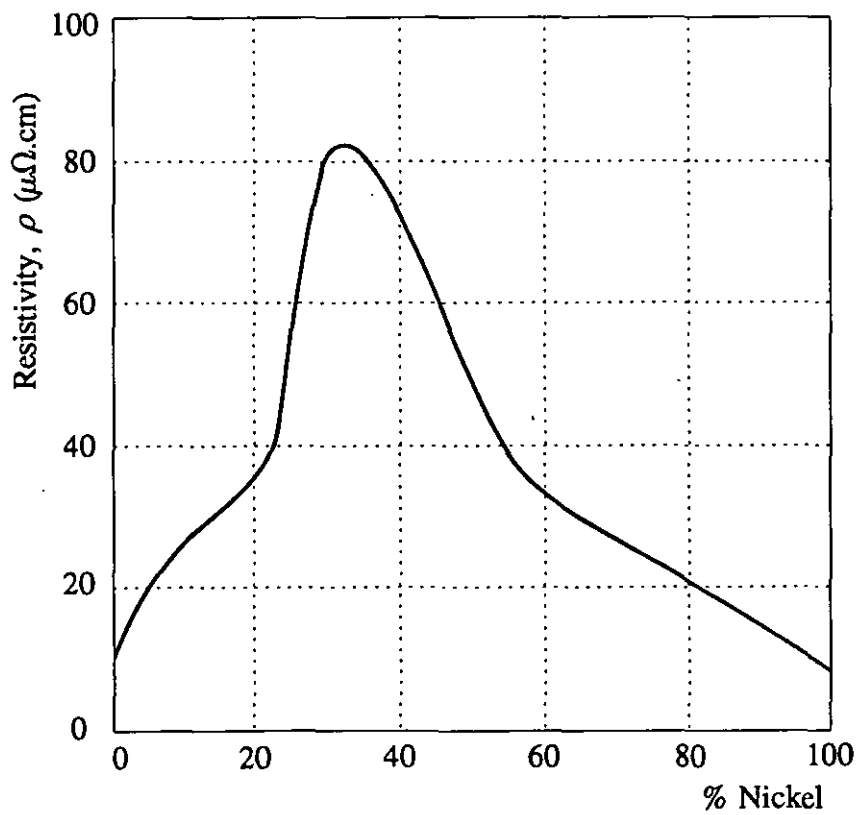


Fig. 3.10 Electrical resistivity of nickel-iron alloys



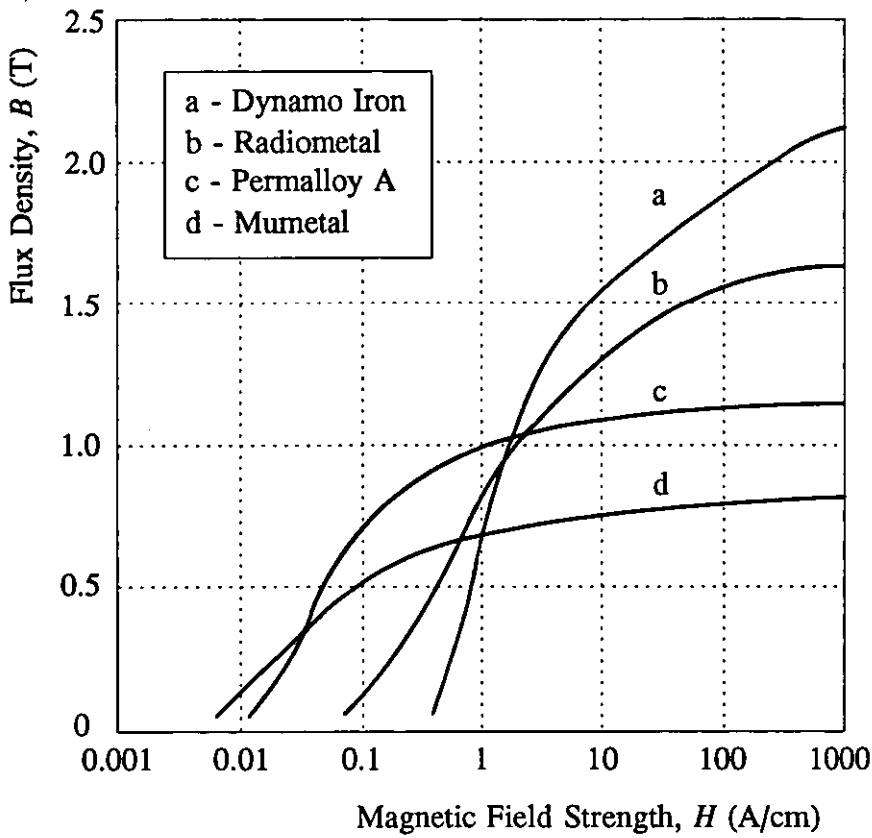


Fig. 3.11 Comparison of BH curves of various nickel-iron alloys with iron

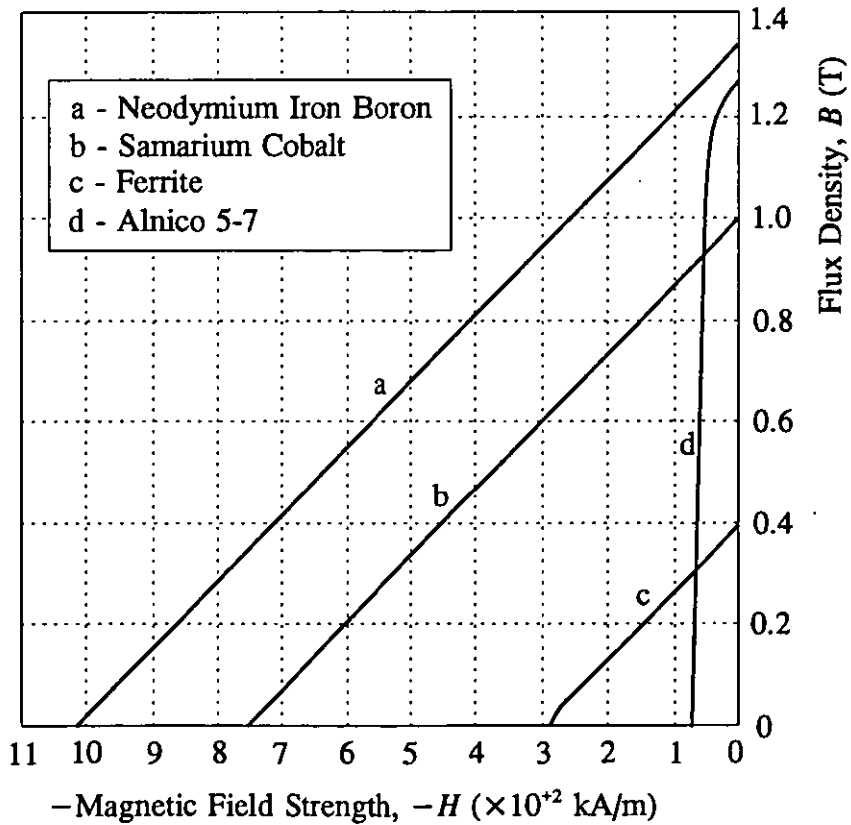


Fig. 3.12 Comparison of four commercial permanent magnet materials

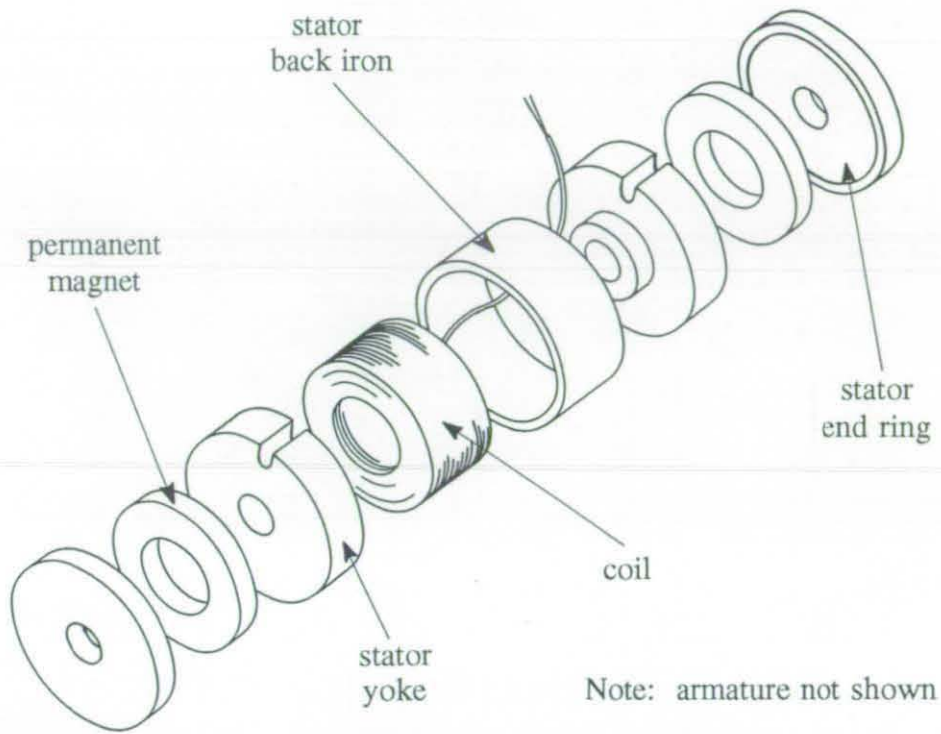


Fig. 3.13 Construction of the linear reluctance motor



Fig. 3.14 Linear reluctance motor housing, stator and armature

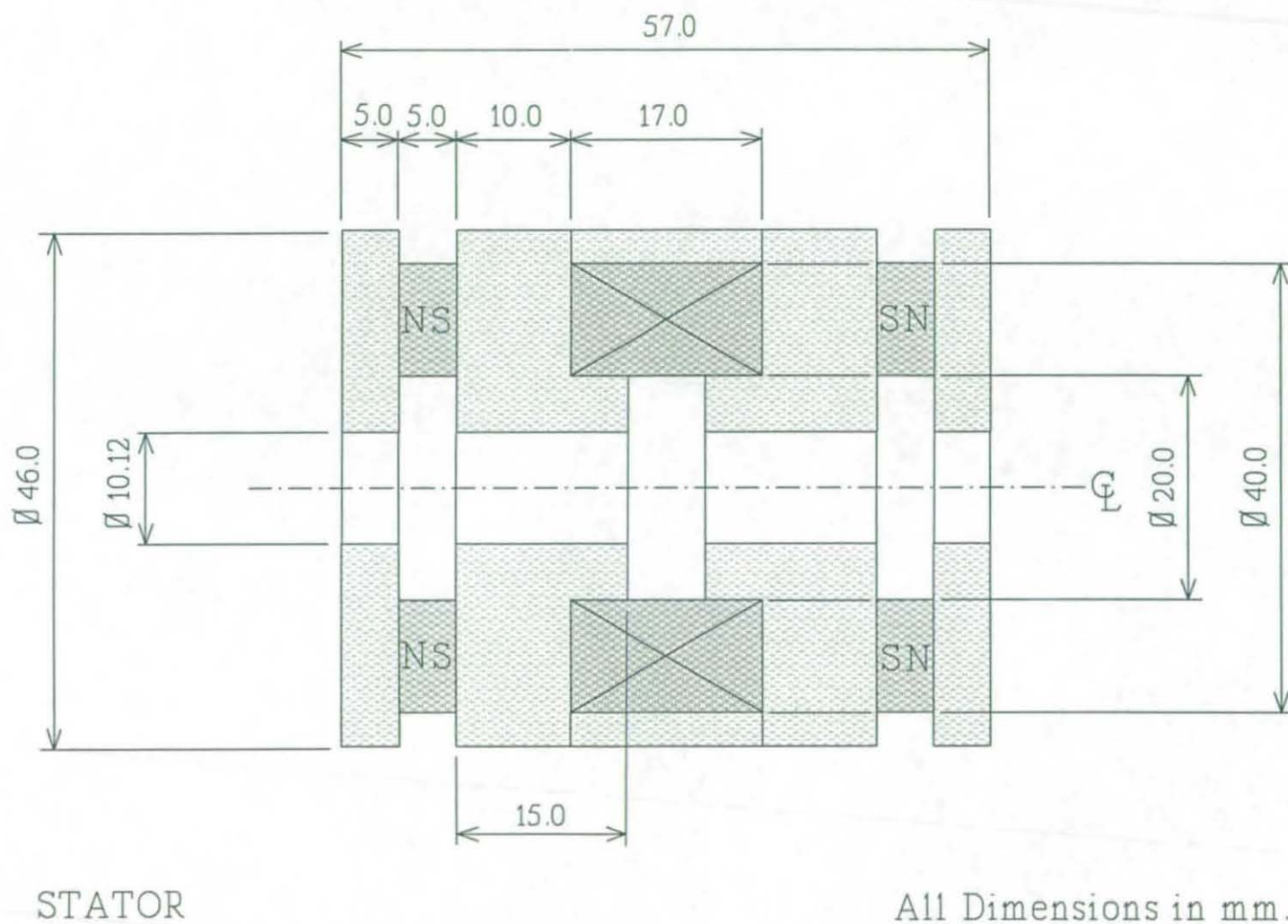
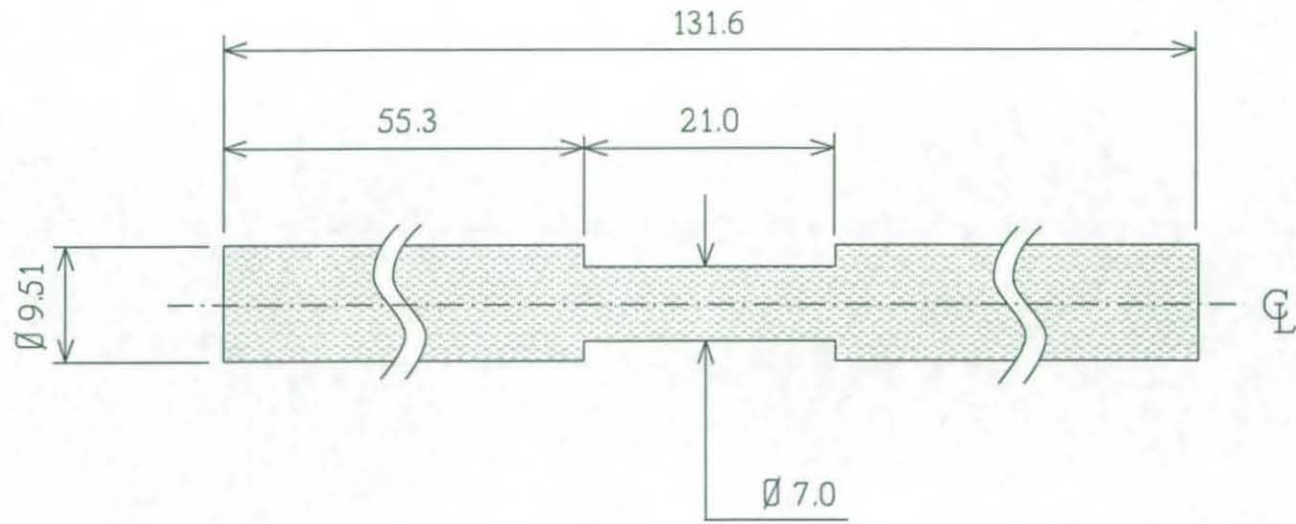


Fig. 3.15(a) Main dimensions of the prototype motor stator



ARMATURE

All Dimensions in mm.

**Fig. 3.15(b)** Main dimensions of the prototype motor armature



**FINITE ELEMENT ANALYSIS AND MODELLING**

Electromagnetic fields govern the behaviour of all electromagnetic devices, and to analyze and predict the performance of an electrical machine, Maxwell's equations have to be solved. In the past, analytical methods were used extensively, but to enable a solution to be obtained these machine models had to be simplified to such an extent that they led to inaccurate field distributions in many applications. In addition, with complicated magnetic structures and magnetic non-linear materials it was at best very difficult to solve a problem with any accuracy. However, numerical formulations can handle accurately both complex structures and non-linearities and can faithfully predict the performance of a machine. With the continuing advances in computer processor speed and memory capacity, a large model can now be solved within a matter of minutes, and today such methods are almost exclusively employed.

**4.1 NUMERICAL METHODS IN ELECTRICAL ENGINEERING**

In the 1940's, finite differences formed the basis of the main methods used for machine simulation. The problem region is discretized into a rectangular grid, usually an approximation to the geometry of the problem, and the magnetic field is solved at all the grid points. Curved boundaries and varying sources cannot however be modelled using general data structures, and since general purpose software is difficult to write for complicated problems a new program was usually required for every new machine analyzed. The most powerful numerical method used today is the finite element method [45-47]. The problem region is now divided into smaller regions, known as elements. A trial function is assumed over each element with the nodes at the vertices of each element being the variables of the trial functions. The finite element method consists basically of solving for the unknown nodal variables, by minimizing some quantity related to the stored field energy. The method allows large and complicated electromagnetic field problems to be solved very easily and reliably, and it has numerous advantages over other numerical methods, including the finite

difference method. It is very simple mathematically, with general data structures, and by making the finite elements very small it is possible to increase the accuracy of the solution in regions of particular interest, making it very flexible. The elements can have various shapes to accommodate easily any intricate geometry, and it is also easy to include boundary conditions in the formulation of a problem. Using the method results in a sparse symmetric and positive definite matrix to be solved, which is economical on computer memory and thus processing time.

The finite element method was initially used in the electrical engineering field in the late 1960's, for designing magnetic lenses and accelerator magnets, and for low frequency power applications utilising saturable magnetic materials in the form of two-dimensional magnetostatic techniques in the early 1970's [48]. It was subsequently applied to electrical machine problems [49, 50]. The use of the method soon became widespread and, today, the very sophisticated software that is in use provides a fast, powerful, accurate, and easy to use tool for solving very large two- and three-dimensional, static and transient problems involving complex structures, moving conductors and material non-linearity. It is the numerical technique that is used to model the magnetic field in the linear reluctance motor under consideration.

## 4.2 REPRESENTATION OF THE MAGNETIC FIELD IN THE MOTOR

Modelling and analyzing the linear motor requires the solution of both time invariant and time variant magnetic fields. In the next two sections the equations that have to be numerically solved are formulated.

### 4.2.1 Time Invariant Magnetic Field

The sources of the magnetic field in the linear motor are a constant current of density  $J$ , from the excited coil, and the two permanent magnets which have a remanent flux density  $B_r$ . In differential form the Maxwell equation that describes the first of these is:

$$\nabla \times \mathbf{H} = \mathbf{J} + \frac{\partial \mathbf{D}}{\partial t} \quad (4.1)$$

where  $\nabla$  is the partial differential operator and  $\times$  is the vector product [51, 52].  $\mathbf{H}$  is the magnetic field strength and  $\mathbf{D}$  is the displacement current density. The two permanent magnets, are defined by:

$$\mathbf{B} = \mu_m \mathbf{H} + \mathbf{B}_r \quad (4.2)$$

where  $\mathbf{B}$  is the magnetic flux density and  $\mu_m$  is the absolute permeability of the permanent magnet material. Combining equations (4.1) and (4.2) [53], yields:

$$\nabla \times \mathbf{H} = \mathbf{J} + \nabla \times \frac{1}{\mu_m} \mathbf{B}_r + \frac{\partial \mathbf{D}}{\partial t} \quad (4.3)$$

For a time invariant case any changes with respect to time are zero, the last term of equation (4.3) is therefore zero and the equation simplifies to:

$$\nabla \times \mathbf{H} = \mathbf{J} + \nabla \times \frac{1}{\mu_m} \mathbf{B}_r \quad (4.4)$$

The constitutive equation that describes the behaviour of the linear materials in the linear motor (including the surrounding air) is:

$$\mathbf{B} = \mu \mathbf{H} \quad (4.5)$$

where  $\mu$  is the absolute permeability. Lines of constant  $\mathbf{B}$  are always in a closed form, so that:

$$\nabla \cdot \mathbf{B} = 0 \quad (4.6)$$

where  $\cdot$  is the scalar product. Equation (4.6) is another of Maxwell's equations, which, using a secondary vector  $\mathbf{A}$  (the magnetic vector potential), can be expressed as:

$$\mathbf{B} = \nabla \times \mathbf{A} \quad (4.7)$$

Rearranging equation (4.5) for  $\mathbf{H}$  and eliminating  $\mathbf{B}$  using equation (4.7) yields:

$$\mathbf{H} = \frac{1}{\mu} \nabla \times \mathbf{A} \quad (4.8)$$

Substituting equation (4.8) into (4.4) results in:

$$\nabla \times \frac{1}{\mu} \nabla \times \mathbf{A} = \mathbf{J} + \nabla \times \frac{1}{\mu_m} \mathbf{B}_r \quad (4.9)$$

Using the vector identity [45, 51]:

$$\nabla \times (\nabla \times \mathbf{A}) \equiv \nabla(\nabla \cdot \mathbf{A}) - \nabla^2 \mathbf{A} \quad (4.10)$$

and for  $\mathbf{A}$  to be unique and determinable, its divergence and curl have to be defined, therefore  $\nabla \cdot \mathbf{A}$  is set to zero. The first term on the right-hand side of equation (4.10) is then zero. Substituting the second term into equation (4.9) and rearranging gives:

$$-\frac{1}{\mu} \nabla^2 \mathbf{A} = \mathbf{J} + \nabla \times \frac{1}{\mu_m} \mathbf{B}_r \quad (4.11)$$

The left-hand side of equation (4.11) and the first term on the right-hand side is the vector *Poisson equation*, that describes the magnetic field of an electromagnetic device containing no magnets. The second term on the right-hand side of equation (4.11) is the permanent magnet source, so that equation (4.11) describes the static field of a permanent magnet device, and has to be solved to find the magnetic field distribution. To determine the distribution in the air region involves solving:

$$\nabla^2 \mathbf{A} = 0 \quad (4.12)$$

This equation is identical to equation (4.11), with the source terms set to zero since air is not a source of flux. Equation (4.12) is the vector *Laplace equation*. The solution to equations (4.11) and (4.12) is achieved using the finite element method [45-47].

## 4.2.2 Time Variant Magnetic Field

The source of the time variant magnetic field in the linear motor is the current density  $\mathbf{J}$  in the exciting coil, and the derivation of the corresponding equation is initially



similar to that given above in section 4.2.1. When time variation is introduced the magnetic field affects the initial electric field and by using equation (4.7) results in:

$$\nabla \times \mathbf{E} = -\frac{\partial \mathbf{B}}{\partial t} = \nabla \times -\frac{\partial \mathbf{A}}{\partial t} \quad (4.13)$$

where  $\mathbf{E}$  is the electric field intensity.  $\mathbf{E}$  and  $-\partial \mathbf{A}/\partial t$  only have the same curl if:

$$\mathbf{E} = -\frac{\partial \mathbf{A}}{\partial t} - \nabla \phi \quad (4.14)$$

where  $-\nabla \phi$  is the imposed electric field and  $-\partial \mathbf{A}/\partial t$  is the induced electric field. Substituting equation (4.14) into (4.3) and using  $\mathbf{J} = \sigma \mathbf{E}$ ,  $\mathbf{H} = \mathbf{B}/\mu$  and neglecting the time variant displacement current density  $\mathbf{D}$  which is negligible in low frequency power applications yields [45]:

$$\nabla \times \frac{1}{\mu} \nabla \times \mathbf{A} = -\sigma \nabla \phi - \sigma \frac{\partial \mathbf{A}}{\partial t} + \nabla \times \frac{1}{\mu_m} \mathbf{B}_r \quad (4.15)$$

where  $\sigma$  is the conductivity of the materials. The imposed current density  $\mathbf{J}_0 = -\sigma \nabla \phi$ . Using equation (4.10) and the gauge  $\nabla \cdot \mathbf{A} = 0$ , results in [45]:

$$-\frac{1}{\mu} \nabla^2 \mathbf{A} + \sigma \frac{\partial \mathbf{A}}{\partial t} = \mathbf{J}_0 + \nabla \times \frac{1}{\mu_m} \mathbf{B}_r \quad (4.15a)$$

which is the vector *Diffusion equation*. The solution to the above equation is achieved using the finite element method and a suitable time marching algorithm, such as the Crank-Nicholson technique.

### 4.3 AXI-SYMMETRIC FORMULATION

It is of paramount importance that the motor model is as simple as possible, containing as few elements and nodes as practicable. The cylindrical structure of the motor enables it to be modelled in cylindrical coordinates  $r, \theta, z$ . However, since the motor is symmetrical about its central axis the model can be reduced from three-dimensions  $r, \theta, z$  to only two-dimensions  $r, z$  which drastically reduces the size of the problem and also achieves a reduction in the computation time.

Fig. 3.13 shows that the linear motor is not strictly axi-symmetric, due to the two slots in the stator yokes which allow the coil leads to be brought out. However, neglecting these will have only a very small effect on the accuracy of the solution. Fig. 4.1 shows the reduction of the problem from three-dimensions to two. The field quantities, such as the flux density  $\mathbf{B}$ , obtained from a two-dimensional axi-symmetric analysis are function of  $r$  and  $z$  only, so that, from equation (4.7), the magnetic vector potential  $\mathbf{A}$  is a function of  $\theta$  only. The coil in the motor rotates symmetrically around the central axis and because the current density  $\mathbf{J}$  in the coil has only the one component  $J_\theta$  the magnetic field strength  $\mathbf{H}$  has only the two components  $r$  and  $z$ , satisfying the equation  $\nabla \times \mathbf{H} = \mathbf{J}$ , therefore:

$$\mathbf{A} = u_\theta A \quad (4.16)$$

$$\mathbf{J} = u_\theta J \quad (4.17)$$

where  $u_\theta$  is a vector of unit length in the  $\theta$  direction. This permits equations (4.11) and (4.15), to be simplified respectively as:

$$-\frac{1}{\mu} \nabla^2 A_\theta = J_\theta + \nabla \times \frac{1}{\mu_m} B_{rz} \quad (4.18)$$

and:

$$-\frac{1}{\mu} \nabla^2 A_\theta + \sigma \frac{\partial A_\theta}{\partial t} = J_\theta + \nabla \times \frac{1}{\mu_m} B_{rz} \quad (4.19)$$

where  $B_{rz}$  is the remanent flux density vector. The vector  $\mathbf{B}_r$  has only one component, which as shown in Fig. 4.1 is in the direction of magnetization of the permanent magnets (the  $z$  direction).

#### 4.4 ELECTROMAGNETIC FINITE ELEMENT ANALYSIS SOFTWARE

The finite element method applied to electromagnetic problems is explained in detail elsewhere [45, 47]. The software employed for modelling the linear motor requires the following features:

- 2D axi-symmetric magnetostatic and transient formulations based on  $A$ ;
- Non-linear permeability for both magnetostatic and transient formulations;
- Modelling of permanent magnets with a linear demagnetization characteristic;
- Current- and voltage-forced coils of a specific resistance;
- Movement of sub-sections of meshes and;
- Extensive pre-processing and post-processing facilities.

The non-linear permeability is required, to model accurately the magnetic material used in the device. The problem only requires linear permanent magnets to be modelled, since NdFeB has a linear demagnetization characteristic. A wound coil needs to be simulated, with a specific resistance for voltage forcing the coil when analyzing the dynamic behaviour of the device. The movement of a minor region of the mesh is necessary to move the armature to various positions with respect to the stator. Comprehensive pre-processing facilities are needed to model the magnetic circuit of the device and to allow dimensional changes to be made quickly and easily. Finally, a post-processor is required that allows equipotential plots to be displayed, forces, energies and flux linkages to be calculated, etc..

The software that was used was *MEGA* which was developed by the Applied Electromagnetics Research Centre at the University of Bath, UK. The *MEGA* program solves the low frequency, no displacement current, subset of Maxwell's equations using the finite element method [53].

#### 4.5 MODELLING OF MAGNETIC MATERIAL PROPERTIES

The material chosen for the initial design of the linear motor was Radiometal 4550 (a nickel-iron alloy). In modelling the magnetic properties of materials the *MEGA* software ignores phenomena such as hysteresis and anisotropy, although the mean magnetization ( $BH$ ) curve, shown in Fig. 4.2, is modelled in the software. The curve illustrates the locus of the tips of the minor hysteresis loops that are observed with an increasing excitation field. The axes of the characteristic given in Fig 4.2 are on a logarithmic scale, which allows the region of the curve near the origin that rises in a

concave manner (the Rayleigh region [46]) to be modelled with some precision. A number of points from the curve were entered into the software and a cubic spline [54] was used to produce an approximation function that is continuous in the function and the first derivative. The spline can be represented as [46]:

$$a(x) = \sum_{i=1}^n q_i f_i(x) \quad (4.20)$$

where  $f_i(x)$  is a cubic polynomial,  $q_i$  are the set of coefficients for each polynomial that makes up the spline fit and  $a(x)$  is the resulting approximation function. The spline fit is shown in Fig. 4.3. The characteristic is extrapolated within the software so that magnetic flux densities beyond what is modelled can still be handled. The extrapolation function used is the linear function equation:

$$B = \mu_0 H + B_i \quad (4.21)$$

where  $B_i$  is the value at which the straight line would intercept the  $B$  axis if extrapolated backwards. The gradient of the function is the permeability of the material and is set equal to the permeability of free space  $\mu_0$ , which would be the case in the portion of the curve represented by the extrapolation function. The complete mathematical representation of the magnetization curve is illustrated in Fig. 4.4.

The cubic spline approximation has many advantages over exponential series [55-57], rational fraction functions [58], power series and Fourier series [59], because it can more accurately model the Rayleigh region and the knee-point of the magnetization curve. However, the approximation equation is more complicated and considerable numerical effort is required to interpolate a selected third-order polynomial. Nevertheless it was preferred over the other methods which are computationally less intensive but less precise. The *MEGA* software does not use the  $BH$  curve to represent the property of a magnetic material, because it is computationally more efficient, when solving for the magnetic vector potential  $A$ , to model the material property as the reluctivity as a function of the square of the flux density  $B$  [46], shown in Fig. 4.5.

#### 4.6 PERMANENT MAGNET REPRESENTATION

To model the permanent magnets in the linear motor, the field equation governing the problem was modified to include the effect of the remanence of the magnets. The magnets that are used are made from the rare earth material NdFeB and the form of the demagnetization characteristic enables them to be modelled as a linear material. The relevant data supplied by the manufacturer is:

Magnetic Property	Value	
	min.	max.
Remanent flux density, $B_r$ , (T)	1.08	1.17
Coercive force, $H_c$ , (kA/m)	800	890

**Table 4.1** Specification of NdFeB permanent magnets (VACODYM 351 WZ)

From the above data, the absolute permeability of the recoil line  $\mu_m$  of the magnets characteristic can be calculated using equation (4.5). Taking average values yields:

$$\mu_m = \frac{B_r}{H_c} = \frac{1.125}{845 \times 10^3} = 1.331 \times 10^{-6} \quad (4.22)$$

and the value of the relative permeability of the magnet  $\mu_{mr}$  is:

$$\mu_{mr} = \frac{\mu_m}{\mu_0} = \frac{1.331 \times 10^{-6}}{4\pi \times 10^{-7}} = 1.059 \quad (4.23)$$

This value was entered into the *MEGA* software and used with the relative permeability of free space  $\mu_0$  to define the permeability of the magnets  $\mu_m$  used in equations (4.18) and (4.19). The ability of the *MEGA* software to model magnets with a linear demagnetization characteristic makes the use of the equivalent current sheet method unnecessary [60, 61], which would require the finite element mesh to be modified.

## 4.7 PRE-PROCESSING OPERATIONS

An accurate model for the linear motor will result in the subsequent solution having minimal errors, allowing the performance of the motor to be faithfully predicted. There are basically five distinct parts of the modelling process that have to be correctly interpreted in order to achieve a precise model:

- the geometry and dimensions of the device need to be accurately defined;
- a discretized numerical model has to be produced that will generate, when solved, a good approximation to the magnetic field being simulated;
- all materials need to be accurately represented;
- boundary conditions need to be specified;
- all sources of excitation need to be described.

The third item in the above list has already been described in sections 4.5 and 4.6, and the other processes are described below.

### 4.7.1 Problem Geometry and Mesh Construction

Representing the linear motor as a two-dimensional axi-symmetric problem, as described in section 4.3, allows the modelling of only half of the cross-section of the device, see Fig. 4.1. When modelling axi-symmetric problems using *MEGA*, the axis of symmetry, the  $z$  axis in cylindrical coordinates, is represented in the software as the  $y$  axis in the Cartesian coordinate system. Due to this the linear motor was modelled in a vertical orientation, as shown in Fig. 4.6. The first step in constructing the finite element mesh is to define a finite bounded area where the linear motor will be modelled. The distant boundaries are placed at a remote distance so as not to affect the numerical solution of the field within the motor, see Fig. 4.6(a). The next step is to enter the key coordinates of one half of the magnetic circuit of the device into the *MEGAVIEW* pre-processor. Having defined a set of coordinates within the bounded area, or problem domain, a coarse mesh is constructed around these coordinates to discretize the motor cross-section, as shown in Fig. 4.6(b). The mesh comprises both

triangular and quadrilateral first-order elements and the field inside an element can therefore be approximated by a linear polynomial function. The mesh was refined in the motor region, to produce a mesh with small elements in the area of the magnetic circuit and larger elements in the surrounding air, as shown in Fig. 4.6(c).

The mesh was designed in such a way that areas of near constant flux density are modelled using only a few large elements, whereas in areas of highly varying flux density the elements are made small to minimise solution errors. A very fine mesh was created in the air-gap, which included eight layers of elements, where high accuracy is needed for post-processing operations. The complete mesh was created with geometric anisotropy [46], see Figs. 4.6 and 4.7, to produce an accurate solution for all flux line orientations. All elements were constructed with good aspect ratios, and elements with very large or very small angles were avoided. However, long thin elements are unavoidable in some areas, in particular the air-gap, where as Fig. 4.8 shows the largest element aspect ratio is approximately 8:1. The mesh was kept symmetrical about the centre-section of the motor.

The mesh was split into two parts; one for the linear motor stator and surrounding air and the other for the armature. The two meshes were then joined using Lagrange Multipliers [53, 54, 62] to enable the armature to be moved relative to the stator, and to eliminate re-meshing of the air-gap or re-editing of element region properties when armature movement is involved. All the constituent parts of the motor, i.e. the magnetic material, copper coil, permanent magnets and surrounding air, have a separate region, (a region being a group of elements sharing the same identity), and each region has its own material properties. The complete mesh is shown in Fig. 4.6, and contains 6204 elements and 6324 nodes.

#### 4.7.2 Distant Boundaries and Boundary Conditions

The solution of the differential equations that describe the linear motor problem requires a closed mathematically defined boundary to be identified. The artificial boundaries used in the problem are situated away from the motor so that the magnetic

field solution in and near the device is unaffected by the boundaries. The general rule that the boundary should be a few device diameters away [46] allowed the stray leakage flux outside the device to be accurately modelled. It can be seen from Fig. 3.7 that the flux lines are parallel to the axis of symmetry, so that the axis of symmetry is a flux line. In a two-dimensional axi-symmetric problem, flux lines are not equipotential lines of  $A_\theta$  but rather are lines of constant  $rA_\theta$  [45, 46]. On the axis of symmetry the product  $rA_\theta$  is obviously zero and, because this axis is an equipotential line,  $A_\theta$  is constant along the line and is set to the reference potential of  $A_\theta = 0$ . In addition, since the axis of symmetry is joined to two sides of the distant boundary,  $A_\theta$  is set to zero along all the boundary sides. This boundary is described as a Dirichlet boundary, and is illustrated in Fig. 4.9.

### 4.7.3 Modelling of Excitation Sources

The modelling and representation of the permanent magnets in *MEGA* was discussed in sections 4.2.1 and 4.6. Defining the excitation winding as a wound coil results in the source current being uniformly distributed over the cross-section [53]. In a magnetostatic analysis one end of the coil is fed with a specified current while the other is connected to ground. To force the coil with a specified voltage  $V$  a series resistance  $R$  is included [63], so that the dc current  $I$  flowing through the coil is  $(V/R)$ . This feature is essential in a transient analysis where a defined voltage waveform, e.g. a step input  $V$ , is applied to the coil. The current  $I$  increases, over time, to a steady value of  $(V/R)$  whilst the emf  $E$  induced in the coil decays to zero.

## 4.8 POST-PROCESSING OPERATIONS

When seeking an optimum design, the main physical properties that have to be evaluated are:

- magnetic stiffness characteristic;
- force versus displacement characteristic for various coil currents;



- linearity of the device, established by analyzing the coil current versus armature displacement characteristic;
- dynamic performance, by employing a suitable mathematical model and;
- minimisation of stray and leakage fields.

All the above properties are obtained by post-processing the solution of the finite element analysis. The four main quantities thus obtained and used to find the above properties are:

- plots of equipotential lines;
- the flux linking the coil and;
- the electromagnetic force acting on the armature.

The following sections describe in detail the post-processing operations.

#### **4.8.1 Equipotential Plots**

For equipotential plots to be valuable in the re-designing process, they are produced in equal magnitude steps and are first used to check if the field solution in the motor appears to be credible. Boundary conditions can also be examined by a simple inspection, since equipotential lines should be tangential to a Dirichlet boundary condition. The plots also allow regions of high flux density to be located and they can be employed to determine the direction of the electromagnetic forces acting on the armature.

#### **4.8.2 Flux Linkage Computation**

The flux linking the coil is required to evaluate the incremental inductance for inclusion in the mathematical model, and is needed from both static and transient field solutions.

#### 4.8.2.1 Flux Linkage Computation from a Static Field Solution

The flux  $\phi$  that links a single turn of a coil can be evaluated from:

$$\phi = \int \mathbf{B} \cdot d\mathbf{S} \quad (4.24)$$

where  $S$  is the area enclosed by the single turn. If the coil contains  $N$  turns the total flux linking the coil is:

$$\lambda = N\phi \quad (4.25)$$

Substituting equation (4.24) into equation (4.25) enables the flux linkage to be calculated, but it assumes that the flux linked by every turn in the coil is the same. More correctly, a number of surfaces  $m$  spanning the complete cross-section of the coil can be defined and the flux linkage computed for each surface. These are then averaged to find a more realistic value from:

$$\lambda = \frac{N}{m} \sum_{i=1}^m \int_{S_m} \mathbf{B} \cdot d\mathbf{S}_m \quad (4.26)$$

Using equation (4.26) produced satisfactory flux linkage results, but required the implementation of numerous numerical operations. A more elegant method [46] is to evaluate the flux linkage from energy considerations as:

$$\lambda = \frac{1}{I} \int_U \mathbf{A} \cdot \mathbf{J} dU \quad (4.27)$$

where  $I$  is the current flowing through the coil,  $U$  its volume and  $\mathbf{A} \cdot \mathbf{J}$  is twice the stored magnetic energy [54]. Equation (4.27) requires only one integral to be performed, and since the calculation produces more accurate results than equation (4.26) and is quicker to implement in the *MEGA* software it was employed throughout the research programme.

#### 4.8.2.2 Flux Linkage Computation from a Transient Field Solution

The flux linking the coil in a transient field solution is calculated from the electrical circuit equation. With the armature locked in a specified position yields:

$$V = iR + \frac{d\lambda}{dt} \quad (4.28)$$

where  $V$  is the applied coil voltage, (which in this case is a step input),  $i$  is the instantaneous coil current and  $R$  is the coil resistance. Rearranging equation (4.28) and integrating yields:

$$\lambda = \int_{t_0}^{t_1} (V - iR) dt \quad (4.29)$$

where  $t_0$  and  $t_1$  are respectively the start and end times of the transient field solution. All the above numerical operations, including the integration, are performed in the *MEGA* software. To obtain accurate values of flux linkage requires a time-step, in the transient analysis, of at most  $\tau_c/2$  where  $\tau_c$  is the time constant of the coil.

### 4.8.3 Force Computation

Computation of the force acting on the armature is necessary for the implementation of the mathematical model and in assessing the linearity of the motor characteristics. There are three basic methods by which the force can be determined:

- the virtual work principle;
- the finite element implementation of the virtual work principle, also known as Coulomb's virtual work method, and;
- the Maxwell stress tensor method.

The following sections highlight the advantages and disadvantages of each of these methods.

#### 4.8.3.1 The Virtual Work Principle

If the armature is displaced by a very small distance  $\delta x$ , the change in force  $\delta F_x$  to move the armature is negligible and the force  $F_x$  can be assumed to remain constant throughout. The work done in displacing the armature is equal to the change in

magnetic stored energy  $\delta W$  in the linear motor, and therefore:

$$F_x = -\frac{\delta W}{\delta x} \quad (4.30)$$

The disadvantage of this method is that two static field solutions are required to obtain the force and, because the difference of two near identical stored energy values is needed, the method is prone to rounding off errors. However, this is not a problem when analyzing the linear motor, since a number of armature positions are investigated when finding the complete force characteristic. Thus the stored energies can be obtained at each position and a smooth curve fitted to the discrete points. Differentiating this curve with respect to the armature position will produce the force characteristic.

#### 4.8.3.2 Finite Element Implementation of the Virtual Work Principle

This method [64-66] is based on the concept that armature movement will, if possible, physically distort the mesh. The elements that would be distorted, or stretched, are those located between the stator and moving armature, i.e. the air-gap elements, which are described as virtually distorted elements [65]. The force is obtained from the derivative of the energy stored in the magnetic field versus the displacement of the armature, as described by equation (4.30). In a finite element solution, the force is determined by, firstly, defining a region of elements, i.e. one layer surrounding the armature, as the virtually distorted elements. The derivatives of the coordinates of the element nodes in the virtually distorted region versus the virtual displacement of the armature are then calculated, and the force is obtained from the magnetic stored energy  $W$  expressed as [54]:

$$W = \int_V \int_0^H (H \cdot dB) dV \quad (4.31)$$

where  $V$  is the volume of the entire finite element mesh. Partially differentiating equation (4.31) with respect to the direction of movement of the armature  $x$  to determine the force  $F_x$  yields [65]:

$$F_x = -\frac{\partial W}{\partial x} = -\sum_e \left[ \int_{V_e} \mathbf{H} \frac{\partial \mathbf{B}}{\partial x} dV + \int_{V_e} \int_0^{\mathbf{B}} \mathbf{H} d\mathbf{B} \frac{\partial}{\partial x} (dV) \right] \quad (4.32)$$

where  $V_e$  is the volume of a distorted element and the integral is summed over all of the distorted elements  $e$ .

To implement this method requires the virtually distorted elements in the air-gap to be defined as a specific region having their own identity, to enable information regarding their nodal coordinates, element topologies and nodal potentials to be extracted from the *MEGA* software to a data file. A computer program was developed [65] using *FORTRAN 77* to read in the data file and to implement the above force calculation. Finally, only one field solution is required to determine the force acting on the armature and so this method is computationally more efficient than the technique described above.

#### 4.8.3.3 Maxwell Stress Tensor Method

The Maxwell stress method calculates the local stress at all points of a surface  $S$  that surrounds the armature, and integrates the local stresses along the surface to obtain the resultant force  $F$ . From [46] the force can be stated as:

$$\mathbf{F} = \frac{1}{\mu} \oint_S \mathbf{T} \cdot d\mathbf{S} \quad (4.33)$$

where  $\mathbf{T}$  is the Maxwell stress tensor and  $d\mathbf{S}$  is the normal vector to the surface  $S$ . The surface should be placed in the centre of the air-gap as far away from iron parts as possible, where the closest approximations to the flux density are obtained [67]. To determine the force on the motor armature only requires a contour integral to be computed, as the problem is only two-dimensional. To achieve this, the normal and tangential components of the flux density at each point along the contour bounding the armature are calculated, and integrated along the contour to find the force, thus [68]:

$$F_x = \int_C \frac{1}{2\mu_0} (B_n^2 - B_t^2) ds \cdot t + \int_C \frac{1}{\mu_0} (B_n B_t) ds \cdot n \quad (4.34)$$

where  $C$  is the contour bounding the armature and  $t$  and  $n$  are unit vectors tangential and normal to the contour. The *MEGA* software includes the Maxwell stress force calculation in the *MEGAVIEW* post-processor [54] and no separate computer program was necessary.

#### 4.8.3.4 Comparison of Methods

Analyzing and optimizing the linear motor requires a substantial number of force characteristics to be obtained, and each one may include up to forty-one separate force computations over the complete stroke length. Therefore, the method selected to calculate the force needs to be both fast and easy to implement. The virtual work principle requires a smooth curve to be fitted to the magnetic stored energy values, and the curve to be differentiated at every point along the stroke length of the motor. The method would undoubtedly take time to implement and was soon dismissed. The finite element implementation of the virtual work principle enables force values to be obtained directly from the field solution, and is therefore better suited to the present application. However, writing out the force values to a file and then using a separate computer program to obtain the results is again time consuming. Since the Maxwell stress force calculation included in the *MEGAVIEW* post-processor allows force values to be obtained with only a few key presses it was the preferred method to employ.

There are, however, a number of problems associated with the Maxwell stress force computation. To obtain an accurate force a very fine local mesh is required in the air-gap region [69, 70], as shown in Fig. 4.8, because this is the only part of the field solution used in the computation. Problems arise when modelling the linear motor, because unlike a rotary motor no periodicity conditions exist and the whole motor has to be modelled. A very finely discretized mesh throughout the length of the air-gap produces a very large mesh that will undoubtedly increase the solution time dramatically, and the refinement of the air-gap region clearly has to be limited.

## 4.9 CONCLUSIONS

This chapter has described in detail the magnetic field in the linear motor and introduced the electromagnetic finite element analysis software package used in the research programme. Modelling of the motor materials, including the soft magnetic materials and the permanent magnets, have also been described and pre-processing operations, such as mesh construction and boundary conditions have been explained. Finally, post-processing procedures, such as flux linkage and force calculations have been presented.

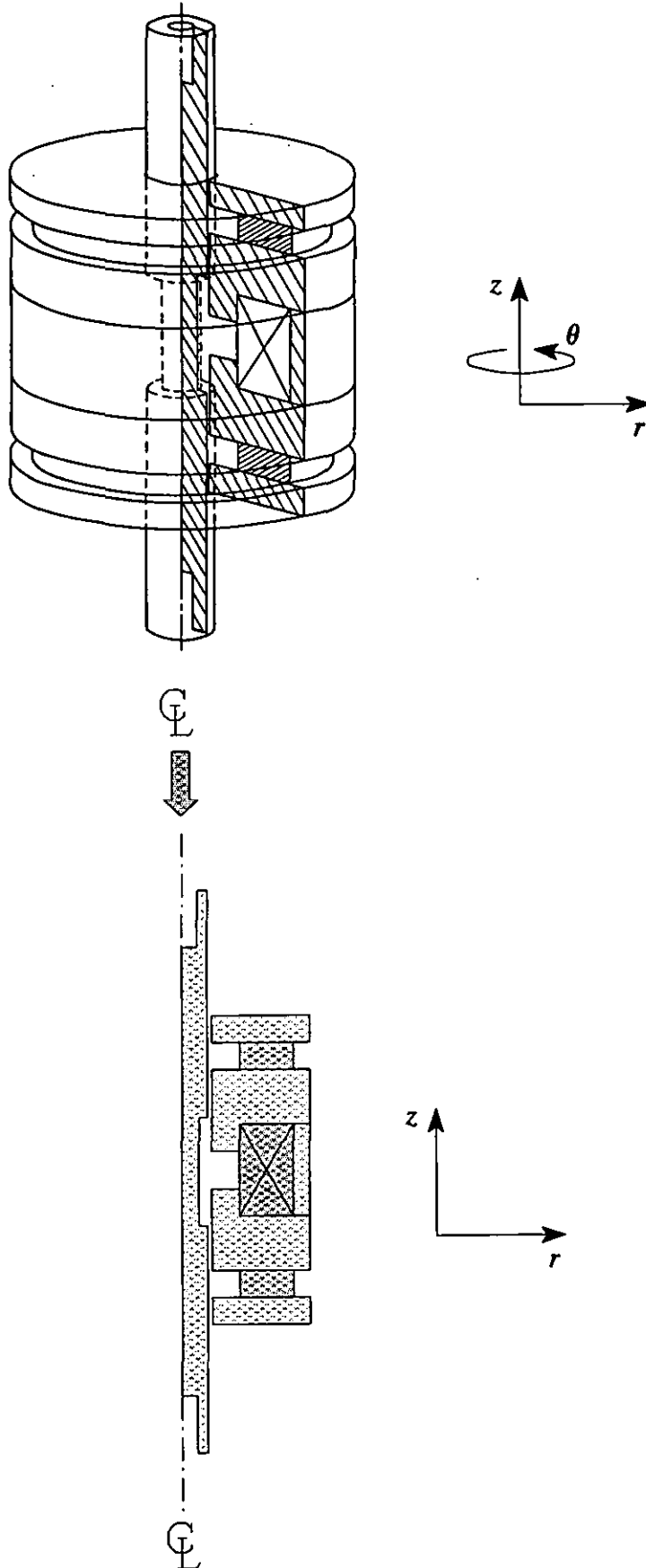


**Fig. 4.1** Reduction of the problem to two-dimensions



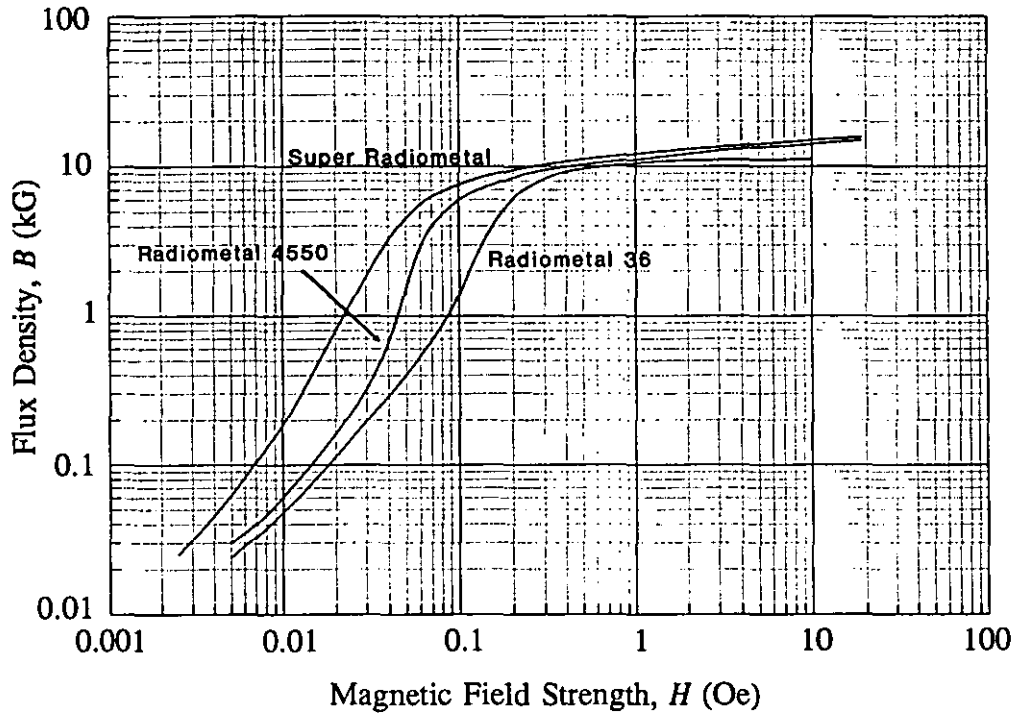


Fig. 4.2 Mean magnetization curve of Radiometal 4550<sup>1</sup>

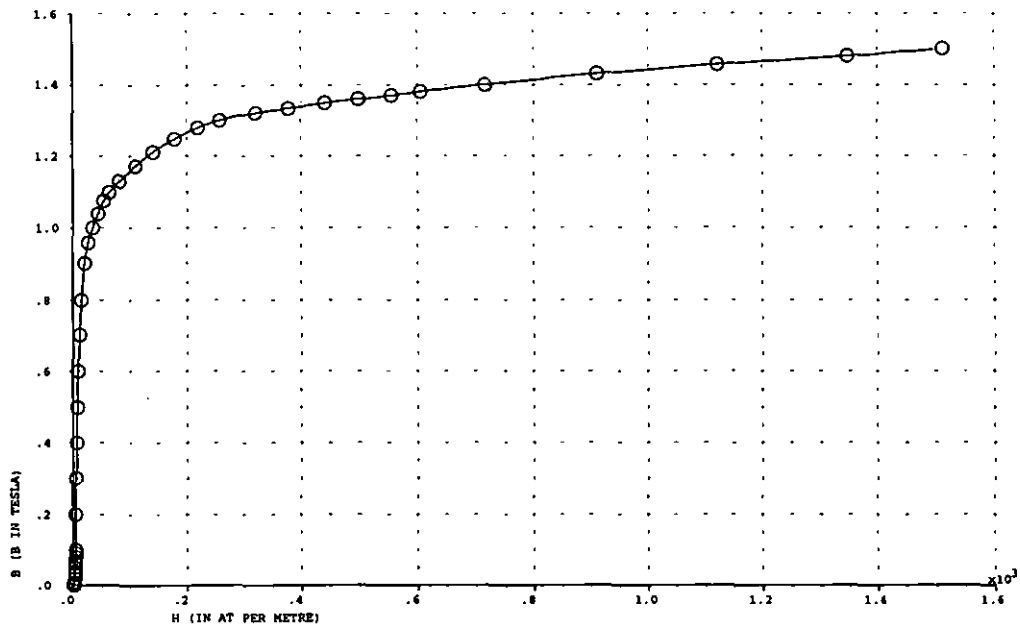


Fig. 4.3 Spline fit of the mean magnetization curve

<sup>1</sup> Reproduced from data supplied by TELCON LIMITED, Crawley, West Sussex, UK.

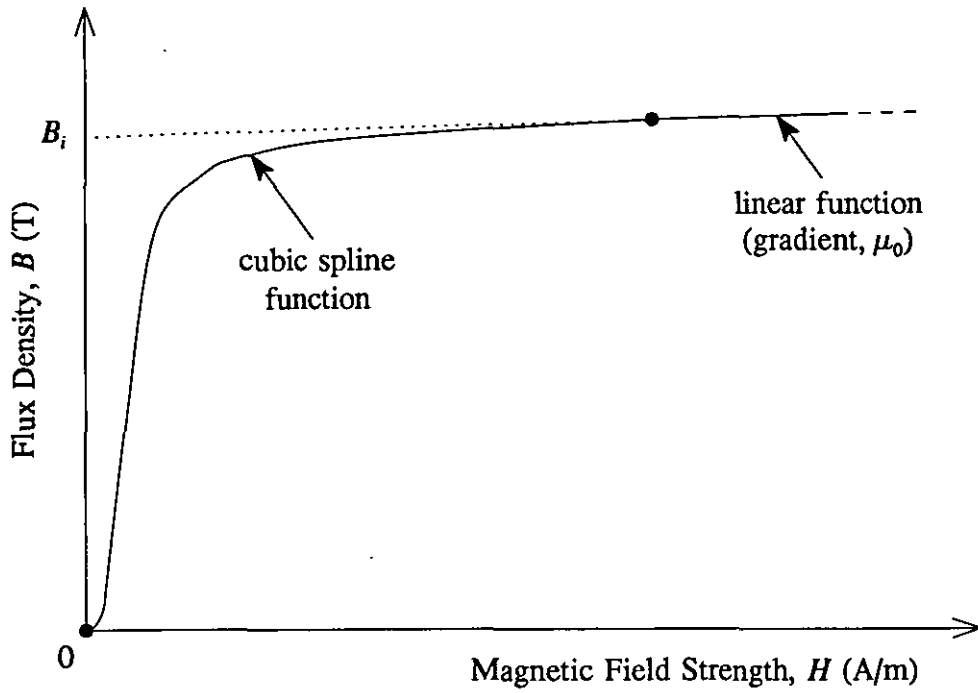


Fig. 4.4 Complete mathematical representation of the mean magnetization curve

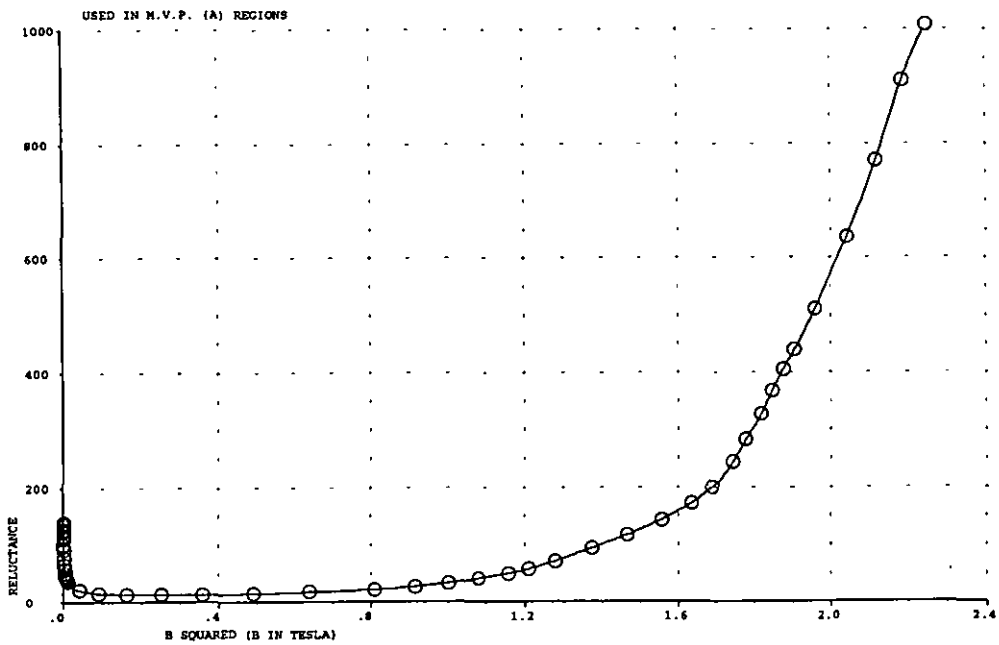


Fig. 4.5 Reluctance versus the square of the magnetic flux density curve

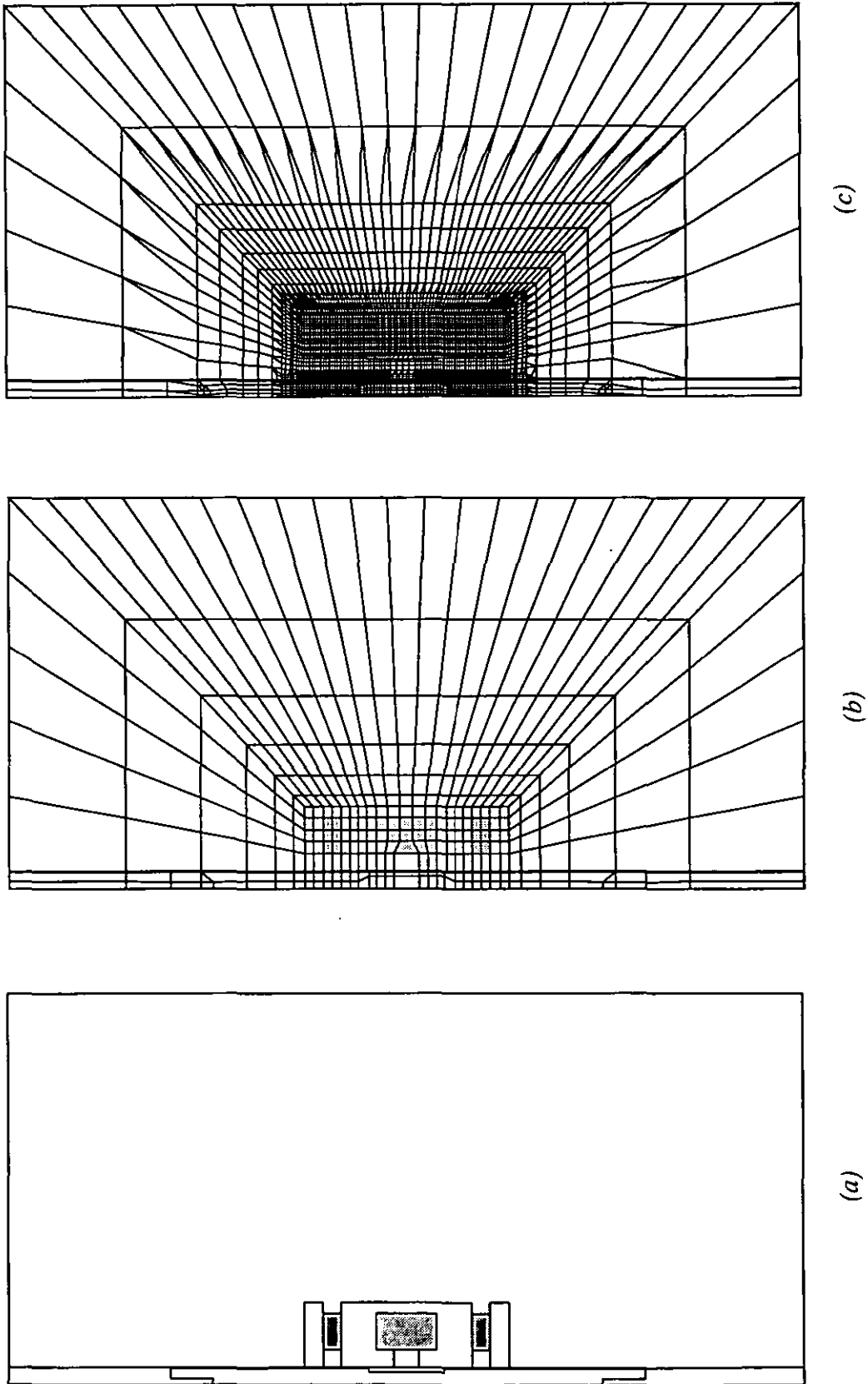


Fig. 4.6 Development of the finite element mesh

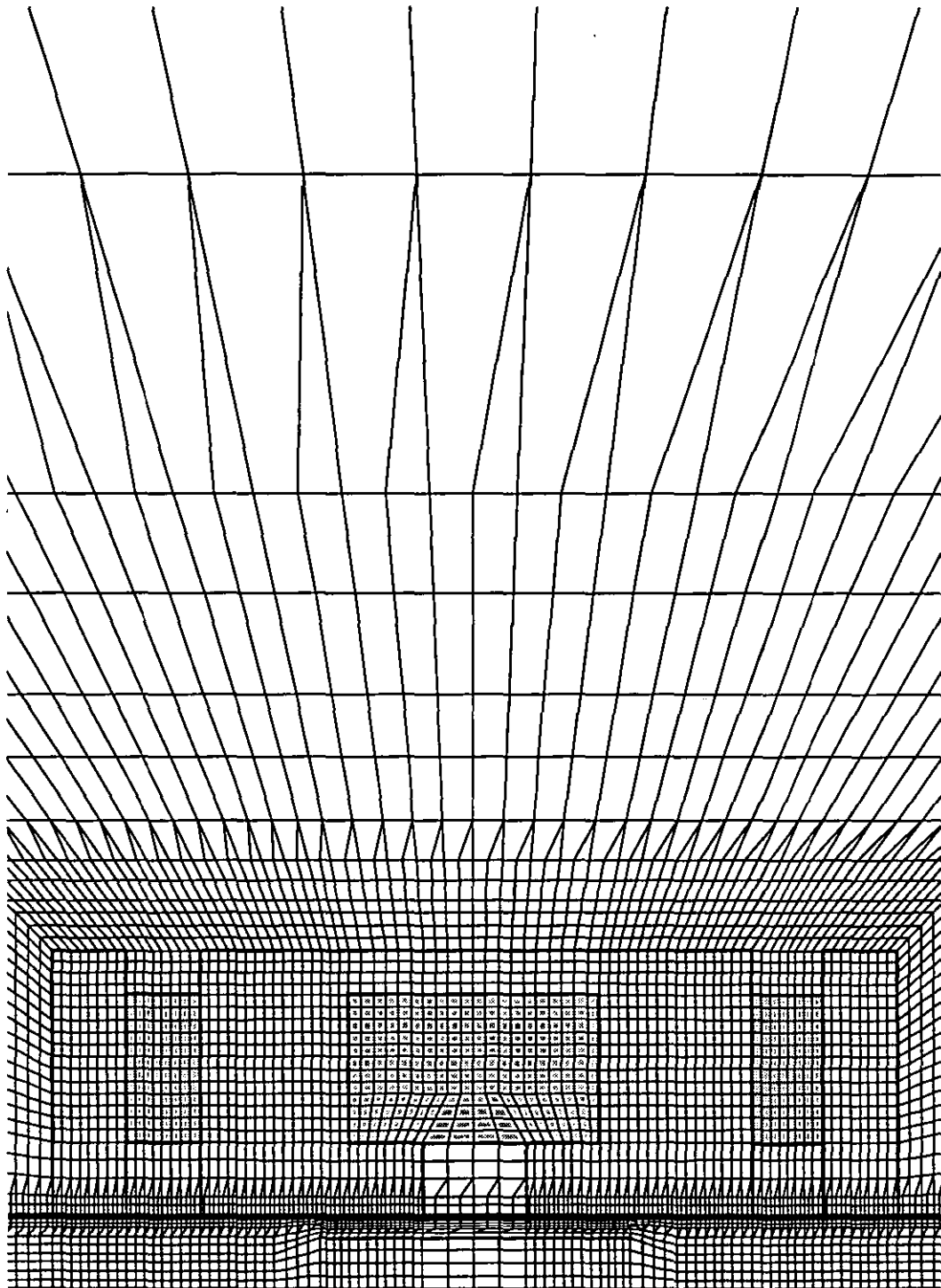
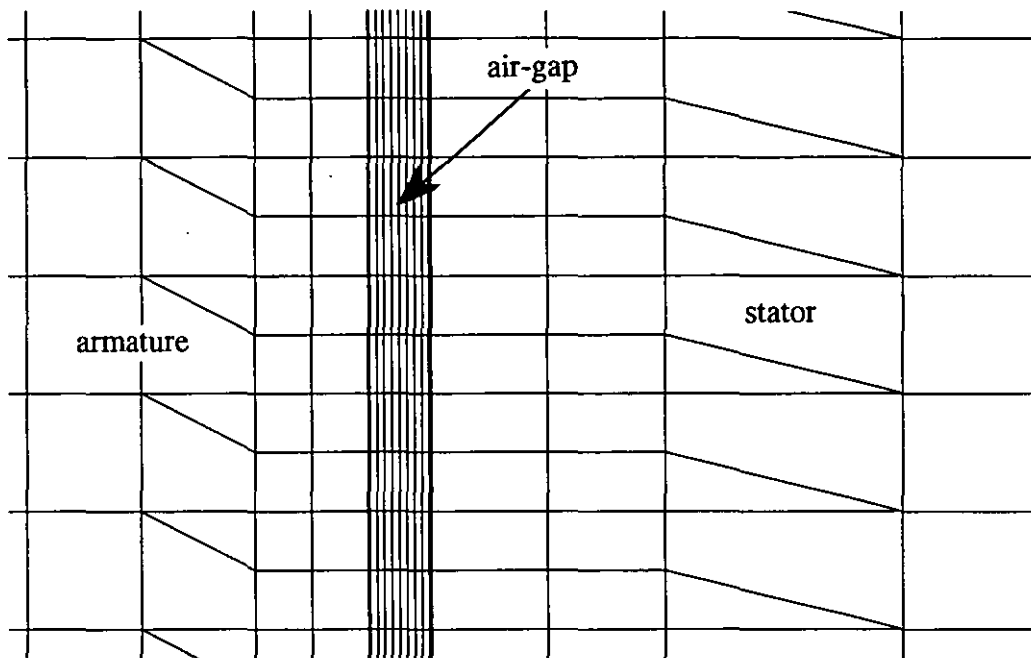
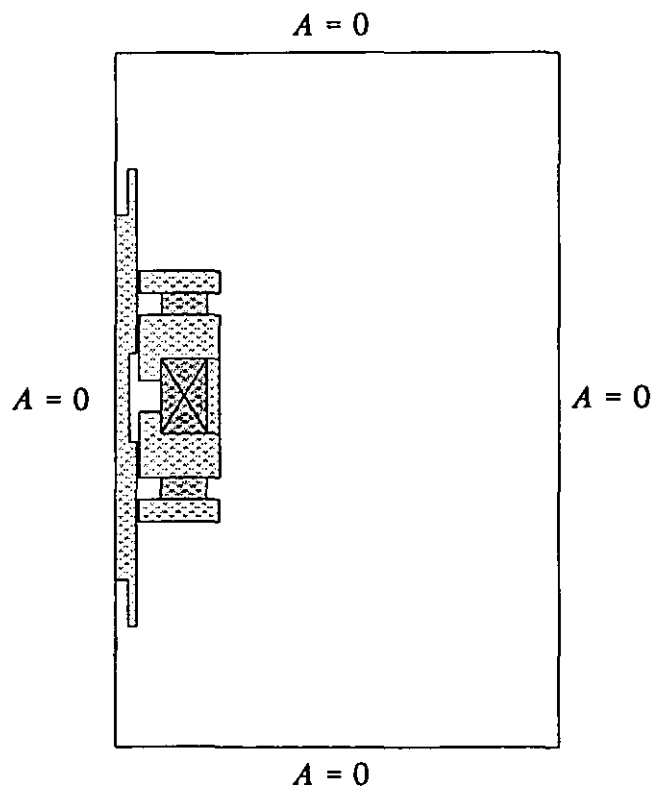


Fig. 4.7 Finite element mesh of the linear motor region



**Fig. 4.8** Fine mesh discretization of the air-gap region



**Fig. 4.9** Problem boundary conditions

## **STATIC ANALYSIS OF THE LINEAR RELUCTANCE MOTOR**

The prototype linear motor is investigated in this chapter using finite element field analysis, and the force and flux linkage characteristics are determined. Experimental results are presented, wherever possible, to assess the accuracy of the modelling technique.

### **5.1 MAGNETIC FIELD SOLUTION**

The magnetic field solutions with both an unexcited and an excited coil are examined initially. Conclusions are drawn and possible improvements to the initial prototype design are suggested.

#### **5.1.1 Magnetic Flux Distribution with the coil unexcited**

With the coil unexcited and the armature in its central position, the vector equipotential plot (lines of constant  $A_\theta$ ) is as shown in Fig. 5.1(a), where the symmetrical lines and a significant amount of leakage flux are clearly seen. Fig. 5.1(b) shows the plot in more detail, and this illustrates the poor positioning of the permanent magnets as the cause of the unacceptable leakage. This effect could be reduced by repositioning the magnets, so that their outer diameter is the same as that of the magnetic circuit, to reduce the flux that is being lost through the outer diameter edge of the end-rings. The inner diameter is adjusted accordingly to keep the magnet volume constant. The flux density plot of Fig. 5.2 shows that the section of the armature nearest to each magnet is heavily saturated, which is due to the large reduction of 12:1 between the cross-sectional areas of the magnets and the armature. All the flux from the magnets, with the exception of the leakage flux, is compressed into the small cross-sectional area of the armature, producing a maximum flux density of 1.79 T near the surface. To produce an optimized motor, a high air-gap flux density has to be produced and, in achieving this, parts of the magnetic circuit will

inevitably be highly saturated. Fig. 5.2 also highlights the large leakage flux density of 0.30 T in the air surrounding the magnets.

The two components of the flux density ( $B_r$  and  $B_z$ ) throughout the complete air-gap are shown in Fig. 5.3 when the armature is in its central position. The flux density in the air-gap under each end-ring is nearly all radially directed, and approaches 0.8 T. The flux density opposite to the magnets is nearly all axially directed, with the magnitude of 0.3 T being mostly leakage. The modulus of the flux density throughout the complete air-gap, also shown in Fig. 5.3, illustrates the localised increase of the flux density at the stator-yoke pole-face edges, where the maximum flux density is approximately 0.53 T compared with 0.4 T along the rest of the pole-face.

Fig 5.4 shows the armature displaced by  $\pm 7.0$  mm from its central position, which results in a high flux density of 1.15 T under the stator-yoke poles. This small pole-face overlap is responsible for the large returning force attempting to centralise the armature. The force on the armature is a function of the flux density on its surface, so that to increase the restoring force, the surface area of the armature needs to be increased, suggesting the need for a larger diameter armature. Fig. 5.5 shows one end of the motor in detail, with the armature centralised. The arrows indicate the magnitude and direction of the flux density, and the direction of magnetization of the permanent magnet, with the other magnet opposing. The operating point of the magnet is about 0.72 T. For NdFeB, with its linear demagnetization characteristic, the most efficient point of operation is at the point on the recoil line where  $B = B_r/2$  and the energy product ( $BH$ ) is a maximum, which is at about 0.56 T. However, the larger is the flux density in the magnet, the larger will be the air-gap flux density and for an optimum motor design, the magnets should not necessarily operate at the maximum ( $BH$ ) point.

Fig. 5.6 illustrates that virtually all the energy in the magnetic field is stored in the magnets and the air-gap, which is expected when using very high permeability magnetic material.

### 5.1.2 Magnetic Flux Distribution with the coil excited

When the motor is unloaded and the coil is excited with a current of 0.30 A the armature moves until the force acting on it is zero, at 3.65 mm from the central position. The corresponding vector equipotential plot is shown in Fig. 5.7(a), where an unsymmetrical flux distribution is now evident. The flux density plot of Fig. 5.7(b) illustrates that the narrow centre-section of the armature is saturated, with  $B \approx 1.50$  T, suggesting again that a larger diameter armature is required. Detailed examination of this figure shows that the operating point of the magnet has moved slightly to about 0.79 T. This implies that the magnet operates at a point on the recoil line at about 0.72 T, moving approximately  $\pm 0.07$  T when the coil is excited with an alternating current of 0.3 A peak and the armature is free to oscillate.

## 5.2 FORCE CHARACTERISTIC

Before examining the results of the non-linear analysis, it is of interest to evaluate initially the results from a linear analysis. Although these are theoretical and of limited practical value, they however assess the performance of the motor without the added influence of the magnetic non-linearity.

### 5.2.1 Linear Analysis Results

The relative permeability of the magnetic material was set to 1000. The force acting on the armature was calculated by the Maxwell stress method, using equation (4.34), when the armature was moved from its central position to displacements of  $\pm 8.0$  mm from this position, in increments of 0.5 mm. The force characteristics in Fig. 5.8, for the complete stroke length of the armature for various coil currents indicates that the magnetic stiffness, (i.e. the force at 0 A, when the armature is displaced  $\pm 2.0$  mm from the central position), produces an armature centralising force of about 1.4 N. When the coil current is 0.60 A, the maximum force acting on the armature is 22.5 N, when it is displaced 7.5 mm from the central position. As expected, the force/coil current characteristic at the central position, shown in Fig. 5.9, is linear. The force



produced by the excited coil  $F_{coil}$  on the armature can be obtained from the characteristic shown in Fig. 5.8, by subtracting  $F_{mag}$  from all the curves. The  $F_{coil}$  characteristics at  $I = 0.2$  A, 0.4 A and 0.6 A are shown, together with the  $F_{mag}$  characteristic, in Fig. 5.10. For a specific coil current, the position at which the two curves intersect defines the stable rest position. From this, the coil current/armature displacement characteristic of Fig. 5.11 can be obtained, which is seen to be quite linear up to approximately 6.20 mm displacement.

### 5.2.2 Non-linear Analysis Results

The non-linear analysis was implemented using the  $BH$  curve for Radiometal 4550, given in Fig. 4.3. With the coil unexcited, the magnetic stiffness characteristic was obtained. Experimental results were also obtained from the prototype motor, loading the armature with weights of total mass  $M$ , to enable the load force  $F_{load}$  to be calculated ( $F_{load} = Mg$ ). Fig. 5.12 presents the results obtained from the finite element analysis, together with the experimental results, and the two sets compare very favourably. The figure highlights however a major problem with the prototype design and that is the poor stiffness characteristic. It shows that there is very little force attempting to return the armature to its central position at displacements of up to  $\pm 4.0$  mm from this position, resulting in a device in which the armature will never centralise itself due to the non-linear magnetic material. At  $\pm 2.0$  mm from the central position there is virtually no force attempting to centre the armature, compared with approximately 1.4 N from the linear analysis results.

The two equal and opposite forces acting on the armature can be calculated by integration over half the motor air-gap as approximately 0.48 N. The extreme position of the armature, at which the stator and armature pole-face overlap approaches zero, is about 8.0 mm from the central position. This condition produces the largest possible force on the armature, which is 14.0 N compared with approximately 13.0 N from the linear analysis.

The coil was then excited with dc up to 0.7 A, in increments of 0.1 A, and the force was calculated for each current at 0.5 mm increments over the complete stroke length. Experimental results are obtained using the technique described earlier, and these are compared in Fig. 5.13(a) with the finite element results, for coil currents up to 0.3 A, and in Fig. 5.13(b), for coil currents from 0.4 A up to 0.7 A. The difference between the finite element results and the experimental results, particularly noticeable in Fig. 5.13(b), is thought to be due to friction between the armature and the supporting linear bearings.

Fig. 5.14 illustrates this problem; the Maxwell stress force calculation computes ( $F_{mag} + F_{coil}$ ), whereas the experimentally obtained results  $F_{load}$  are measurements of ( $F_{mag} + F_{coil} + F_r$ ), where  $F_r$  is a friction force. This force opposes the applied load force and is seen from Fig. 5.13(b) to be about 1.5 N. Due to manufacturing tolerances of the motor and housing it is very difficult to align the armature concentrically with the stator bore, and in practice a force will be produced that will attract the armature to the nearer side of the stator bore which causes a large friction force between the armature and the linear bearings. In practice this caused the surface of the armature to be damaged by the harder material of the bearings.

Fig. 5.15 shows the force/coil current characteristic obtained from Fig. 5.13 when the armature is in its central position. It can be seen that there is little gain in supplying the coil with a current above 0.3 A. For a specific current, the armature position at which the steady-state force characteristic is zero is the stable position and this can be seen from Fig. 5.13. For example, the armature will move to a position approximately 3 mm from the central position for all currents up to 0.7 A. Examining the force characteristic in more detail to find more accurate positions at which the force is zero results in Fig. 5.16, which is the coil current/armature displacement characteristic. The figure also contains experimental results that compare poorly with the finite element results, which is again thought to be due to friction between the armature and the bearings.

Fig. 5.16 also shows that the coil current/armature displacement characteristic obtained from the finite element analysis is highly non-linear, which is another problem with the prototype design. The  $F_{coil}$  characteristics at  $I = 0.2$  A, 0.4 A and 0.6 A are shown together with the  $F_{mag}$  characteristic in Fig. 5.17. It can be seen that all the  $F_{coil}$  curves intersect the  $F_{mag}$  curve at approximately 3.7 mm, which agrees with Fig. 5.16.

### 5.3 FLUX LINKAGE CHARACTERISTIC

The method of calculating the flux linking the coil from the finite element field solution was discussed in section 4.8.2. In order to verify this calculation, the flux linking the coil, for increasing coil currents up to 0.7 A, was experimentally obtained at the armature central position. This position was chosen because when no current flows through the coil there is no linking flux; unlike other positions of the armature where an initial flux linkage will exist due to the unsymmetrical flux distribution that is created. The experimental technique employed to find the flux linkage uses a dc inductance bridge, and is described in the next section.

#### 5.3.1 DC Inductance Bridge

Although this method of determining flux linkage has been applied previously to large rotary electrical machines [71, 72], it can be applied equally to the linear motor under consideration. The technique uses the Wheatstone-bridge arrangement shown in Fig. 5.18, where  $L$  and  $R$  are the self-inductance and resistance of the coil, and  $R_1$ ,  $R_2$  and  $R_3$  are non-reactive resistors. Using a current  $I$ , and keeping  $R_2$  and  $R_3$  equal, the bridge is balanced by varying  $R_1$ . The current through the bridge is then reversed by means of the switch  $SW$ , and the instantaneous voltage  $v$  across the bridge during this transient period is detected by the fluxmeter  $\phi$ . This produces a deflection proportional to the time integral of the voltage:

$$\lambda = \int_{t_1}^{t_2} v dt \quad (5.1)$$

where  $\lambda$  is the flux linking the coil. The bridge supply is reversed instead of being switched off, to nullify the effect of hysteresis. A full analysis of the method is given

elsewhere [73]. Resistors  $R_2$  and  $R_3$  were  $200 \Omega$  and when the bridge was balanced,  $R_1$  was equal to  $R$ . The non-reactive resistor  $R_s$ , in parallel with the fluxmeter, was used to keep the resistance seen across terminals  $A$  and  $B$  equal to  $30 \Omega$ , which was needed for the Grassot type fluxmeter to give a correct reading. The value of  $R_s$  is given by the expression:

$$R_s = \frac{30R}{R_c - 30} \quad (5.2)$$

The fluxmeter readings were then multiplied by a correction factor  $k_{cf}$  given by:

$$k_{cf} = \frac{R + R_s}{R_s} \quad (5.3)$$

Experimental results obtained using this method are shown in Fig. 5.19, together with finite element derived results using equation (4.27). It is evident that the agreement between the two is very good. Fig. 5.20 shows the finite element derived flux linkage characteristic for coil currents between  $-0.7 \text{ A}$  and  $+0.7 \text{ A}$  for nine positions of the armature; the central position, and  $\pm 2.0$ ,  $\pm 4.0$ ,  $\pm 6.0$  and  $\pm 8.0 \text{ mm}$  from this position.

## 5.4 CONCLUSIONS

This chapter has illustrated the important characteristics of the initial prototype design and a number of conclusions can be drawn. The permanent magnets need re-positioning to reduce the leakage flux, and the volume of the magnets also needs to be investigated to maximise the air-gap flux density. A larger diameter armature is required to increase the useful force from the motor, and since this will also improve the stiffness it will enable the armature to return to its central position in the absence of control mmf. The linearity of the coil current/armature displacement characteristic also needs to be improved to provide a device which is more controllable. Finally, a fast dynamic response is another important requirement of the motor, which has not yet been examined, and this will be investigated in the next chapter.

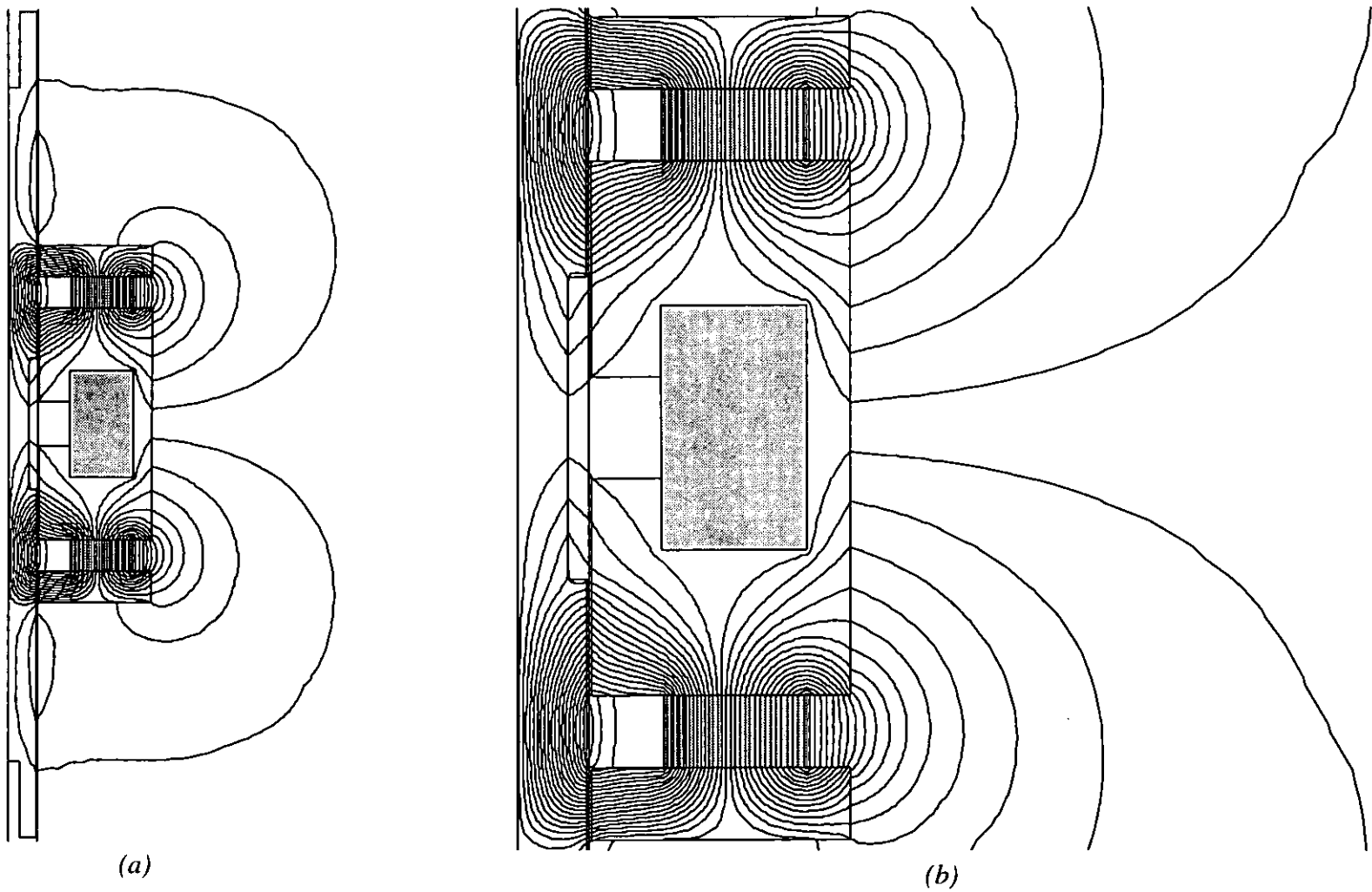


**Fig. 5.1** Magnetic vector equipotential plot in (a) the linear motor and surrounding air and (b) the linear motor in detail

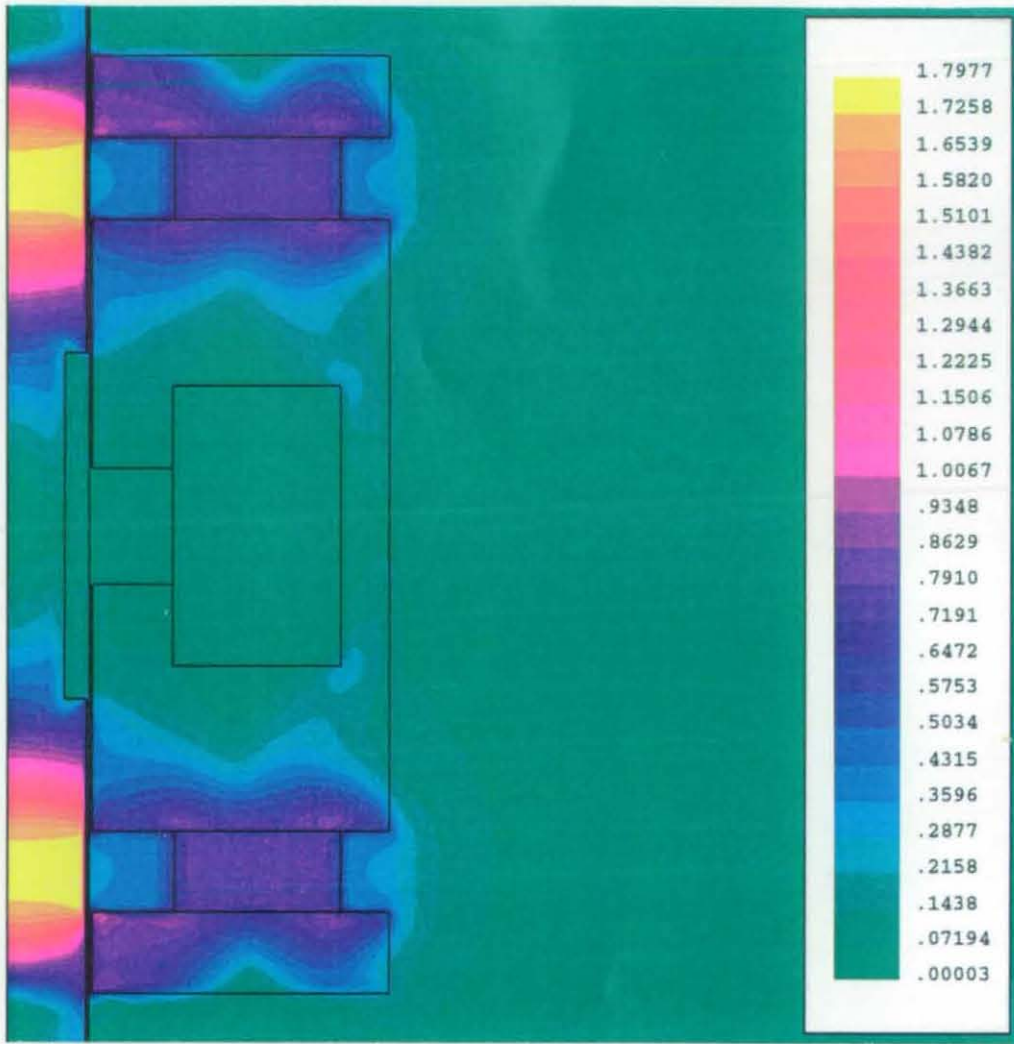


Fig. 5.2 Flux density in the linear motor.

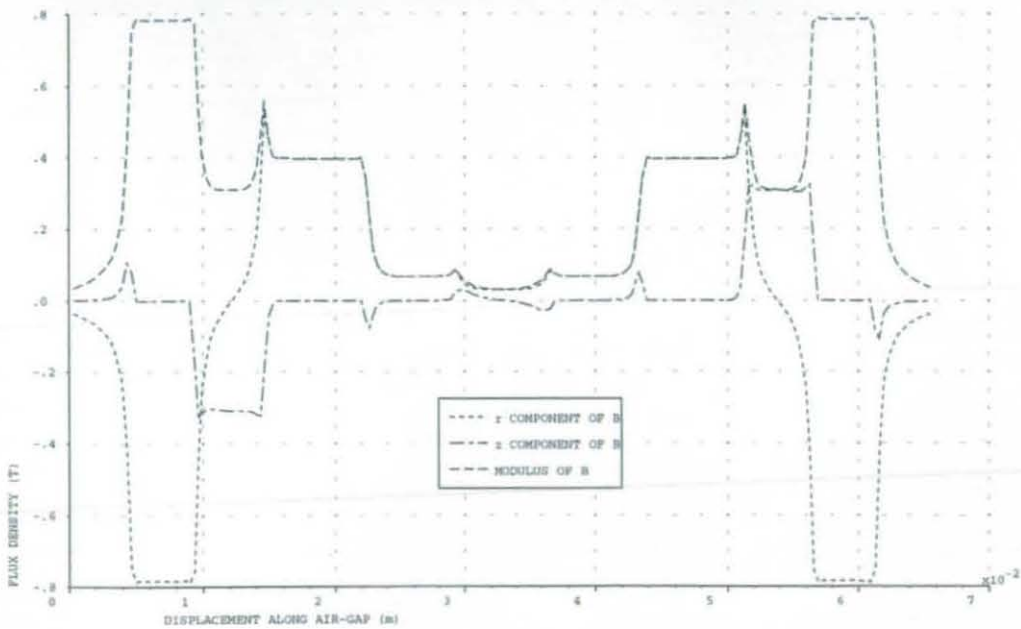


Fig. 5.3 Air-gap flux density (armature central position)



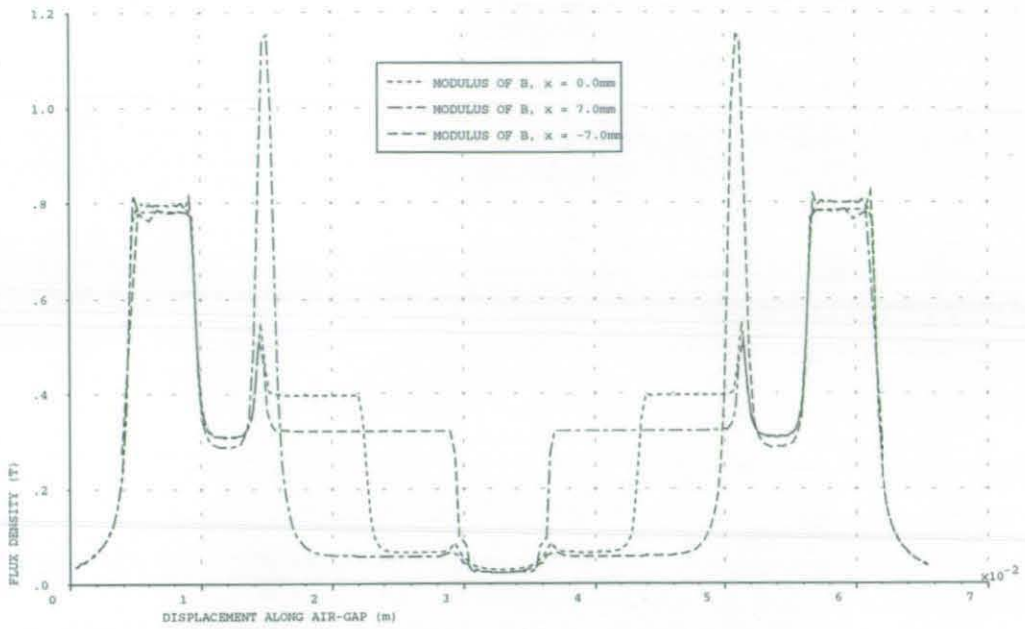


Fig. 5.4 Modulus of air-gap flux density for three armature positions.

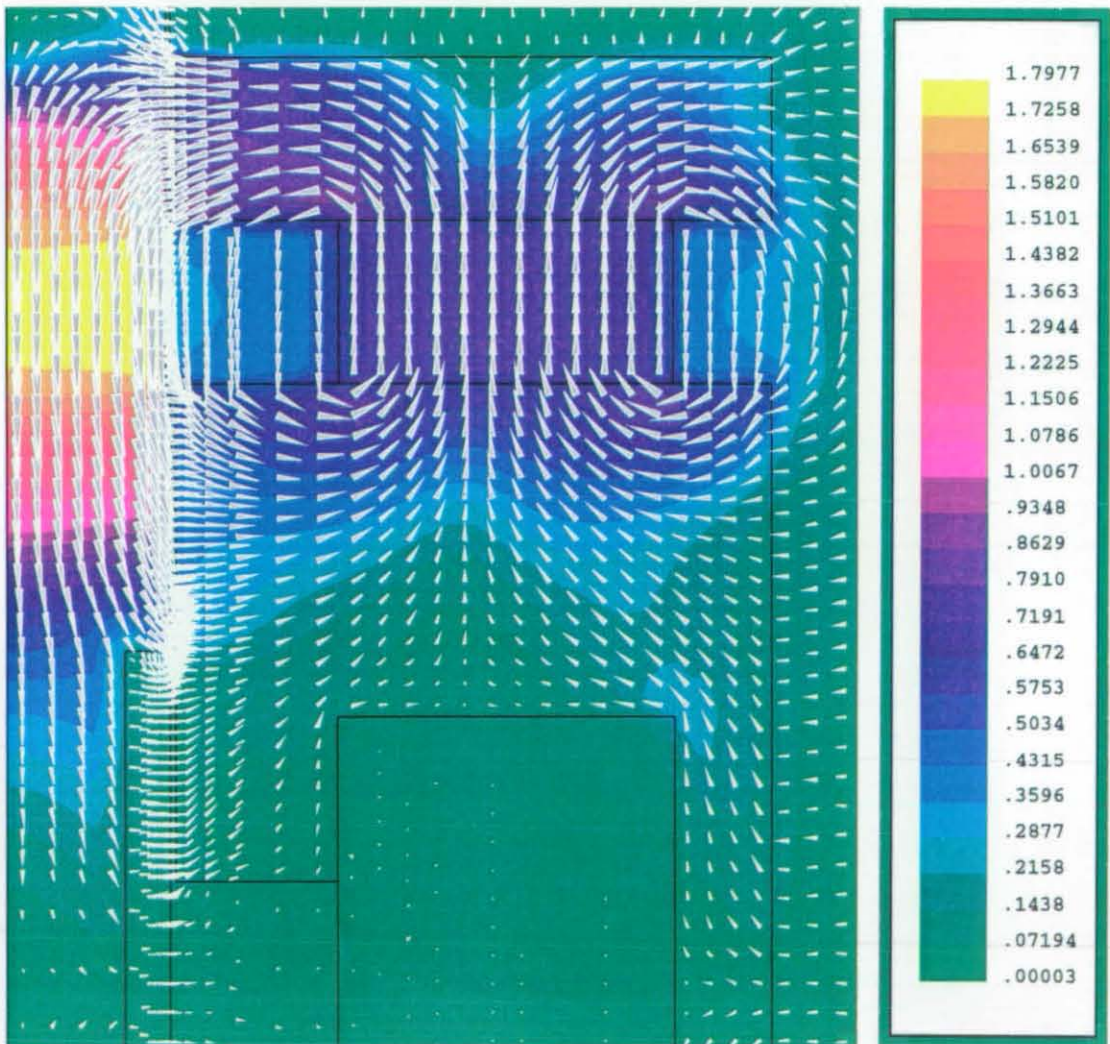
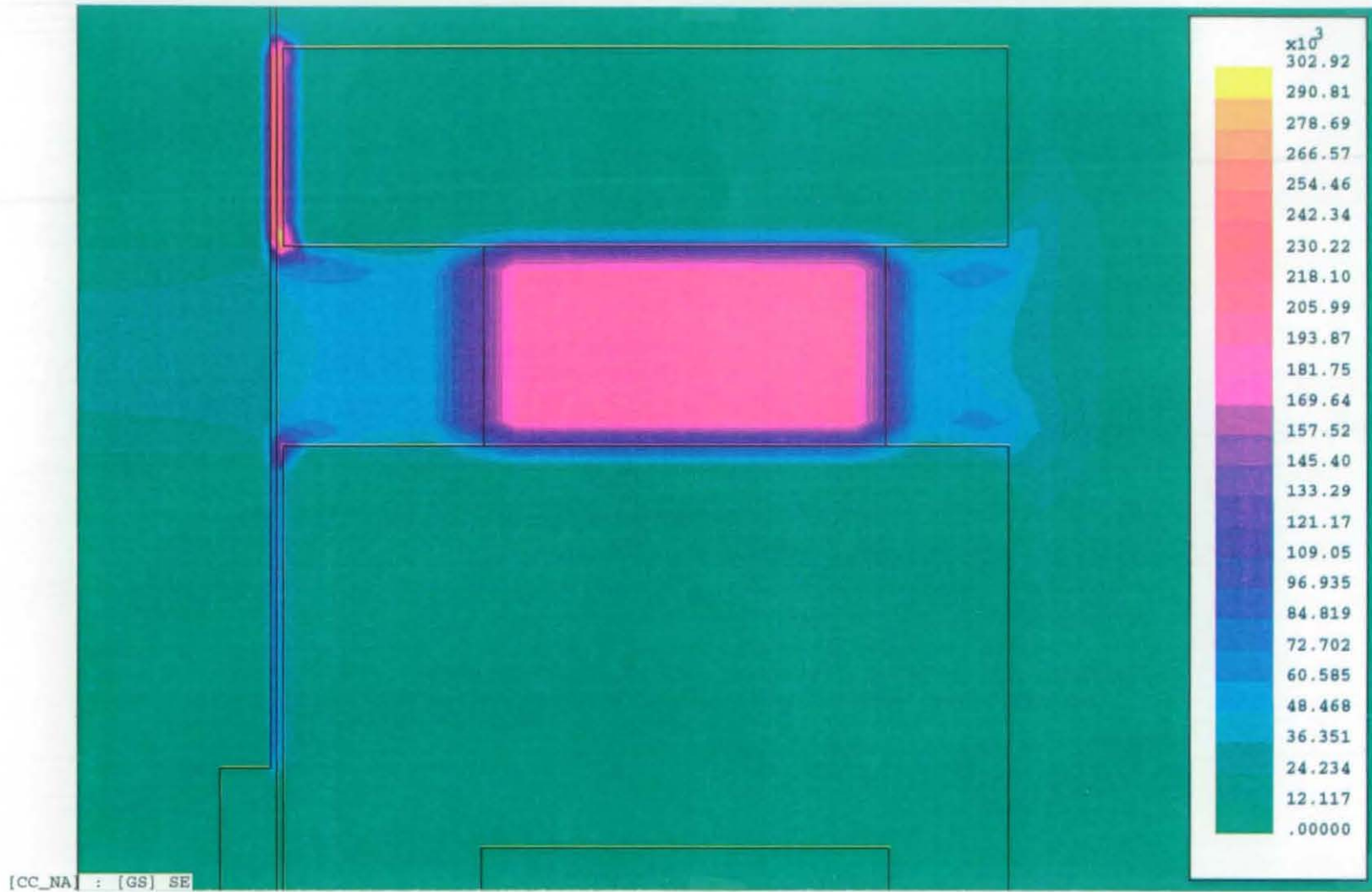
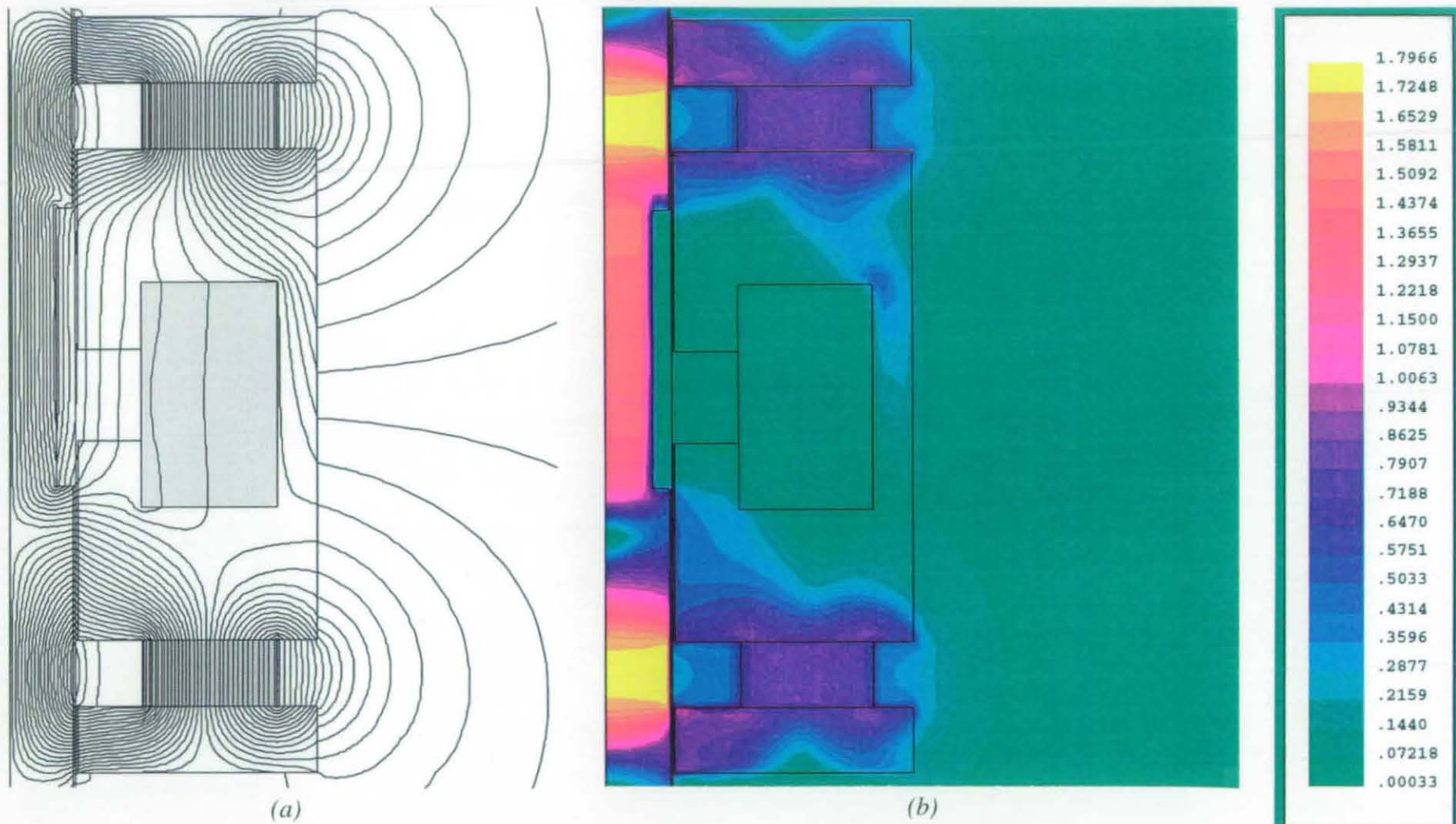


Fig. 5.5 Flux density at one end of the motor (armature central position).



**Fig. 5.6** Magnetic stored energy at one end of the motor (armature central position). Units of contour key in energy density ( $\text{J/m}^2$ )





**Fig. 5.7** Magnetic field in the linear motor for the new stable armature position

(a) vector equipotential plot (b) flux density plot

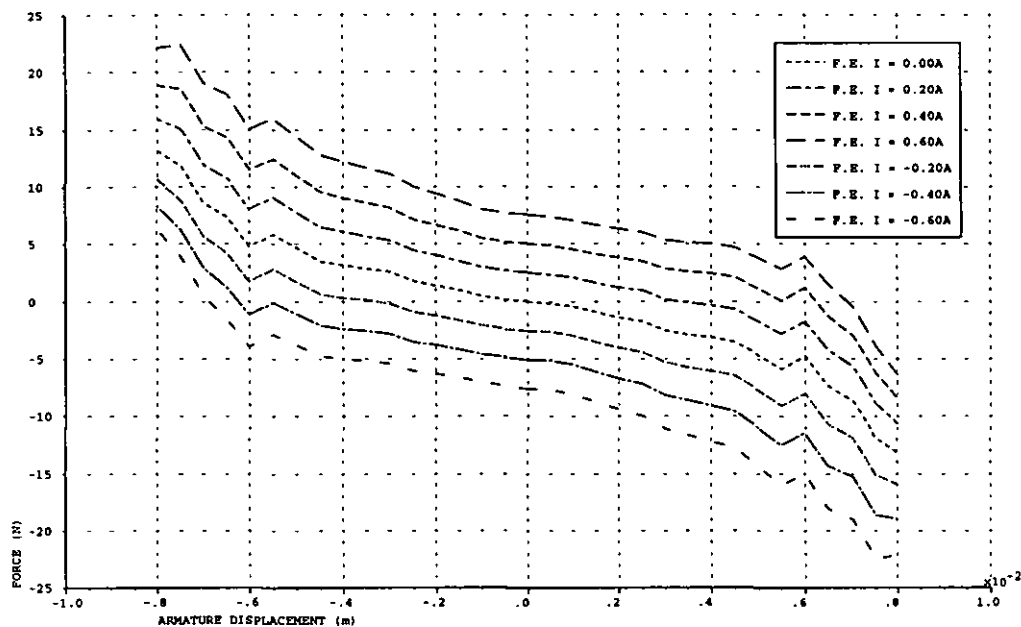


Fig. 5.8 Force/armature displacement characteristic for various coil currents from a linear finite element analysis

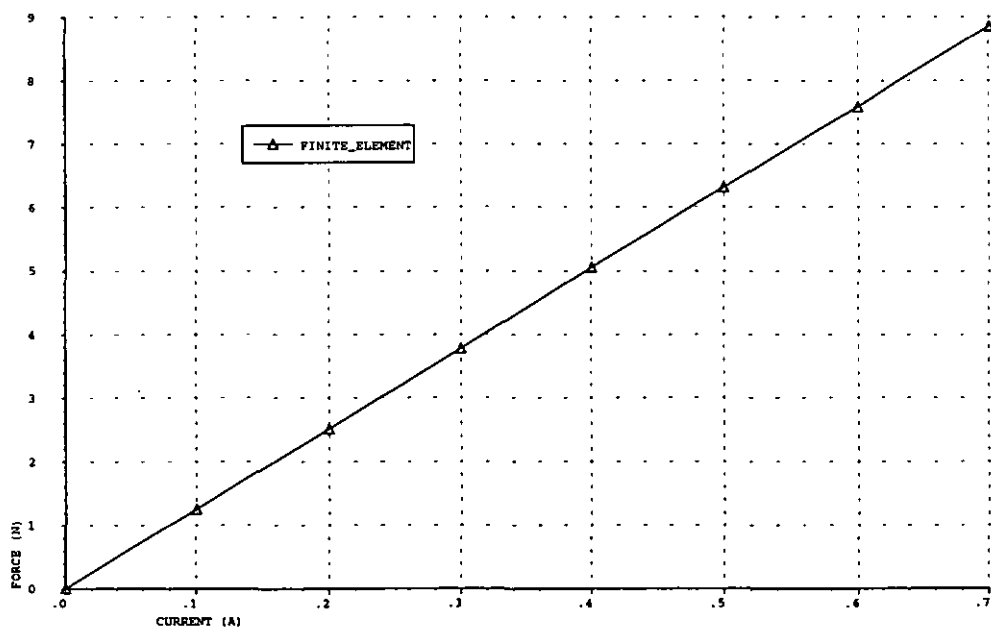


Fig. 5.9 Force/coil current characteristic from a linear finite element analysis (armature central position)

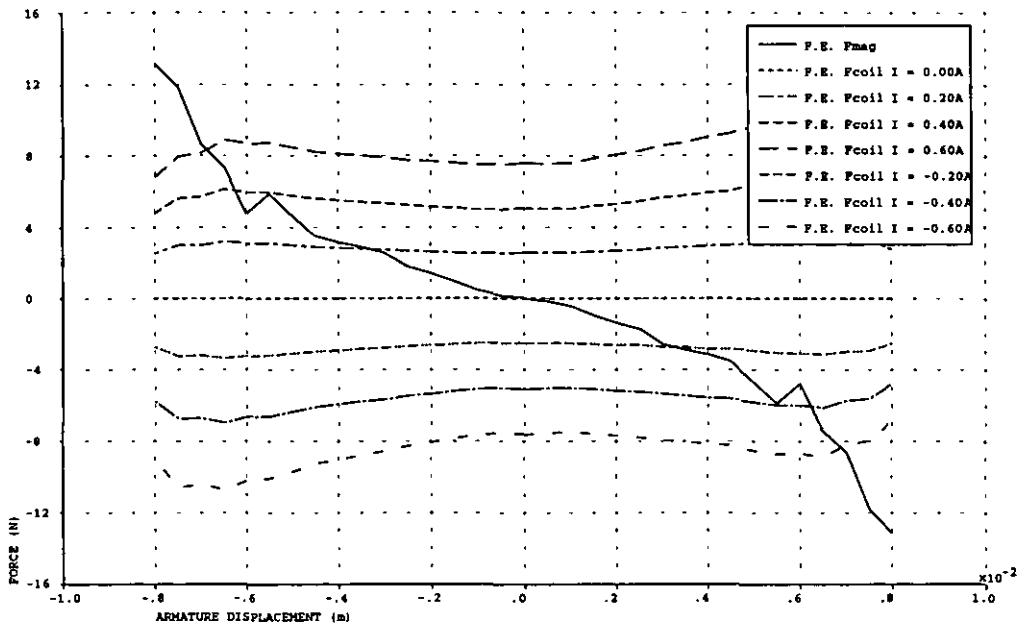


Fig. 5.10 Two components of the force characteristic from a linear finite element analysis

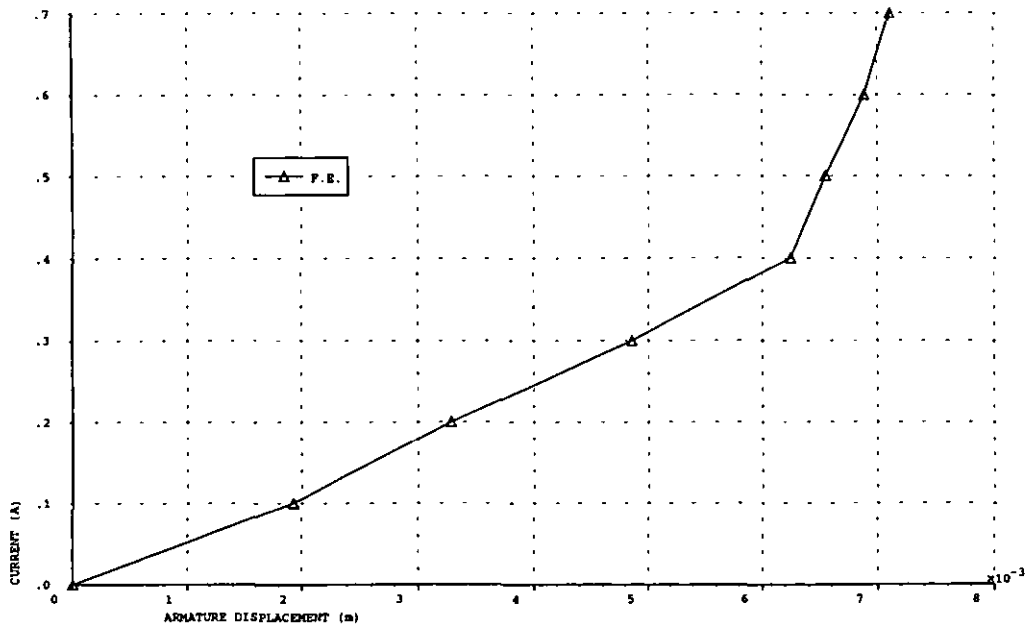


Fig. 5.11 Coil current/armature displacement characteristic from a linear finite element analysis

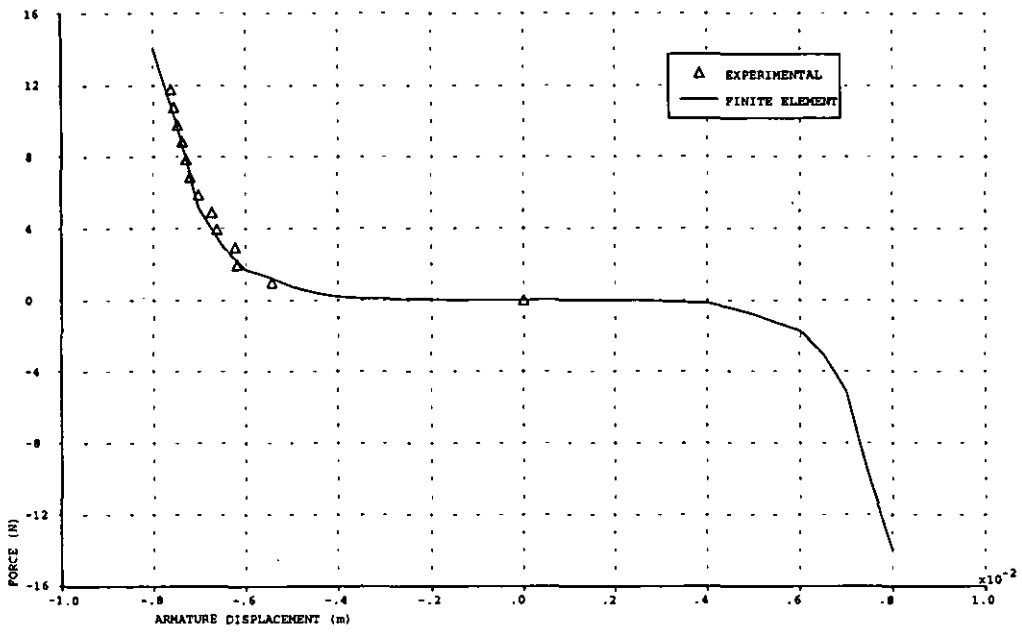


Fig. 5.12 Magnetic stiffness characteristic.

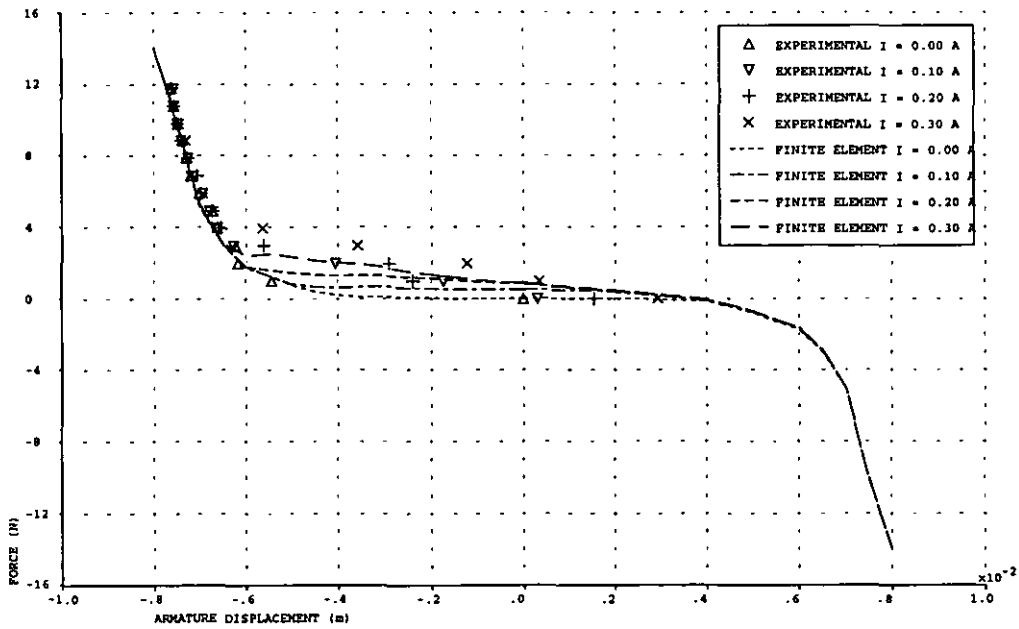


Fig. 5.13(a) Comparison between the experimental and the finite element obtained force characteristic for coil currents from 0 A to 0.3 A

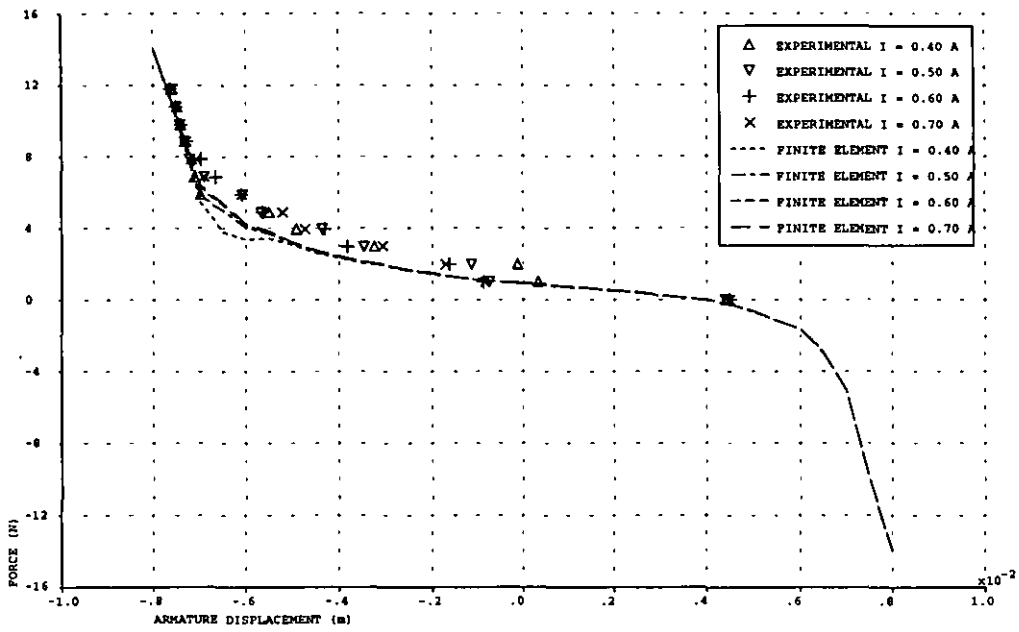


Fig. 5.13(b) Comparison between the experimental and the finite element obtained force characteristic for coil currents from 0.4 A to 0.7 A

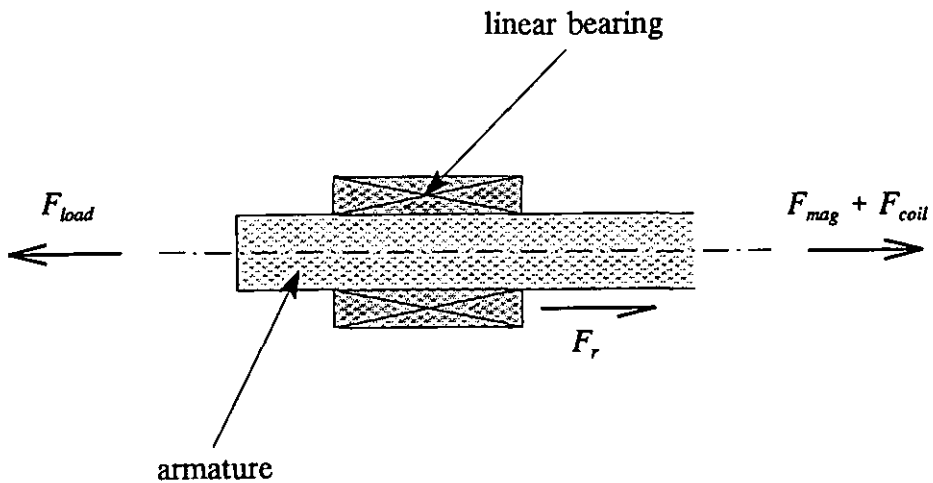


Fig. 5.14 Balance of forces acting on the armature

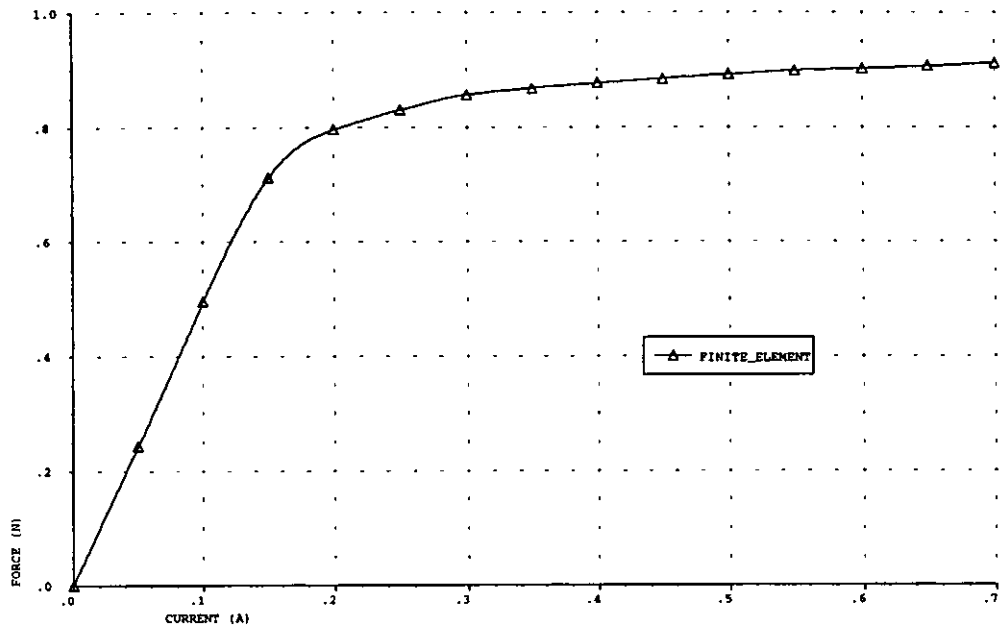


Fig. 5.15 Force/coil current characteristic (armature central position)

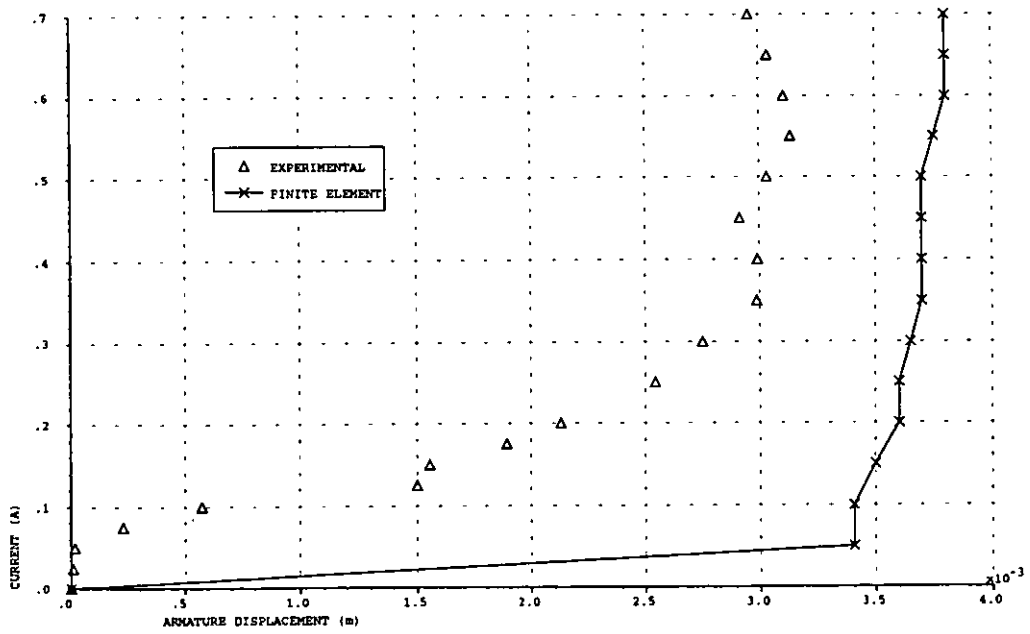


Fig. 5.16 Coil current/armature displacement characteristic

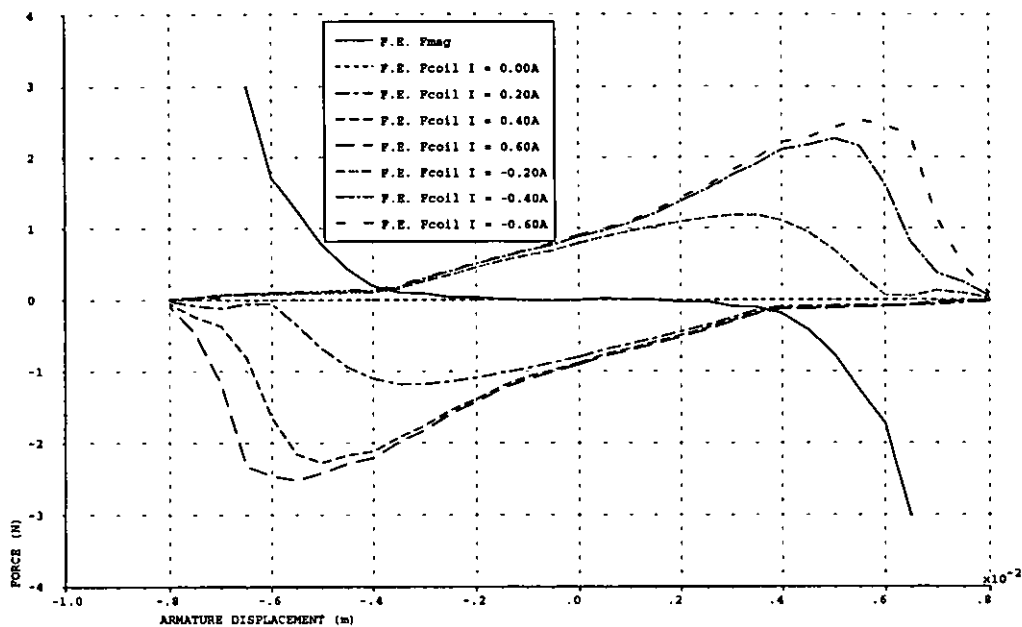


Fig. 5.17 Two components of the force characteristic

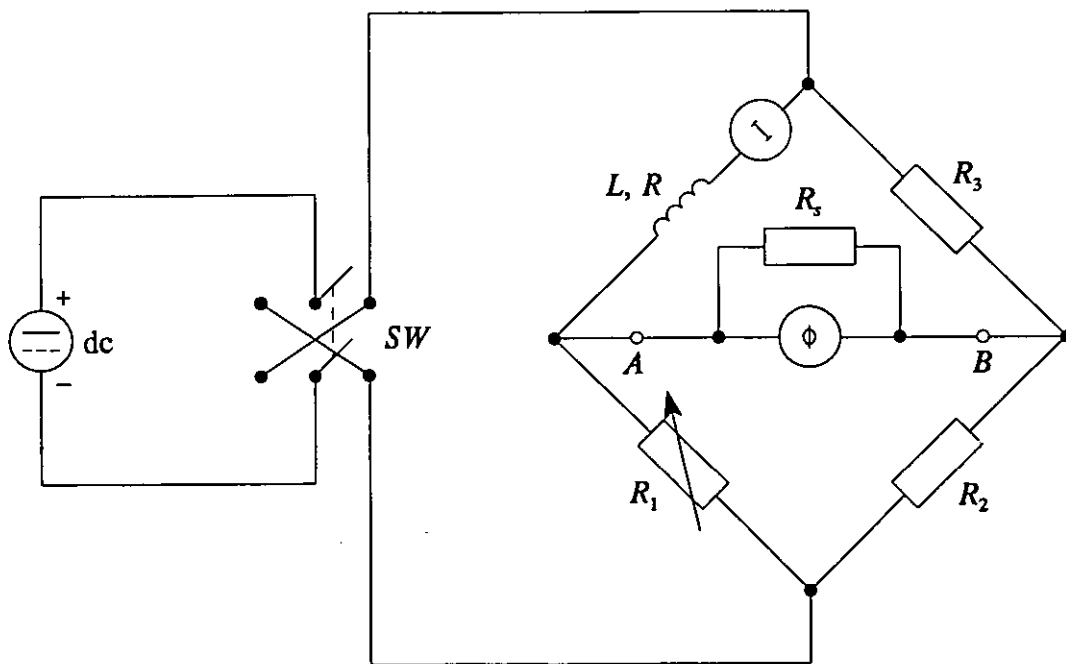


Fig. 5.18 DC inductance bridge

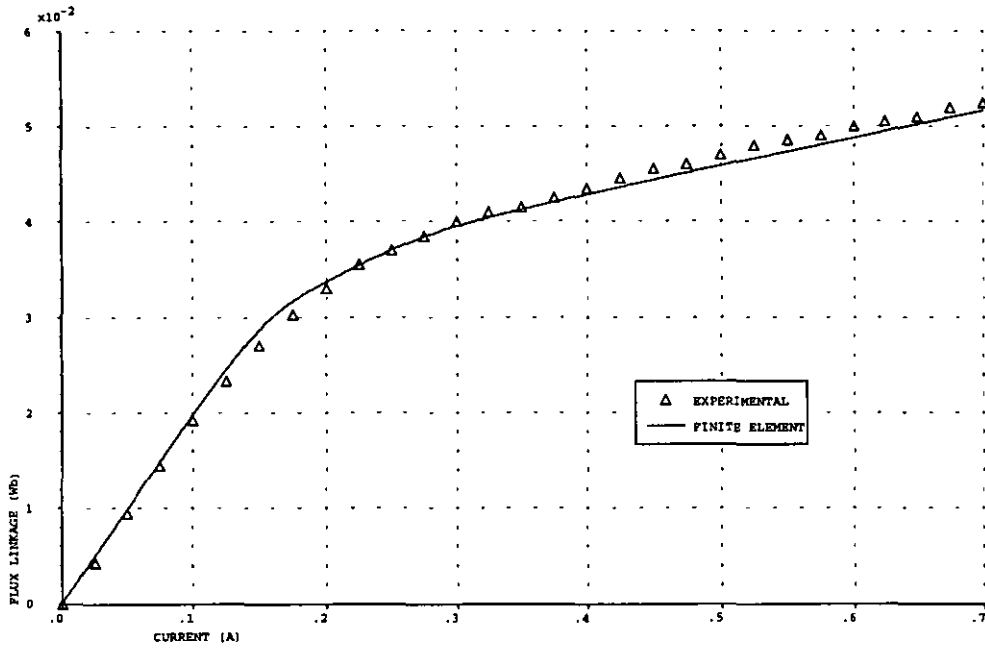


Fig. 5.19 Flux linkage/coil current characteristic (armature central position)

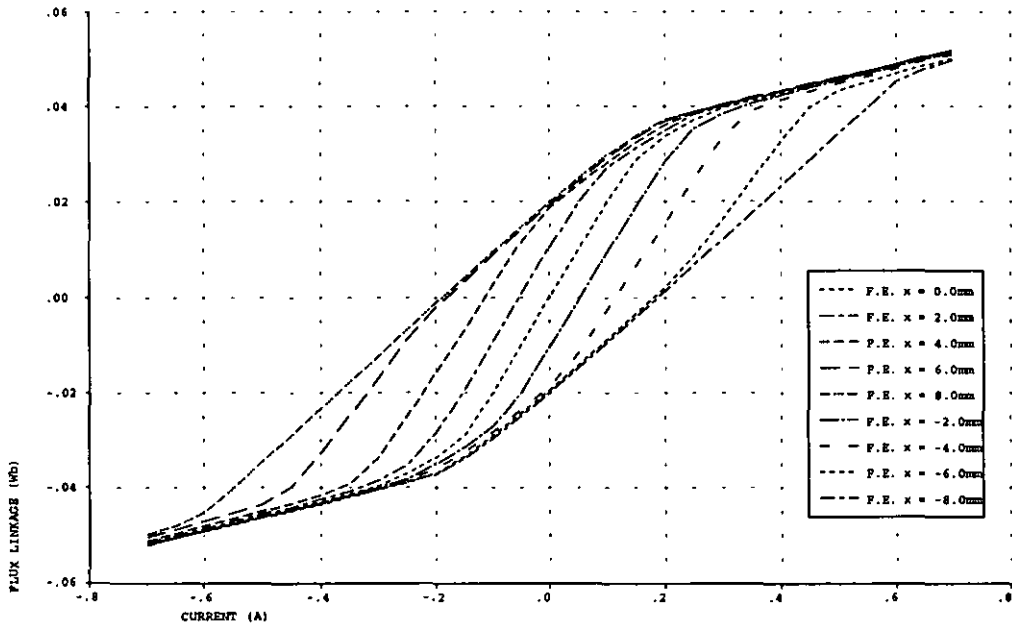


Fig. 5.20 Flux linkage characteristic at various positions of the armature for various coil currents



## DYNAMIC ANALYSIS OF THE LINEAR RELUCTANCE MOTOR

The design and development of an optimised linear motor requires the accurate prediction of both the static and dynamic performance. The static characteristics of the initial prototype design were examined in chapter 5 and conclusions were drawn as to possible improvements. In this chapter, the dynamic behaviour of the motor is evaluated using a mathematical model in the form of a set of first-order differential equations, which are solved using numerical techniques. Two models are developed; the first consists of the motor in isolation, while the second employs a full-bridge dc-to-dc converter connected to the motor, to provide four-quadrant drive operation using a tolerance band current control scheme. Experimental results for the motor are presented and compared with simulated results to illustrate the effectiveness of the mathematical model.

### 6.1 DYNAMIC SIMULATION ANALYSIS SOFTWARE

The linear motor can be described in terms of differential and algebraic equations. There are several methods available for solving such equations, and these include the development of a dedicated program using a high-level computer language such as *FORTRAN 77* or *C*, etc., where libraries are available for solving the differential equations, manipulating matrices, and graphically displaying results in the language chosen by using the *Numerical Algorithm Group (NAG)* library routines. General simulation programs are also available, such as *MATLAB* and *ACSL*, as well as *SABER* [74, 75], which is a program suited to simulating dynamic non-linear systems.

The development of a dedicated *FORTRAN 77* program was chosen to simulate the system, because the highly non-linear nature of the motor characteristics, already illustrated in chapter 5, could be modelled very accurately using such a program. *FORTRAN 77* was chosen rather than *MATLAB* or *ACSL*, because of familiarity with the language. Although *SABER* is ideal for simulating the dc-to-dc converter it was

rejected, because problems were foreseen in modelling the non-linear motor characteristics as accurately as could be achieved by use of a dedicated simulation program. However, recently, *SIMULINK* has been shown to be ideal for simulating electromagnetic devices [76].

## 6.2 MATHEMATICAL MODEL

Accurate modelling of the motor requires the assembly of the relevant differential equations, and the accurate definition of the non-linear coefficients of the system. The first simulation program, which predicts the dynamic performance of the motor when step input voltages are applied to the coil is described below.

### 6.2.1 Motor Differential Equations

The dynamic behaviour of the motor can be described by two coupled differential equations; the electrical circuit equation which models the coil, and the mechanical motion equation which models the armature movement and subsequent force generation. The two equations must be solved simultaneously.

#### 6.2.1.1 Electrical Circuit Equation

The electrical circuit equation is expressed by:

$$V = iR + \frac{d\lambda(x, i)}{dt} \quad (6.1)$$

where  $V$  is the voltage applied to the coil,  $i$  the coil current,  $R$  the coil resistance and  $\lambda$  the coil flux linkage. The coil flux linkage, shown in Fig. 5.20, is a function of the coil current  $i$  and the armature position  $x$ . Therefore, the last term on the right-hand side of equation (6.1) can be represented mathematically as:

$$\frac{d\lambda(x, i)}{dt} = \left(\frac{\partial\lambda}{\partial i}\right)\frac{di}{dt} + \left(\frac{\partial\lambda}{\partial x}\right)\frac{dx}{dt} \quad (6.2)$$

where the partial derivatives  $(\partial\mathcal{N}/\partial i)$  and  $(\partial\mathcal{N}/\partial x)$  are obtained from the finite element field solution. The description of how they are acquired is given in section 6.2.2.1.

### 6.2.1.2 Mechanical Motion Equation

The mechanical equation of motion of the motor is:

$$F_{coil}(x, i) = M \frac{d^2x}{dt^2} + k_d \frac{dx}{dt} + F_{mag}(x) \quad (6.3)$$

where  $M$  is the armature mass,  $k_d$  the viscous damping coefficient,  $F_{coil}$  the force produced by the excited coil and  $F_{mag}$  the magnetic stiffness. The two forces are obtained from the finite element analysis field solution, described in sections 6.2.2.2 and 6.2.2.3. Equation (6.3) is a second-order equation, which can be reduced to a pair of simultaneous first-order equations, to enable their solution, and these are given by:

$$F_{coil}(x, i) = M \frac{dv}{dt} + k_d v + F_{mag}(x) \quad (6.4)$$

and

$$v = \frac{dx}{dt} \quad (6.5)$$

where  $v$  is the armature velocity. Equations (6.4) and (6.5) are re-arranged into their state-variable form described below.

### 6.2.1.3 Differential Equations in State-Variable Form

Substituting equation (6.2) into (6.1) and re-arranging produces:

$$\frac{di}{dt} = \left( \frac{\partial\lambda}{\partial i} \right)^{-1} \left[ V - iR - \left( \frac{\partial\lambda}{\partial x} \right) \frac{dx}{dt} \right] \quad (6.6)$$

Similarly, re-arranging equations (6.4) and (6.5) yields:

$$\frac{dv}{dt} = M^{-1} [F_{coil} - k_d v - F_{mag}] \quad (6.7)$$

$$\frac{dx}{dt} = v$$

The next section describes the method whereby the flux linkage and force characteristics are used to obtain  $(\partial\lambda/\partial i)$ ,  $(\partial\lambda/\partial x)$ ,  $F_{coil}$  and  $F_{mag}$ , for subsequent use in equations (6.6) and (6.7).

### 6.2.2 Non-linear Characteristics

In chapter 5, computed field solutions were used to obtain characteristics of flux linkage and force at discrete armature positions over the whole armature stroke length for various discrete coil currents, and these characteristics are shown in Figs. 5.13 and 5.20. These results can be illustrated in three-dimensional form, with the flux linkage characteristic shown in Fig. 6.1 and the force characteristic in Fig. 6.2. These discrete values of flux linkage and force are entered into a data file and used in the mathematical model simulation program. To evaluate the flux linkage and force for any other coil current and armature position, other than the computed discrete points, requires a method of curve fitting and interpolation to be implemented. A piece-wise linear fit to the discrete points would not enable the derivatives  $(\partial\lambda/\partial i)$  and  $(\partial\lambda/\partial x)$  to be calculated with any precision and it is impossible to fit a high-order polynomial function to the discrete points. The only possible solution is to fit cubic splines to the characteristics.

The exact method employed used a bicubic spline approximation fitted to the discrete points. This technique of curve fitting produces flux linkage and force characteristics that are continuous in the function and the first derivative, and to obtain the partial derivatives of the flux linkage characteristic with respect to  $i$ ,  $(\partial\lambda/\partial i)$ , and  $x$ ,  $(\partial\lambda/\partial x)$ , simply requires the derivatives of the appropriate cubic polynomial in the bicubic spline fit to be calculated. This method was used in [29] and close agreement between experimental and simulated results was achieved. Similar techniques that use a static finite element field solution to obtain flux linkages and forces have been used

in the past to good effect when analyzing a circuit breaker solenoid actuator [77] and a two-valve solenoid actuator [78].

### 6.2.2.1 Flux Linkage Characteristic Bicubic Spline Approximation

Fig. 6.3(a) shows a typical flux linkage characteristic as a three-dimensional surface, similar to Fig. 6.1, in which the flux linkages that were computed from the static field solution are positioned where the lines on the surface intersect at the discrete coil currents and armature positions. To calculate  $(\partial\lambda/\partial i)$  from this surface first requires fitting a cubic spline through each  $\lambda = f(x)$  at each discrete coil current  $i$ , shown in Fig. 6.3(a), where the thicker lines denote each spline. This can be expressed mathematically as:

$$\lambda_p(x) = \sum_{p=1}^{n+1} \sum_{q=1}^m g_q f_q(x) \quad (6.8)$$

with:

$$f_q(x) = ax^3 + bx^2 + cx + d \quad (6.9)$$

where  $g_q$  are the set of coefficients ( $a$ ,  $b$ ,  $c$  and  $d$ ) of each cubic polynomial segment  $f_q(x)$ , and  $m$  segments make up the spline fit of each  $\lambda = f(x)$  characteristic.  $\lambda_p(x)$  is the resulting set of  $(n + 1)$  approximated  $\lambda = f(x)$  characteristics for every discrete coil current  $i$ , where  $n$  is the number of segments that make up the spline fit of each  $\lambda = f(i)$  curve. Each  $\lambda = f(x)$  characteristic is then solved by substituting into each  $x'$ , where  $x'$  is the present armature position, see Fig. 6.3(b). The result is a set of flux linkage values  $\lambda_p(x')$  for every discrete coil current  $i$ , i.e. a  $\lambda = f(i)$  curve has been created at  $x'$ . A spline is then fitted through this function, expressed as:

$$\lambda(i) = \sum_{p=1}^n h_p f_p(i) \quad |x = x' \quad (6.10)$$

where  $h_p$  are the set of coefficients of each cubic polynomial segment  $f_p(i)$ , and  $\lambda(i)$  is the flux linkage approximation function with respect to the coil current  $i$  at  $x'$ . The present value of the coil current  $i'$  is then substituted into the appropriate polynomial in the spline function, shown in Fig. 6.3(c), which yields:

$$\lambda(i') \Big|_{x=x'} = a(i')^3 + b(i')^2 + c(i') + d \quad (6.11)$$

and differentiating equation (6.11) produces the partial derivative of the flux linkage with respect to  $i$  at  $x'$ :

$$\frac{\partial \lambda(i')}{\partial i} \Big|_{x=x'} = 3a(i')^2 + 2b(i') + c \quad (6.12)$$

Fig. 6.3(d) shows the above graphically.

The calculation of  $(\partial \lambda / \partial x)$  is similar to that described above for  $(\partial \lambda / \partial i)$ . The first step requires fitting a cubic spline through each  $\lambda = f(i)$  characteristic at each discrete armature position  $x$ . Each  $\lambda = f(i)$  function is then solved, by substituting  $i'$  for  $i$  in each function, where  $i'$  is the present coil current. The result is a set of flux linkage values  $\lambda_q(i')$  for every discrete armature position  $x$ , where  $q = 1$  to  $(m + 1)$ , i.e. the number of discrete armature positions. A spline is then fitted through these values and  $x'$  is substituted into the appropriate polynomial in the spline to find  $\lambda(x')$  as:

$$\lambda(x') \Big|_{i=i'} = a(x')^3 + b(x')^2 + c(x') + d \quad (6.13)$$

and the partial derivative of the flux linkage with respect to  $x$  where  $i = i'$  is:

$$\frac{\partial \lambda(x')}{\partial x} \Big|_{i=i'} = 3a(x')^2 + 2b(x') + c \quad (6.14)$$

Fig. 6.4(a-d) shows the above graphically.  $(\partial \lambda / \partial i)$  and  $(\partial \lambda / \partial x)$  are inserted into the electrical circuit equation which is then integrated numerically.

### 6.2.2.2 Force Characteristic Bicubic Spline Approximation

The calculation to obtain  $F_{coil}$  is initially similar to the procedure given above for calculating the flux linkage. The first step is to fit splines through either the  $\lambda = f(x)$  characteristics at each discrete coil current  $i$ , or splines through the  $\lambda = f(i)$  functions at each discrete armature position  $x$ . If splines are fitted to the former, each is solved by substituting  $x'$  into each spline. The result is a set of force values  $F(x')$  for every discrete current  $i$ . A spline is then fitted through these values and  $i'$  is substituted into

the appropriate polynomial segment to find  $F(i')$  as:

$$F(i') \Big|_{x=x'} = a(i')^3 + b(i')^2 + c(i') + d \quad (6.15)$$

When the latter initial step is implemented, the final value of the force acting on the armature is:

$$F(x') \Big|_{i=i'} = a(x')^3 + b(x')^2 + c(x') + d \quad (6.16)$$

The forces obtained from equations (6.15) and (6.16) will have the same magnitude. To obtain  $F_{coil}$  from  $F$  requires subtraction of the magnetic stiffness function  $F_{mag}$ . The next section describes how  $F_{mag}$  is determined.

### 6.2.2.3 Magnetic Stiffness Characteristic Cubic Spline Approximation

The stiffness characteristic  $F_{mag}$ , shown in Fig. 5.12, is a function of  $x$  only and the single cubic spline required to approximate it, takes the form:

$$F_{mag}(x) = \sum_{r=1}^m k_r f_r(x) \quad (6.17)$$

which can be solved by substituting into the appropriate polynomial segment the current position of the armature  $x'$ . Once  $F_{mag}$  has been determined  $F_{coil}$  can be calculated from:

$$F_{coil} = F - F_{mag} \quad (6.18)$$

$F_{coil}$  and  $F_{mag}$  are then inserted into the mechanical motion equation to complete the assembly of the motor equations and to enable numerical integration to follow.

### 6.2.3 Other Motor Parameters

The coil resistance  $R$  of  $7.67 \Omega$  used in the mathematical model was calculated using equation (3.11). The volume of the armature mesh was calculated using *MEGA*, and by using the density of Radiometal 4550 ( $8.25 \text{ g/cm}^3$ ) the armature mass  $M$  of 68.69 g was determined. This value compared favourably with the measured mass of 68.86 g. The total moving mass was the combined (armature + LVDT armature +

accelerometer) mass which equalled  $(68.69 + 12.5 + 11.5) \text{ g} = 92.69 \text{ g}$ . Applying a step voltage input to the motor and comparing the experimental and simulated armature displacement responses enables the damping coefficient  $k_d$  to be obtained, by adjusting the simulated response to agree with the experimental response. The mechanical time constant  $\tau_m$  can then be determined as  $(M/k_d)$ . This process is repeated by exciting the motor with a sinusoidal current over a wide range of frequencies, to adjust further and tune the damping coefficient and hence the mechanical time constant. Using the above method the damping coefficient was found to be about 4.5 Ns/m. The resulting mechanical time constant was subsequently used in later motor designs to calculate the damping coefficients.

#### 6.2.4 Numerical Integration

Various methods are available to solve numerically differential equations, and the most commonly used approaches include Euler and Modified Euler methods, Runge-Kutta methods and multi-step methods [79]. The first of these are single-step methods, which are simple to use but have a major disadvantage in that they are susceptible to errors which can cause a lack of accuracy unless a very small integration step is used. Single-step Runge-Kutta methods are computationally more efficient than Euler methods, and the most widely used technique is the fourth-order Runge-Kutta method. Other techniques, which also give an estimate of the error in a computation, include the Runge-Kutta-Fehlberg and the Runge-Kutta-Merson methods. The advantage of the fourth-order technique is that only four evaluations per integration step are required, compared with five and six evaluations when using the two variants.

Multi-step techniques, such as Adams, Milne's and Adams-Moulton methods are even more efficient than Runge-Kutta methods, but have a major disadvantage in that they cannot be employed at the start of the integration because they utilise past values of the function which do not exist at the beginning of integration and therefore can only be used after several steps of using a single-step method. These techniques also give an estimate of the error in the solution, but Milne's method can be unstable [79], and when any changes of the integration step are required both methods cause problems.



The fourth-order Runge-Kutta method was chosen in this work because it has good stability and can easily handle changes of step length, which is particularly important when implementing the current control scheme described in section 6.5.1.1. Of the accurate single-step methods, it requires the least functional evaluations per step. The next two sections describe the application of the method to the solution of the motor differential equations.

#### 6.2.4.1 Electrical Circuit Equation

Equation (6.6) is a function of  $t$  and coil current  $i$ :

$$f(t, i) = \frac{di}{dt} = \left(\frac{\partial \lambda}{\partial i}\right)^{-1} \left[ V - iR - \left(\frac{\partial \lambda}{\partial x}\right) \frac{dx}{dt} \right] \quad (6.19)$$

The fourth-order Runge-Kutta algorithm employs the following formula:

$$i_{n+1} = i_n + \frac{1}{6} [g_0 + 2g_1 + 2g_2 + g_3] \quad (6.20)$$

where:

$$g_0 = h f(t_n, i_n) = h \left(\frac{\partial \lambda}{\partial i}\right)^{-1} \left[ V - i_n R - \frac{\partial \lambda}{\partial x} \frac{dx}{dt} \right]$$

$$g_1 = h f\left(t_n + \frac{1}{2}h, i_n + \frac{1}{2}g_0\right) = h \left(\frac{\partial \lambda}{\partial i}\right)^{-1} \left[ V - (i_n + \frac{1}{2}g_0)R - \frac{\partial \lambda}{\partial x} \frac{dx}{dt} \right]$$

$$g_2 = h f\left(t_n + \frac{1}{2}h, i_n + \frac{1}{2}g_1\right) = h \left(\frac{\partial \lambda}{\partial i}\right)^{-1} \left[ V - (i_n + \frac{1}{2}g_1)R - \frac{\partial \lambda}{\partial x} \frac{dx}{dt} \right]$$

$$g_3 = h f(t_n + h, i_n + g_2) = h \left(\frac{\partial \lambda}{\partial i}\right)^{-1} \left[ V - (i_n + g_2)R - \frac{\partial \lambda}{\partial x} \frac{dx}{dt} \right]$$

The coil current  $i$  is updated on each loop of the program. i.e. at every step interval  $h$ .

### 6.2.4.2 Mechanical Motion Equation

Equation (6.7) is a function of  $t$ , armature velocity  $v$  and displacement  $x$ :

$$f(t, v, x) = \frac{dv}{dt} = M^{-1} [F_{coil} - k_d v - F_{mag}] \quad (6.21)$$

$$g(t, v, x) = \frac{dx}{dt} = v$$

which results in two fourth-order Runge-Kutta algorithms:

$$v_{n+1} = v_n + \frac{1}{6} [k_0 + 2k_1 + 2k_2 + k_3] \quad (6.22)$$

$$x_{n+1} = x_n + \frac{1}{6} [l_0 + 2l_1 + 2l_2 + l_3]$$

where:

$$k_0 = h f(t_n, v_n, x_n) = h M^{-1} [F_{coil} - k_d v_n - F_{mag}]$$

$$l_0 = h g(t_n, v_n, x_n) = h v_n$$

$$k_1 = h f\left(t_n + \frac{1}{2}h, v_n + \frac{1}{2}k_0, x_n + \frac{1}{2}l_0\right) = h M^{-1} \left[ F_{coil} - k_d \left( v_n + \frac{1}{2}k_0 \right) - F_{mag} \right]$$

$$l_1 = h g\left(t_n + \frac{1}{2}h, v_n + \frac{1}{2}k_0, x_n + \frac{1}{2}l_0\right) = h \left( v_n + \frac{1}{2}k_0 \right)$$

$$k_2 = h f\left(t_n + \frac{1}{2}h, v_n + \frac{1}{2}k_1, x_n + \frac{1}{2}l_1\right) = h M^{-1} \left[ F_{coil} - k_d \left( v_n + \frac{1}{2}k_1 \right) - F_{mag} \right]$$

$$l_2 = h g\left(t_n + \frac{1}{2}h, v_n + \frac{1}{2}k_1, x_n + \frac{1}{2}l_1\right) = h \left( v_n + \frac{1}{2}k_1 \right)$$

$$k_3 = h f(t_n + h, v_n + k_2, x_n + l_2) = h M^{-1} [F_{coil} - k_d (v_n + k_2) - F_{mag}]$$

$$l_3 = h g(t_n + h, v_n + k_2, x_n + l_2) = h (v_n + k_2)$$

Computation of the above algorithm alternates between calculating the coefficients of the velocity formula and the displacement formula, e.g., to calculate  $l_1$  requires the prior determination of  $k_0$ .

### 6.3 COMPUTER IMPLEMENTATION

Fig. 6.5 shows a flow chart for the program that implements the bicubic spline approximations, described in sections 6.2.2.1 and 6.2.2.2, and the cubic spline approximation, described in section 6.2.2.3, and then solves numerically the motor equations derived in section 6.2.1. The bicubic spline approximation routine was developed from a single cubic spline fit routine given in [80].

The program commences by declaring and initializing all variables, setting the initial conditions to zero and specifying the integration time increment  $h$ . The data for the non-linear characteristics of flux linkage, force and magnetic stiffness are read into the program, followed by other motor parameters, such as armature mass, viscous damping coefficient and coil resistance. Further constants read into the program at this stage include the amplitude of the step demand voltage.

The next step is to fit cubic splines to all the  $\lambda = f(x)$  characteristics read in previously, and to store, in arrays in the program, the coefficients of each polynomial segment of the spline fits. This is then repeated for all of the  $\lambda = f(i)$  characteristics at every discrete armature position, and all the  $F = f(i)$  characteristics. A spline does not have to be fitted to all the  $F = f(x)$  functions at every discrete current, because the partial derivatives of the force with respect to coil current or armature position do not have to be determined. It suffices therefore to fit splines through only one set of force functions, i.e.  $F = f(i)$  in this program, to determine the force  $F$ . The initial conditions are then written to the output files and the loop count is updated to commence the main section of the program which is repeated a number of times depending on the loop count final value.

The main section of the program first updates the voltage applied across the coil, which can either be a step or a sinusoidal function. The values of  $(\partial\lambda/\partial i)$ ,  $(\partial\lambda/\partial x)$ ,  $F_{coil}$  and  $F_{mag}$  are then determined following the procedures described in section 6.2.2. The third force that causes acceleration  $a$  of the armature,  $F_{accel}$ , is then calculated from:

$$F_{accel} = Ma = F_{coil} - k_d v + F_{mag} \quad (6.23)$$

The force values obtained from this calculation are compared with experimentally obtained values in section 6.4. The motor equations are then formulated with the updated non-linear parameters and integrated numerically, as described in section 6.2.3, to obtain new values for the state-variables. At the end of every program loop, the time  $t$  is incremented by  $h$ , and the computed values of coil current, voltage, armature position, armature velocity and acceleration force are written to the output files for analyzing and displaying graphically. The program loop is repeated until the loop count final value is reached.

#### 6.4 SIMULATED AND EXPERIMENTAL RESULTS

Experimental measurements of the armature displacement were obtained using a linear variable differential transformer (LVDT) displacement transducer, that was connected to the armature shaft and is linear over a movement of  $\pm 15$  mm. The force  $F_{accel}$  was measured by an accelerometer attached to the armature. The acceleration force was determined from the product of the acceleration and the combined (armature + LVDT armature + accelerometer) mass. The accelerometer was capable of measuring up to  $\pm 25$  g at a frequency range from 2 Hz to 8 kHz.

Fig. 6.6 compares the simulated and experimental results from the prototype motor when the coil voltage is reversed from +2.28 V to -2.28 V, thus reversing the current from +0.3 A to -0.3 A. The current overshoot in the experimental result, shown in Fig. 6.6(b), is probably due to the capacitance of the power supply in the test circuit producing a second-order effect compared with the first-order simulation. The simulated armature displacement result produces a small overshoot which is absent from the experimental result, shown in Fig. 6.6(d). The difference is possibly due to bearing friction which inhibits armature movement resulting in a much reduced overshoot and a subsequent small static positional error. The experimental acceleration force peaks at about 0.90 N compared with the simulated peak force of 0.71 N from Figs. 6.6(e) and (f). The discrepancy could be due to the viscous

damping coefficient in the mathematical model being too large and resulting in a reduction in the force, although a reduced damping coefficient will produce a larger armature positional overshoot.

Fig. 6.7 compares the simulated and experimental results when the coil voltage is reversed from +4.57 V to -4.57 V, which reverses the current from +0.6 A to -0.6 A. The experimental results obtained are very similar in appearance to the results shown in Fig. 6.6. However, an experimental armature positional overshoot is now seen, as shown in Fig. 6.7(d), but a static positional error of about 0.7 mm is still evident. Fig. 6.7(f) shows the experimental acceleration force which peaks at about 1.33 N, compared with the smaller simulated peak force of 1.16 N. Both experimentally obtained acceleration forces are not as smooth as the simulated forces and this again is probably due to bearing friction.

Figs. 6.8(a) and (b) show the armature velocities for the two simulations described above. The two opposing forces that balance each other, the stiffness  $F_{mag}$  and the coil force  $F_{coil}$ , when the armature is stationary and the coil excited are shown in Figs. 6.8(c), (d) and Fig. 6.8(e), (f) for the two simulations. The equal and opposite forces are seen to be about 0.23 N for each simulation. This highlights the detrimental effect of armature saturation, because although the coil current in the second simulation is double that of the first, the force produced is the same.

## 6.5 CONTROLLING THE CURRENT IN THE LINEAR MOTOR COIL

To assess the dynamic performance of the various designs of motor, it is useful to supply a sinusoidal exciting current of constant peak amplitude, over a wide range of demand frequency. This enables the performance of various designs to be examined, with the differing results being due to the geometry of the magnetic circuit alone and independent of the electrical circuit. This can be achieved using a dc-to-dc converter with a control scheme to force any required current waveform through the coil by controlling the switching pattern of the converter switches. The next section describes the principle of operation of the system.

### 6.5.1 Principle of Operation

In order to produce four-quadrant operation, both the output voltage and current must be able to reverse in polarity, as shown in Fig. 6.9. A linear operational amplifier can satisfy the above requirement, but due to its low efficiency it is limited to a very low power range [81]. Another method, which employs a full-bridge dc-to-dc converter (also known as an H-bridge or switch-mode inverter), is shown in Fig. 6.10. The line frequency ac input is rectified using a diode rectifier and then filtered to obtain the dc source shown. Use of all four converter switches, ( $SW_1$  to  $SW_4$ ), during each cycle of the demand results in four-quadrant operation with continuous conduction, where both  $V$  and  $i$  can reverse independently. To improve the dynamic response of the system, a current loop is used to control the motor current. Two methods available for current control include variable-frequency tolerance band control (also known as Hysteresis band control) and fixed-frequency control [81]. In the system developed for this work, the former is used and is described below.

#### 6.5.1.1 Tolerance Band Control

The overall system arrangement to implement this control strategy is shown in Fig. 6.11, where the demand reference  $I_{demand}$  can be any required waveform. The actual current  $I_{actual}$  is compared with the tolerance band around the demand reference. If the actual waveform attempts to go above the upper tolerance band, or upper current limit, the appropriate switch  $SW_1$  is turned-off, stopping current from the supply from being fed to the coil and diverting the existing current to the diode in the lower leg of the bridge  $D_4$  to decay or freewheel. The converse switching occurs if the actual current tries to go below the lower current limit. The switching pattern is illustrated in Fig. 6.12, together with the voltages across  $SW_1$  and  $SW_4$  for the complete demand cycle. For low demand frequencies, typically less than 20 Hz, Fig. 6.13 shows the switching strategy and mesh conduction sequence, where meshes a, b, d and e, (known as the reduced network), correspond to the conduction paths through the switch-mode inverter, shown in Fig. 6.15.

However, if the frequency of the demand reference is sufficiently high, i.e. greater than about 20 Hz, a modified switching strategy must be employed on the part of the sinusoidal waveform where the gradient is negative, i.e. between  $\pi/2$  to  $\pi$  radians, and  $3\pi/2$  to  $2\pi$  radians. In this part of the waveform, the freewheeling current cannot decay at a faster rate than the demand current, due to the self-inductance of the excitation coil. A situation may arise in which the freewheeling current attempts to go beyond the upper current limit, and if a modified switching strategy is not implemented (four-quadrant operation) current control is lost. The modified strategy exploits the high instantaneous voltage ( $L di/dt$ ) across the coil which, when all switches are turned-off, forces the current to flow back into the supply. This occurs due to the voltage across the coil  $V$  exceeding the dc source voltage  $V_{dc} = 50$  V, i.e. regenerative operation. This mode of operation increases the rate of decay of the actual current even further than the freewheeling mode, and by keeping the actual current within the tolerance band, maintains current control. Fig. 6.14 shows this modified switching strategy, and illustrates that all meshes a-f are now used; meshes c and f are shown in Fig. 6.15.

Thus, the switching frequency is variable and is dependent on how fast the current changes from the upper limit to the lower limit and vice versa, and the rate of change of current depends on the incremental inductance and back-emf of the exciting coil and the dc source voltage  $V_{dc}$ .

### 6.5.2 Modelling of the Switch-Mode Inverter Circuit

The modelling process employs tensor methods [82, 83] to assemble automatically the differential equations of the motor for any instantaneous conduction pattern of the semiconductor switches and diodes. Tensor methods have been employed previously for simulating various types of electrical machine and power electronic converter [84, 85] and close agreement has been obtained between simulated and experimental results [86].

### 6.5.2.1 Positive Current Flow Sign Convention

When using tensor methods, it is necessary to define both branch and mesh reference frames and the transformation relationship between them. In the first step of the analysis, an arbitrary direction of positive current flow is assigned to each branch of the circuit, and when the branch currents and voltages are obtained their polarity will be relative to these directions. Arrows in Fig. 6.10 show the positive direction of current flow in all ten branches of the circuit, with each branch labelled with its own branch number, i.e.  $SW_1$  is branch (1) and the dc supply is branch (10), etc.. The direction of current flow through each semiconductor device was used to determine the positive flow of current in each branch. Positive current flow through the motor coil branch was arbitrarily chosen as left to right and the flow of current from the dc supply was chosen to be positive. The associated voltage drops across components in the circuit are taken as of positive sense if they oppose the flow of current.

### 6.5.2.2 Modelling of the Semiconductor Switches and Diodes

When a switch is in the off-state, it is treated simply as an open-circuit, and when in its on-state it is modelled as a voltage source in series with a resistance, similar to the method described in [87]. The voltage source represents the forward conduction voltage drop across the device when it is forward-biased and the resistance represents the low-resistance of the device when conducting. Diodes are modelled in a similar manner, i.e. when a diode is in the forward-biased state, it is modelled identical to a semiconductor switch in the on-state and when reversed-biased, it is treated as an open-circuit. Fig. 6.16 illustrates the method of representing the semiconductor devices in the on-state.

### 6.5.2.3 Voltage Equation Assembly

The next step in the analysis is to disconnect the ten branches from the inverter circuit and apply to each branch a hypothetical voltage source  $e_b$ . When branches are replaced in the inverter by identical voltage sources  $e_b$ , this modified circuit will



behave identically to the original circuit, even though the individual components in every branch have been removed. The branch reference frame voltage equation, given in equation 6.24, consists of ten equations, each describing one of the ten separate meshes of the primitive network shown in Fig. 6.17. Thus:

$$\begin{bmatrix} V_{SW_1} \\ V_{SW_2} \\ V_{SW_3} \\ V_{SW_4} \\ V_{D_1} \\ V_{D_2} \\ V_{D_3} \\ V_{D_4} \\ 0 \\ V_{dc} \end{bmatrix} + \begin{bmatrix} e_{b1} \\ e_{b2} \\ e_{b3} \\ e_{b4} \\ e_{b5} \\ e_{b6} \\ e_{b7} \\ e_{b8} \\ e_{b9} \\ e_{b10} \end{bmatrix} = \begin{bmatrix} R_{SW_1} & 0 & 0 & 0 & 0 & 0 & 0 & 0 & 0 & 0 \\ 0 & R_{SW_2} & 0 & 0 & 0 & 0 & 0 & 0 & 0 & 0 \\ 0 & 0 & R_{SW_3} & 0 & 0 & 0 & 0 & 0 & 0 & 0 \\ 0 & 0 & 0 & R_{SW_4} & 0 & 0 & 0 & 0 & 0 & 0 \\ 0 & 0 & 0 & 0 & R_{D_1} & 0 & 0 & 0 & 0 & 0 \\ 0 & 0 & 0 & 0 & 0 & R_{D_2} & 0 & 0 & 0 & 0 \\ 0 & 0 & 0 & 0 & 0 & 0 & R_{D_3} & 0 & 0 & 0 \\ 0 & 0 & 0 & 0 & 0 & 0 & 0 & R_{D_4} & 0 & 0 \\ 0 & 0 & 0 & 0 & 0 & 0 & 0 & 0 & R+Lp & 0 \\ 0 & 0 & 0 & 0 & 0 & 0 & 0 & 0 & 0 & R_{dc} \end{bmatrix} \begin{bmatrix} i_{b1} \\ i_{b2} \\ i_{b3} \\ i_{b4} \\ i_{b5} \\ i_{b6} \\ i_{b7} \\ i_{b8} \\ i_{b9} \\ i_{b10} \end{bmatrix}$$

$$+ Bpx \quad (6.24)$$

where  $p = (d/dt)$ ,  $R$  is the coil resistance,  $L$  is the incremental inductance ( $\partial\lambda/\partial i$ ),  $i_{b1-10}$  are the ten branch currents,  $x$  is the armature displacement, and  $B$  is a  $10 \times 1$  matrix, where only position (9, 1) is non-zero, which is the back-emf coefficient  $B$  ( $\partial\lambda/\partial x$ ). Using Happ's tensor notation [83] equation (6.24) can be re-written as:

$$(V_b + E_b) = (R_{bb} + L_{bb}p)I^b + B_{bb}px^b \quad (6.25)$$

where  $V_b$  is the branch voltage vector,  $E_b$  is the branch source voltage vector,  $I^b$  is the branch current vector,  $x^b$  is the armature displacement vector,  $R_{bb}$  is the branch resistance matrix,  $L_{bb}$  is the branch incremental inductance matrix and  $B_{bb}$  is the back-emf matrix.

In the semiconductor switch and diode conduction pattern for the inverter shown in Fig. 6.15, six independent meshes are formed for the six different modes of operation of the system. Mesh a is supplying current in a positive direction to the exciting coil of the motor, mesh b is the free-wheeling mode and mesh c is regenerating current back to the supply. Meshes d, e and f are similar to the first three, except that the

current is flowing in the opposite direction through the exciting coil. These six meshes are defined in abbreviated form by the mesh reference frame voltage equation:

$$(V_m + E_m) = (R_{mm} + L_{mm}p)I^m + B_{mm}px^m \quad (6.26)$$

where the terms in the equation are the corresponding mesh vectors and matrices. Inspection of Fig. 6.15, yields the branch to mesh current transformation tensor  $C_m^b$  shown in Table 6.1 below.

Branch	Mesh					
	a	b	c	d	e	f
1	1	0	0	0	0	0
2	1	1	0	0	0	0
3	0	0	0	1	0	0
4	0	0	0	1	1	0
5	0	0	0	0	0	1
6	0	0	0	0	1	1
7	0	0	1	0	0	0
8	0	1	1	0	0	0
9	1	1	1	-1	-1	-1
10	1	0	-1	1	0	-1

Table 6.1 Branch/mesh currents transformation tensor  $C_m^b$

Assuming power invariance between reference frames [83], the relationship between the branch current vector  $I^b$  and the mesh current vector  $I^m$  using the above tensor is:

$$I^b = C_m^b I^m \quad (6.27)$$

Similarly, the relationship between the branch source voltage vector  $E_b$ , and the mesh source voltage vector  $E_m$ , is:

$$E_m = C_m^b E_b \quad (6.28)$$

where  $C_m^b$  is the transpose of  $C_m^b$  and:

$$x^b = C_m^b x^m \quad (6.29)$$

The relationships between the branch and mesh vectors have been defined above, the next section develops the mathematics that leads to the relationships between the branch and mesh matrices.

#### 6.5.2.4 Branch/Mesh Transformation

Following an established procedure in [88], re-arranging equation (6.25) yields:

$$E_b = (R_{bb} + L_{bb}p)I^b + B_{bb}p x^b - V_b \quad (6.30)$$

Substituting equation (6.30) into (6.28) gives:

$$E_m = C_m^b R_{bb} I^b + C_m^b L_{bb} p I^b + C_m^b B_{bb} p x^b - C_m^b V_b \quad (6.31)$$

and substituting equations (6.27) and (6.29) into (6.31) produces:

$$E_m = C_m^b R_{bb} C_m^b I^m + C_m^b L_{bb} C_m^b p I^m + C_m^b B_{bb} C_m^b p x^m - C_m^b V_b \quad (6.32)$$

or on re-arranging:

$$C_m^b V_b + E_m = C_m^b R_{bb} C_m^b I^m + C_m^b L_{bb} C_m^b p I^m + C_m^b B_{bb} C_m^b p x^m \quad (6.33)$$

Comparing equation (6.33) with (6.26), yields the relationships:

$$V_m = C_m^b V_b \quad (6.34)$$

and:

$$\begin{aligned}
 R_{mm} &= C_m^b R_{bb} C_m^b \\
 L_{mm} &= C_m^b L_{bb} C_m^b \\
 B_{mm} &= C_m^b B_{bb} C_m^b
 \end{aligned} \tag{6.35}$$

Equations (6.34) and (6.35) show the relation between each matrix in the different reference frames. It is worth noting that the non-zero terms in both  $L_{mm}$  and  $L_{bb}$ , and also in  $B_{mm}$  and  $B_{bb}$ , will be equal, since the only non-zero terms existing in each branch matrix, are the values of  $L$ ,  $(\partial\lambda/\partial i)$  and  $B$ ,  $(\partial\lambda/\partial x)$ . The next section describes the program that simulates the switch-mode inverter and linear motor drive system.

## 6.6 COMPUTER IMPLEMENTATION

The flowchart for the computer implementation of the drive, with tolerance band current control, is shown in Fig. 6.18. The program starts by declaring and initializing all variables, setting all the initial conditions to zero and specifying the step length  $h$  needed for the numerical integration routine. The upper and lower limits of the tolerance band current control scheme are then specified, the interpolation flag is nulled and the initial switching topology set. The initial topology, with switches  $SW_1$  and  $SW_2$  on, provides a positive current flow to the motor coil from the dc supply. The next step is to set up the branch resistance matrix  $R_{bb}$ , incremental inductance matrix  $L_{bb}$ , back-emf matrix  $B_{bb}$ , branch voltage matrix  $E_b$  and the master transformation matrix  $C_m^b$  together with its transpose  $C_m^b$ . The data for the non-linear characteristics of flux linkage, force and magnetic stiffness are then read into the program, followed by the other motor and demand parameters, such as the voltage amplitude and the frequency. The next stage of the program is similar to the first program, whereby cubic splines are fitted to all the  $\lambda = f(x)$  characteristics at every discrete coil current read in, and the resulting polynomial segment coefficients are then stored in the program. This process is repeated for the functions  $\lambda = f(i)$ ,  $F = f(i)$  and  $F_{mag} = f(x)$ , and the initial conditions are written to the output files, the time updated by  $h$  and the loop count incremented to commence the main section of the program.

The main section first determines updated values for  $(\partial\mathcal{N}/\partial i)$ ,  $(\partial\mathcal{N}/\partial x)$ ,  $F_{coil}$ ,  $F_{mag}$  and  $F_{accel}$ , (which is compared with experimentally obtained values in section 6.7). The next step, not shown in the flowchart, ensures that the demand current never exceeds the largest value in the data tables, by implementing a limit of 0.7 A on the maximum coil current. The switching topology of the inverter is then updated, with three modes possible for a certain direction of current flow, and these are supplying current, freewheeling and regenerating current back to the supply. The mesh matrices  $E_m$ ,  $R_{mm}$ ,  $L_{mm}$  and  $B_{mm}$  are obtained using equations (6.28) and (6.35), the state variables are stored, in the event that the loop has to be repeated, and the motor differential equations are re-formulated with the updated non-linear coefficients. The differential equations are numerically integrated, using the fourth-order Runge-Kutta numerical integration routines described in sections 6.2.4.1 and 6.2.4.2, and the branch current vector is calculated using equation (6.27), where the branch current  $i_{bp}$  represents the actual coil current  $I_{actual}$ .

The next stage of the program calculates the error between the actual current and the demand current and, depending on the error, implements one of four steps, shown in Fig. 6.18. These steps are:

- (i) if the error is greater than the upper current limit, as shown in Fig. 6.19, re-integrate up to the upper limit by integrating over a reduced time step interval of  $h'$ , such that:

$$h' = \left[ \frac{I_{+limit} - I_{error(n)}}{I_{error(n+1)} - I_{error(n)}} \right] h \quad (6.36)$$

where  $I_{+limit}$  is the upper current limit,  $I_{error}$  is the error between the actual and demand current and  $n$  represents the loop count at which the re-integration process commences, as shown in Fig. 6.20;

- (ii) if the error is greater than the lower current limit, re-integrate up to the lower limit by integrating again over a reduced time step interval  $h'$  where:

$$h' = \left[ \frac{-I_{\text{limit}} - I_{\text{error}(n)}}{I_{\text{error}(n+1)} - I_{\text{error}(n)}} \right] h \quad (6.37)$$

where  $I_{\text{limit}}$  is the lower current limit;

- (iii) if the re-integration process has just been implemented change the switching topology on the next loop and reset the time step interval back to  $h$ ;
- (iv) if the loop just implemented is the one immediately after the re-integration loop then set the re-integration flag to null.

Once the correct decision has been implemented, the results are written to the output files, and the time  $t$  is incremented by the integration step length  $h$ . Finally, the loop count is incremented and the main section repeated until the loop count has reached its final value.

## 6.7 SIMULATED AND EXPERIMENTAL RESULTS

Experimental results were not obtained using a switch-mode inverter with tolerance band control, but instead using a linear power operational amplifier *L465A*, as discussed in section 6.5.1 and shown in Fig. 6.21, where the current forced through the coil is  $(V_{in}/R)$ . The peak output current of the power amplifier is 4 A which was more than adequate for the application, and the technique was considered adequate to provide experimental results.

Fig. 6.22 shows the dynamic response of the motor when fed with a 0.6 A peak sinusoidal current. The simulated results agree favourably with the experimental results. Fig. 6.23(a) and (b) show the simulated and experimental results when the coil is excited with a 0.4 A peak 20 Hz sinusoidal current. The experimental results obtained using the linear operational amplifier compare favourably with the simulation results produced using the switch-mode inverter program. When comparing the armature displacement waveforms, Figs. 6.23(c) and (d), a slight difference is seen, where the simulated result peaks at 0.78 mm is lower than the experimental peak of 0.86 mm. Similarly, Figs. 6.23(e) and (f) show a simulated acceleration force peak of about 1.25 N, compared with an experimental peak of 1.42 N. These two small

differences could be due to the viscous damping coefficient in the mathematical model being slightly too large.

Fig. 6.24(a) and (b) shows respectively the stiffness force and coil force for the above simulation. The stiffness force is very small due to the poor stiffness characteristic. Fig. 6.24(c) shows that the armature velocity is cosinusoidal in appearance as expected compared with the sinusoidal armature displacement waveform of Fig. 6.23(c). The simulated voltage across the coil is shown in Fig. 6.24(d) and in detail in Fig. 6.24(e) and illustrates the chopper action of the switch-mode inverter. Fig. 6.24(f) shows in detail the tolerance band coil current control action.

Fig. 6.25 shows the simulated and experimental results when the coil is excited with a 0.6 A peak 15 Hz triangular current waveform. Again, a small difference is seen in the simulated and experimental armature displacements of Figs. 6.25(c) and (d), and the acceleration forces of Figs. 6.25(e) and (f), where the values are 1.55 mm and 1.50 mm, and 1.45 N and 1.47 N respectively. The oscillations seen on the experimental acceleration force are probably due to the damaged armature surface caused by the bearings.

## 6.8 CONCLUSIONS

This chapter has evaluated the dynamic behaviour of the prototype motor using a mathematical model in the form of first-order differential equations, which are solved using numerical techniques. Two models have been developed; the first consists of the motor in isolation, and the second employs a full-bridge dc-to-dc converter connected to the motor, to provide four-quadrant operation using a tolerance band current control scheme. An experimental assessment of the motor has also been presented and these results are compared with simulated results to illustrate the effectiveness of the dynamic modelling method.

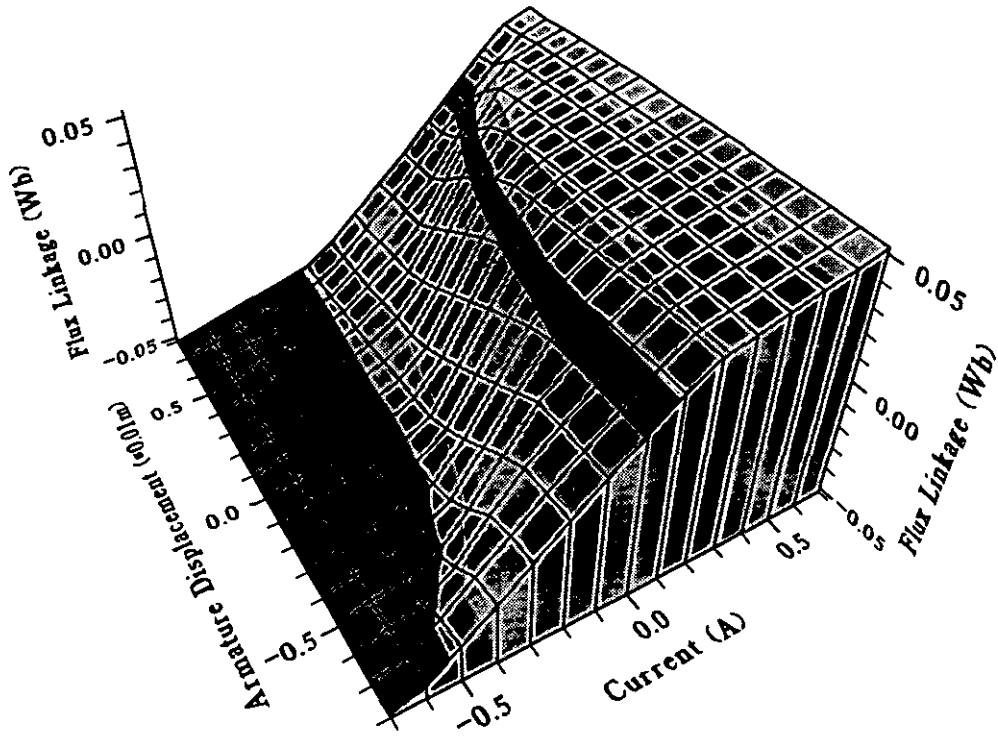


Fig. 6.1 Flux linkage characteristic

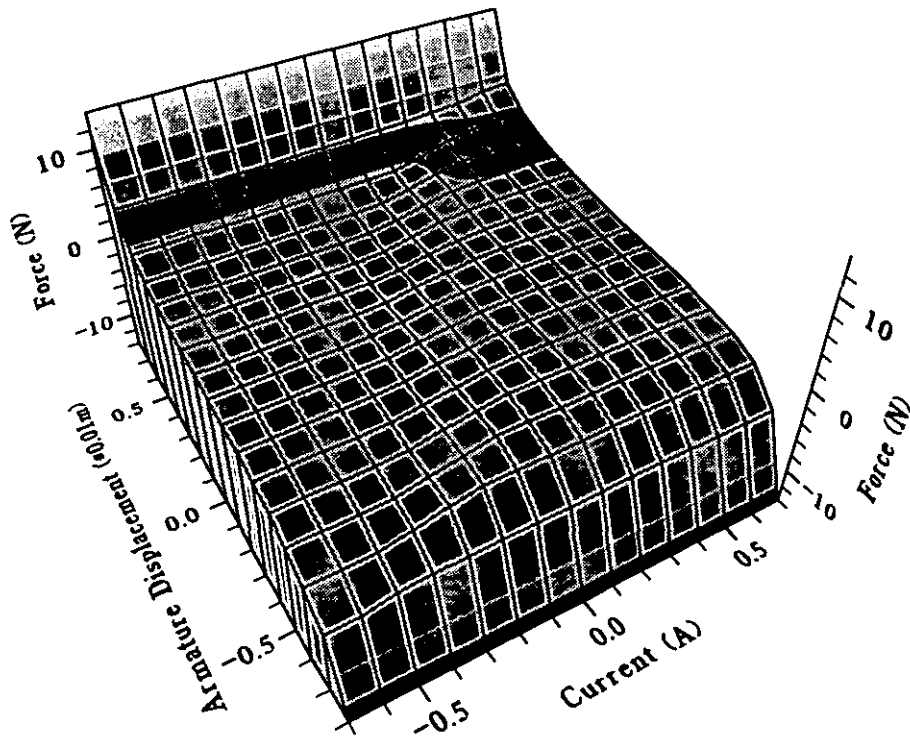
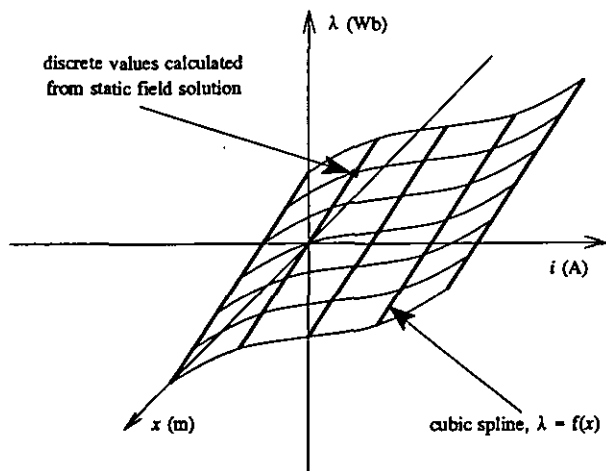
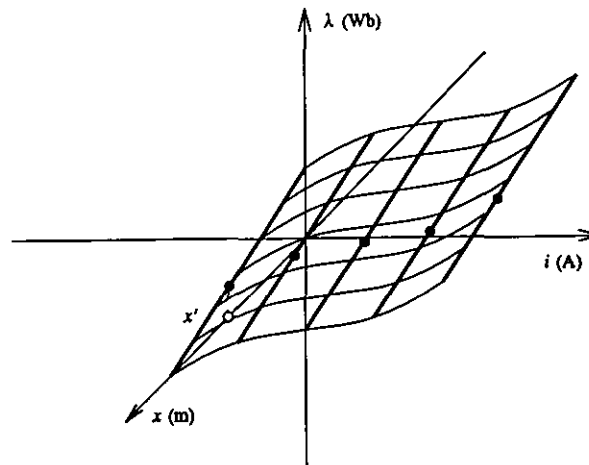


Fig. 6.2 Force characteristic

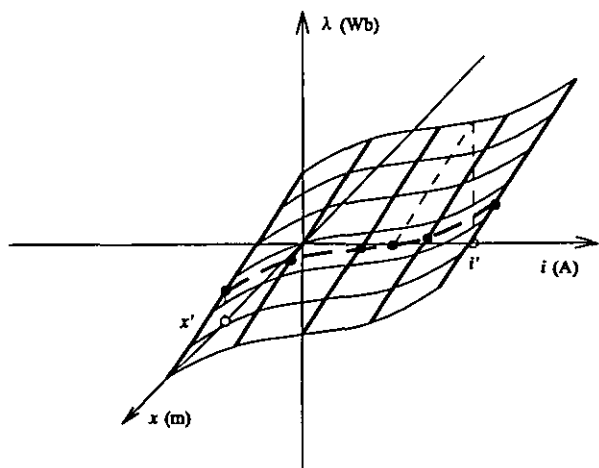




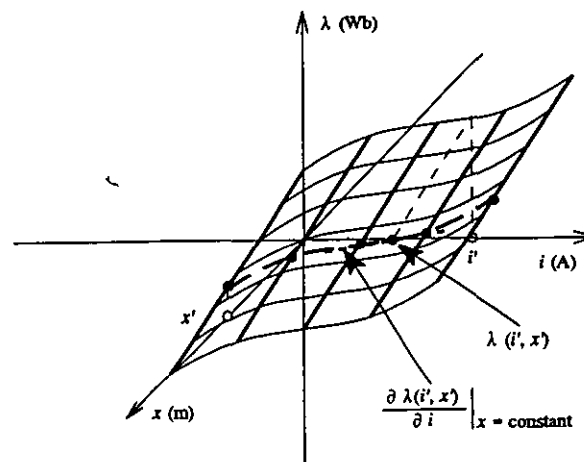
(a) Fit spline to each  $\lambda = f(x)$  characteristic



(b) Substitute  $x'$  into each spline

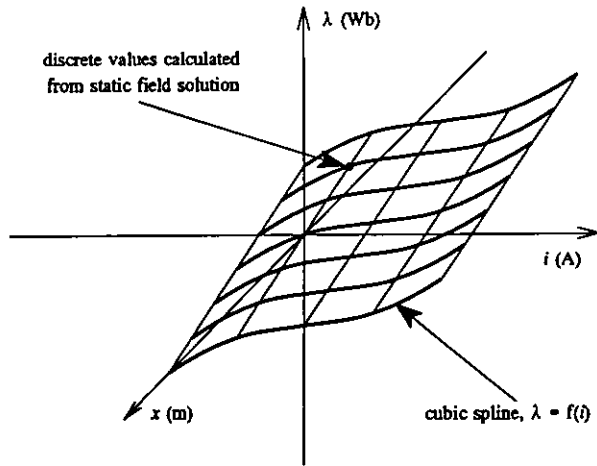
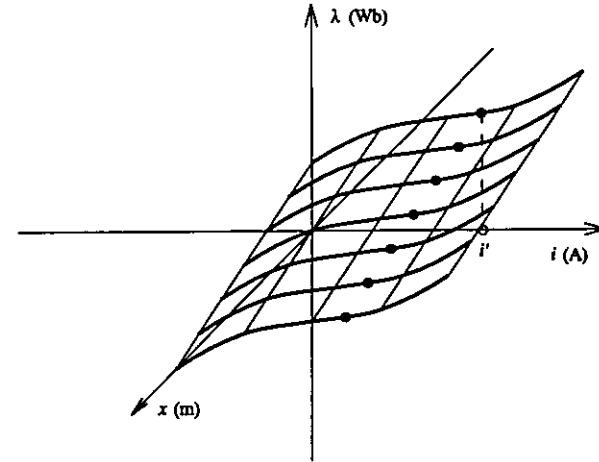
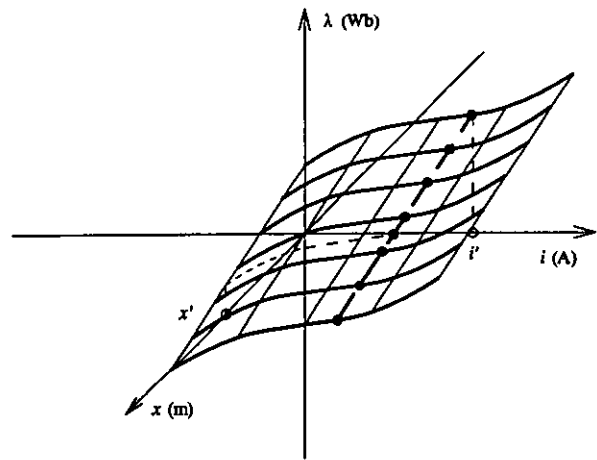
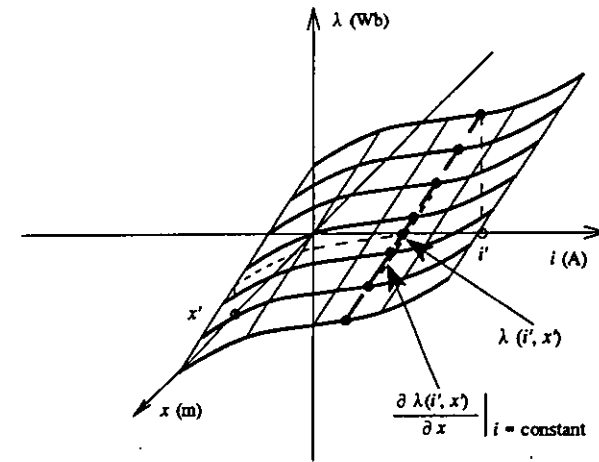


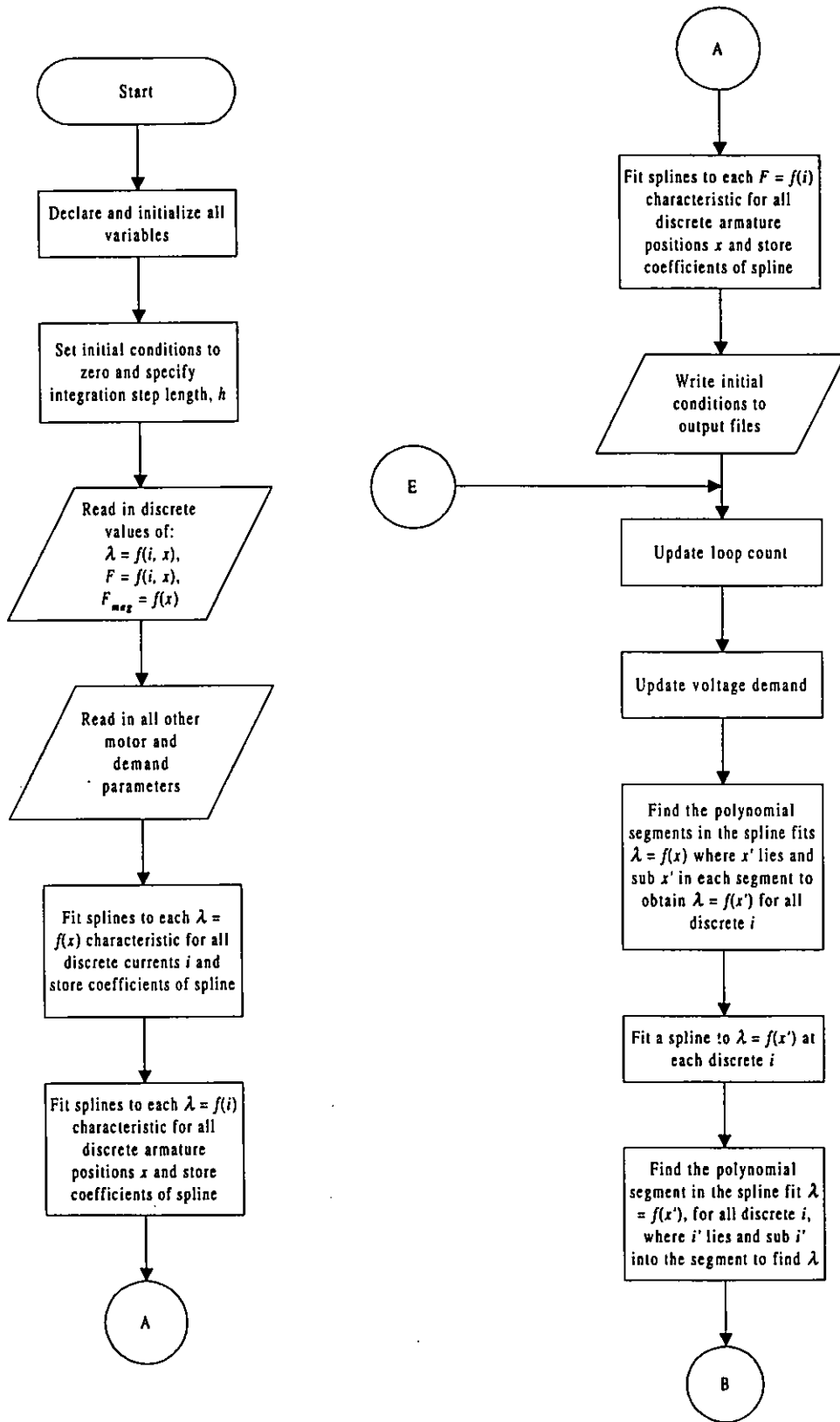
(c) Fit spline through new function at  $x'$  and sub. in  $i'$



(d) Find the value of  $\lambda$  and  $(\partial\lambda/\partial i)$

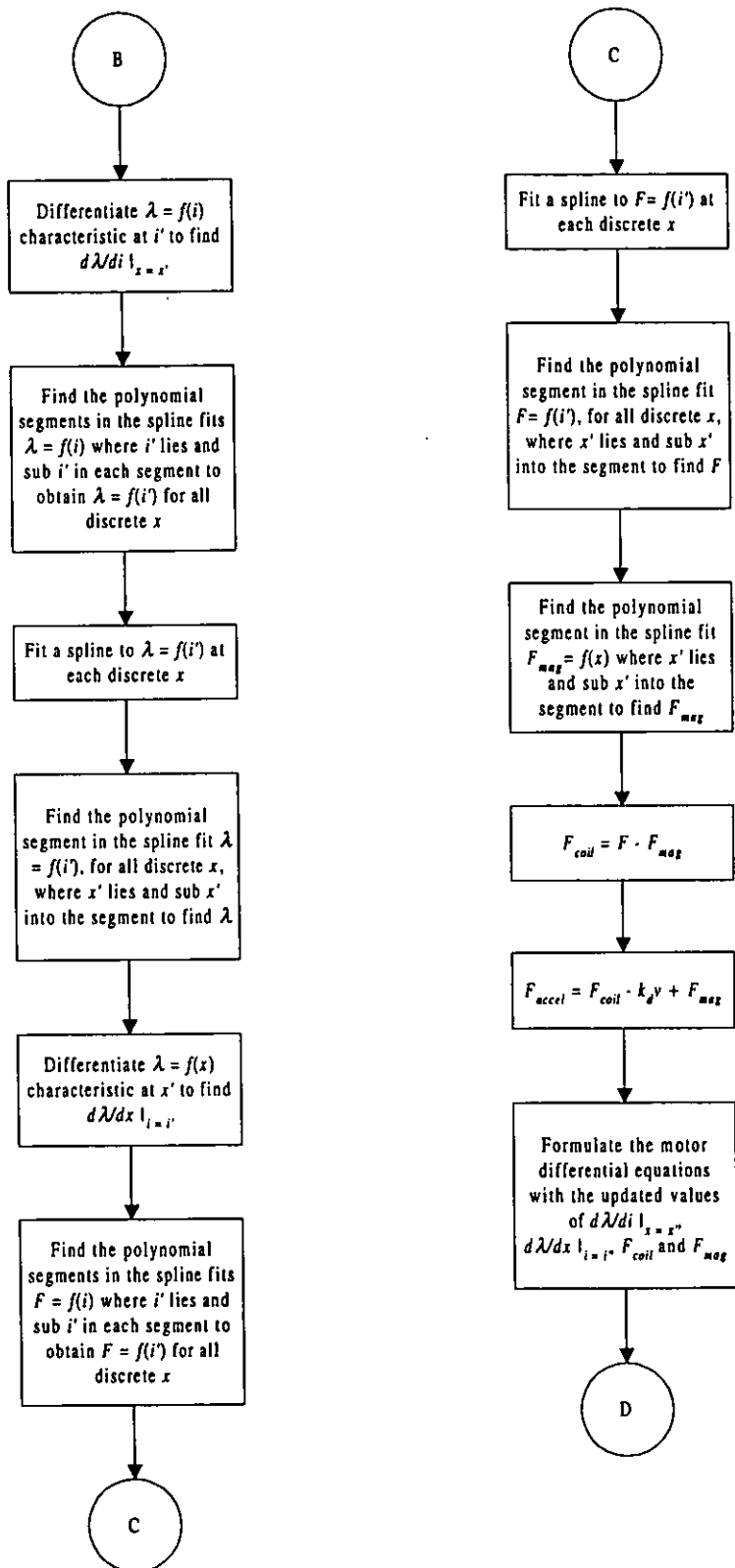
Fig. 6.3 Determination of  $(\partial\lambda/\partial i)$

(a) Fit spline to each  $\lambda = f(i)$  characteristic(b) Substitute  $i'$  into each spline(c) Fit spline through new function at  $i'$  and sub. in  $x'$ (d) Find the value of  $\lambda$  and  $(\partial \lambda / \partial x)$ Fig. 6.4 Determination of  $(\partial \lambda / \partial x)$

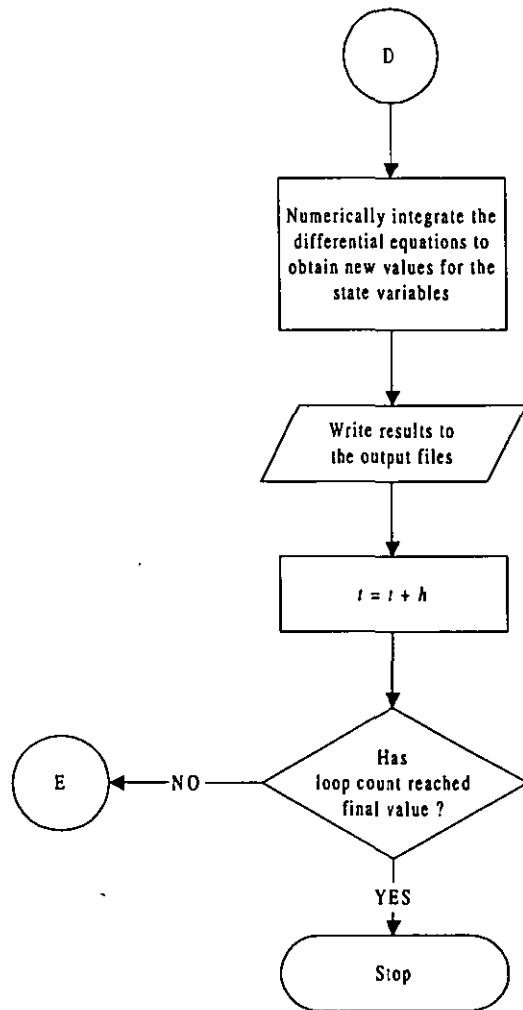


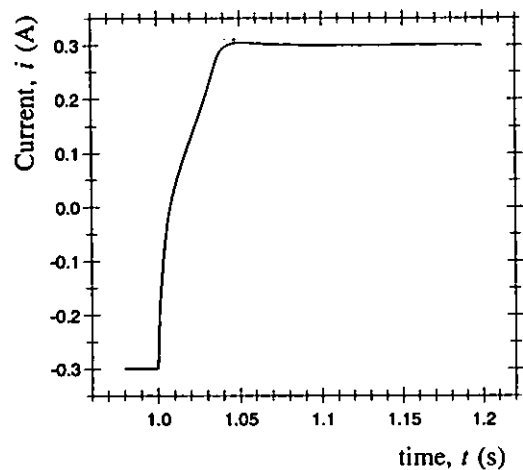
continued

Fig. 6.5 Linear motor simulation program

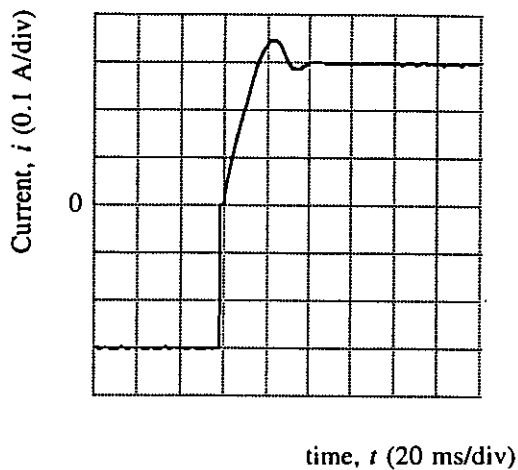


continued

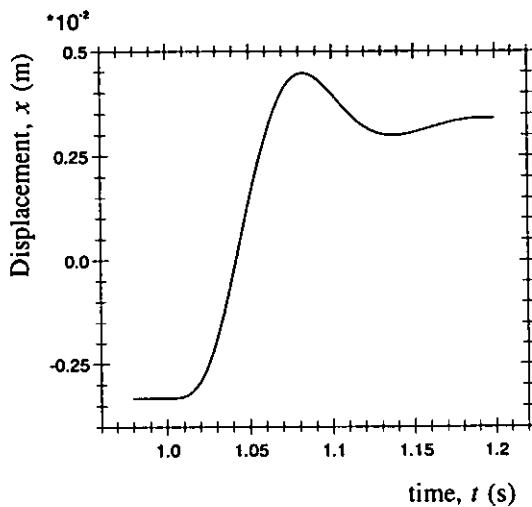




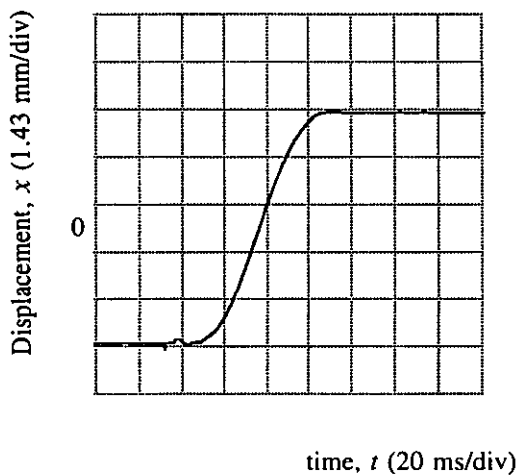
(a) Simulated current response



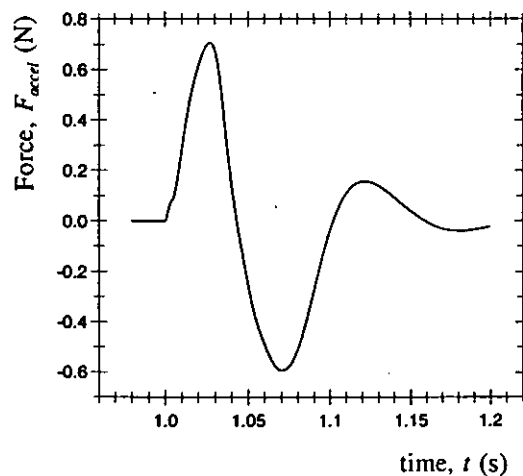
(b) Experimental current response



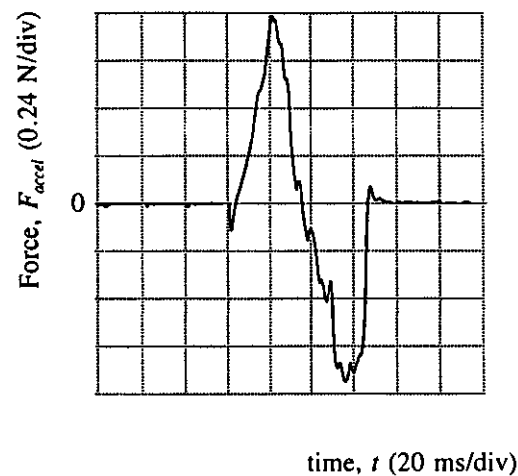
(c) Simulated armature displacement



(d) Experimental armature displacement

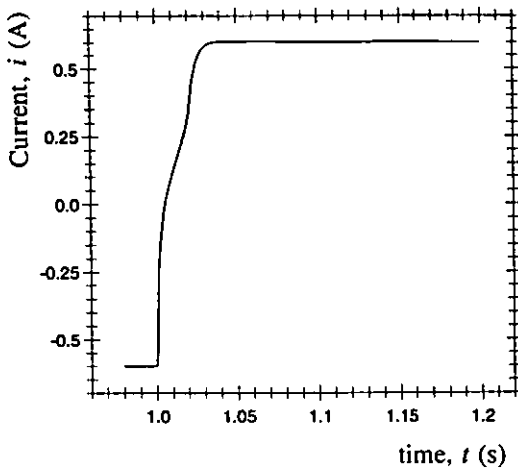


(e) Simulated acceleration force

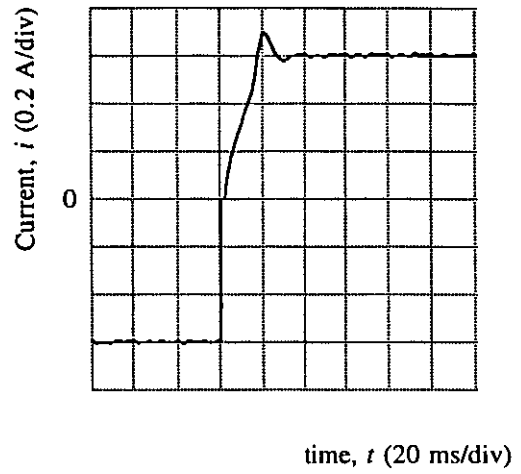


(f) Experimental acceleration force

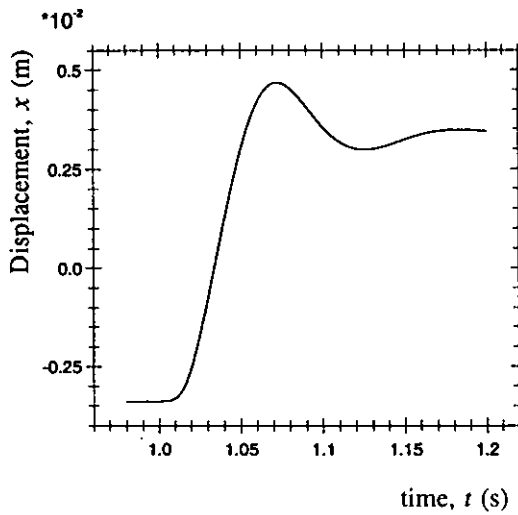
**Fig. 6.6** Simulated and experimental results for a coil voltage reversal of  $\pm 2.28$  V, ( $I = \pm 0.30$  A)



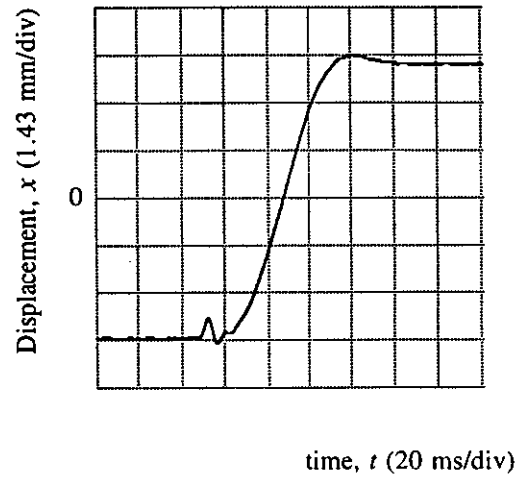
(a) Simulated current response



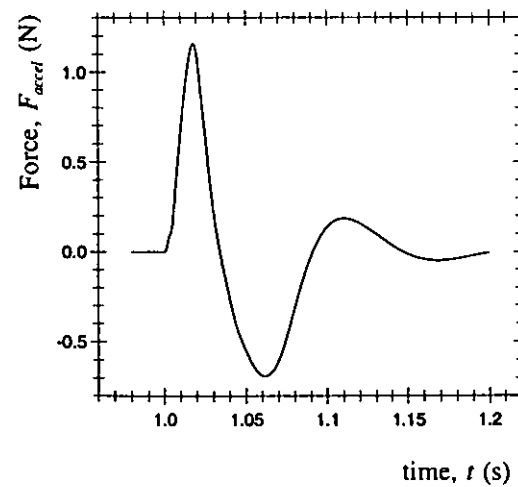
(b) Experimental current response



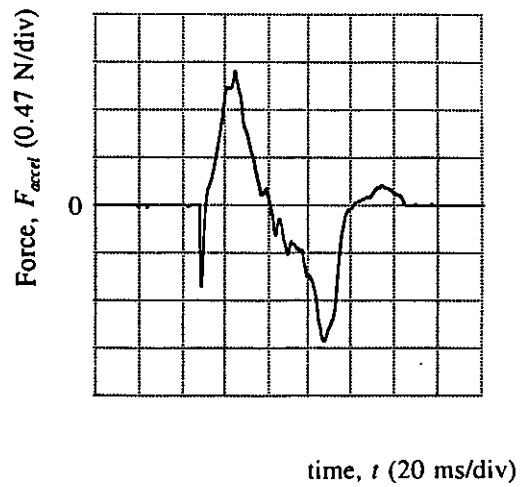
(c) Simulated armature displacement



(d) Experimental armature displacement

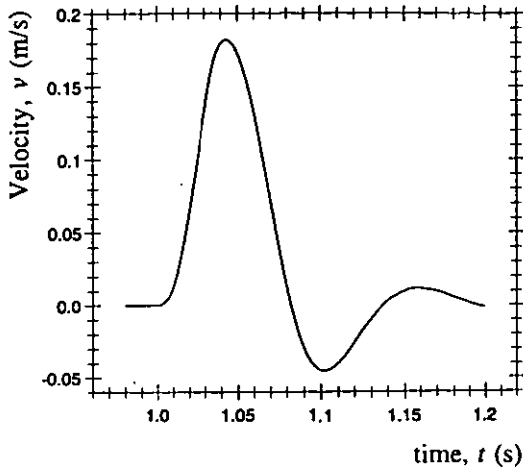
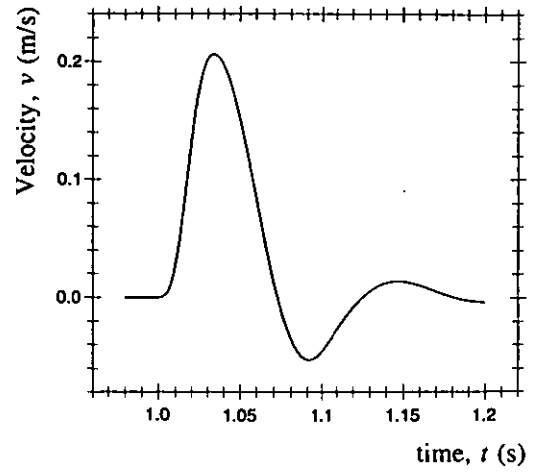
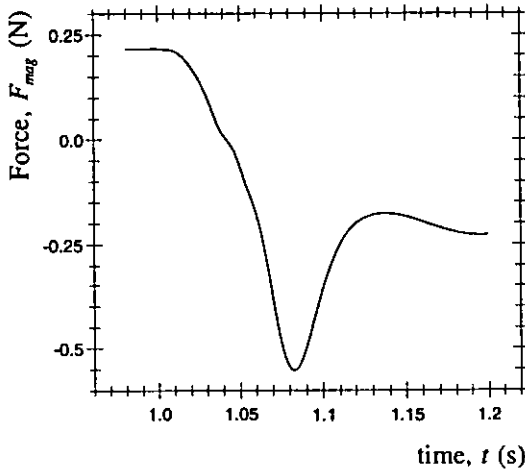
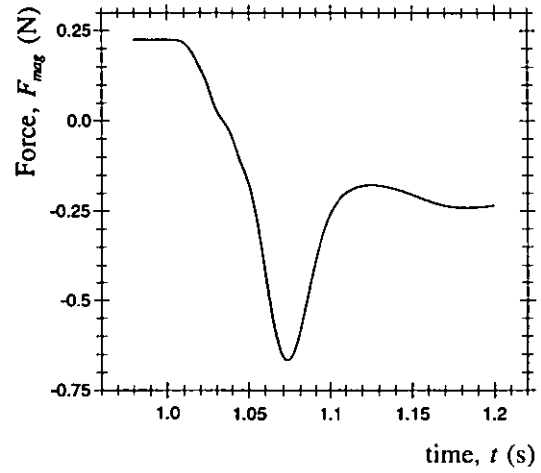
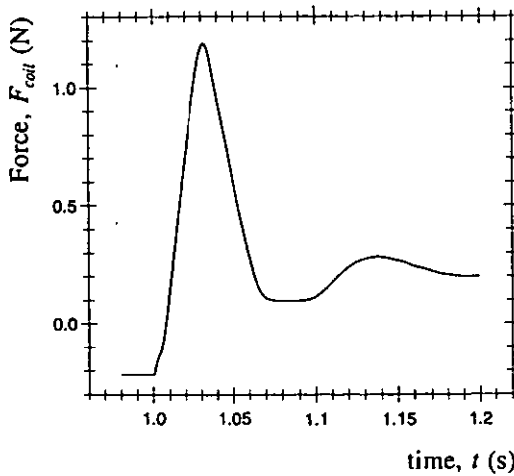
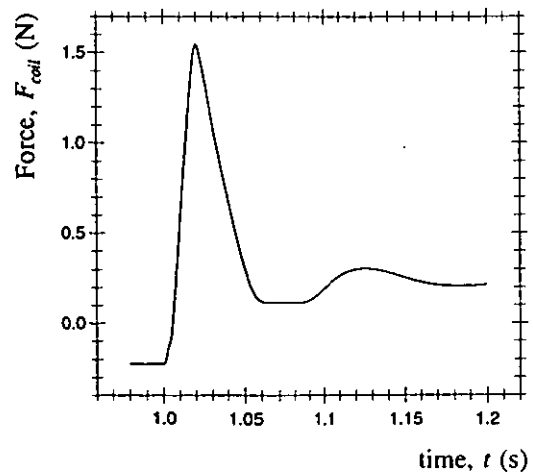


(e) Simulated acceleration force



(f) Experimental acceleration force

**Fig. 6.7** Simulated and experimental results for a coil voltage reversal of  $\pm 4.57$  V, ( $I = \pm 0.60$  A)

(a) Simulated armature velocity<sup>1</sup>(b) Simulated armature velocity<sup>2</sup>(c) Simulated stiffness force<sup>1</sup>(d) Simulated stiffness force<sup>2</sup>(e) Simulated coil force<sup>1</sup>(f) Simulated coil force<sup>2</sup>

**Fig. 6.8** Simulated results for coil voltage reversals of  $\pm 2.28$  V, ( $I = \pm 0.30$  A)<sup>1</sup> and  $\pm 4.57$  V, ( $I = \pm 0.60$  A)<sup>2</sup>



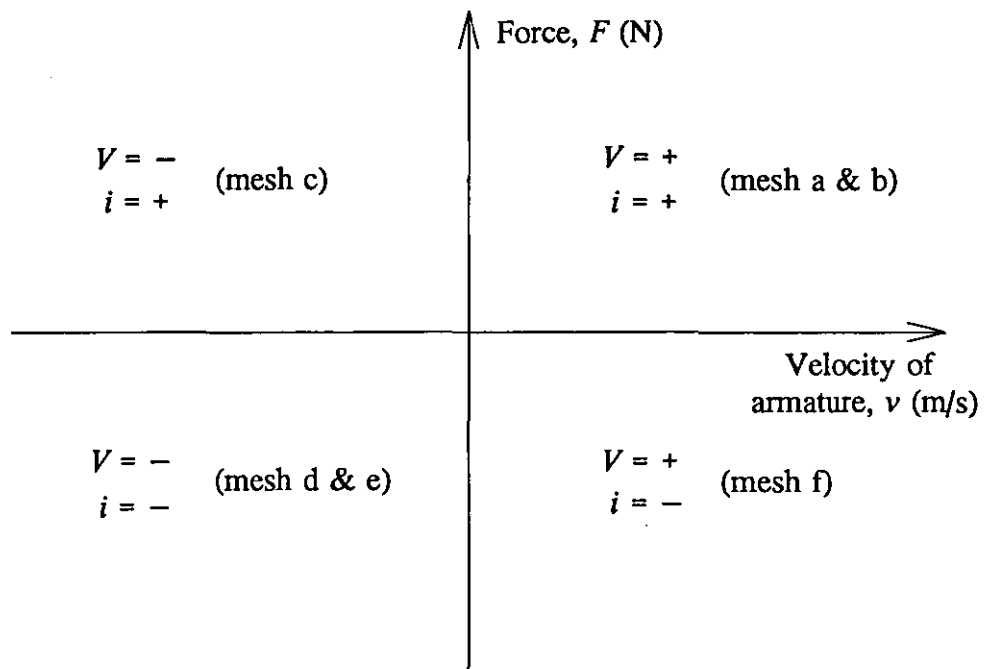


Fig. 6.9 Four-quadrant operation of the full-bridge dc-to-dc converter

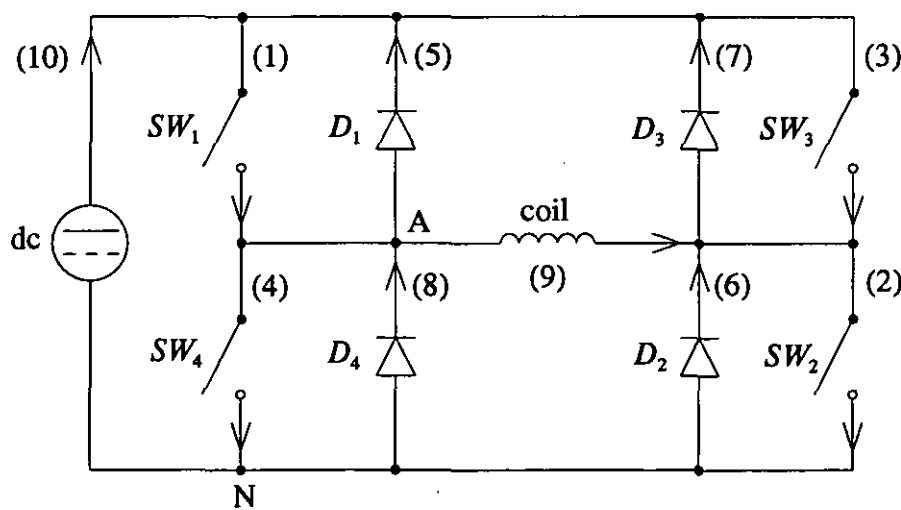


Fig. 6.10 Full-bridge dc-to-dc converter

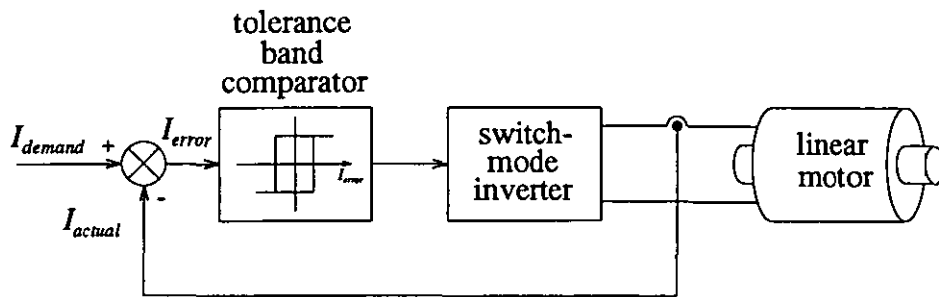


Fig. 6.11 Overall system arrangement

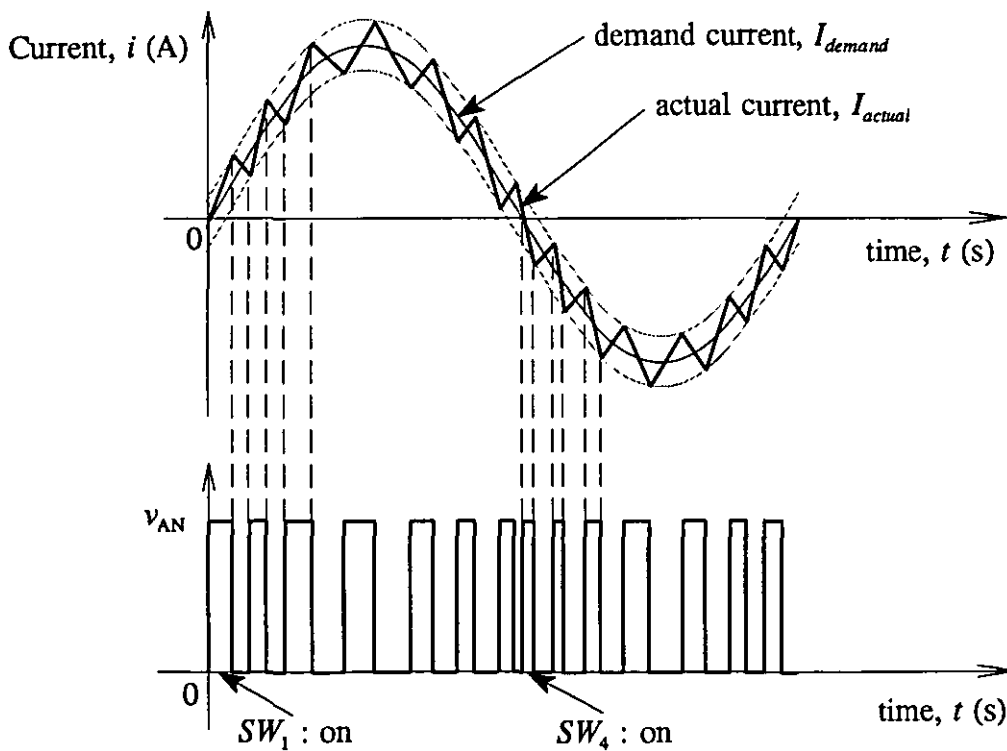


Fig. 6.12 Tolerance band control

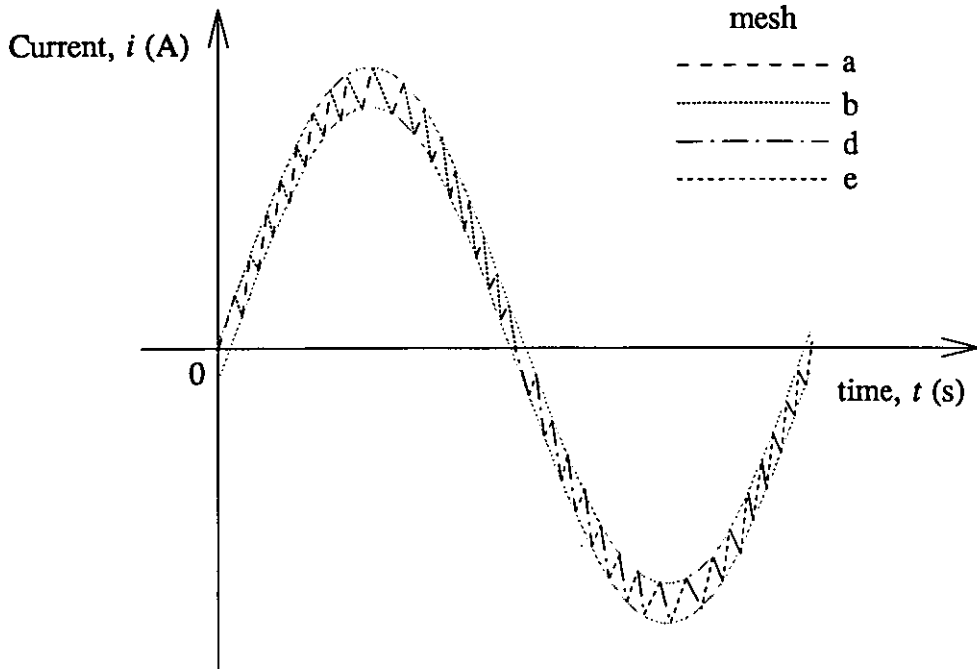


Fig. 6.13 Switching pattern at low demand frequencies

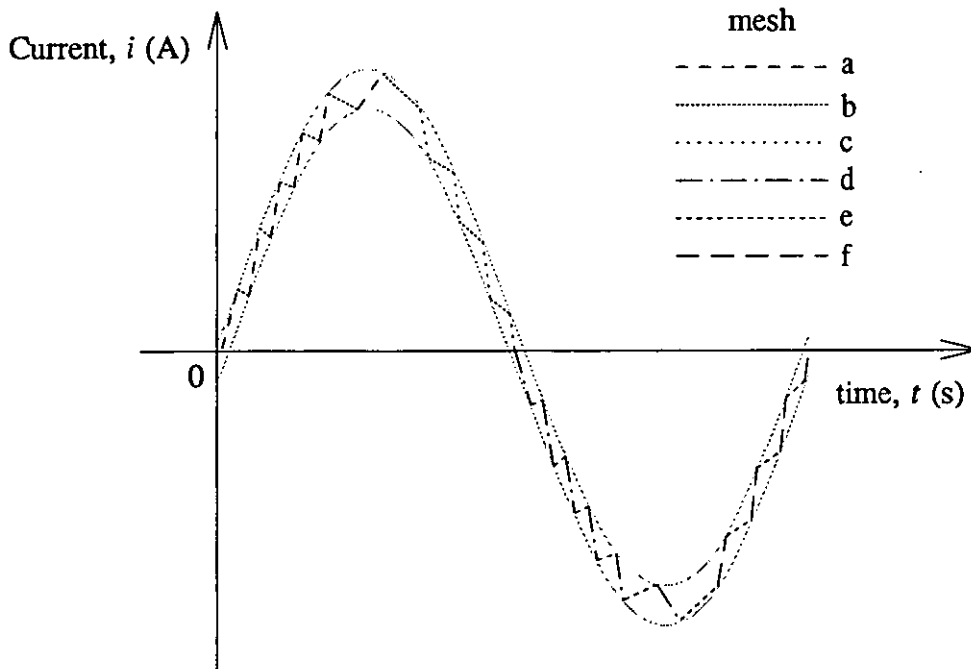
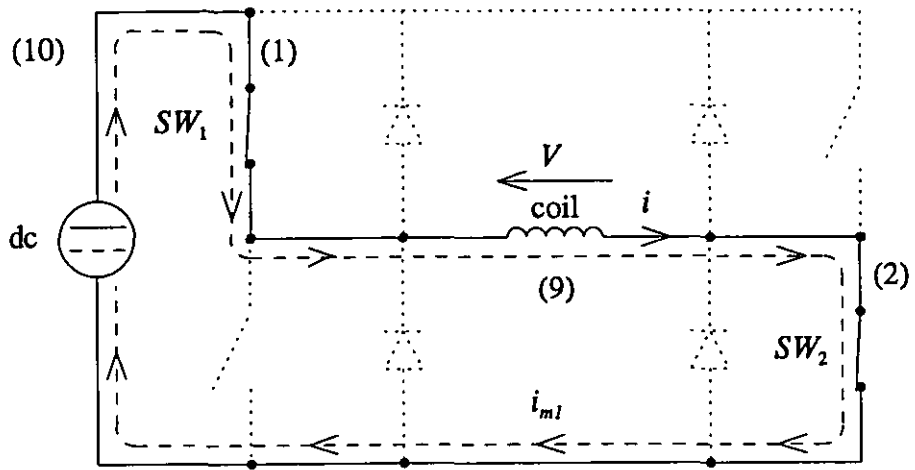
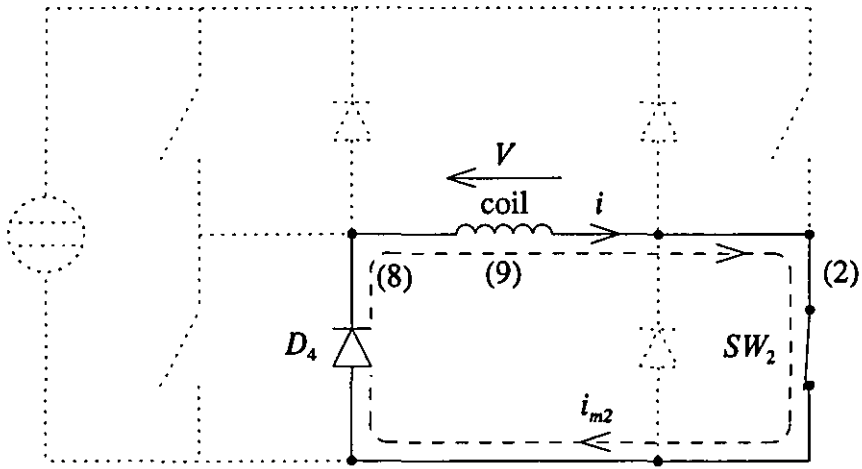


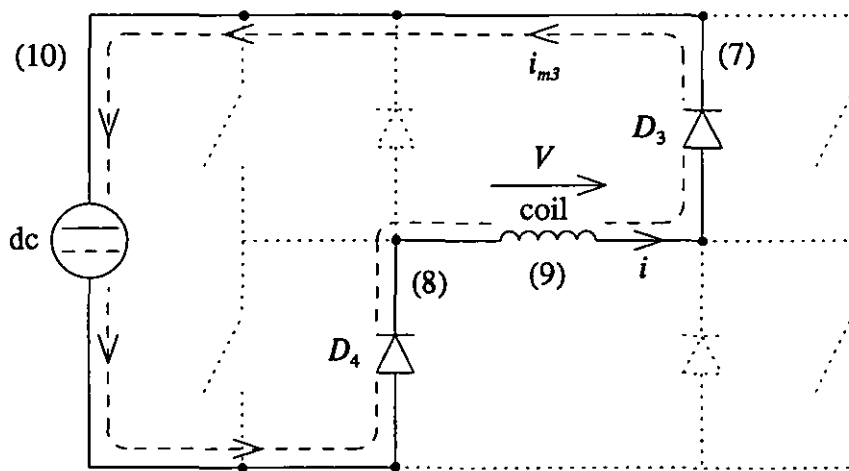
Fig. 6.14 Switching pattern at high demand frequencies



(a) Mesh a



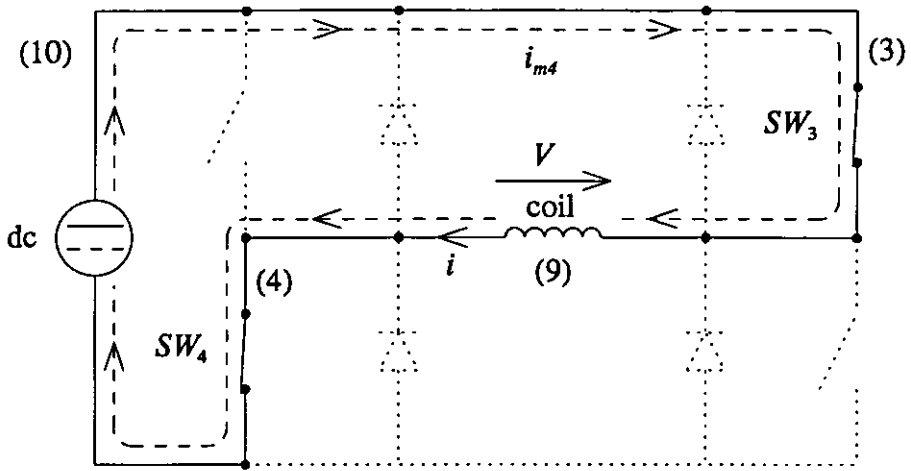
(b) Mesh b



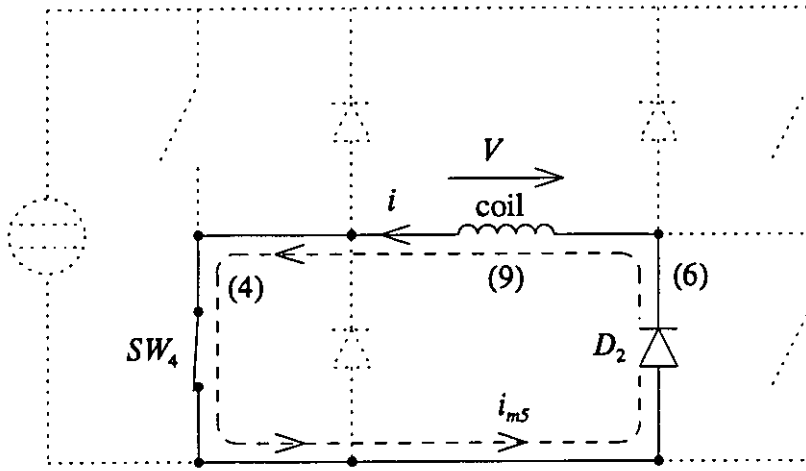
(c) Mesh c

continued

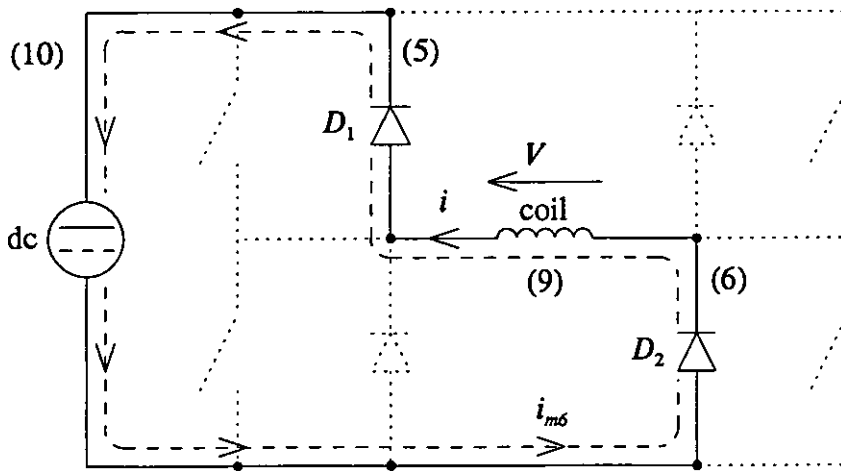
Fig. 6.15 Converter conduction paths



(d) Mesh d



(e) Mesh e



(f) Mesh f

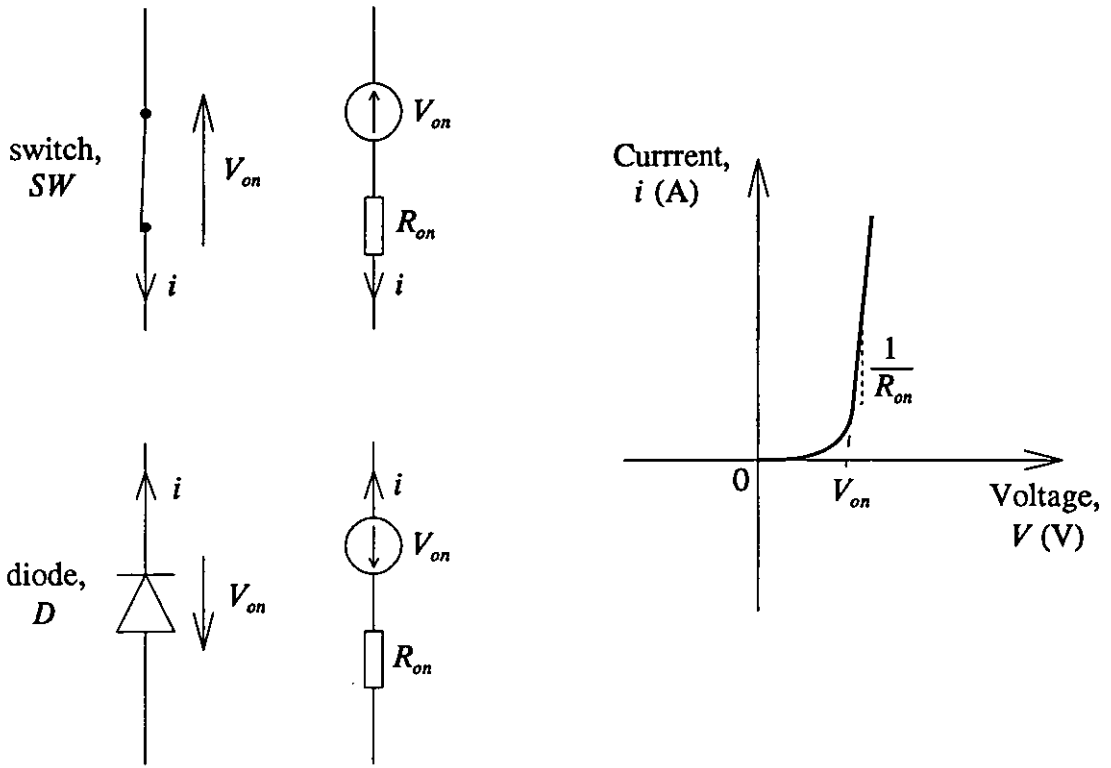


Fig. 6.16 Model of on-state semiconductor switches and diodes

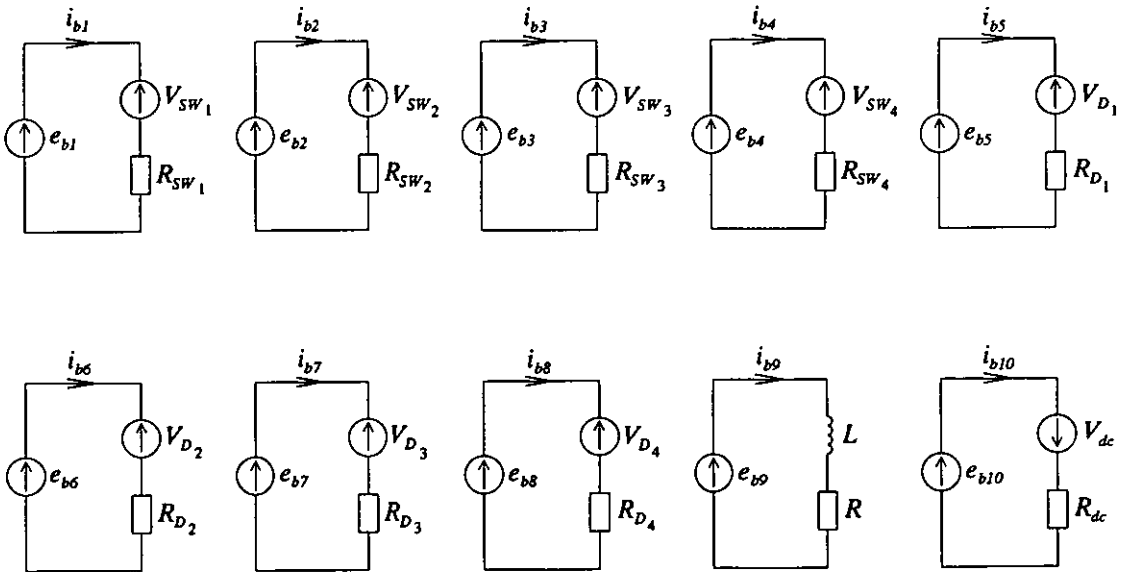
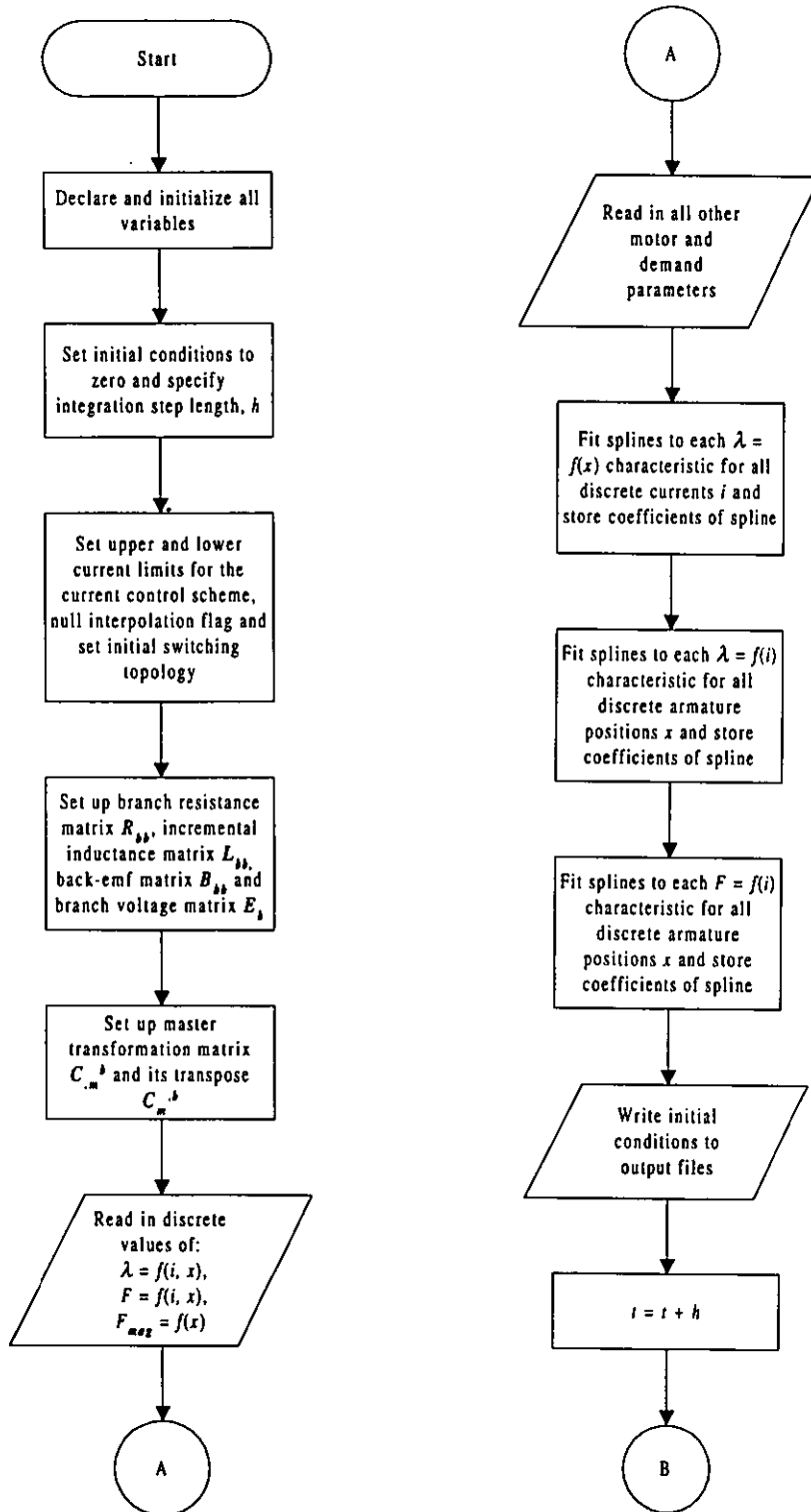
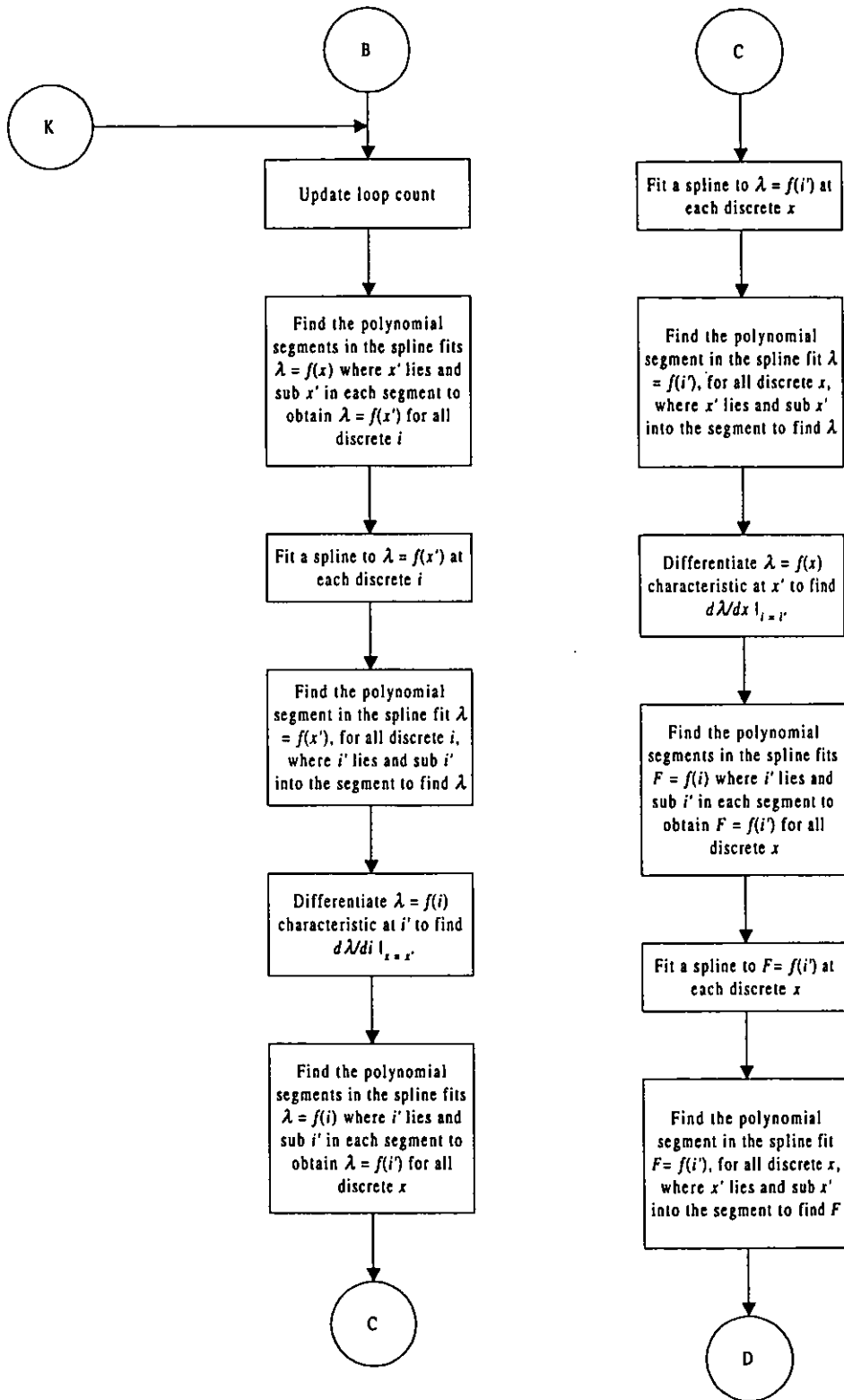


Fig. 6.17 Primitive network



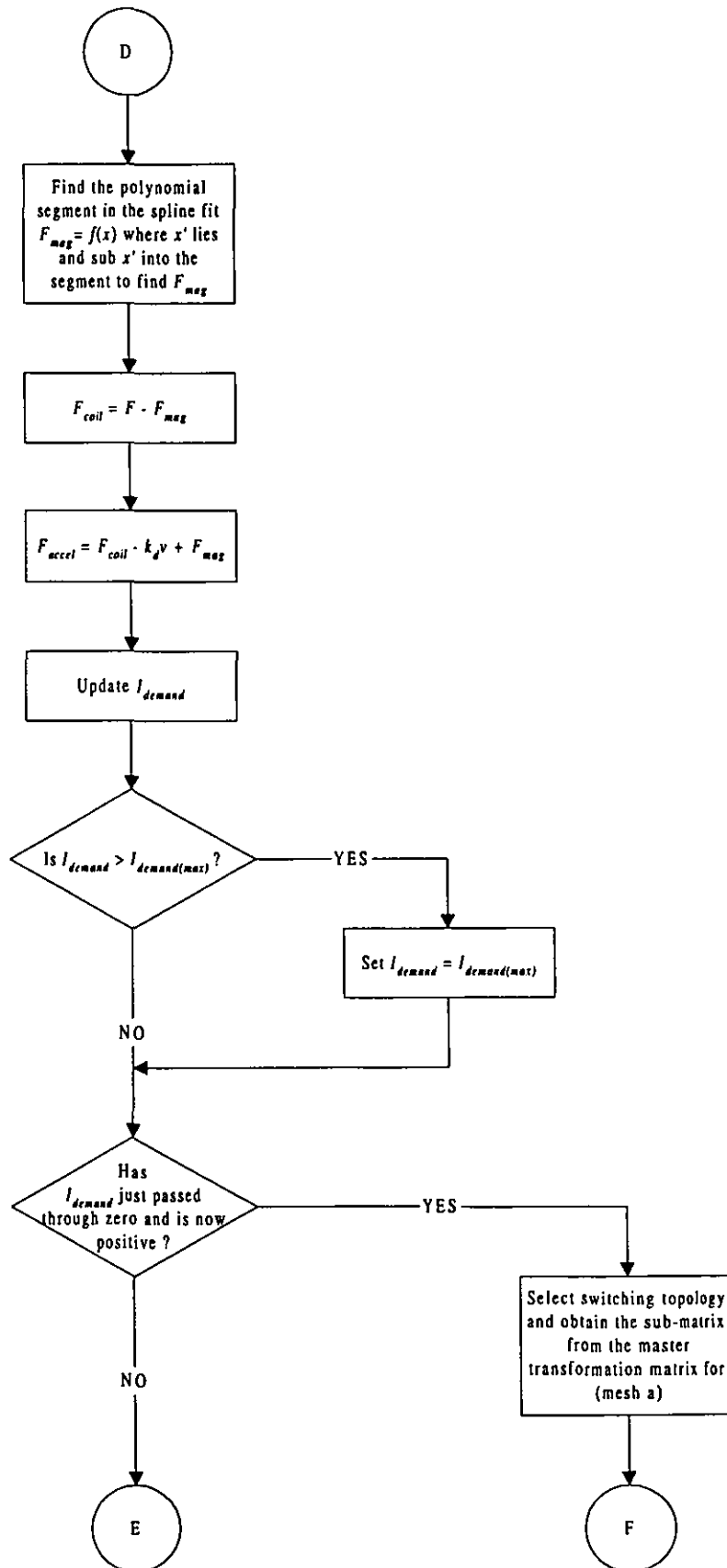
continued

Fig. 6.18 Full-bridge dc-to-dc converter, linear motor and tolerance band control simulation program

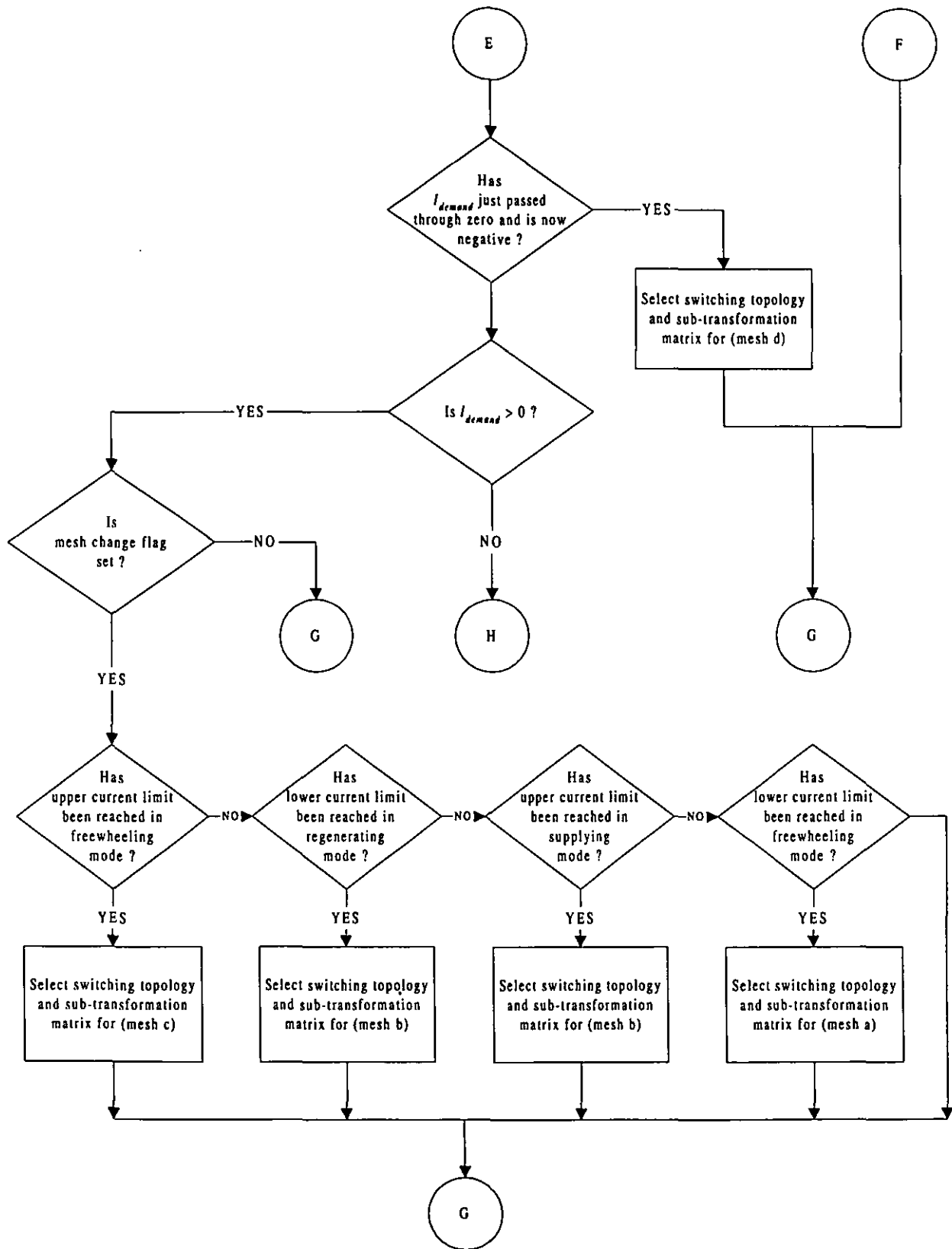


continued

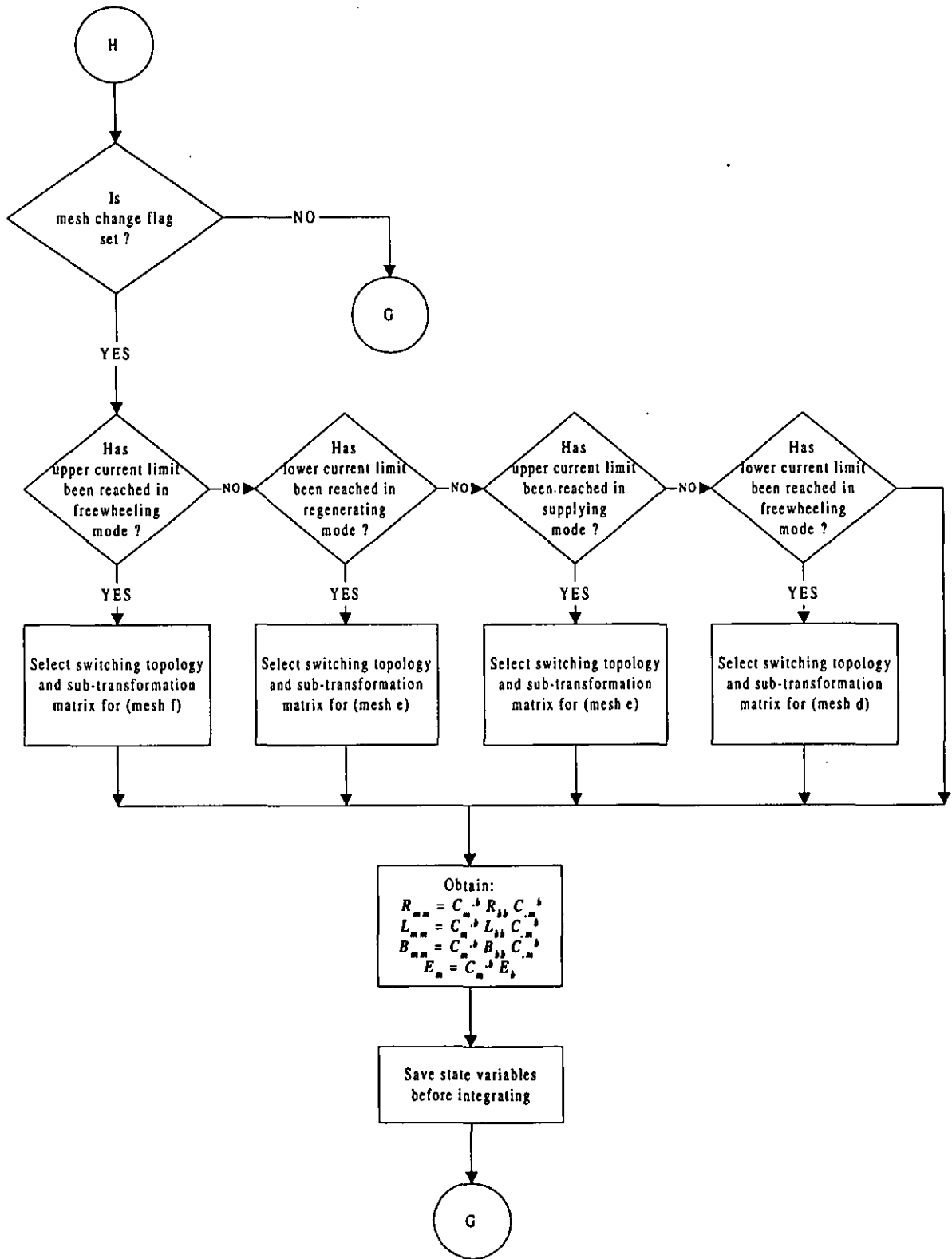




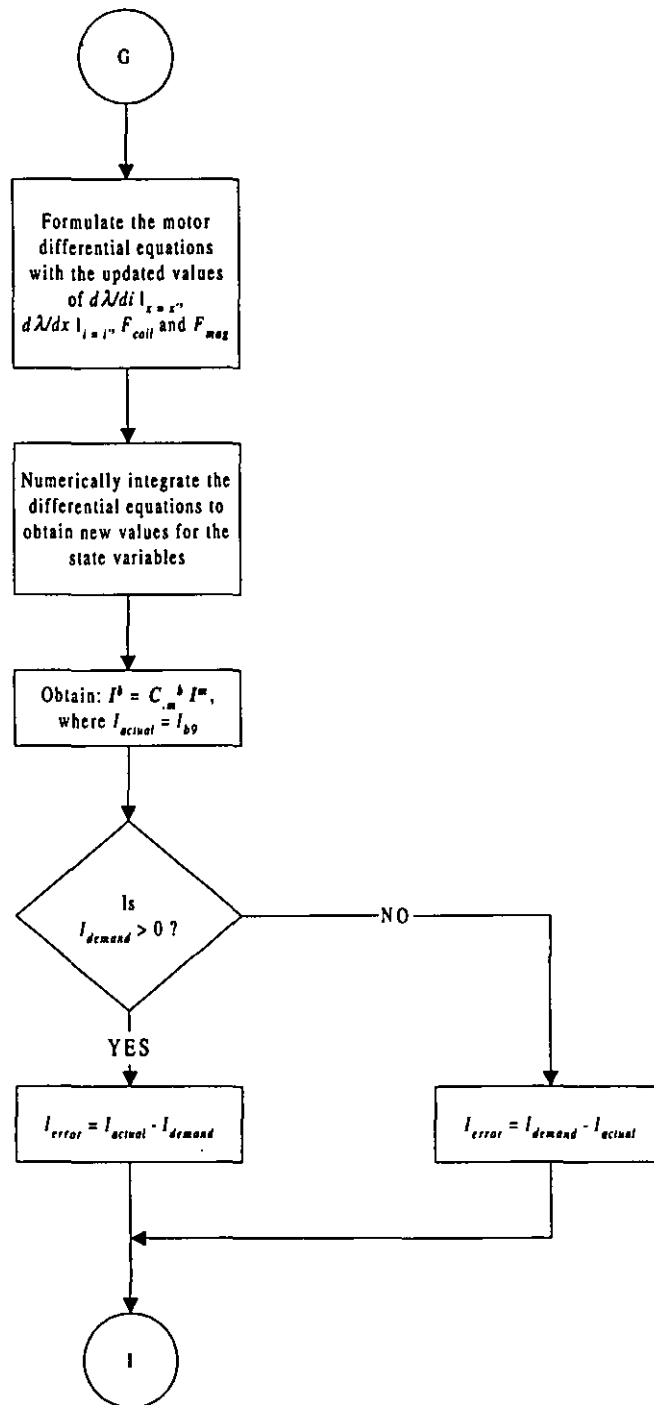
continued



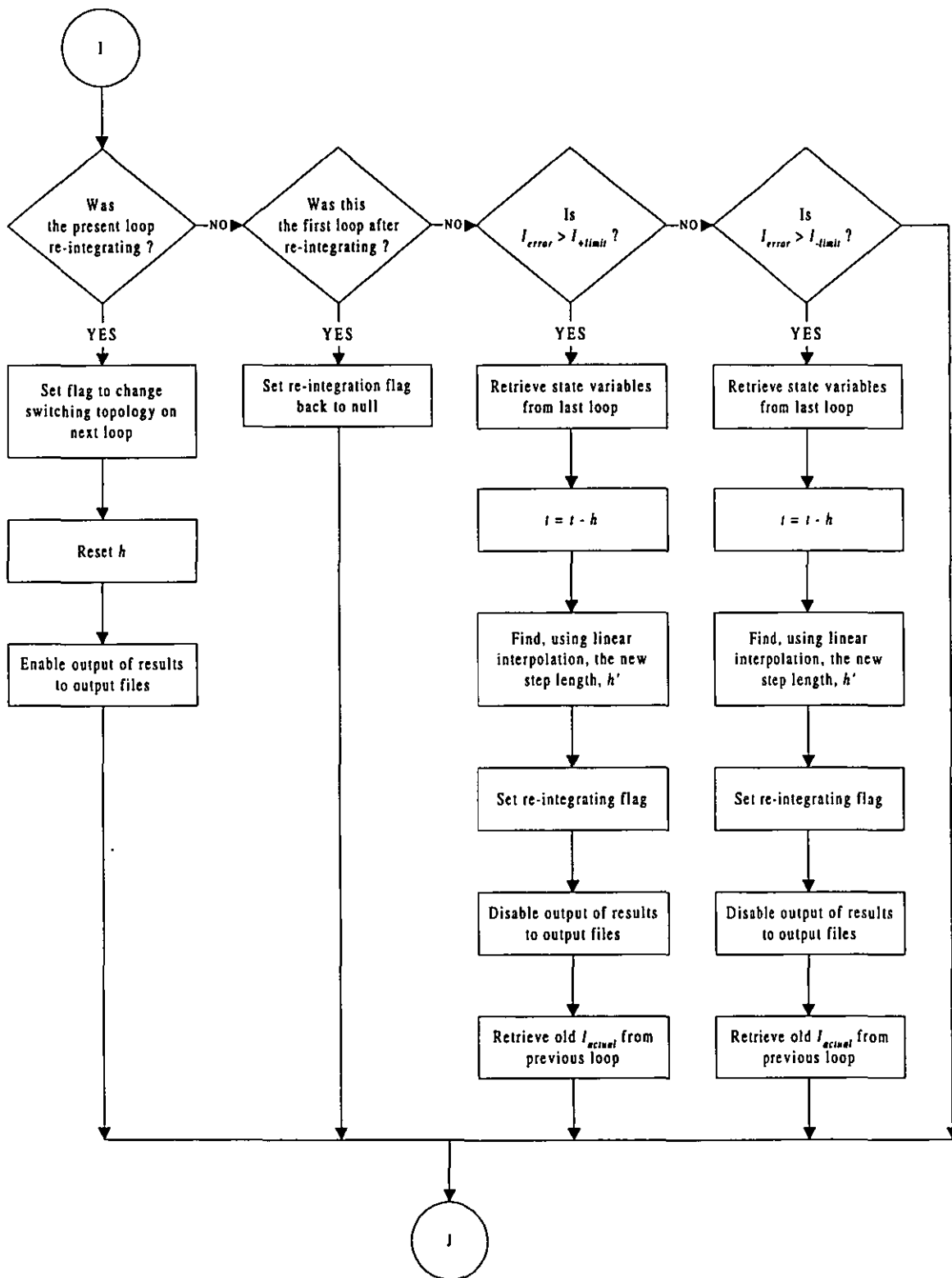
continued



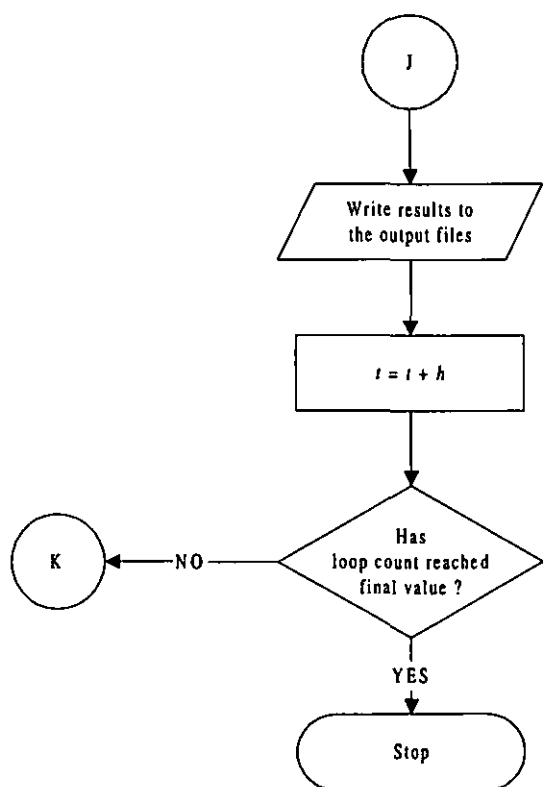
continued



continued



continued



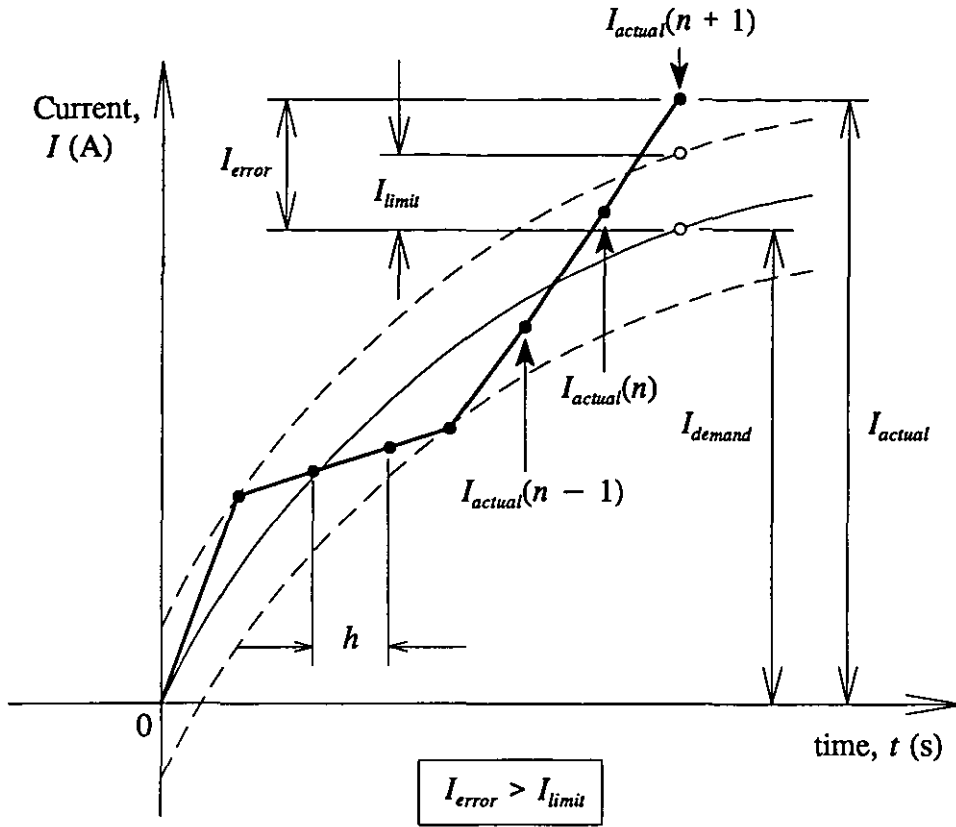


Fig. 6.19 Tolerance band control simulation

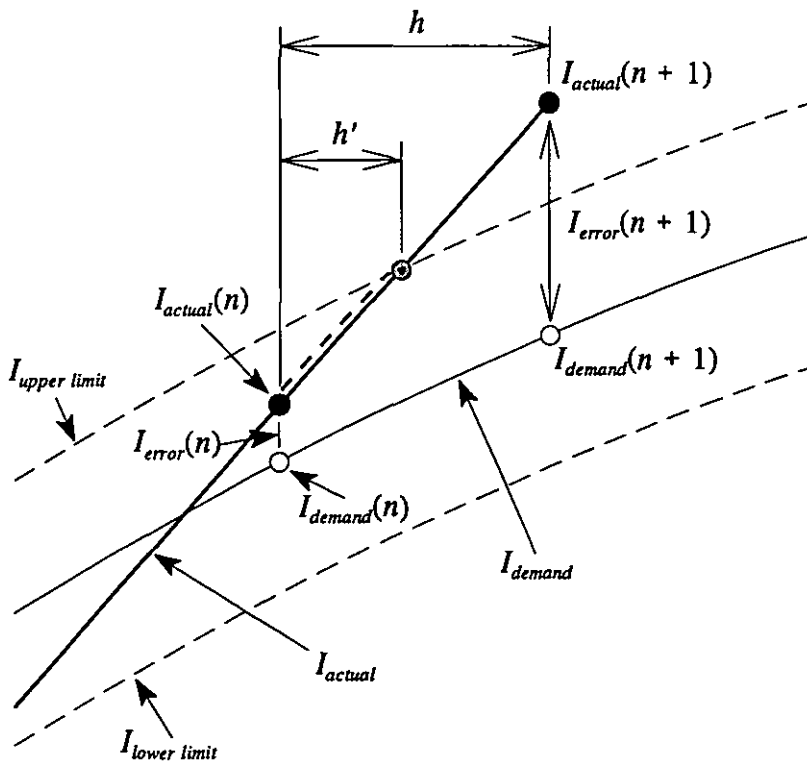


Fig. 6.20 Re-integration over a reduced time step interval

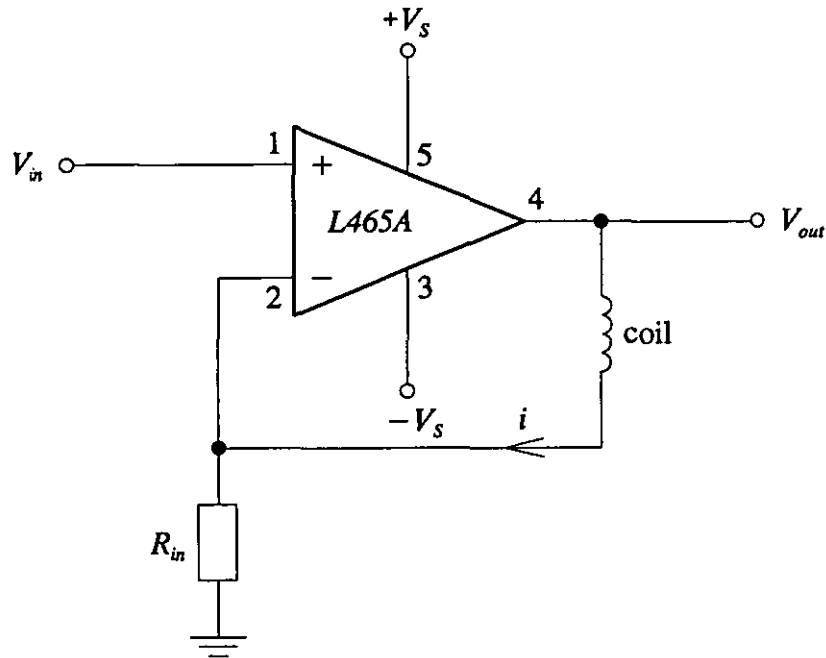


Fig. 6.21 Linear power amplifier experimental circuit

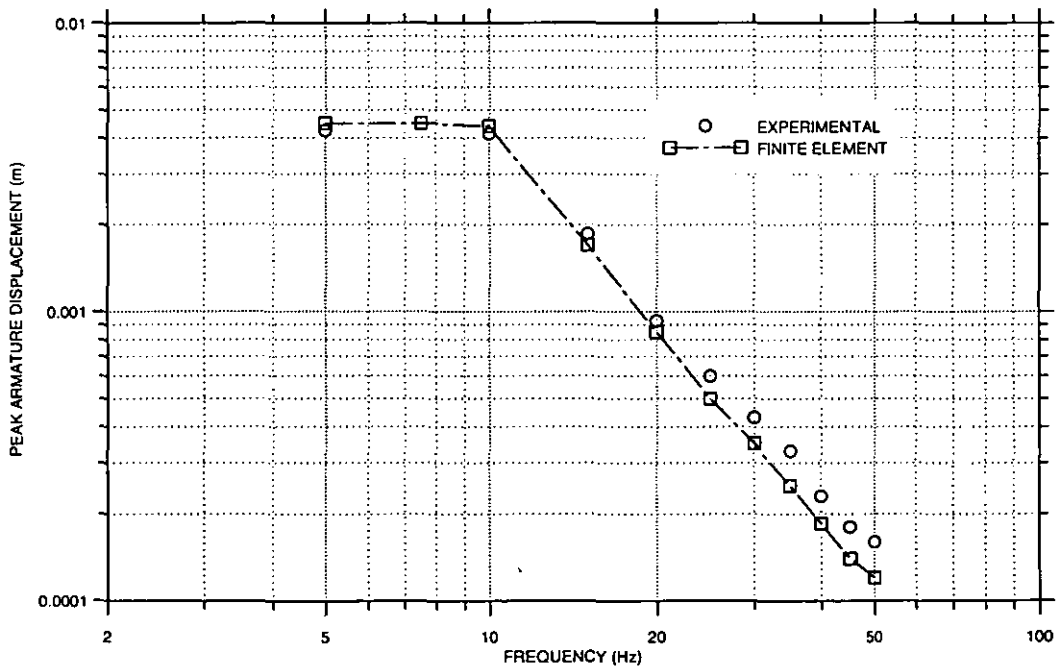
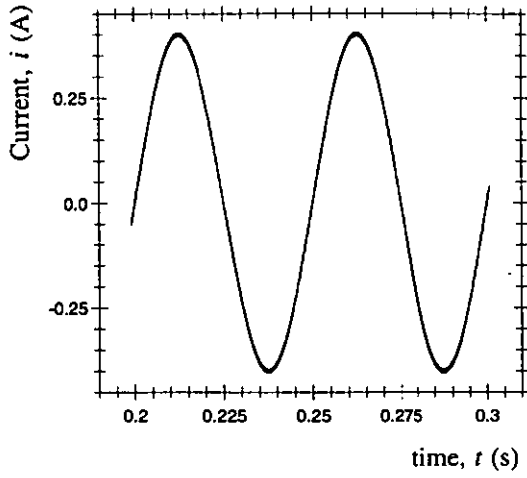
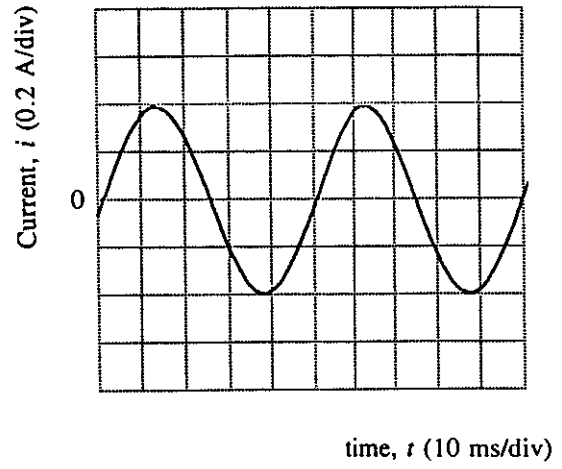


Fig. 6.22 Simulated and experimental dynamic response characteristics for the prototype motor at 0.60 A peak sinusoidal current

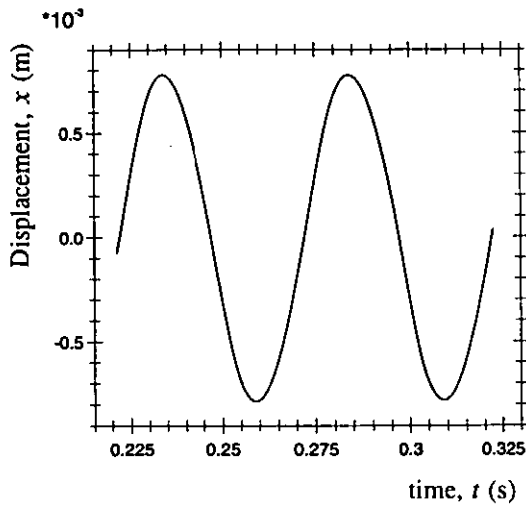




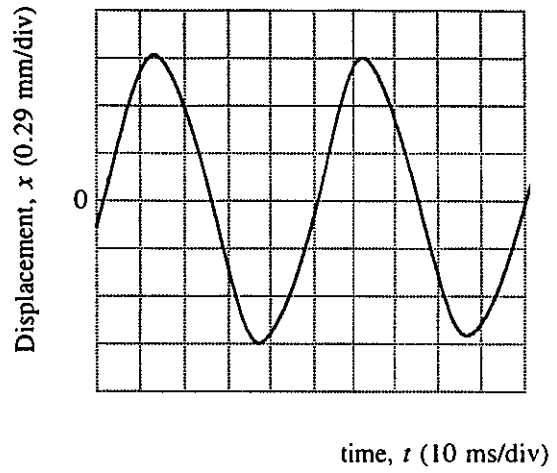
(a) Simulated current waveform



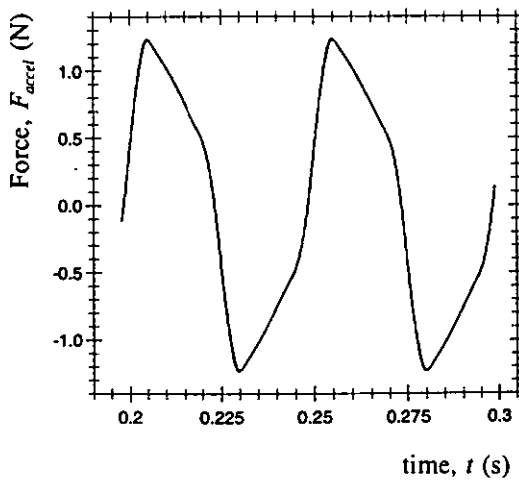
(b) Experimental current waveform



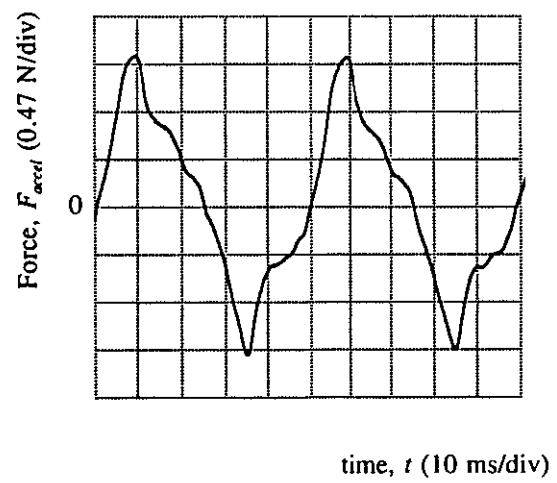
(c) Simulated armature displacement



(d) Experimental armature displacement

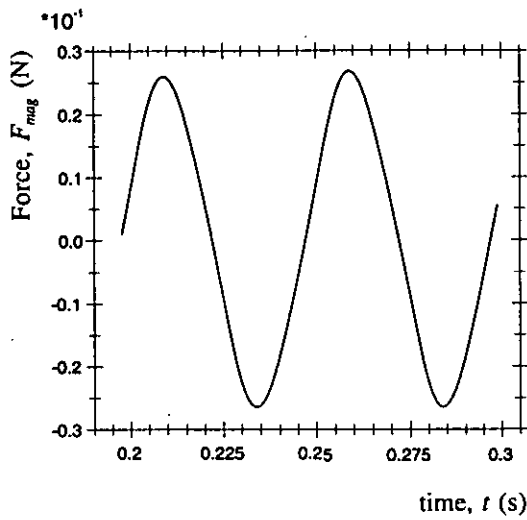


(e) Simulated acceleration force

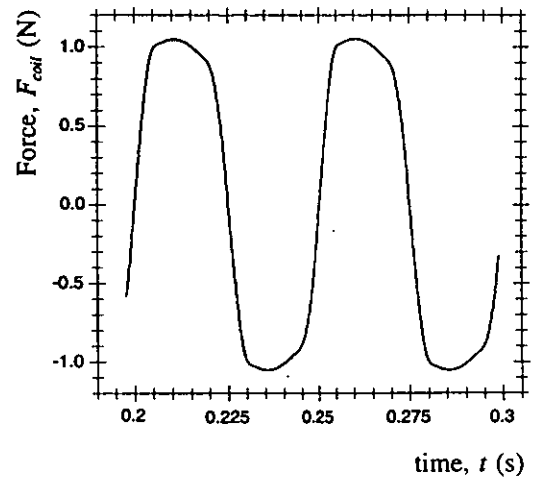


(f) Experimental acceleration force

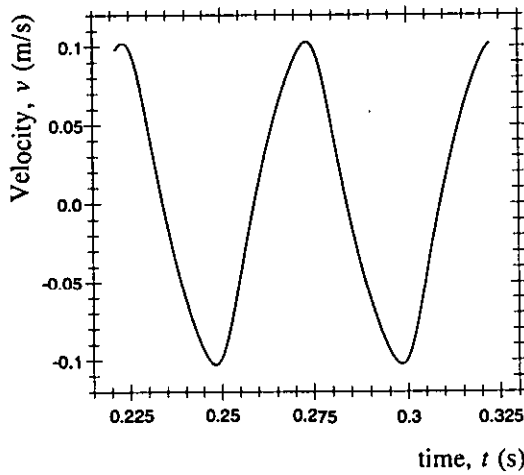
**Fig. 6.23** Simulated and experimental results for a 0.40 A peak sinusoidal 20 Hz coil current



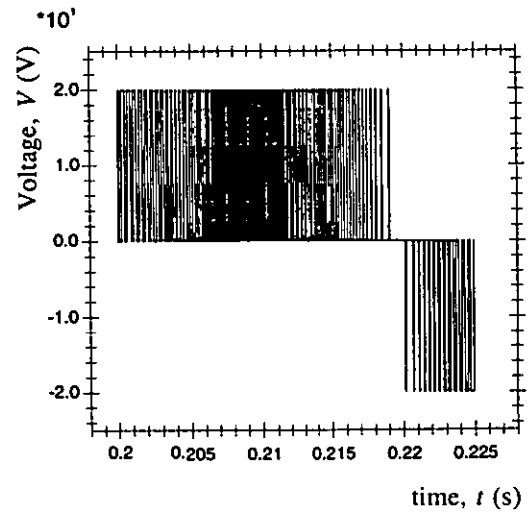
(a) Simulated stiffness force



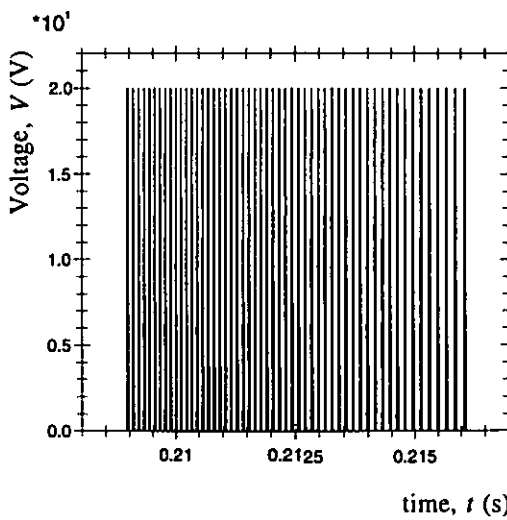
(b) Simulated coil force



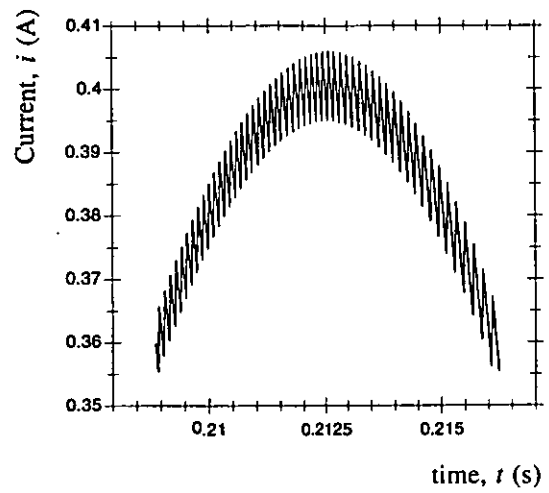
(c) Simulated armature velocity



(d) Simulated coil voltage

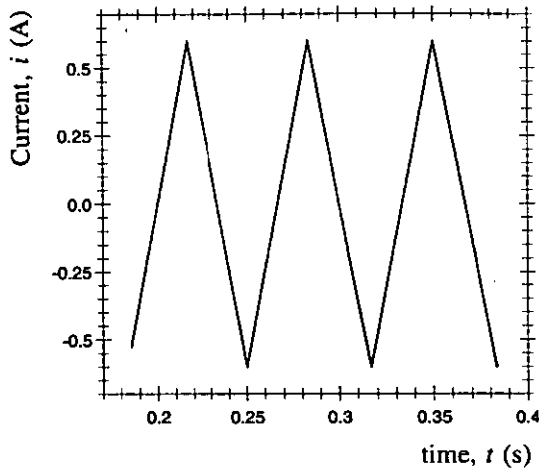


(e) Simulated coil voltage in detail

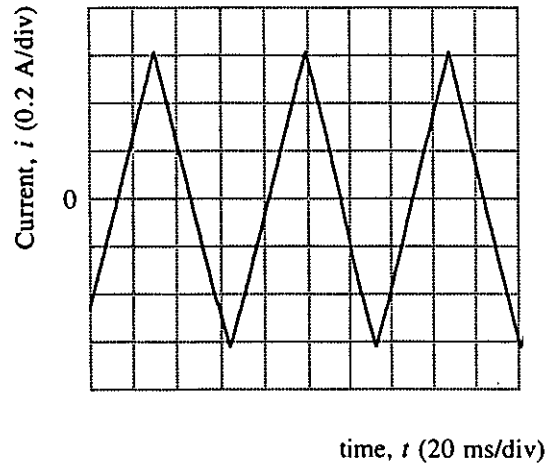


(f) Simulated tolerance band control

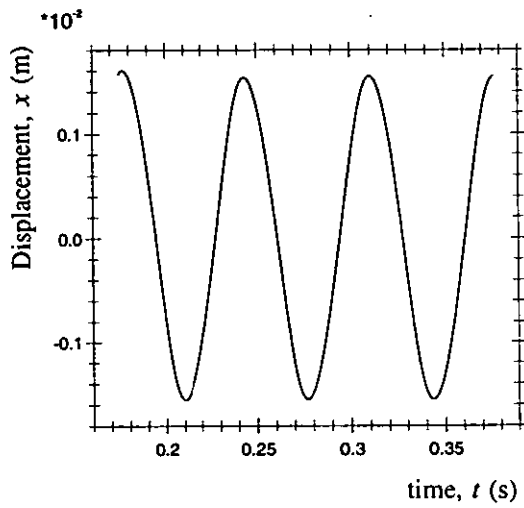
**Fig. 6.24** Simulated results for a 0.40 A peak sinusoidal 20 Hz coil current



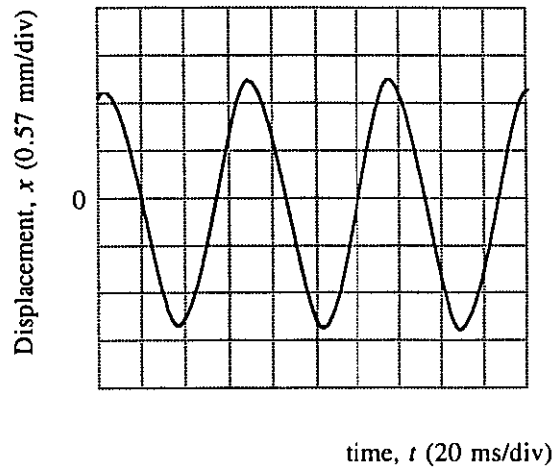
(a) Simulated current waveform



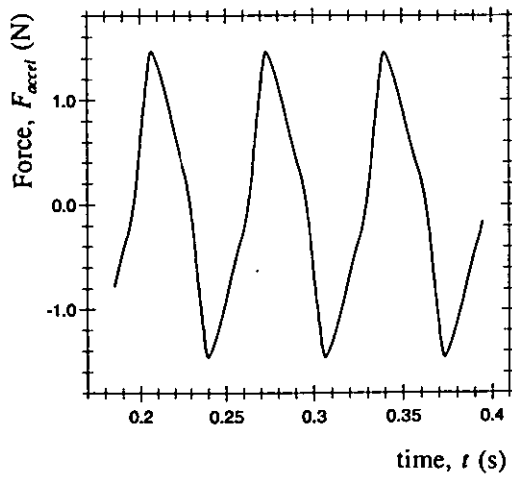
(b) Experimental current waveform



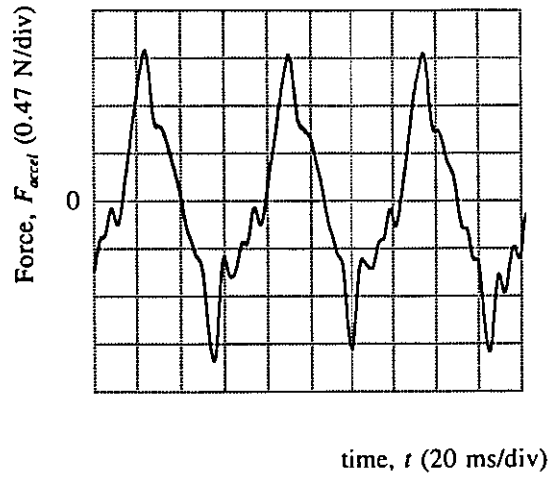
(c) Simulated armature displacement



(d) Experimental armature displacement



(e) Simulated acceleration force



(f) Experimental acceleration force

**Fig. 6.25** Simulated and experimental results for a 0.60 A peak triangular 15 Hz coil current

**RE-FORMATION OF THE LINEAR RELUCTANCE MOTOR I**

To improve the static and dynamic characteristics presented in chapters 5 and 6, it was necessary to modify the various dimensions of the magnetic circuit of the motor. The aim of the present chapter is to study ways in which the force acting on the armature can be increased, and improvements brought about in the magnetic stiffness, dynamic performance and linearity. A parametric study was undertaken in which the various dimensions were varied, one at a time, to allow an assessment to be made of the effect resulting from each alteration. A second prototype motor was designed and manufactured, which allowed further comparison to be made between theoretical and experimental characteristics to illustrate the effectiveness of the modelling technique.

**7.1 INITIAL GEOMETRIC PARAMETER MODIFICATIONS**

The parameters that were modified were:

- (i) the size and position of the permanent magnets on the stator;
- (ii) the chamfering of the stator end-rings;
- (iii) the armature diameter;
- (iv) the armature centre-section length and;
- (v) the armature centre-section diameter.

The affect of each change was investigated at excitation currents up to 0.7 A and over the complete armature stroke. The following sections describe the effects of each change on the performance of the motor.

**7.1.1 Re-positioning the Permanent Magnets**

Initial consideration was given to the size and position of the permanent magnets, as considerations of the flux distribution in the initial design had made clear that these

were poorly positioned, (see section 5.1.1). This resulted in substantial leakage flux, and it was decided that this would be reduced by making both magnet outer diameters equal to the stator outer diameter, but with the volume of each magnet  $V_m$  kept constant. The initial prototype design had a 40.0 mm outer diameter  $d_o$ , a 20.0 mm inner diameter  $d_i$  and was 5.0 mm in length  $l$ , resulting in a volume of:

$$\begin{aligned} V_m &= \frac{\pi l}{4} (d_o^2 - d_i^2) = \frac{\pi (5.0 \times 10^{-3})}{4} [(40.0 \times 10^{-3})^2 - (20.0 \times 10^{-3})^2] \\ &= 4.71 \times 10^{-6} \text{ m}^3 \end{aligned} \quad (7.1)$$

The outer diameter  $d_o$  of the re-positioned magnets was made equal to the 46.0 mm stator outer diameter. Re-arranging equation (7.1) for the magnet inner diameter  $d_i$  and substituting for  $V_m$  and  $l$  (which was also kept constant), gives the new diameter as:

$$d_i = \sqrt{d_o^2 - \frac{4V_m}{\pi l}} = \sqrt{(46.0 \times 10^{-3})^2 - \frac{4(4.71 \times 10^{-6})}{\pi (5.0 \times 10^{-3})}} \approx 30.3 \times 10^{-3} \text{ m} \quad (7.2)$$

For convenience during the finite element mesh construction, and possibly also in manufacture, this figure was approximated as 30.0 mm. This produced a negligible increase in the volume of each magnet of 1.3%, and these inner and outer magnet diameters were maintained throughout the investigation.

### 7.1.2 Chamfering of the Stator End-Rings

A simple but effective method of reducing the flux leaking from the stator end-rings, shown in Fig. 5.2, is to chamfer the outer edges of the stator end-rings by 45°, to create a better magnetic path through the end-rings from the magnets to the air-gap. One possible manufacturing problem is that machining the chamfer up to the outer diameter will risk this dimension being reduced slightly, causing difficulties in aligning the component concentric in the motor housing. However, this problem was not considered serious and the modifications discussed above are both included in the motor design when investigating the armature diameter.

### 7.1.3 Armature Diameter

In section 5.1.1, the 10 mm diameter armature of the initial design was considered to be too small. The largest possible diameter would be slightly less than the inner diameter of the magnets, which was 30.0 mm. A diameter of 28.0 mm would allow only a 1.0 mm gap between the inner magnet edge and the armature surface, which would inevitably produce leakage across the gap. The largest armature diameter was therefore taken to be 25.0 mm, with the resulting gap of 2.5 mm being considered adequate. Armature diameters of 15.0 mm and 20.0 mm were also investigated, producing four different motor designs.

The half cross-sections of the four designs, together with the initial design, are shown in Fig. 7.1, and all the new designs feature the re-positioned magnets and chamfered stator end-rings discussed above. All other dimensions of the four designs were kept fixed, with some, but not all, being equal to those of the initial prototype. The back-iron thickness did however vary, depending on the armature size, but this was not considered a critical part of the motor that would affect a comparison of the different characteristics. The fixed dimensions included the outer diameter, overall length, permanent magnet volume and all stator end-ring, yoke and air-gap dimensions. However, in the 25.0 mm diameter armature model the cross-sectional area of the coil was slightly smaller than in the other three models, due to the large diameter armature. This produced a higher current density in the coil, but this was considered unimportant in an investigation of the static force characteristics and the dynamic response. All four designs had stator coils with 825 turns.

Fig. 7.2 shows the vector equipotential plots for each different armature diameter design, with the coils unexcited and the armatures in the central equilibrium positions. Each plot displays 40 contours, with the increment between each contour being equal to enable valid comparisons to be made. Table 7.1 presents the vector equipotential contour plot information. It is apparent from the plots that the leakage flux is reduced as the diameter of the armature is increased, i.e. the 10 mm diameter armature design, (Fig. 7.2(a)), has five contours in the air surrounding the device, whereas there are

Contour	Magnetic Vector Potential
Minimum	-9.3569E-03
Maximum	+9.3569E-03
Increment	4.7984E-03

**Table 7.1** *Magnetic vector equipotential contour plot information*

only two in the 25 mm diameter armature design, (Fig. 7.2(d)). This is due to the differing cross-sectional areas of the armatures, with the smaller diameter armature saturating at a smaller value of flux and causing the remaining flux to leak from the magnetic circuit.

It is also possible in Fig. 7.2 to see areas of highly saturated iron. These always appear in the armatures and the stator end-rings, and also in the stator yoke pole-shoes in the larger diameter designs. The flux density plots of Fig. 7.3 illustrate this further, with the saturated areas in the 25 mm diameter armature design experiencing a maximum flux density of 1.60 T. Due to the small armature cross-section in Figs. 7.3(a) and (b), the maximum flux densities of 1.82 T and 1.75 T are greater than the 1.66 T and 1.60 T of the two larger diameter armature designs, Figs. 7.3(c) and (d). As discussed in section 5.1.1, the operating point of the permanent magnets should be high to produce the largest possible flux density in the air-gap, and Table 7.2 shows the operating points of the magnets in each motor, with the coils unexcited and the armatures in their central positions.

The various air-gap flux densities are shown in Fig. 7.4 and it is clear that the 25 mm diameter design produced the highest flux density, which peaks at 1.50 T under the stator end-rings. This is a large increase above the value of 0.80 T obtained with initial design and greatly increased the stiffness, Table 7.2 shows the values of the centralising force acting on each armature at its central position. Analyzing the flux density graphs highlights further the unacceptable leakage from the smaller diameter

Armature Diameter (mm)	Operating Point of Permanent Magnets (T)	Centralising Force (N)
10.0 (Initial Design)	0.72	$\pm 0.48$
10.0	0.70	$\pm 0.54$
15.0	0.76	$\pm 1.81$
20.0	0.83	$\pm 4.15$
25.0	0.92	$\pm 6.98$

**Table 7.2** Magnet operating points and armature centralising forces

designs, where the leakage between the stator end-rings and the adjacent stator yokes in the 10 mm diameter design is about 0.33 T, compared with only 0.06 T in the largest diameter design.

The stiffness characteristics of each armature design are shown in Fig. 7.5, and it is clear that the 25 mm diameter armature design produces the largest stiffness, whereas the two smallest diameter armatures produced unacceptable characteristics which result in the armatures never returning to the central positions. It is evident from Figs. 7.5 and 7.2(d) that the 25 mm diameter armature design is the best in terms of both stiffness and leakage reduction.

The four coils were excited with currents up to 0.7 A, in increments of 0.1 A, and for each current the force was calculated at 0.5 mm increments over the complete stroke length. The finite element results for coil currents up to 0.6 A are shown in Fig. 7.6, for increments of 0.2 A. The results for the 10 mm diameter armature Fig. 7.6(a) are similar to the original prototype, with the stiffness being poor and the crowded force characteristics above 0.2 A showing that this is sufficient current to saturate the iron. The peak force obtained is only 18.0 N. The force characteristic for the 15 mm diameter armature in Fig. 7.6(b) exhibits the same problems as the smallest diameter armature; although the peak force has increased to 28.0 N.



A major improvement was provided by the 20 mm diameter armature, which Fig. 7.6(c) shows to produce a stiffness characteristic that would enable the armature to return to its central position in the absence of control flux. Detailed examination of this stiffness characteristic highlights however a problem between the central position and  $\pm 1.0$  mm displacement, where the restoring force is very low and a small amount of bearing friction would prevent the armature from returning to the central position. The force characteristics at each coil current are still not equi-spaced and linear operation is impossible, either loaded or unloaded. However, crowding of the force curves has been eliminated, suggesting that the iron is not highly saturated, and the peak force is increased to 36.0 N.

The force characteristics for the 25 mm diameter armature design of Fig. 7.6(d) would enable near linear operation to be achieved, both loaded or unloaded. This is due to the near equi-spaced and parallel curves at different coil currents. The stiffness has also improved, which would enable the armature to return to its central position even with significant bearing friction. The maximum force available of approximately 47.0 N was the largest value achieved.

The ideal characteristic for the two components of the total force, (the stiffness and the coil force), is shown in Fig. 7.7. The stiffness should be linear and the coil force characteristics should be linear, parallel, equi-spaced and parallel to the zero force axis. The stiffness characteristic should intersect the coil force functions at equal displacements to achieve linear movement. The characteristics of the two components of force obtained from the finite element analysis are shown in Fig. 7.8, and further illustrates the problem of saturation in smaller diameter designs whereby the force produced on the 10 mm armature is relatively small (Fig. 7.8(a)) and far from the ideal characteristic of Fig. 7.7. The 15 mm diameter armature characteristic (Fig. 7.8(b)) still suffers from saturation, as does the 20 mm diameter armature (Fig. 7.8(c)) but to a lesser extent.

However, the force produced on the largest diameter armature, (Fig. 7.8(d)) resembles the ideal characteristic, and would allow near linear operation to be obtained. The coil

current/armature displacement characteristics of Fig. 7.9, clearly shows only a small deviation from linearity with the largest diameter armature design. The two smallest diameter armatures result in motors that are little more than bistable actuators with stable positions only at full travel in each direction, whereas the characteristic for the 20 mm diameter design lies between the two extremes.

The force/coil current characteristics when the armature is at its central position are shown in Fig. 7.10. This again highlights the saturation in the two smaller diameter armatures, with no gain achieved by operating the 10 mm diameter armature design above 0.1 A or the 15 mm diameter armature design above 0.2 A. The most acceptable results are achieved with the 25 mm diameter armature design, which can create a force on the armature of about 9.7 N at 0.7 A, compared with only 0.7 N with the smallest diameter.

So far only the static characteristics have been examined, but another important criteria is the dynamic response. In order to compare the dynamic response of the four designs, the coil resistance, armature mass and viscous damping coefficient need to be determined for each. The coil resistances were calculated as described in section 3.3.2 and the armature masses were obtained as described in section 6.2.3. The viscous damping coefficients were calculated using the mechanical time constant determined in section 6.2.3. Table 7.3 shows the parameters for each motor, together with the total mass, which includes the armature, all stator components, permanent magnets and coil but neglects the motor housing and linear bearings. The table shows that the most satisfactory design established so far, the largest diameter armature design, also has the largest mass, whereas if the motor is to be used in aircraft it should be as small as possible.

The dynamic response of the four motor designs between 5 Hz to 50 Hz is shown in Fig. 7.11. The frequency response is influenced by the armature mass and the 25 mm diameter armature suffers due to its appreciably larger mass. The 10 mm diameter design has the smallest mass but the poorest dynamic response, due probably to the small armature force. On balance, the 15 mm diameter armature design produces the

Armature Diameter (mm)	Coil Resistance ( $\Omega$ )	Armature Mass (g)	Damping Coefficient ( $\text{Ns}^2/\text{m}$ )	Motor Mass (g)
10.0	8.811	34.78	1.610	582
15.0	10.65	86.69	4.013	581
20.0	12.48	162.43	7.519	588
25.0	13.40	261.96	12.13	640

**Table 7.3** *Electrical and mechanical parameters for each motor design*

most satisfactory results, with an armature displacement of  $\pm 7.5$  mm at 25 Hz compared with only  $\pm 1.2$  mm for the 10 mm diameter design. Both the 20 mm and 25 mm diameter designs have a good response at frequencies below 20 Hz; however above this frequency the displacements decrease rapidly, to  $\pm 3.5$  mm and  $\pm 2.0$  mm at 25 Hz for the 20 mm and 25 mm diameters respectively. This emphasizes that a major problem with the large diameter design is the poor dynamic response at high frequencies. This section has shown that the 25 mm diameter design is the most promising for further development. The next two sections examine the centre-section of the armature in more detail.

#### 7.1.4 Armature Centre-Section Length

Modifying the armature centre-section was expected to change the stiffness of the motor, and since the largest diameter design already possessed a satisfactory stiffness it was decided that a design with a poor stiffness would be modified to see if major improvements could be obtained. The 15 mm diameter design was chosen for this purpose, because it would be advantageous to improve this design to enable its good dynamic response to be utilised. This section, and the next, analyzes the effects of changes made to the length and diameter of this part of the armature.

The initial length of the armature centre-section was approximately 20.5 mm. Two modifications were implemented, changing the length to 24.5 mm, modification *A*, and 16.5 mm, modification *B*, by simply modifying the material properties of the finite elements to effectively add or remove 2.0 mm sections of magnetic material at each end of the narrow centre-section. Fig. 7.12 presents the 15 mm diameter armature design, with the initial centre-section arrangement and the two modifications. The modifications were also expected to alter the maximum stroke length of the armature, and the three stiffness characteristics of Fig. 7.13 show that the original characteristic is not improved but displaced by  $\pm 2.0$  mm.

A 1 mm separation between the coil current/armature displacement characteristics of the modified armature *A* and the initial design is clearly seen in Fig. 7.14. However, the modified armature *B* moves only 0.3 mm further than the initial design, due probably to the flux level in the overlap under the pole-shoe becoming a maximum and the armature ceasing to move. This suggests that a longer stroke could be achieved by lengthening the pole-shoes, although a problem could arise if the gap between each pole-shoe became too small and flux leaked from one to the other.

The force/coil current curves with the armature held in its central position are shown in Fig. 7.15 and, as discussed previously, all three characteristics level off due to iron saturation. The modified armature *A* has the highest force sensitivity and the highest saturation force but the smallest maximum armature displacement, with the opposite set of conditions applying for the modified armature *B*.

### 7.1.5 Armature Centre-Section Diameter

The initial armature design was further modified by reducing the radius of the centre-section from 5.40 mm to 4.40 mm in modification *C*, and 3.40 mm in modification *D*, as in Fig. 7.16. This change improved the stiffness characteristic to such an extent that, as Fig. 7.17 shows, the armature will centralise itself if bearing friction is low. This improvement is due to the increase in the centre-section air-gap from 2.1 mm to 4.1 mm in modification *D*, which increases the rate of change of reluctance with

position and thereby the developed force. Fig. 7.19 shows the coil current/armature displacement characteristics, and the modified armature  $D$  moves only to a maximum displacement of 1.65 mm from the central position. This armature appears to saturate first, and the force/coil current characteristics of Fig. 7.18 illustrate that little is gained by using a coil current greater than 0.20 A when using all three armatures. Reducing the centre-section diameter improves the stiffness and the hysteresis due to bearing friction, but also reduces the maximum armature displacement and the saturation force.

## 7.2 SECOND PROTOTYPE LINEAR RELUCTANCE MOTOR

A second prototype motor was manufactured to provide more experimental data. The only information available was from the original design, in which problems such as high bearing friction made meaningful comparisons between theoretical and experimental characteristics very difficult. The force calculation needed further confirmation when the force characteristics approached zero, and the flux linkage characteristics needed to be investigated and compared when the armature was moved from its central position. Three armatures were therefore manufactured, with different centre-section dimensions but for use with one stator arrangement.

### 7.2.1 Stator and Armature Dimensions

The new motor had a 15 mm armature diameter. Although not the best in terms of high stiffness and developed force, it had a good dynamic response and was ideal for checking thoroughly the dynamic simulation programs. The objective was not to manufacture the best motor so far developed, (clearly the 25 mm diameter design), but to obtain more experimental results, and due to the fact that the 15 mm diameter centre-section had already been modified, it was decided to manufacture this design with three different armatures. The stator dimensions of the second prototype were similar to those of the 15 mm diameter model, and although all the three armatures had the same centre-section diameter the length of the centre-sections were different. Fig. 7.20 shows the dimensions of the stator and the three armatures. The diameter of the centre-section was fixed at 10.80 mm, and the length of the centre-sections of

20.5 mm (armature A), 16.5 mm (armature B) and 12.5 mm (armature C) enabled the different maximum armature stroke lengths to be studied.

The half cross-sections of the second prototype motor with the three different armatures are shown in Fig. 7.21, together with the original prototype. The diameters of the second prototype armatures were reduced at their ends to 9.51 mm, to enable the linear bearings from the original prototype motor to be re-used. To avoid any reduction in the outer diameter of the end-rings and thus avoid the potential problem discussed in section 7.1.2, their length was extended to 6.0 mm to produce a 1.0 mm edge on the outer diameter edge after the chamfer was machined. Fig. 7.22 shows a photograph of the motor showing the housing, stator magnetic circuit and armatures.

A coil was manufactured to the dimensions of the window area, using 0.40 mm diameter enamelled copper wire. The coil had 40 turns per layer and 18 layers, producing 720 turns and giving an mmf of 216.0 AT for 0.3 A current. The space factor  $k_{sf}$  of 0.42 compared with 0.48 for the original prototype coil, and the coil resistance obtained from equation (3.11) as 9.626  $\Omega$  was close to the figure of 9.783  $\Omega$  measured by a Wayne-Kerr Electronic Bridge. New NdFeB permanent magnets were also manufactured to the new dimensions and assumed to have a remanent flux density of 1.17 T and a coercive force of 890 kA/m, giving a relative permeability of 1.046.

Two different batches of Radiometal 4550, from different suppliers, were used in building the motor, with the stator end-rings and the stator yokes machined from one batch and the stator back-iron and all three armatures from the other. Heat treatment facilities were unavailable and the magnetization curve of Fig. 4.2 was unsuitable as it was obtained after heat treatment. The magnetization curves for both batches of the un-treated Radiometal 4550 had therefore to be determined experimentally, to enable an accurate comparison between the finite element and experimental results.

### 7.2.2 Determination of the Magnetization Curves

The magnetization curves for the two batches of Radiometal 4550 were measured using the circuit of Fig. 7.23 [89], in which a ring of uniform cross-section with an outer diameter  $d_o$  of 46.0 mm, an inner diameter  $d_i$  of 26.0 mm and thickness  $t$  of 10.0 mm was uniformly wound with an exciting coil of 161 turns of 0.40 mm diameter enamelled copper wire. A search coil of 0.10 mm diameter enamelled copper wire was bi-filar wound with the exciting coil, and connected directly to a Grassot type fluxmeter. Fig. 7.24 shows one of the rings complete with bi-filar wound exciting and search coils.

When the current in the exciting coil is reversed, the corresponding reversal of flux in the ring and the current through the fluxmeter produces a deflection proportional to the change of flux linkage in the search coil. The exciting coil current is reversed a number of times to bring the Radiometal 4550 into a cyclic condition, so that a change in the flux from  $+\phi_s$  to  $-\phi_s$  accompanies a current reversal from  $+I_e$  to  $-I_e$ , the change of flux linking the  $N_s$  turns of the search coil  $\lambda_s$  is:

$$\lambda_s = 2\phi_s N_s \quad (7.3)$$

The flux density  $B_{ring}$  in the ring is therefore:

$$B_{ring} = \frac{\phi_s}{A_{ring}} = \frac{\lambda_s}{2N_s A_{ring}} \quad (7.4)$$

and since  $A = t(d_o - d_i)/2$  is the cross-sectional area of the ring:

$$B_{ring} = \frac{\lambda_s}{N_s t (d_o - d_i)} \quad (7.5)$$

Substituting the ring dimensions and the number of search coil turns gives:

$$B_{ring} = 31.06 \lambda_s \quad (7.6)$$

Since the mean length of the ring is  $\pi(d_o + d_i)/2$  the magnetic field strength  $H_{ring}$  is:

$$H_{ring} = \frac{2I_e N_e}{\pi(d_o + d_i)} \quad (7.7)$$

where  $N_e$ , the number of turns on the exciting coil, is equal to  $N_s$  for a bi-filar wound coil. Substituting into equation (7.7) the ring dimensions and the number of exciting coil turns gives:

$$H_{ring} = 1423.55 I_e \quad (7.8)$$

When the test was carried out with different values of current, the magnetization curves shown in Fig. 7.25 were obtained. The difference between the two experimentally determined curves and that obtained from the suppliers data sheet highlights the inferior initial permeability of the un-treated material, which produces a hysteresis loop with a large remanence and coercive force. This will increase the magnetization losses (which are proportional to the area of the hysteresis loop) and introduce mechanical hysteresis into the motor, and may prevent the armature returning to its central position in the absence of a control flux.

### 7.2.3 Static Force Characteristic

The non-linear finite element analysis was implemented using the magnetization curves of Fig. 7.25, for all three armature models of Fig. 7.21. The three coils were excited with currents up to 0.7 A, in increments of 0.1 A, and the force was calculated using the Maxwell Stress method at 0.5 mm increments over the complete stroke length of each armature. Experimental results were also obtained for each armature as described in section 5.2.2. Finite element and experimental results are compared in Figs. 7.26, 7.27 and 7.28.

The finite element and experimental results for armatures *A* and *B*, Fig. 7.26 and 7.27 agree closely, with the small discrepancy of approximately 2.0 N being due to bearing friction. The comparison for armature *C*, in Fig. 7.28 shows an increased discrepancy, due to the armature and stator components being more out of alignment and the bearing friction increased.



The comparisons of Figs. 7.26 and 7.27 verify that sufficient finite elements are used in the air-gap of the models for the Maxwell Stress calculation to accurately compute the force acting on the armature. However the discrepancies may not be entirely due to friction, as experience has shown that the method used to extrapolate the  $BH$  curve can significantly change the computed results.

Section 4.5 described the extrapolating function within *MEGA* as a linear function with a gradient of  $\mu_0$ . This is only however acceptable if the last few points on the  $BH$  curve entered by the user are in the very highly saturated region of the curve, where the gradient is nearly  $\mu_0$ . The last few  $B$  and  $H$  measurements taken when determining the magnetization curves for the Radiometal 4550 alloys, were in the saturated, but not the very highly saturated region of the curve. (The maximum field strength produced experimentally of 3556 AT/m was obtained with a current density in the exciting coil of 19.9 A/mm<sup>2</sup>, and any higher figure would certainly have damaged the enamelled insulation of the wire). The gradient at the last two experimental points was far from  $\mu_0$ , and when the  $BH$  curve was extrapolated manually at a slightly steeper gradient an improved comparison with experimental results was obtained.

The comparison of the coil current/armature displacement characteristics for armatures  $A$  and  $B$  in Figs. 7.29 and 7.30 further illustrate the friction problem, when there is an initial stiction force to be overcome before the armature moves. The coil force is sufficiently large at a current of about 25 mA to cause motion, when using armature  $A$ , and about 50 mA when using armature  $B$ , and the comparison between theoretical and practical results at currents above 0.1 A shows good correlation for the two armatures. The same is true for the comparison for armature  $C$ , in Fig. 7.31, although above 0.5 A the armature started to move again, up to 6.98 mm at 0.739 A. This was probably due to the near horizontal force characteristics, evident when using armature  $C$ , which are parallel with and very close to the zero force axis at high currents as shown in Fig. 7.28(b). These characteristics probably intersect the constant friction force slightly below the zero force axis, resulting in the balance of force being slightly below the zero force axis which moved the stable point of the armature along the

force characteristics, increasing the movement of the armature. Bearing friction will cause the armature surface to be damaged by the harder bearing material, as with the initial prototype armature discussed in section 5.2.2, the effect will however be lessened, as the armatures are more concentric in the stator bore as a result of the very high tolerances demanded during machining.

#### 7.2.4 Static Flux Linkage Characteristic

The static flux linkage characteristics using armature A are given in Fig. 7.32. Initially, the flux linking the coil with the armature at its central position was measured using a dc inductance bridge. The correlation between the theoretical and experimental characteristics is very good. However, the computed flux linkage characteristic needs to be checked at other armature positions, when an initial flux links the coil and the inductance bridge method cannot be used. An alternative method of measurement was therefore sought.

In the motor under development the measurement of flux linkage is complicated by the presence of the mmf from the magnets. The flux linking the exciting coil is a function of the armature position and coil current, or:

$$v(t) = i(t)r + \frac{d\lambda(x, i)}{dt} \quad (7.9)$$

which when integrated gives:

$$\lambda(x, i) = \int_0^{\infty} [v(t) - i(t)r] dt + \lambda(0) \quad (7.10)$$

in which  $\lambda(0) = \lambda(x=x_0, i=i_0)$ , where  $x_0$  is the armature position,  $i_0$  is the initial coil current. The term  $\lambda(0)$  is the initial flux linkage at which the integration process starts and a known integration constant has to be found. Although the initial linkage cannot be measured directly, it is possible to determine the perturbation in flux linkage due to the permanent magnets by integration of the back-emf while the armature is moving. An actual value cannot be given as the integration constant  $\lambda(0) = \lambda(x=x_0, i=0)$ , but the variation between the flux linkage and armature position can be determined with reference to an arbitrary initial condition.

#### 7.2.4.1 Theoretical Method

The experimental method used to verify the flux linkage characteristic obtained from a series of static field solutions can be simulated by using a transient finite element analysis technique, which closely resembles what will be undertaken experimentally. The method is described in section 4.8.2.2, with a step voltage input applied to the coil causing an exponential growth in the resulting current. The flux linking the coil is then obtained using equation (4.29), which integrates over time the induced emf in the coil.

Fig. 7.33 shows the applied voltage,  $iR$  voltage drop and induced emf waveforms when a step voltage of 0.9783 V was applied, to give a steady state current of 0.1 A, with the armature at its central position. Figs. 7.34 shows similar waveforms when the armature is displaced +4.0 mm from the central position. The step voltage is applied 0.30 s after the start of the analysis, and prior to this the  $iR$  drop and the induced emf are seen to be exponentially decaying to zero. This happens only when the armature is off-centre, due to the solution converging to the flux linkage that exists under these conditions. The induced emf is zero when the armature is in its central position, see Fig. 7.33, as no flux finally links the coil, so that very little linking flux will exist when the solution is converging. It is however evident that a small amount actually links the coil when the solution is converging which may be due to the slightly unsymmetrical mesh generated as it is automatically refined.

The induced emfs with the armature in four different positions are shown in Fig. 7.35. Integrating these waveforms from slightly before the application of the step voltage produces the flux linkage variations with time, shown in Figs. 7.36. The final values of the flux linkages, for every current and armature position, are then added to the initial flux linkages when the excitation current is zero and the armature is displaced throughout its complete stroke length, to produce the initial flux linkage variation with armature displacement. This characteristic could not be found from a transient analysis, which requires the armature to move to produce the motional induced coil emf, and which is impossible to achieve using the *MEGA* software. The values were

determined therefore from the static analysis results. Results from both a static and a transient analysis are compared in Fig. 7.37, with the small discrepancy probably being due to the finite step length employed in the transient analysis.

#### 7.2.4.2 Experimental Measurement Method

The experimental method included two separate tests and is similar to the method used successfully on a hybrid stepping motor [90]. For the first test, the armature is locked in its central position and loaded with a weight sufficient to displace the armature to the near limit of its travel when released. When unlocked, the armature moved by 6.0 mm and the corresponding coil emf was obtained. This was then integrated to determine the perturbation in flux linkage as:

$$\lambda_m(x, i=0) = \int_0^{\infty} e(t) dt + \lambda_m(x=x_0, i=0) \quad (7.11)$$

where  $\lambda_m(x, i=0)$  is the flux linking the coil due to the permanent magnets, and  $\lambda_m(x=x_0, i=0)$  is the arbitrary initial condition at which the integration starts. For simplicity  $x_0 = 0$  mm, where the initial flux linking the coil is zero, due to the equal and opposite magnetized permanent magnets and the symmetrical magnetic circuit. All integration results are therefore relative to this initial value of zero, which simplifies equation (7.11) to:

$$\lambda_m(x, i=0) = \int_0^{\infty} e(t) dt \quad (7.12)$$

In the second test, which is identical to the transient finite element test, the armature is locked at known positions, (0 mm,  $\pm 2.0$  mm,  $\pm 4.0$  mm and  $\pm 6.0$  mm) from the central position and a series of step input voltages are applied to the coil to give steady state currents between 0.1 A and 0.7 A. A digital storage oscilloscope (DSO) was used to record the voltage and current waveforms, which were then used to calculate the corresponding flux linkages with the initial conditions obtained from the first test. The waveforms were down-loaded from the DSO to a personal computer via an RS232 serial communication link, (see Fig. 7.38), saved as files and transferred to the *MEGA* software package, where all the waveform manipulation and the necessary mathematics functions were available to compute the flux linkages. The

first part of the experiment also utilised this method of waveform storage and manipulation technique to store the armature displacement waveform and the induced emf waveform.

The armature displacement shown in Fig. 7.39 resulted in the motional emf in the coil shown in Fig. 7.40, and the corresponding variation of the flux linkage due to the permanent magnets is shown in Fig. 7.41. Discrete data points at 0 mm, 2.0 mm, 4.0 mm and 6.0 mm from the central position were taken from this characteristic and plotted with the finite element characteristic, as shown in Fig. 7.42. The experimental points obtained were plotted in the figure for both positive and negative armature displacements, and good correlation exists between the theoretical and measured results.

An experimentally obtained voltage waveform, to produce a steady state coil current of 0.5 A, is shown in Fig. 7.43, together with the calculated  $iR$  drop and induced emf waveforms, when the armature was locked at  $-4.0$  mm from the central position. Integrating the induced emf with respect to time produces the characteristic shown in Fig. 7.44, where only the final steady state value of 0.15 Wb of the flux linkage is of interest. This value corresponds to the first term on the right-hand side of equation (7.11), with the second term being  $-0.046$  Wb, from Fig. 7.42. This results in a flux linkage of 0.104 Wb which, when included in Fig. 7.45, shows that good correlation exists between the experimental and finite element obtained characteristics.

### 7.2.5 Simulated and Experimental Results

The armature masses were calculated as described in section 6.2.3 and are given in Table 7.4, together with measured values of the armature masses. The viscous damping coefficients were determined experimentally using the method given in section 6.2.3 and were all approximately 7.5 Ns/m. The resulting mechanical time constant was very similar to that calculated for the original motor. The dynamic response of the second prototype motor using armature A are shown in Figs. 7.46(a) and (b). The correlation between the theoretical and experimental results are good at

Design	Calculated Mass (g)	Measured Mass (g)	Damping Coefficient (Ns <sup>2</sup> /m)
A	137.74	136.28	7.5
B	140.06	138.09	7.5
C	142.38	141.42	7.5

**Table 7.4** Mechanical parameters for each armature design

frequencies below 20 Hz, but above this the theoretical results exceed the experimental results. This could be attributed to the computer simulation using flux linkage data obtained from magnetostatic field solutions that neglect the effects of eddy currents in the magnetic circuit, which would inhibit the flow of flux and reduce the armature displacement. Also, the value of the viscous damping coefficient used could be a possible cause. A method of overcoming the neglect of eddy currents is to couple a transient finite element analysis solver into the step-by-step time simulation, and to update the time varying parameters at every time step [91]. Such a technique takes account of the diffusion of the field when the current varies with time and results in a very good comparison between computed and measured results.

Fig. 7.47 compares the simulated and experimental results from the second prototype motor when the coil voltage is reversed from +5.87 V to -5.87 V, thus reversing the current from +0.6 A to -0.6 A. The current overshoot in the experimental result, of Fig. 7.47(b), is again probably due to the capacitance of the test circuit power supply, similar to the effect shown in Figs. 6.6(b) and 6.7(b) for the original prototype motor. The simulated and experimental armature displacement results obtained are very similar in appearance, as shown in Figs. 7.47(c) and (d). The simulated and experimental positional overshoot peaks are both about 6.3 mm, and no static positional error is evident. The experimental acceleration force initially peaks at about

2.4 N compared with the simulated peak force of 2.9 N from Figs. 7.47(e) and (f). The small discrepancy is possibly due to bearing friction.

Fig. 7.48 shows the simulated and experimental results when the coil is excited with a 0.40 A peak 20 Hz sinusoidal current. A comparison of the armature displacement waveforms, shown in Figs. 7.48(c) and (d), is favourable, with the simulated result peaking at 1.95 mm compared with the experimental peak of about 1.9 mm. Figs. 7.48(e) and (f) show a simulated acceleration force peak of about 5.0 N, compared with an experimental peak of about 5.1 N. Fig. 7.49 shows the simulated and experimental results when the coil is excited with a 0.25 A peak 30 Hz triangular current waveform. The comparison of the armature displacement waveforms is again very favourable. In Figs. 7.49(c) and (d), the simulated displacement peaks at about 0.45 mm compared with the experimental value of approximately 0.43 mm. Figs. 7.49(e) and (f) show a simulated peak acceleration force of about 2.95 N, compared with an experimental value of about 2.9 N. The above comparisons illustrate the accuracy of the motor and drive system mathematical model.

### 7.3 CONCLUSIONS

In this chapter it has been shown that re-positioning the permanent magnets and increasing the armature diameter of the initial prototype motor improves its performance considerably. The armature centre-section dimensions have been shown to affect the maximum displacement of the armature and the stiffness characteristic. A second prototype motor has been manufactured with three different armatures to provide experimental results for comparison with finite element derived results. A good level of agreement has been obtained for both the force and flux linkage characteristics suggesting that the finite element model is correct. In the next chapter the modification of the motor magnetic circuit is continued and the use of alternative magnetic materials is studied to improve further the motor performance.

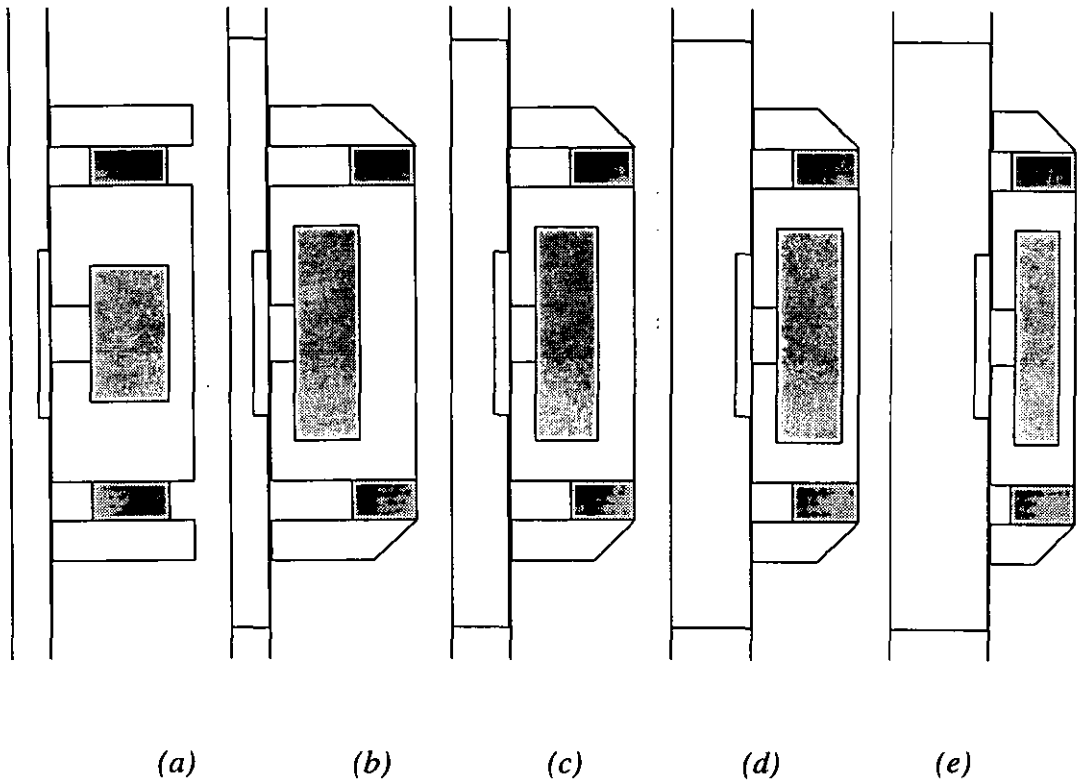


**Fig. 7.1** Half cross-sections of (a) the initial prototype design and the four different armature designs (b) 10 mm (c) 15 mm (d) 20 mm (e) 25 mm diameter armatures



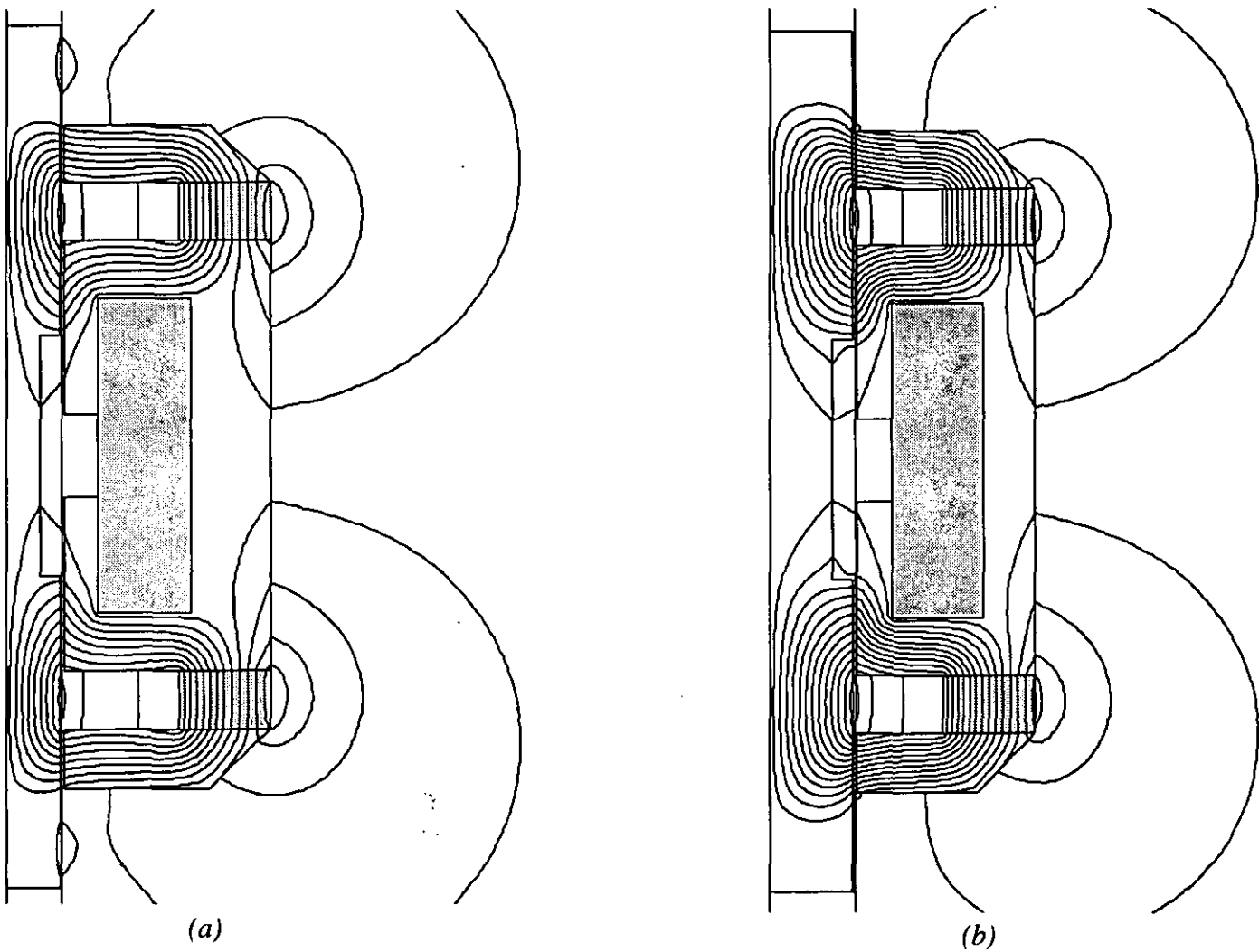


**Fig. 7.2** Magnetic vector equipotential plots (a) 10 mm (b) 15 mm diameter armature motor designs

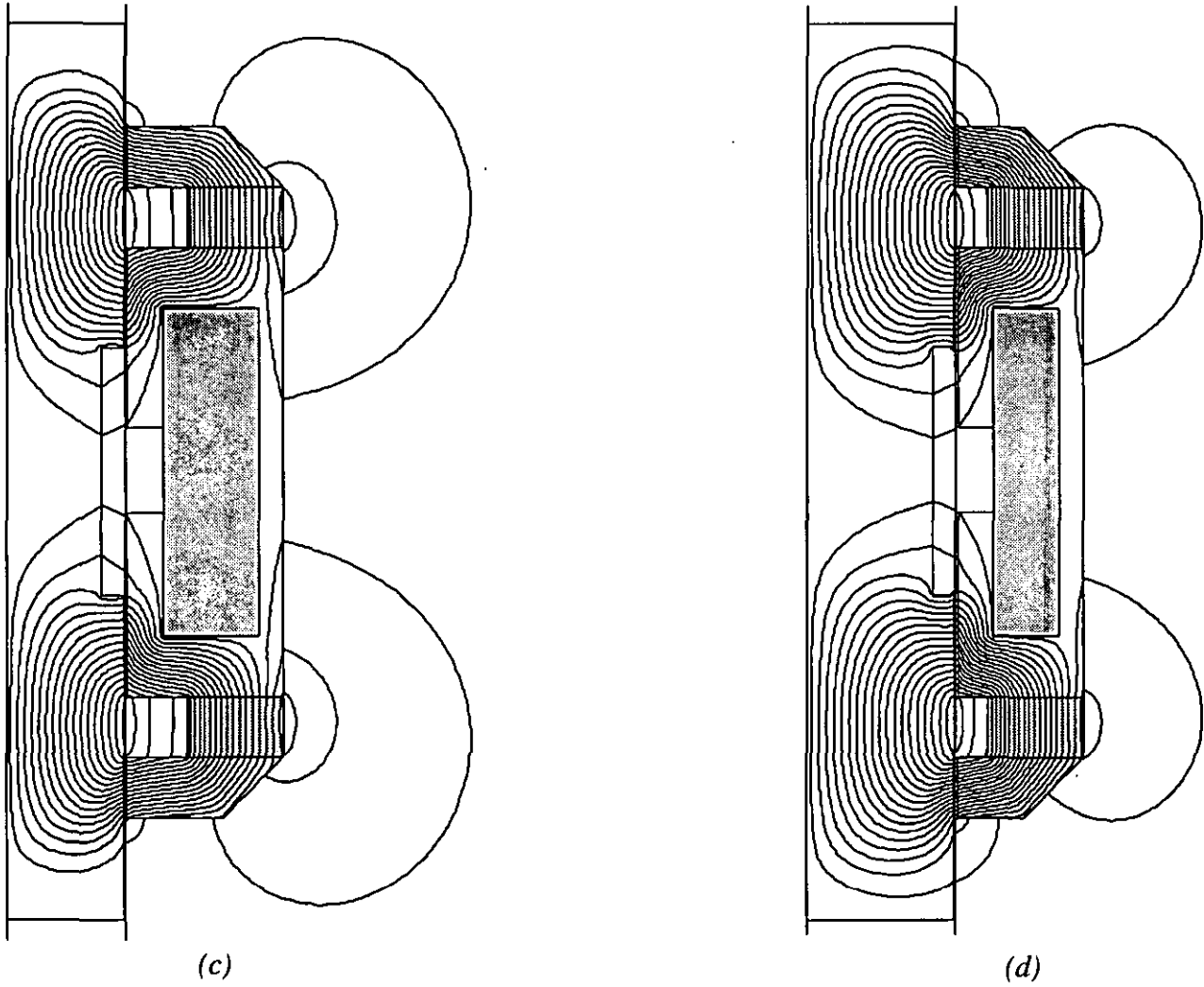


**Fig. 7.2** Magnetic vector equipotential plots (c) 20 mm (d) 25 mm diameter armature motor designs

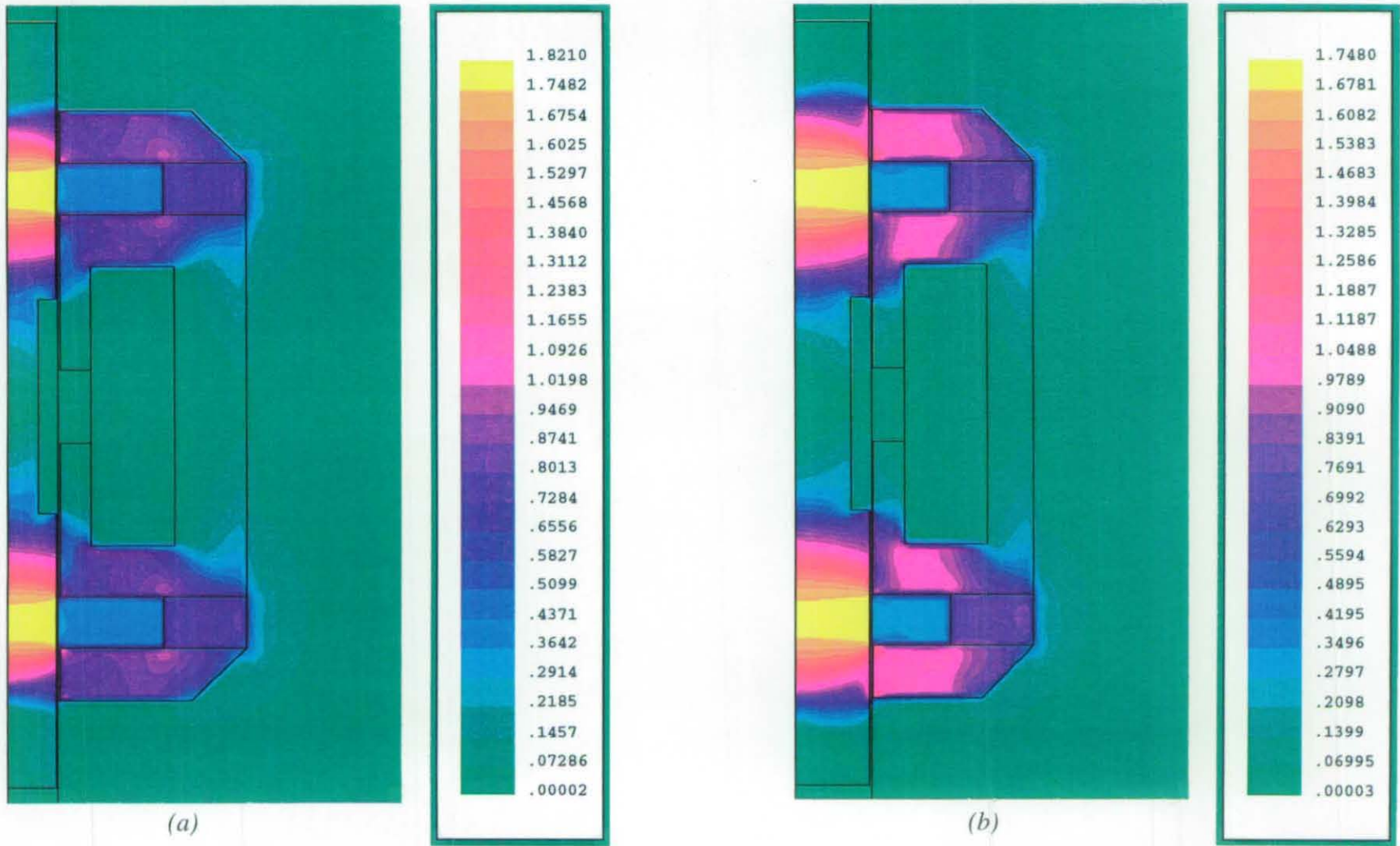


**Fig. 7.3** Magnetic flux density plots (a) 10 mm (b) 15 mm diameter armature motor designs

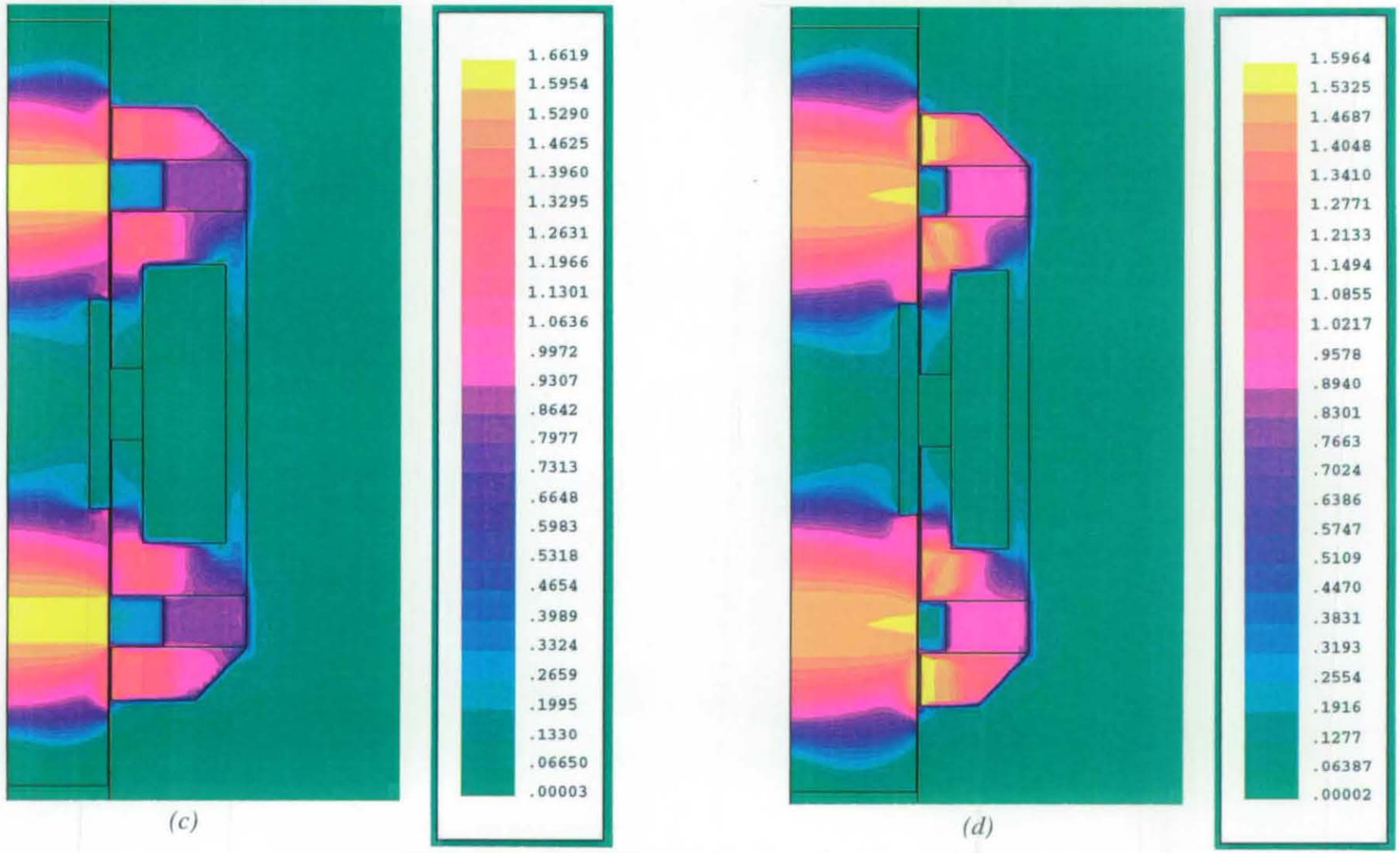


Fig. 7.3 Magnetic flux density plots (c) 20 mm (d) 25 mm diameter armature motor designs

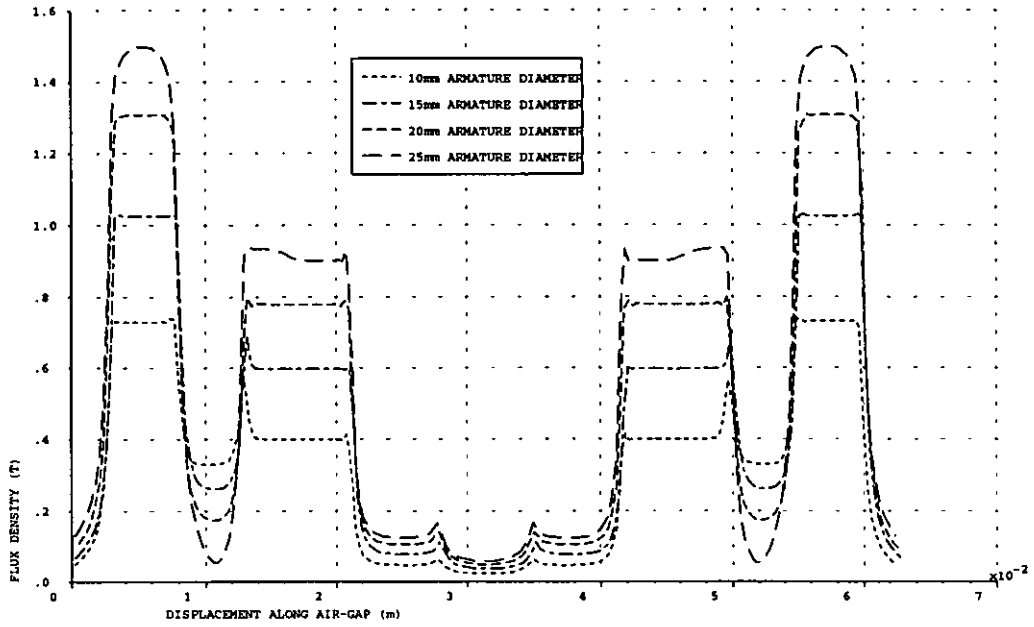


Fig. 7.4 Air-gap flux density for the four different armature diameter motor designs

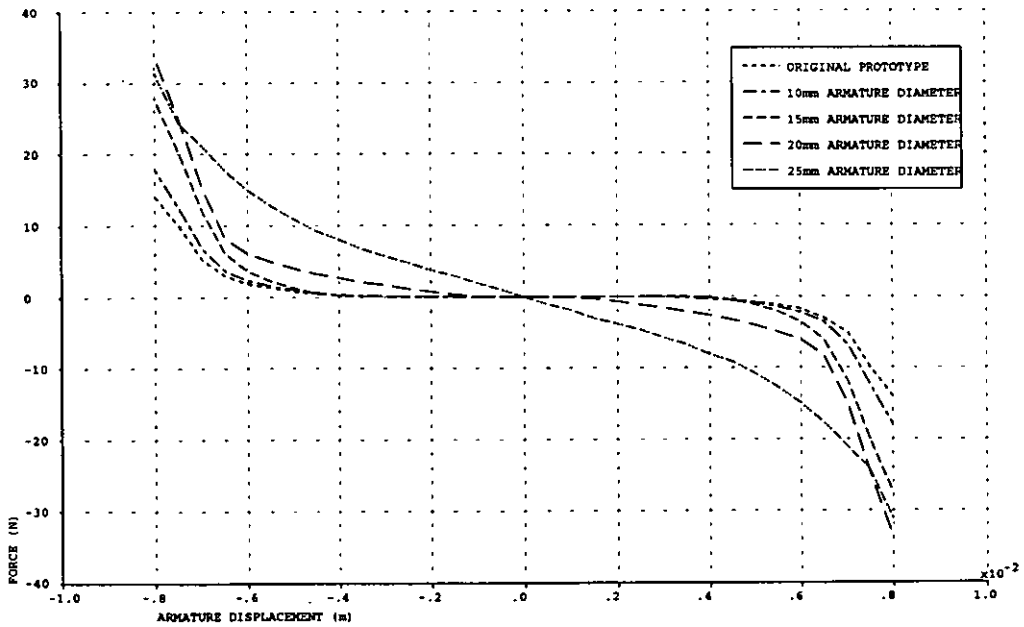


Fig. 7.5 Magnetic stiffness characteristics for the four different armature diameter motor designs

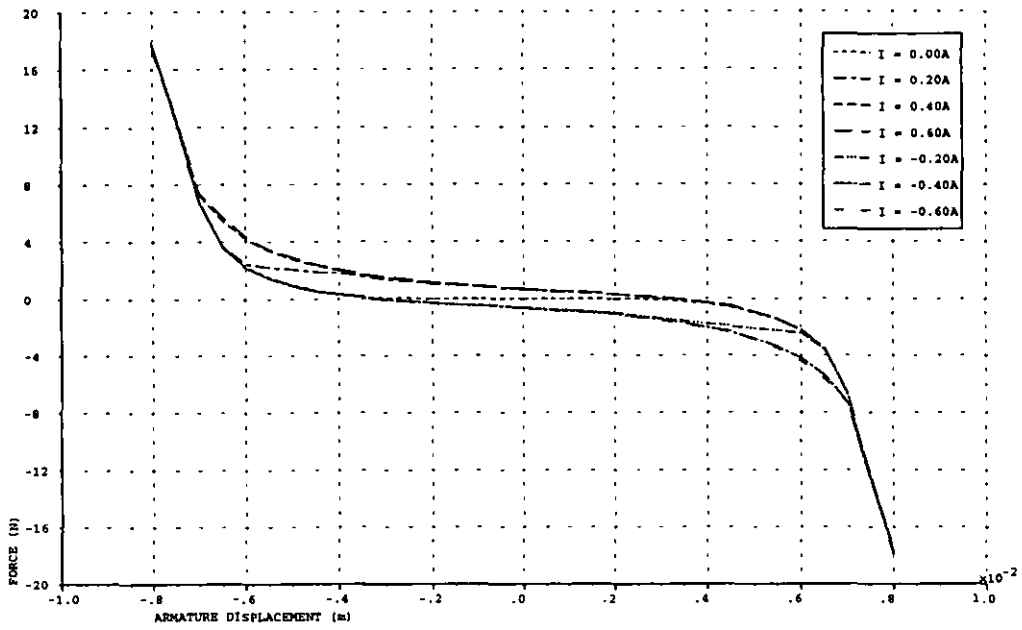


Fig. 7.6(a) Force characteristic for various coil currents for the 10 mm diameter armature motor design

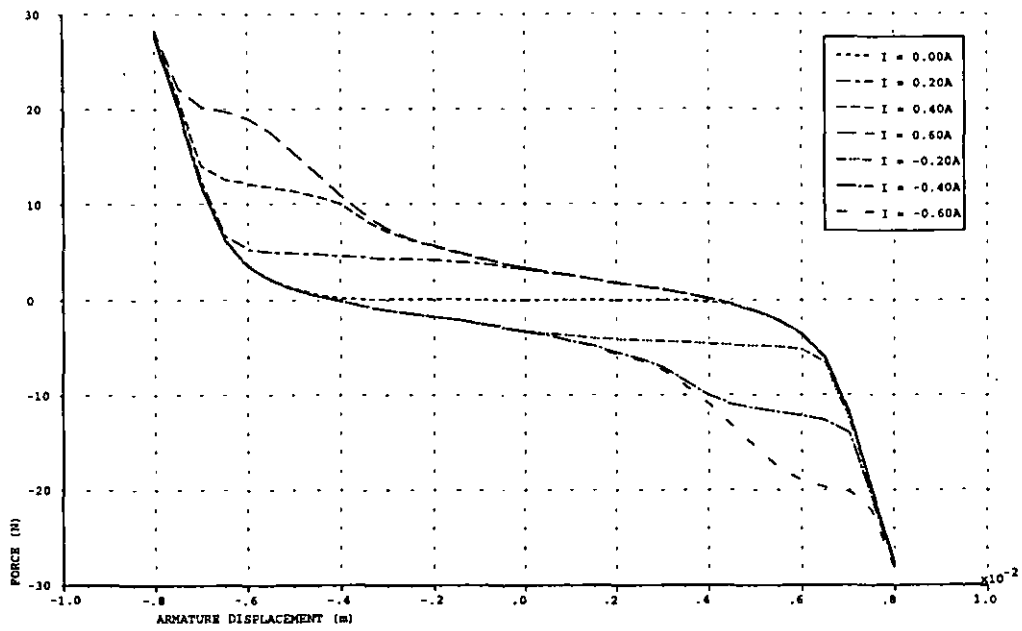


Fig. 7.6(b) Force characteristic for various coil currents for the 15 mm diameter armature motor design

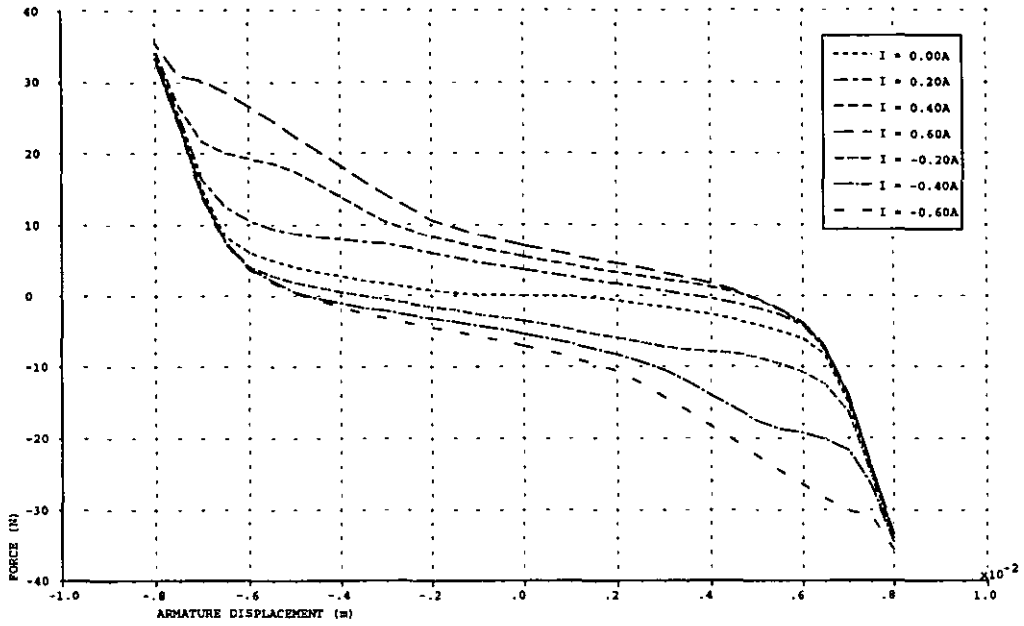


Fig. 7.6(c) Force characteristic for various coil currents for the 20 mm diameter armature motor design

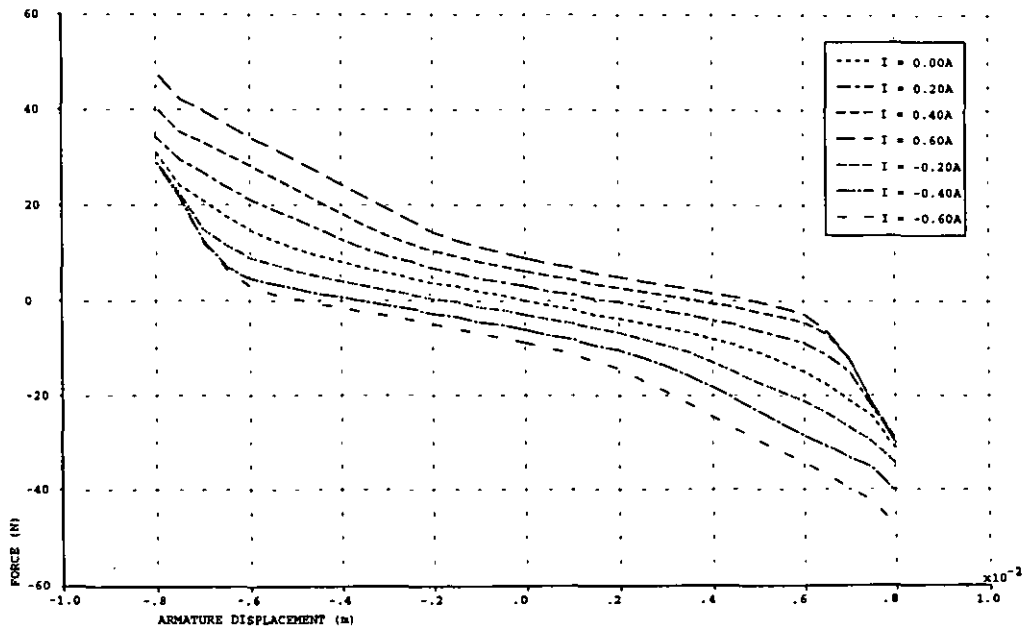


Fig. 7.6(d) Force characteristic for various coil currents for the 25 mm diameter armature motor design

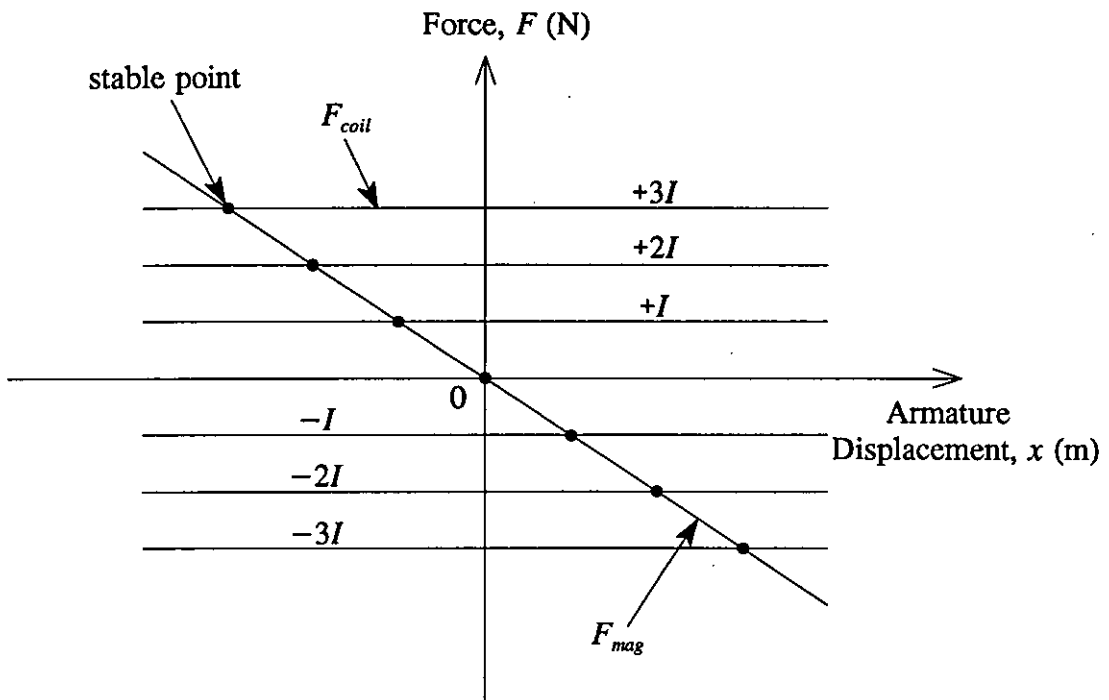


Fig. 7.7 Ideal force characteristic

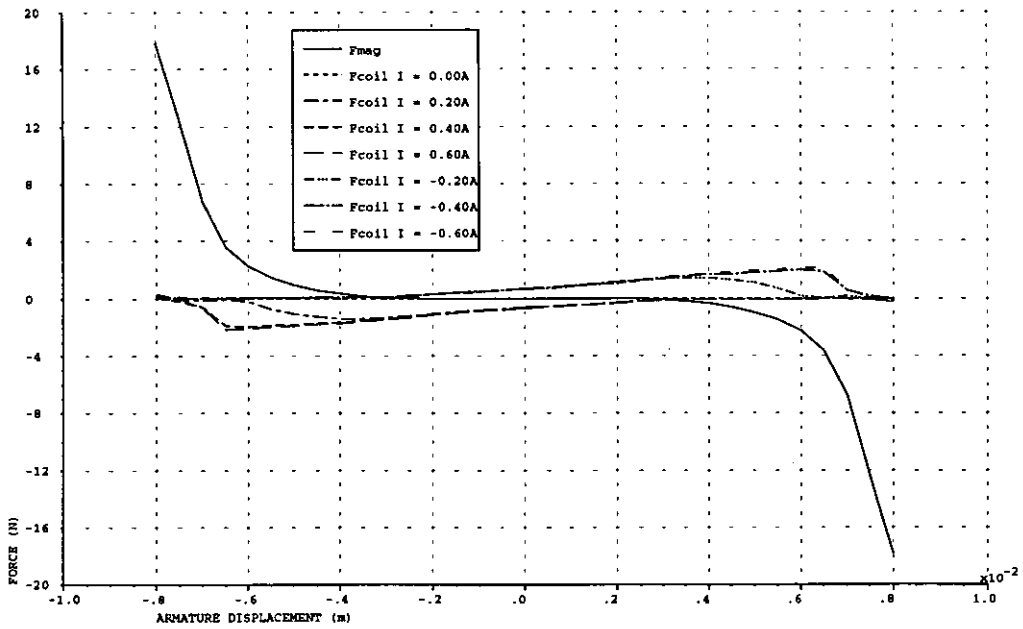


Fig. 7.8(a) Two force components for the 10 mm diameter armature motor design



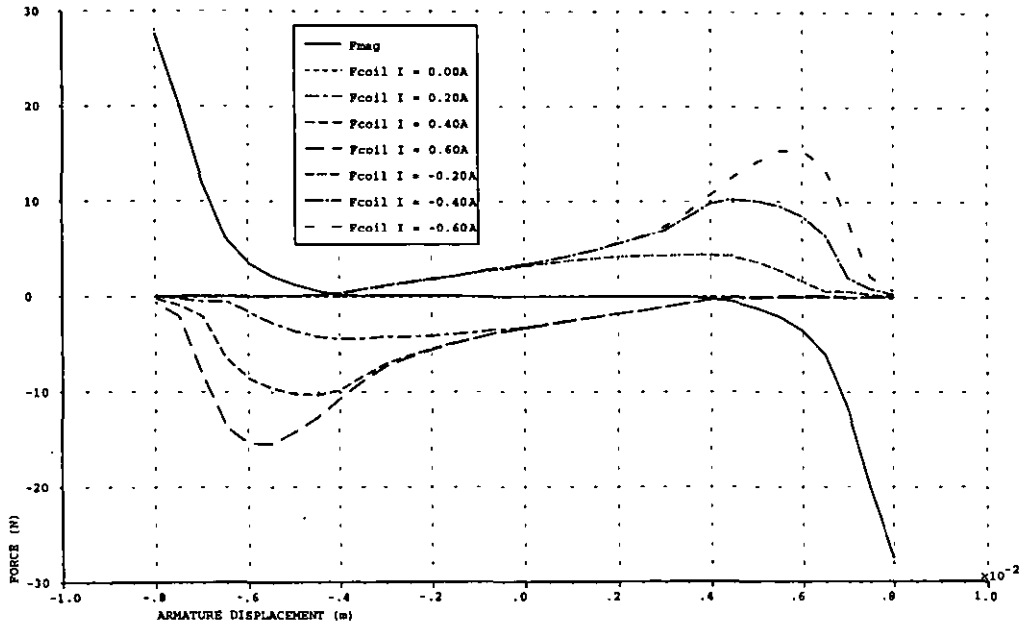


Fig. 7.8(b) Two force components for the 15 mm diameter armature motor design

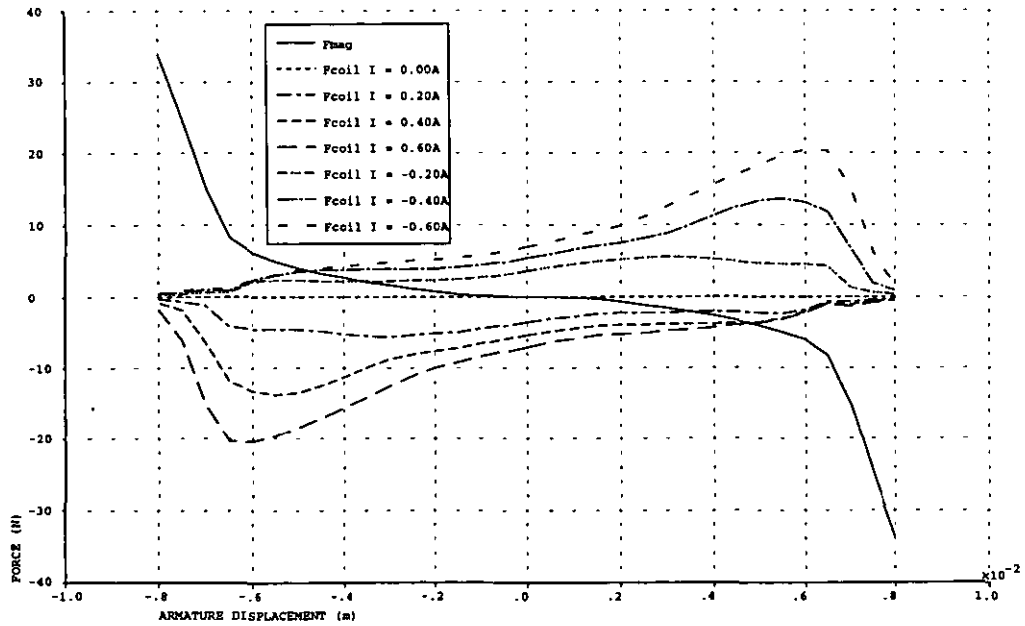


Fig. 7.8(c) Two force components for the 20 mm diameter armature motor design

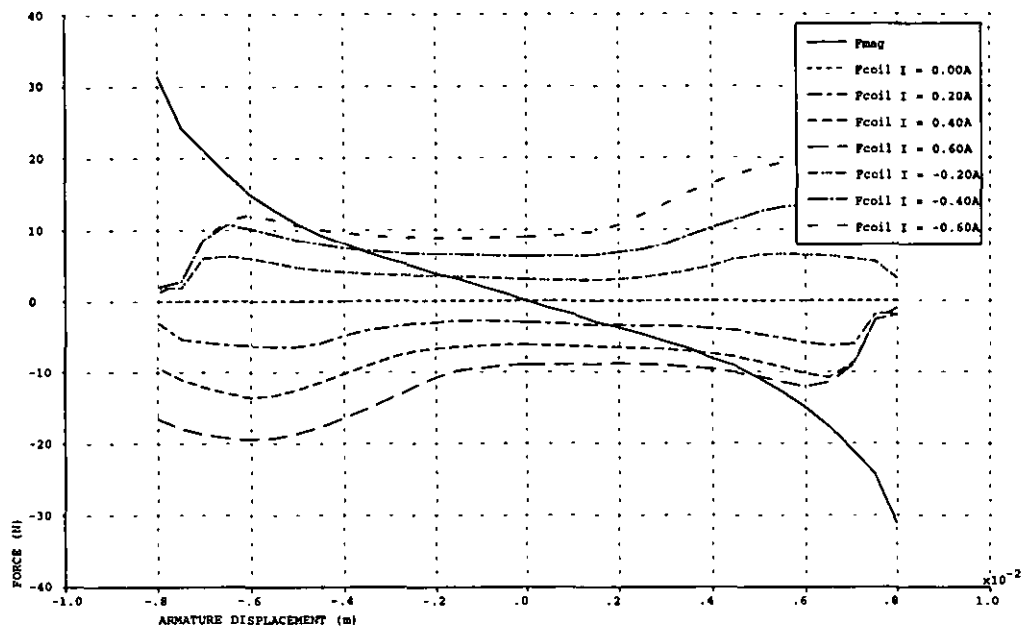


Fig. 7.8(d) Two force components for the 25 mm diameter armature motor design

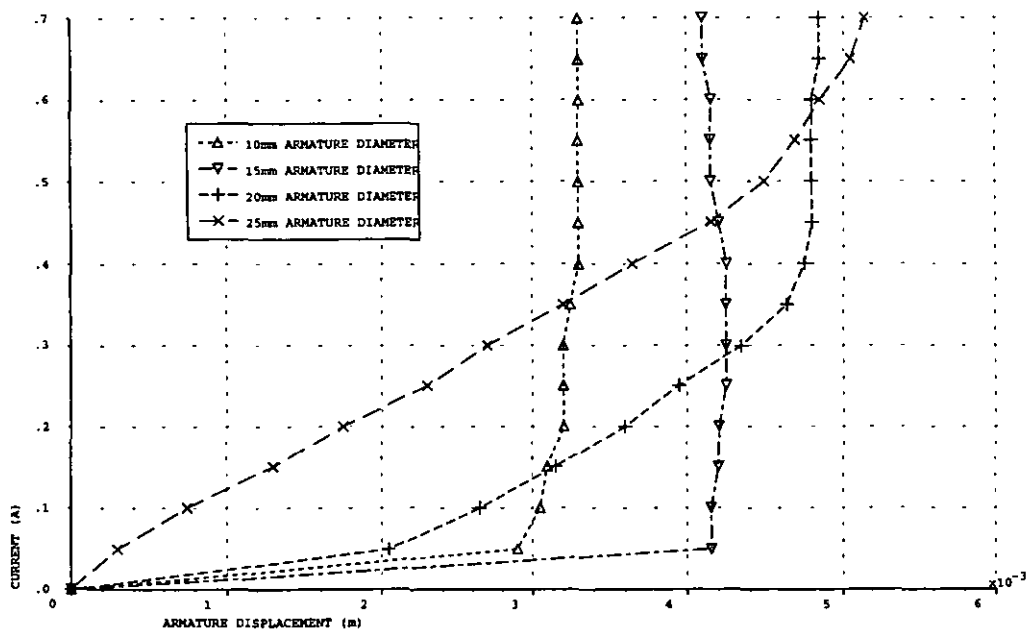


Fig. 7.9 Coil current/armature displacement characteristics for the four different armature diameter motor designs

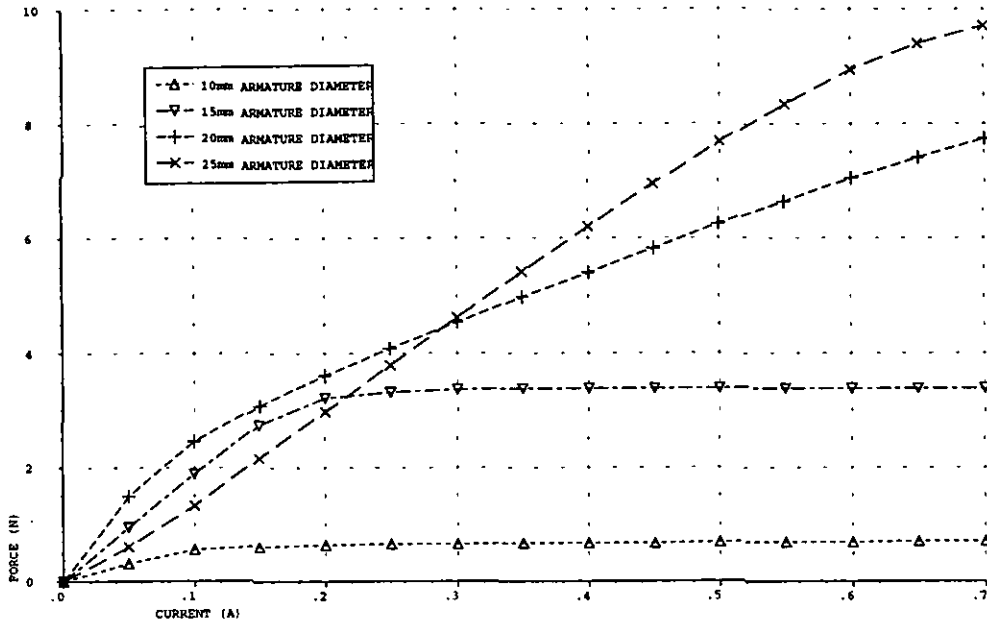


Fig. 7.10 Force/coil current characteristics for the four different armature diameter motor designs (armature central position)

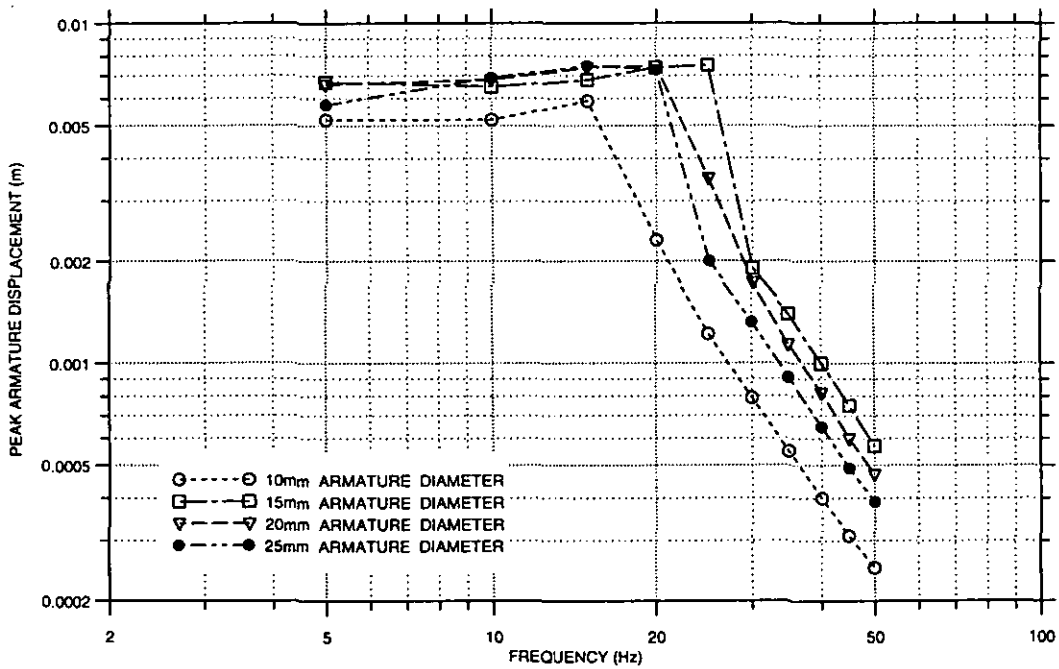


Fig. 7.11 Dynamic response characteristics for the four different armature diameter motor designs

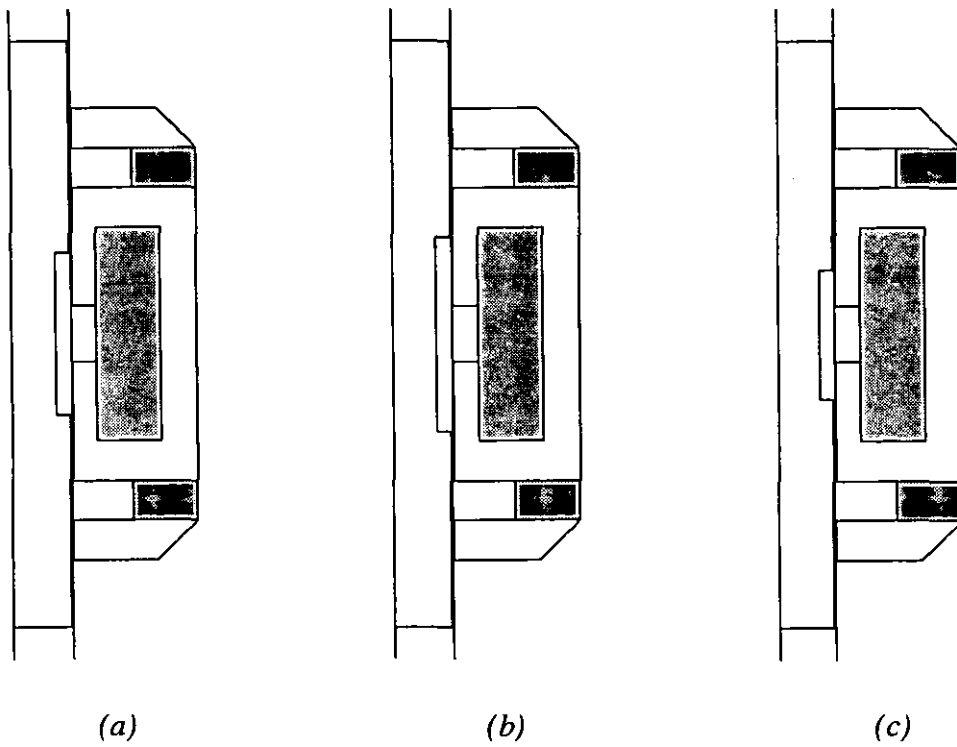


Fig. 7.12 Half cross-sections of (a) the 15 mm diameter armature motor design and (b) armature modification A (c) armature modification B

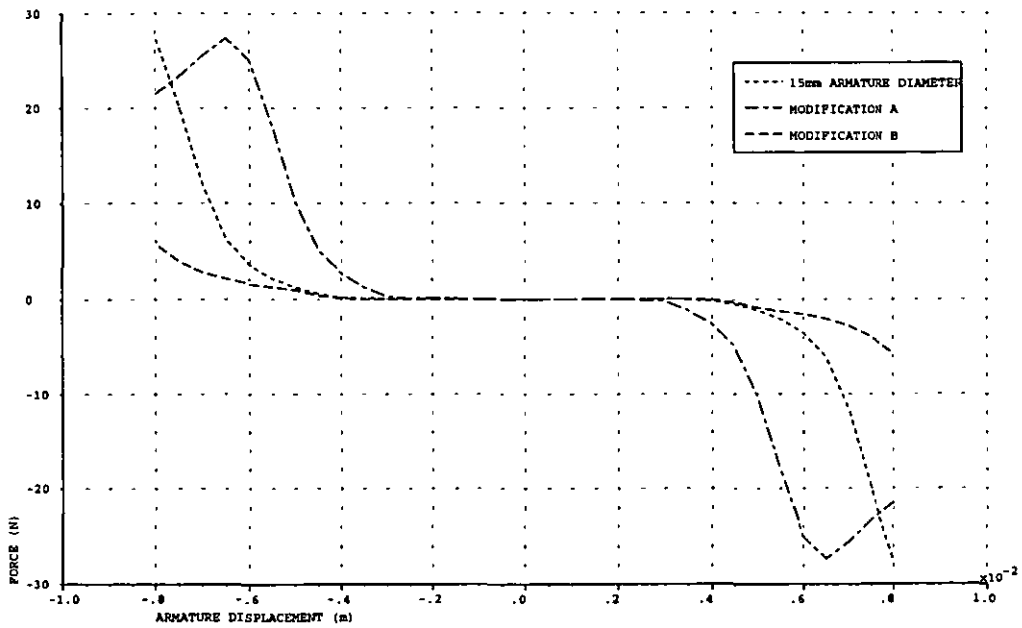


Fig. 7.13 Magnetic stiffness characteristics for the 15 mm diameter armature motor design and the two modified armatures A and B

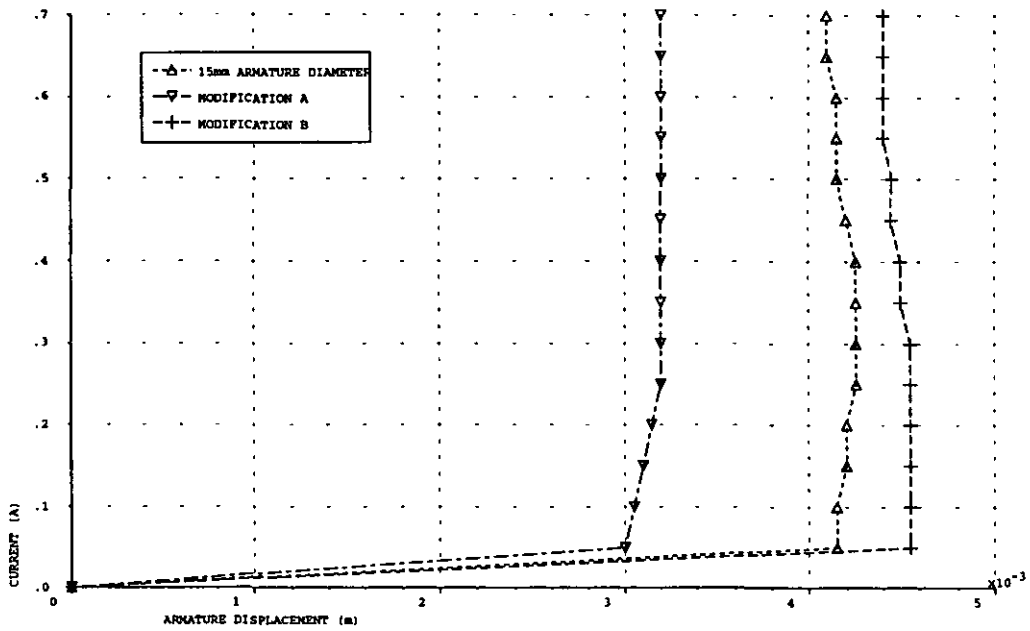


Fig. 7.14 Coil current/armature displacement characteristics for the 15 mm diameter armature motor design and the two modified armatures A and B

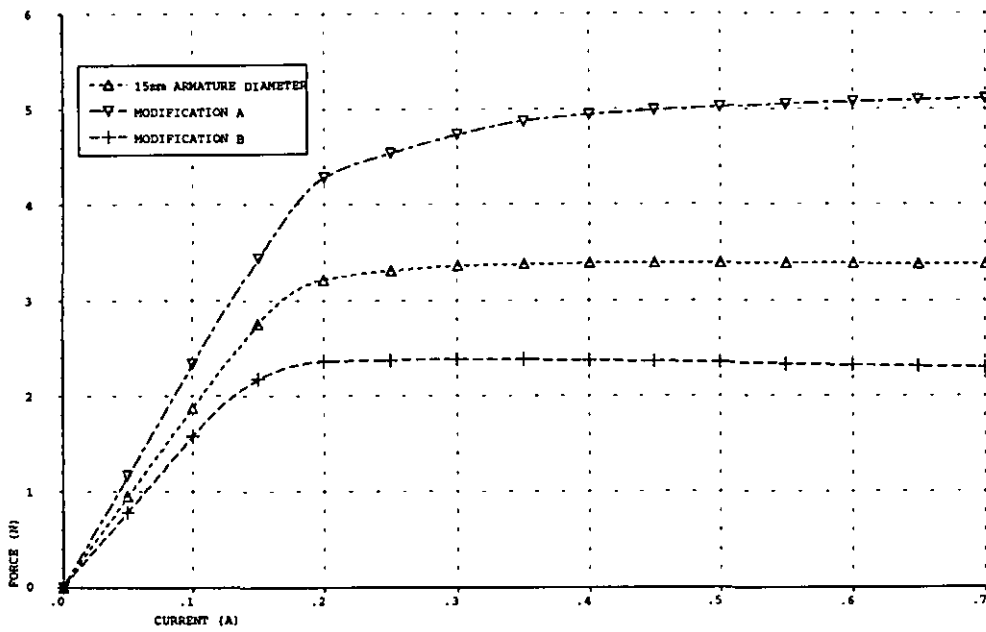


Fig. 7.15 Force/coil current characteristics for the 15 mm diameter armature motor design and the two modified armatures A and B (armature central position)

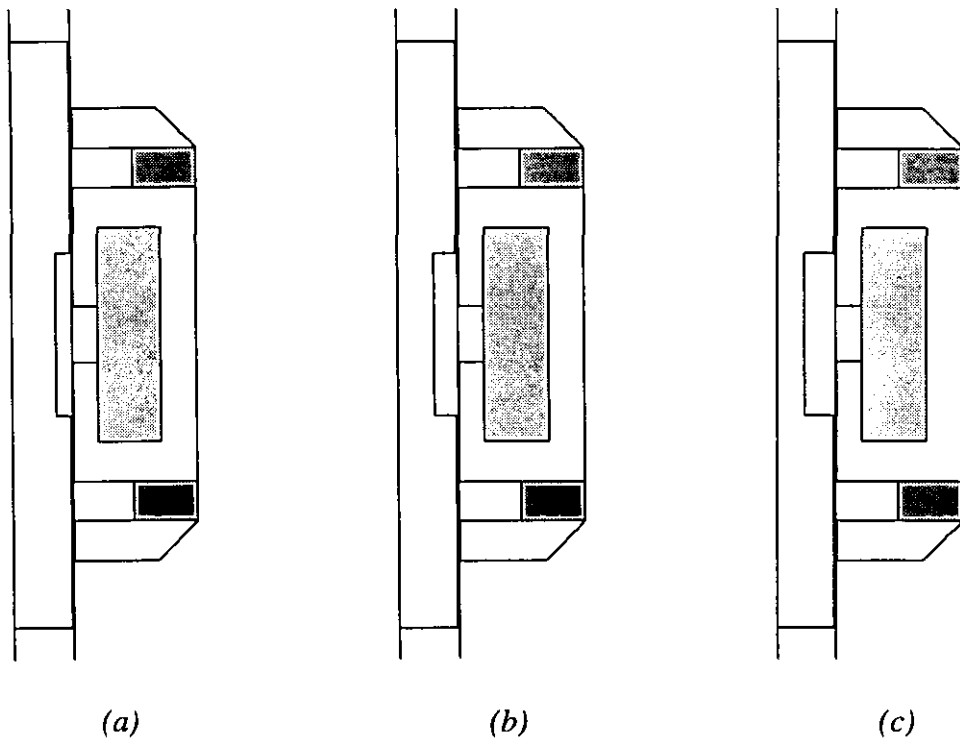


Fig. 7.16 Half cross-sections of (a) the 15 mm diameter armature motor design and (b) armature modification C (c) armature modification D

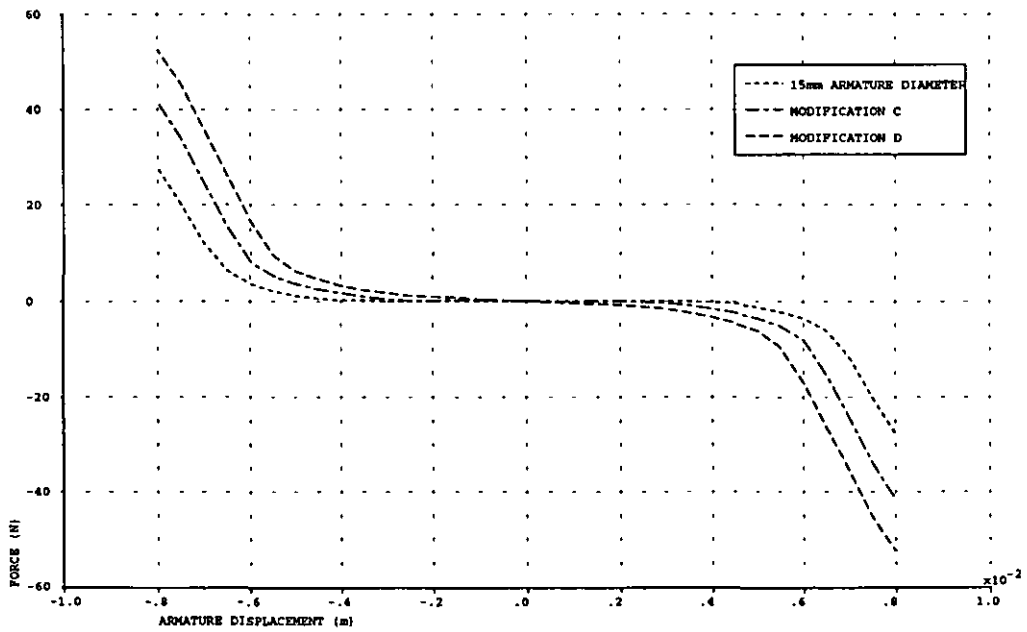


Fig. 7.17 Magnetic stiffness characteristics for the 15 mm diameter armature motor design and the two modified armatures C and D

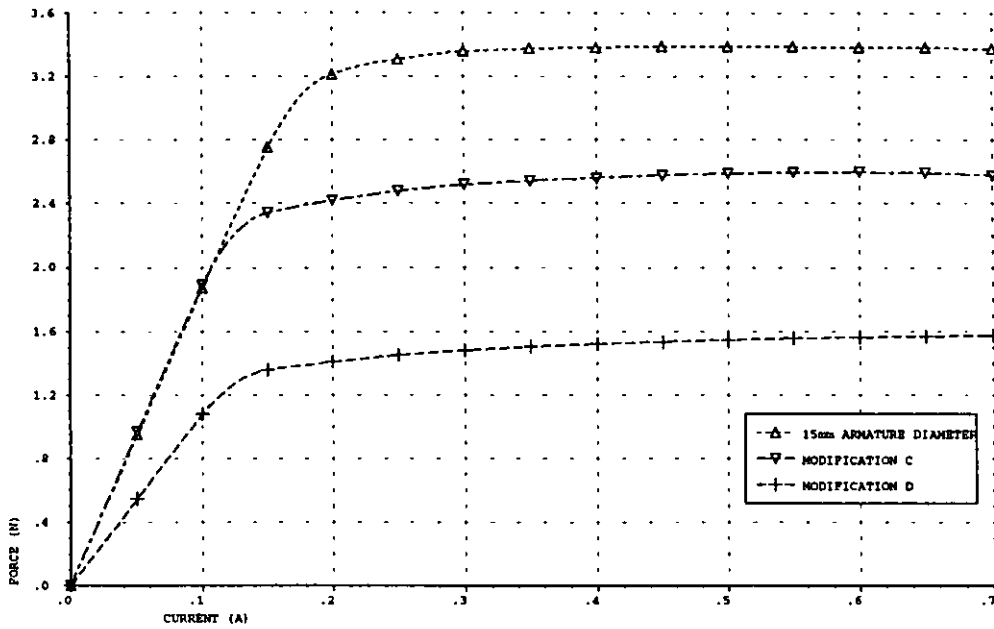


Fig. 7.18 Force/coil current characteristics for the 15 mm diameter armature motor design and the two modified armatures C and D (armature central position)

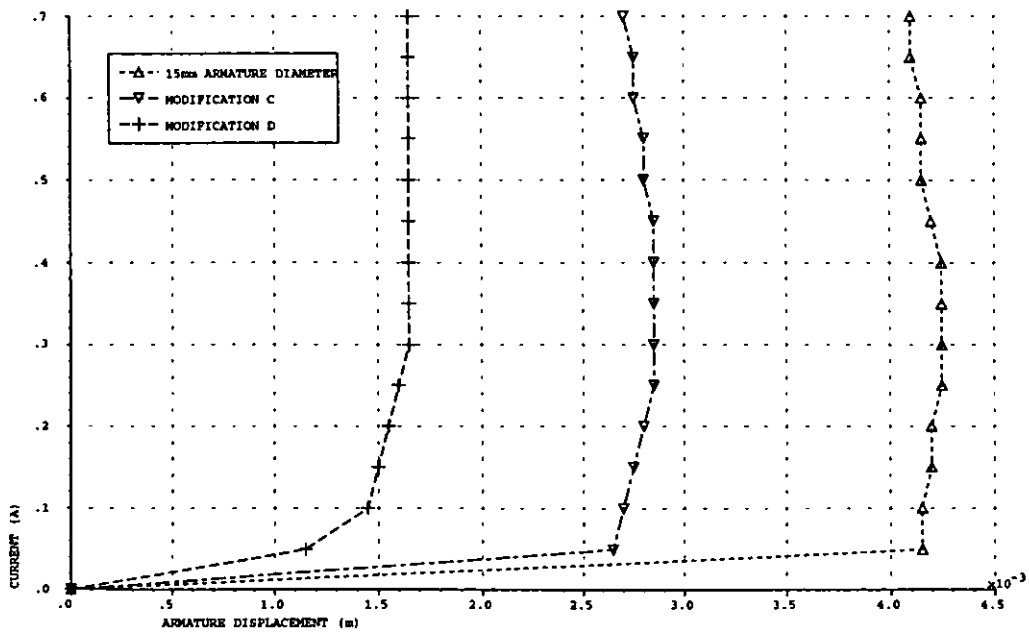
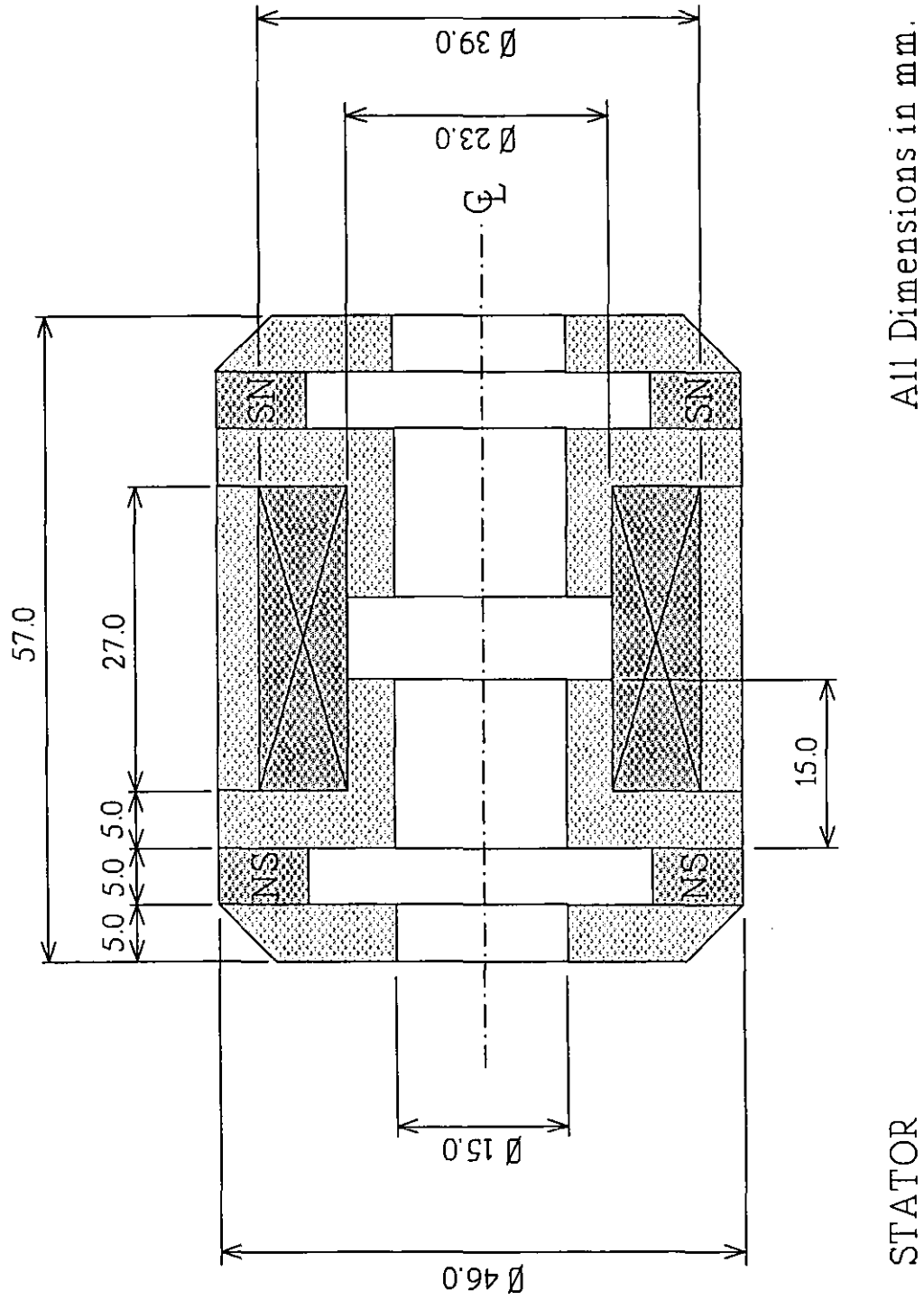
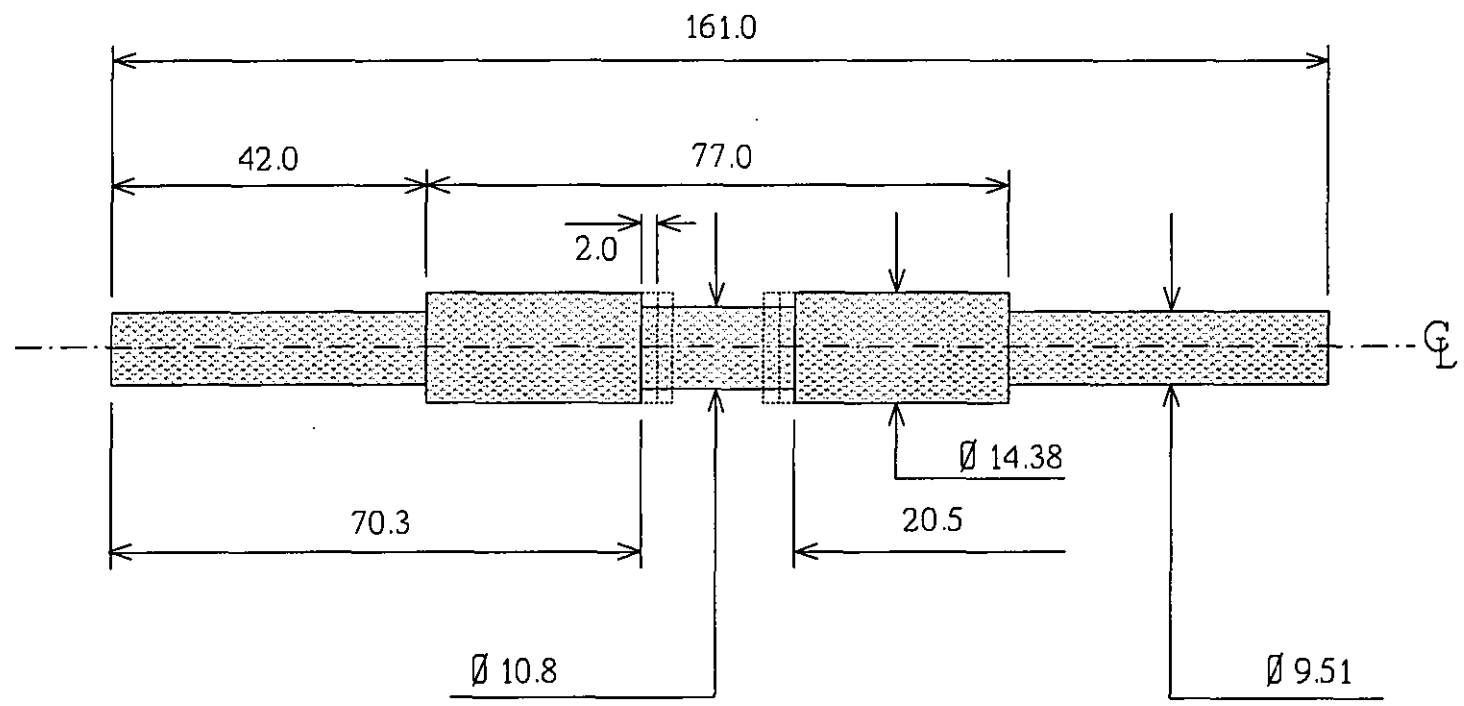


Fig. 7.19 Coil current/armature displacement characteristics for the 15 mm diameter armature motor design and the two modified armatures C and D







ARMATURE

All Dimensions in mm.

Fig. 7.20(b) Main dimensions of the second prototype motor armatures

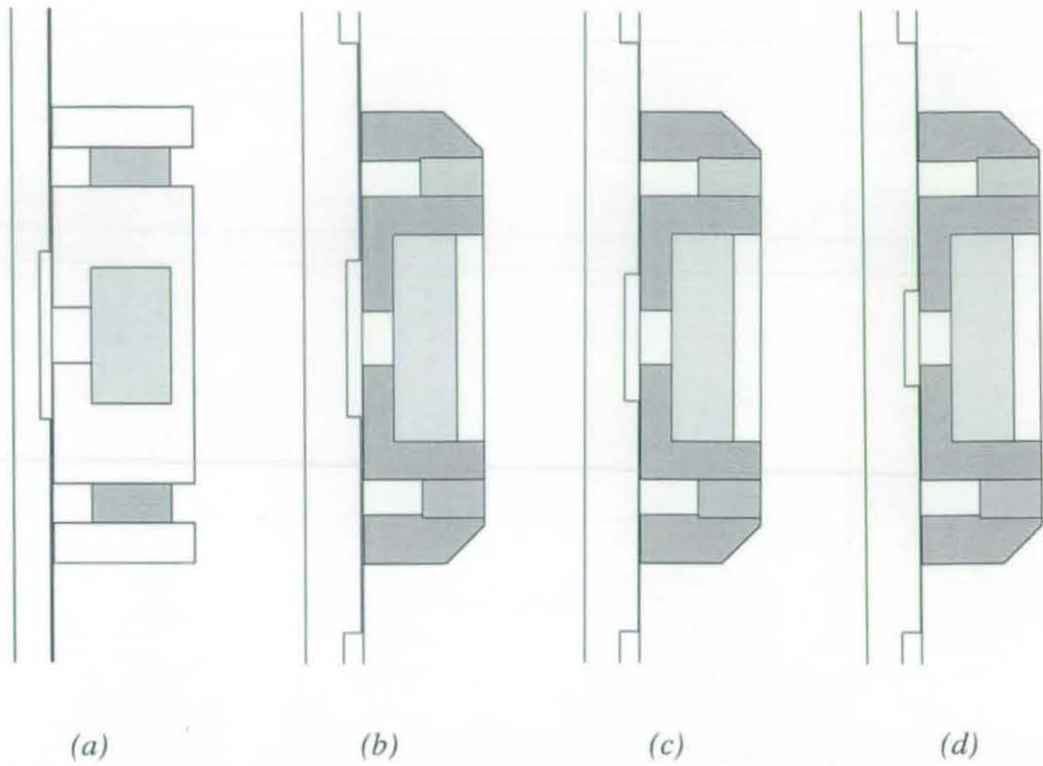


**Fig. 7.21** Half cross-sections of (a) the initial prototype design and the second prototype design with (b) armature A (c) armature B (d) armature C

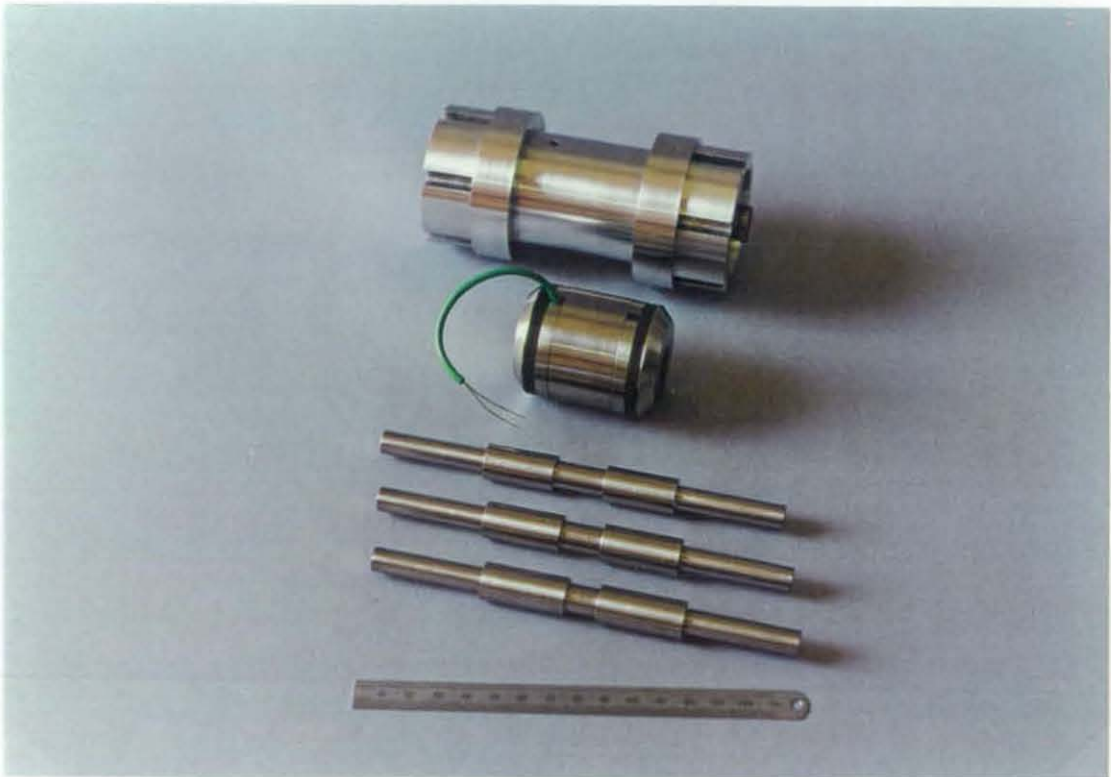


**Fig. 7.22** Second prototype motor (housing, stator and armatures)

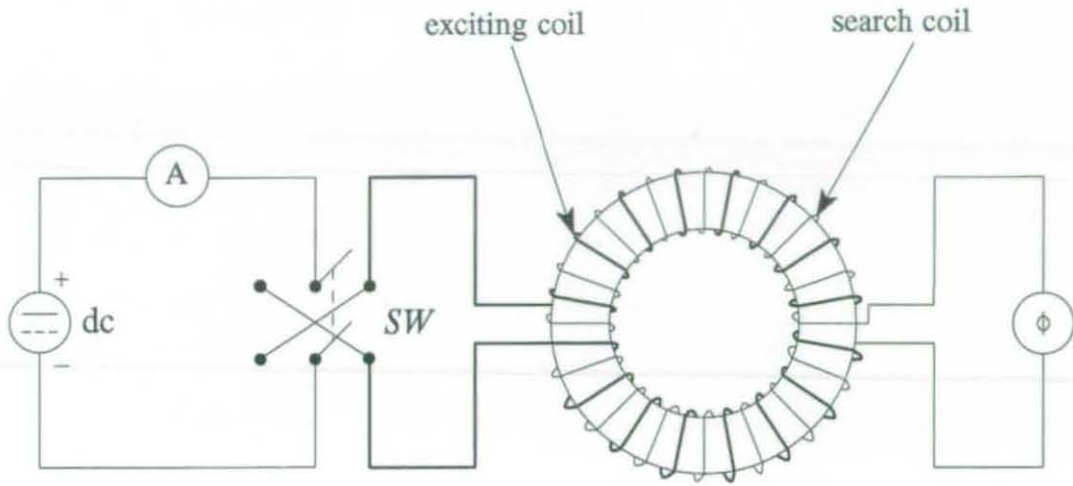


**Fig. 7.23** Determination of the magnetization curve for a steel ring

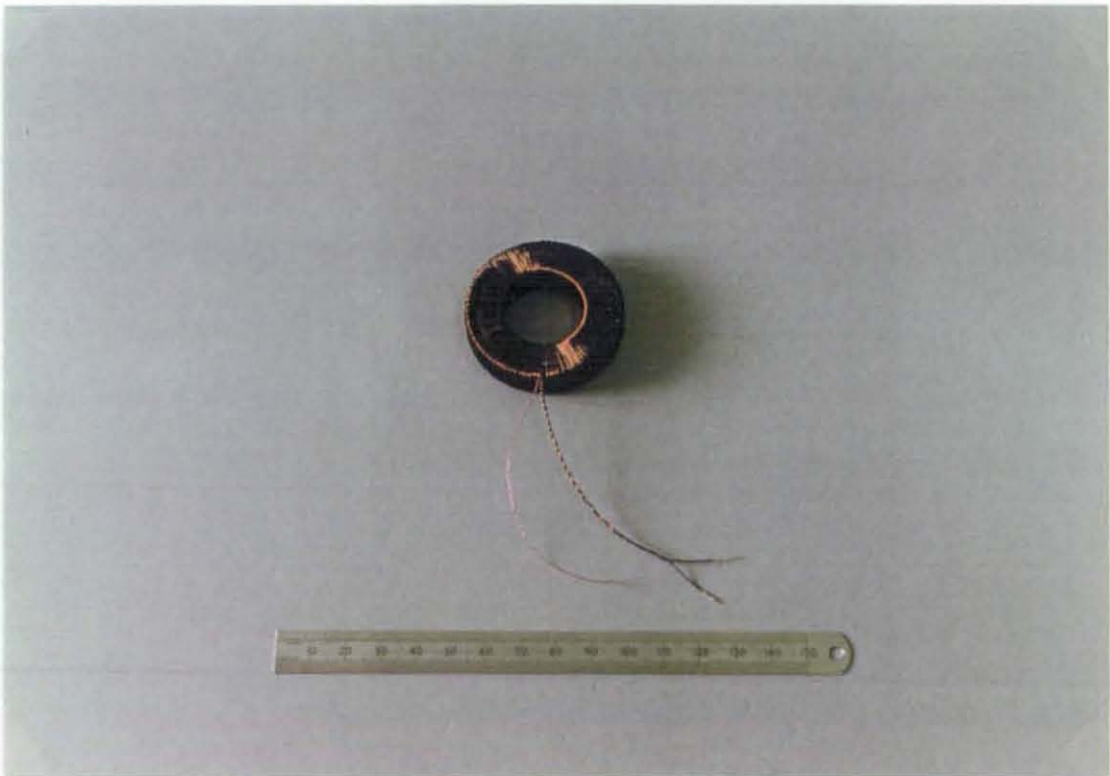


**Fig. 7.24** Radiometal 4550 ring with bi-filar wound exciting coil and search coil

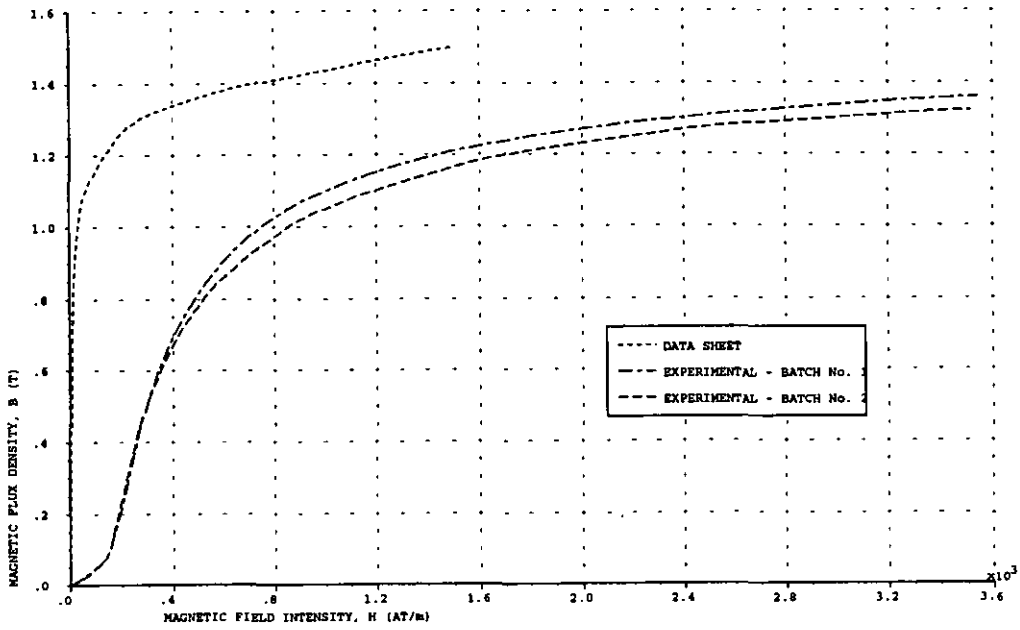


Fig. 7.25 Comparison of magnetization curves of Radiometal 4550

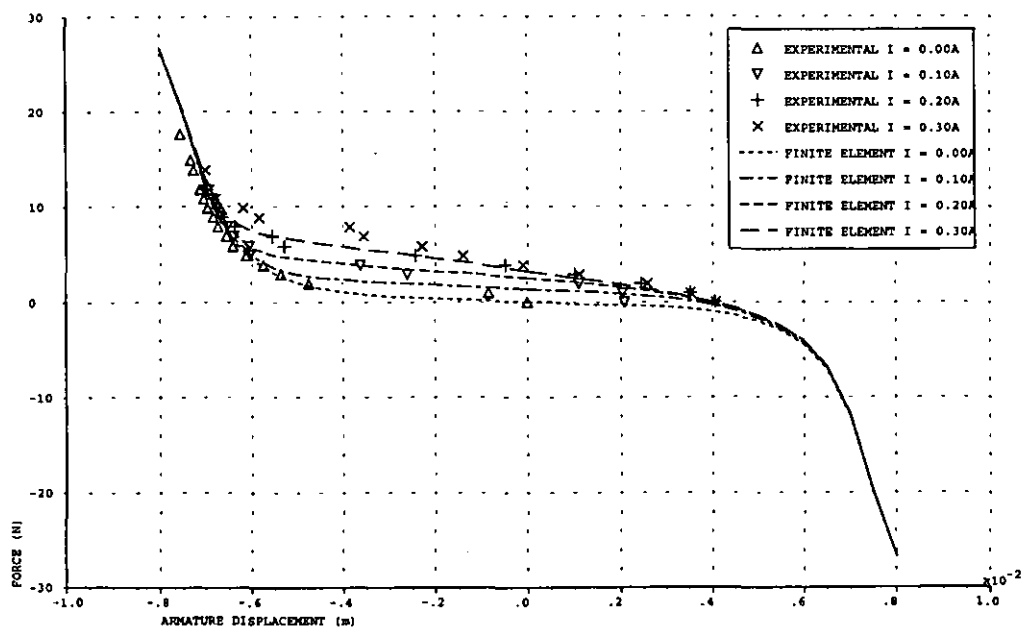
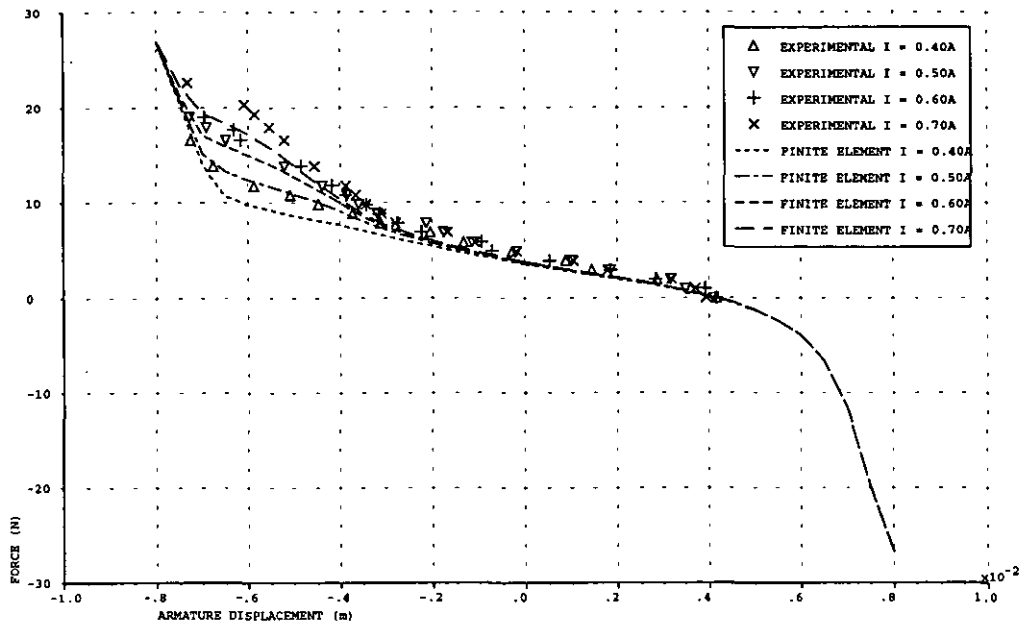
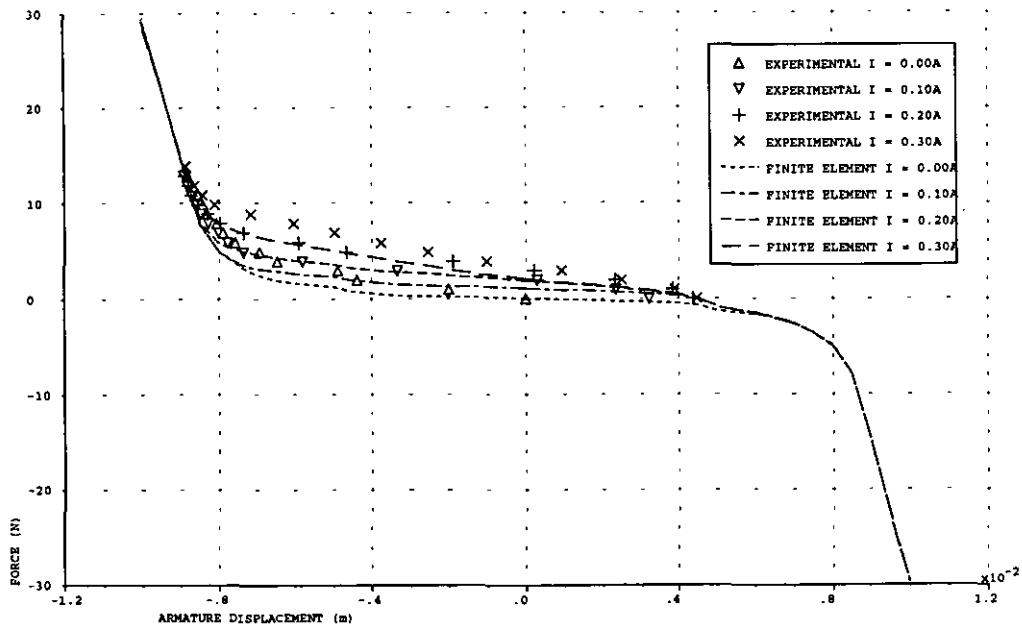


Fig. 7.26(a) Comparison between the experimental and the finite element obtained force characteristic for coil currents from 0 A to 0.3 A for armature A



**Fig. 7.26(b)** Comparison between the experimental and the finite element obtained force characteristic for coil currents from 0.4 A to 0.7 A for armature A



**Fig. 7.27(a)** Comparison between the experimental and the finite element obtained force characteristic for coil currents from 0 A to 0.3 A for armature B

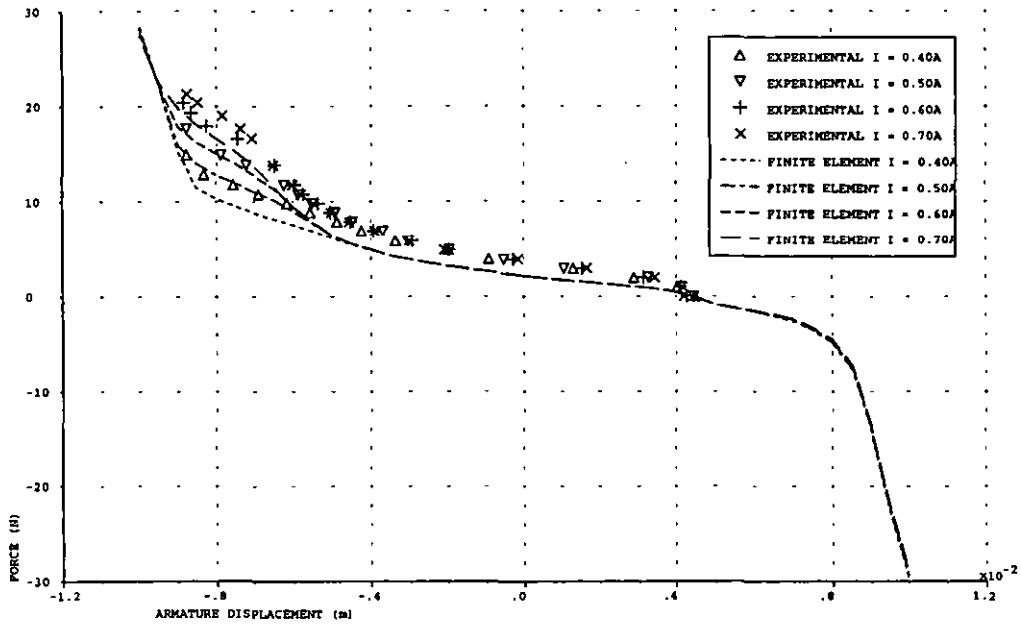


Fig. 7.27(b) Comparison between the experimental and the finite element obtained force characteristic for coil currents from 0.4 A to 0.7 A for armature B

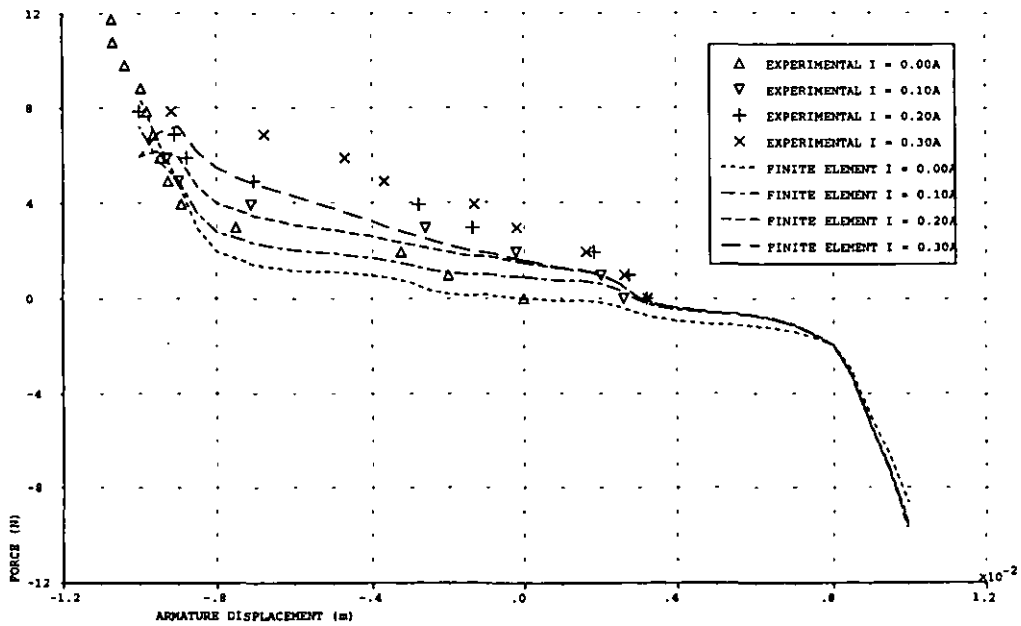


Fig. 7.28(a) Comparison between the experimental and the finite element obtained force characteristic for coil currents from 0 A to 0.3 A for armature C

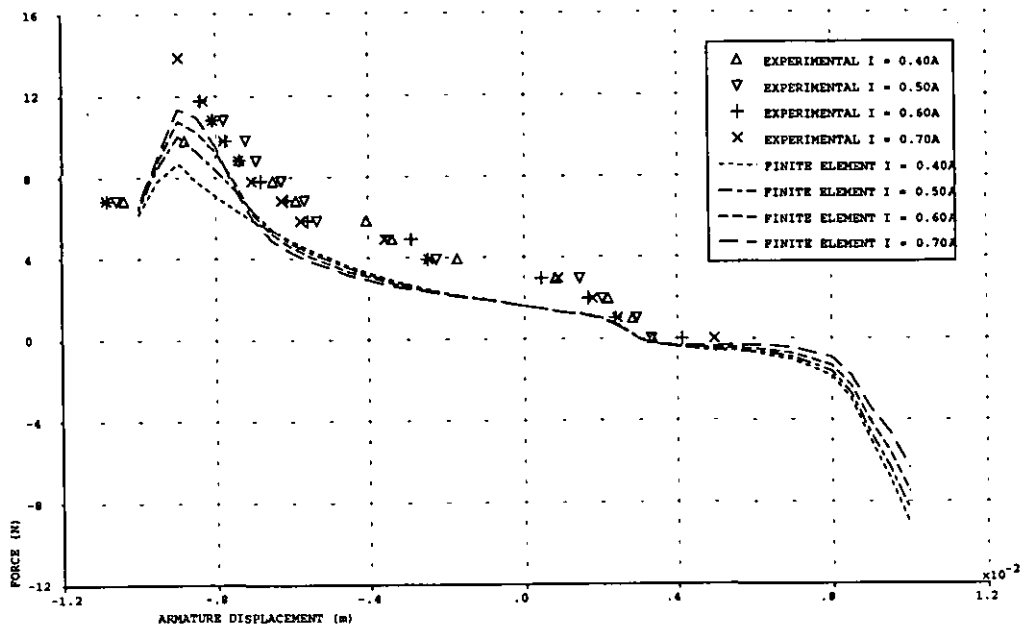


Fig. 7.28(b) Comparison between the experimental and the finite element obtained force characteristic for coil currents from 0.4 A to 0.7 A for armature C

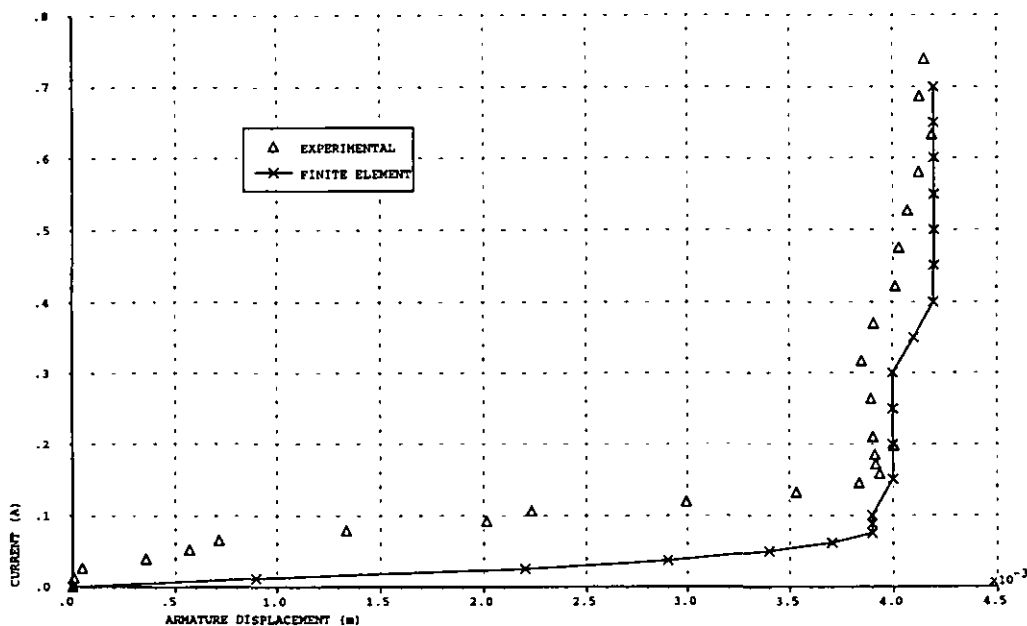


Fig. 7.29 Coil current/armature displacement characteristic for armature A

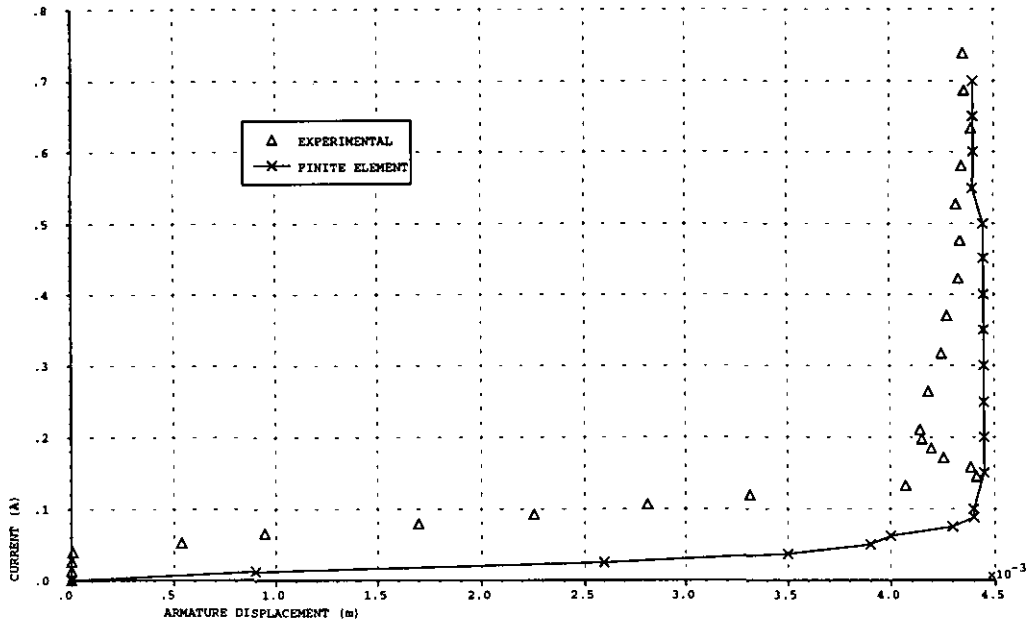


Fig. 7.30 Coil current/armature displacement characteristic for armature B

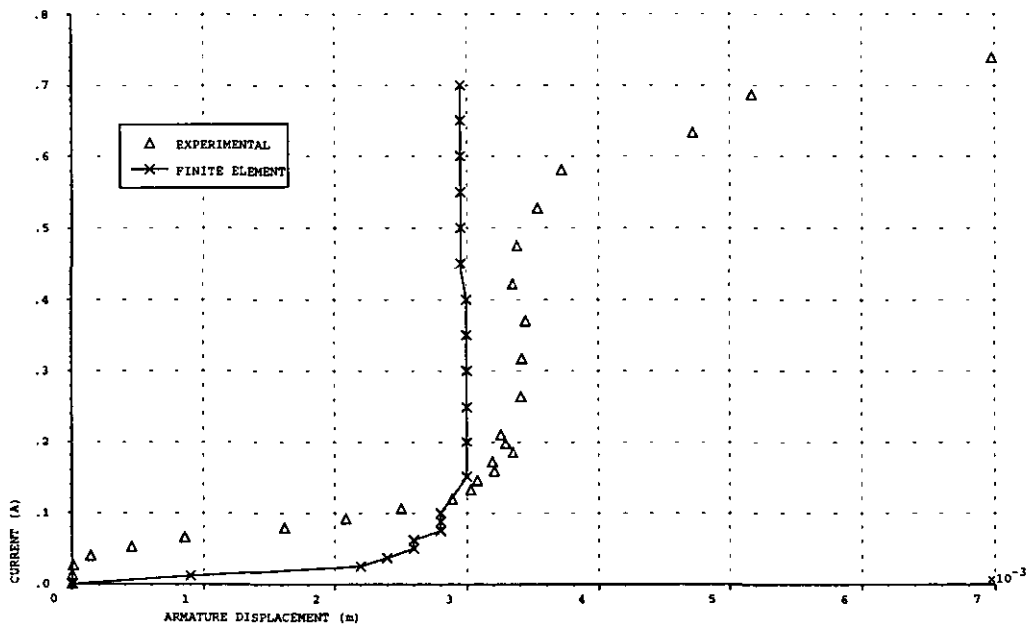


Fig. 7.31 Coil current/armature displacement characteristic for armature C



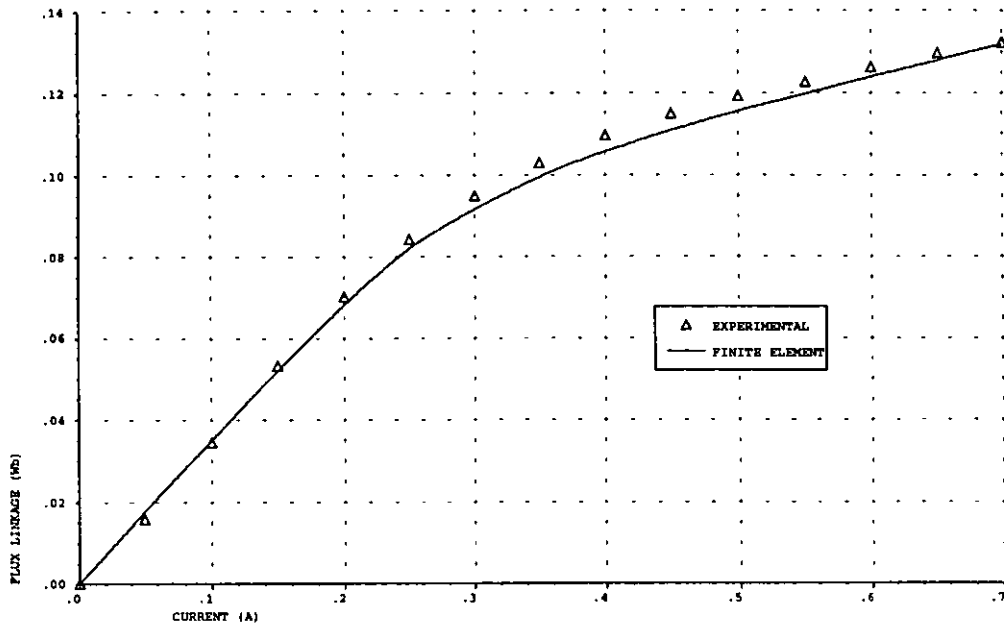


Fig. 7.32 Flux linkage/coil current characteristic for armature A (armature central position)

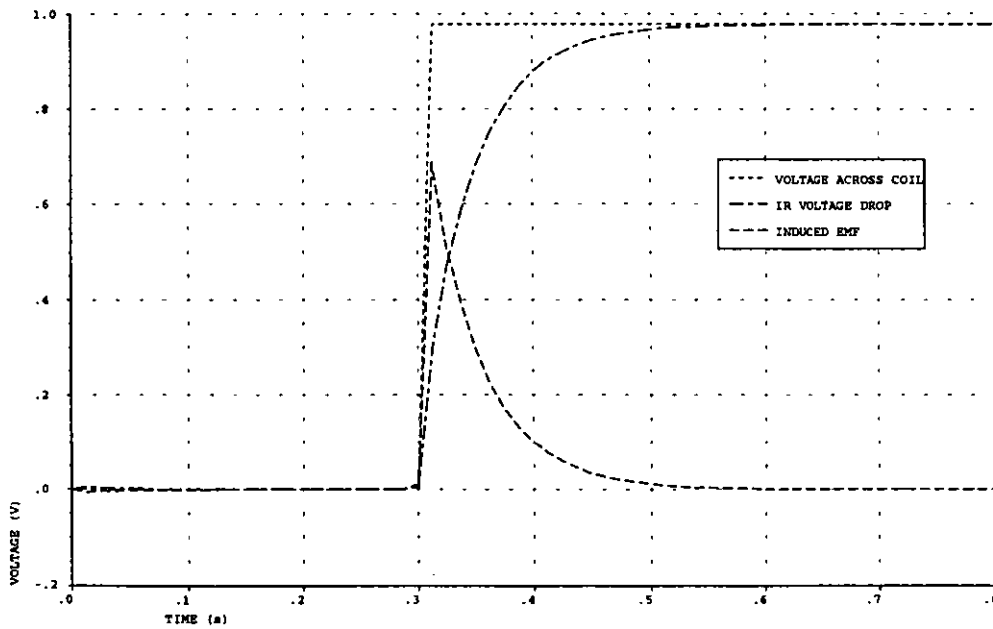


Fig. 7.33 Voltage waveforms produced for a current of 0.1 A (armature central position)

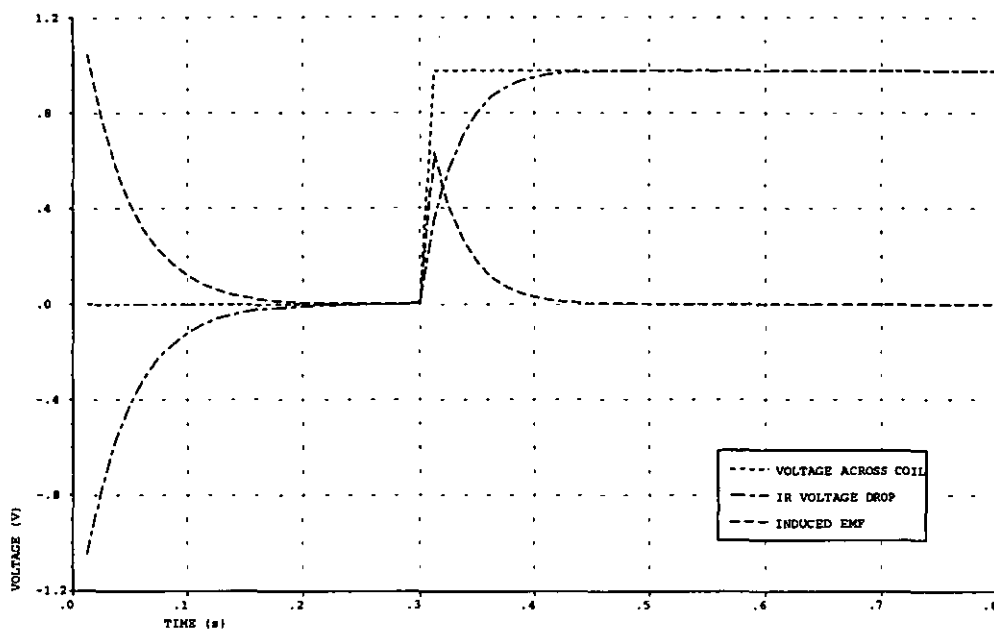


Fig. 7.34 Voltage waveforms produced for a current of 0.1 A (armature displaced by +4.0 mm from the central position)

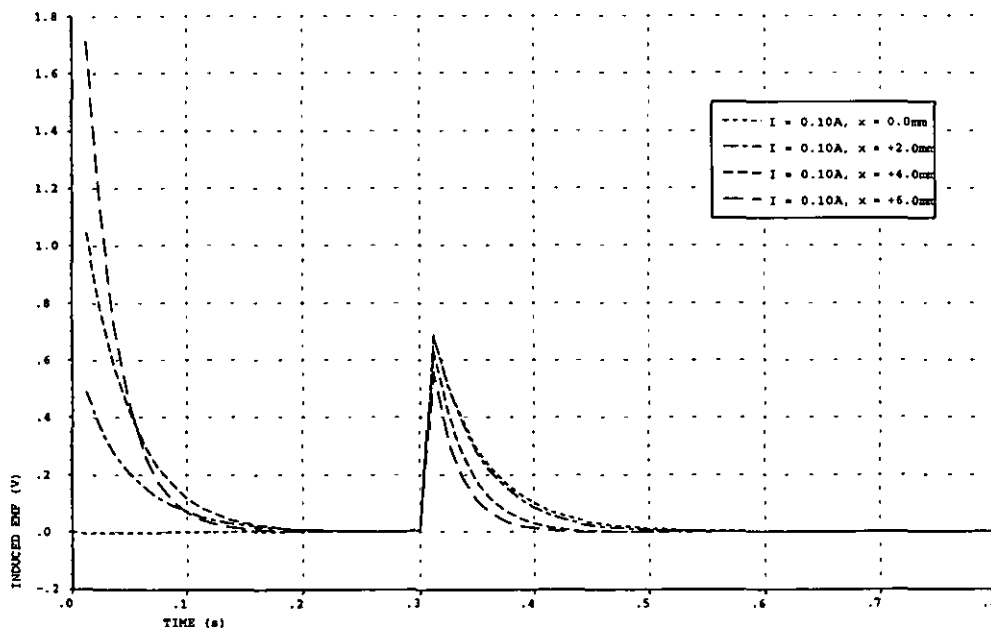


Fig. 7.35 Induced emf for a current of 0.1 A (armature in central position and displaced in a positive sense)

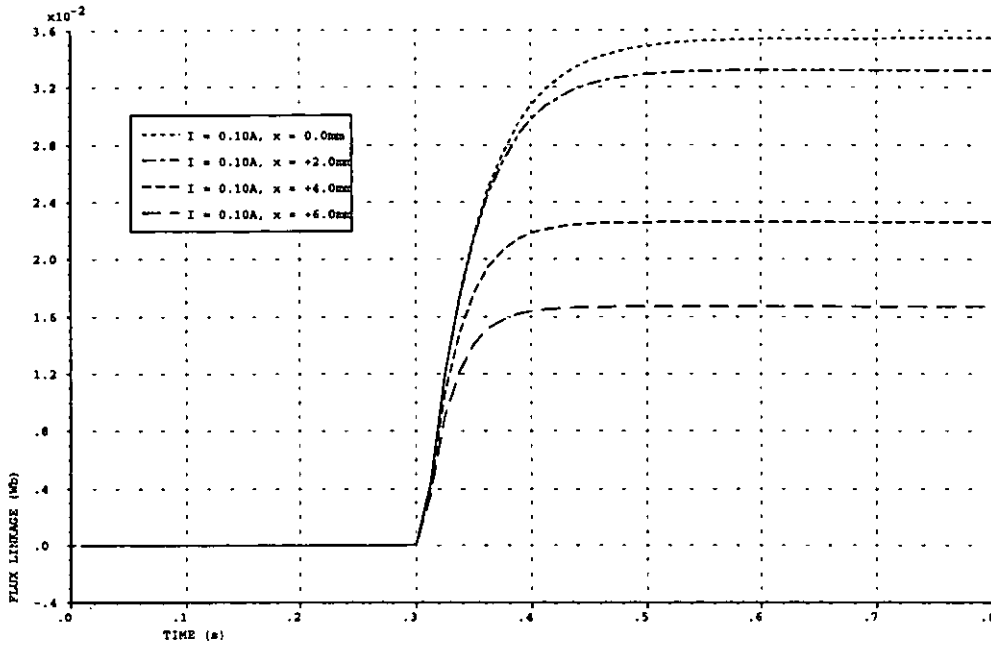


Fig. 7.36 Flux linkage for a current of 0.1 A (armature in central position and displaced in a positive sense)

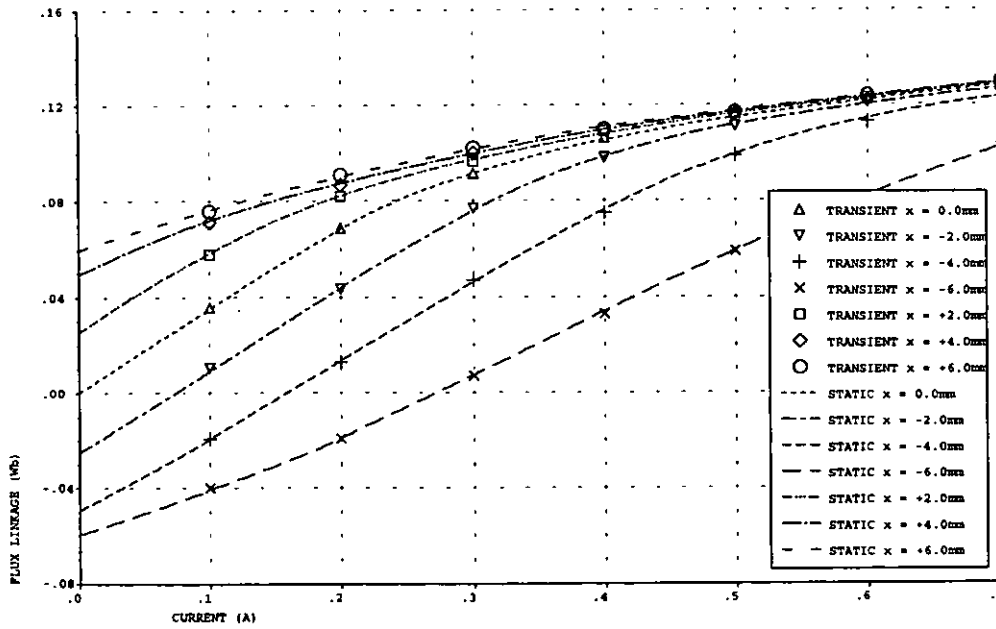
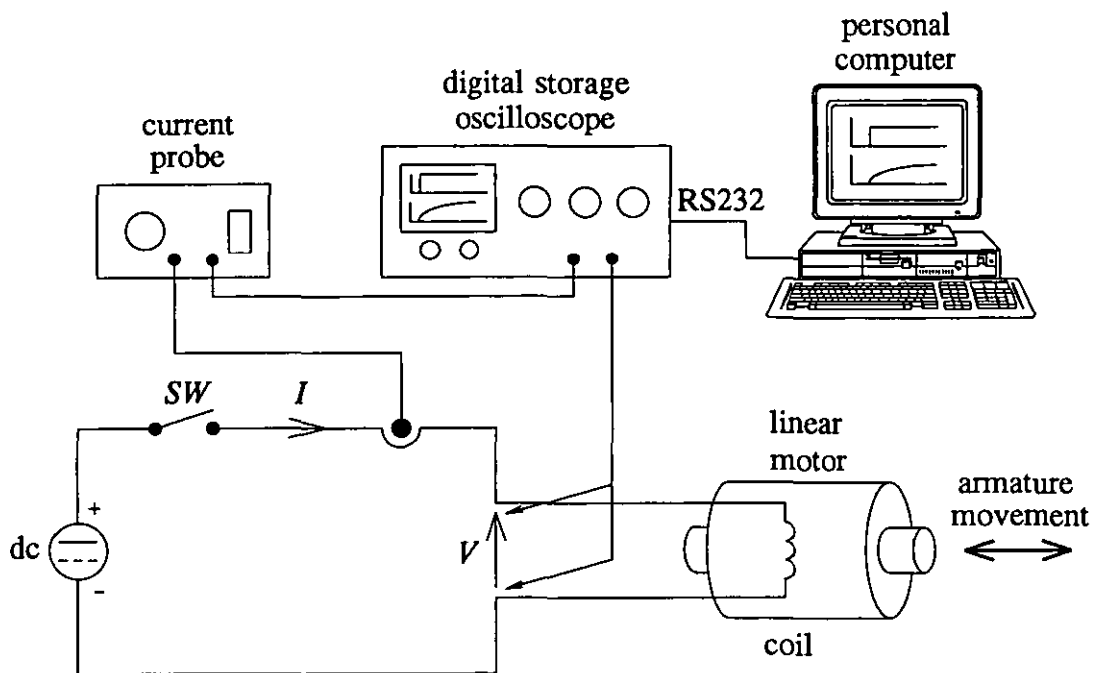
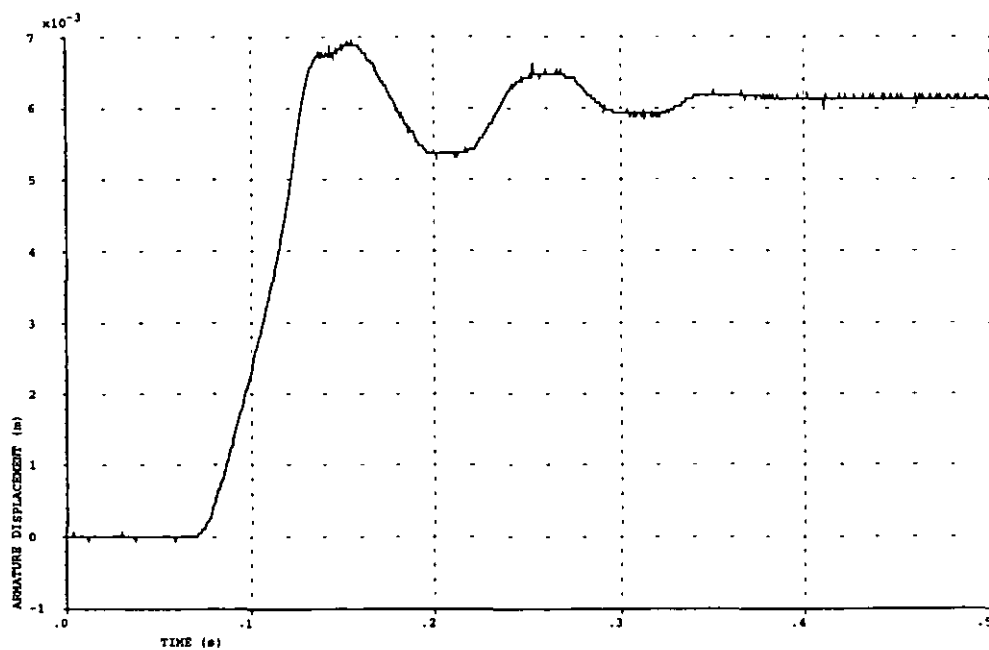


Fig. 7.37 Comparison between the flux linkage characteristics obtained from a transient and static analysis



**Fig. 7.38** Experimental set-up to obtain flux linkage results



**Fig. 7.39** Experimentally obtained armature displacement

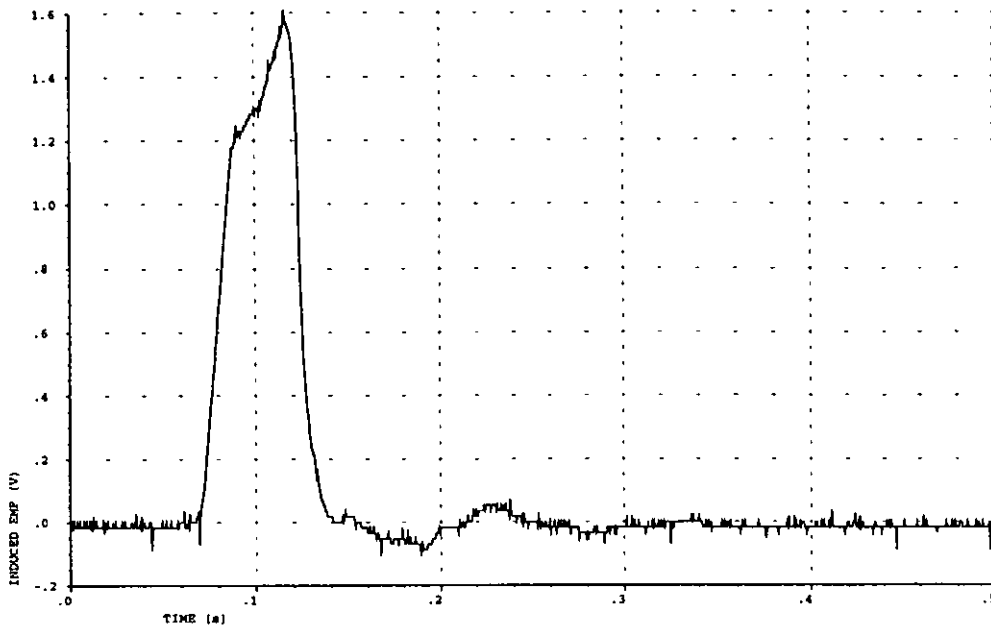


Fig. 7.40 Experimentally obtained motional induced emf waveform

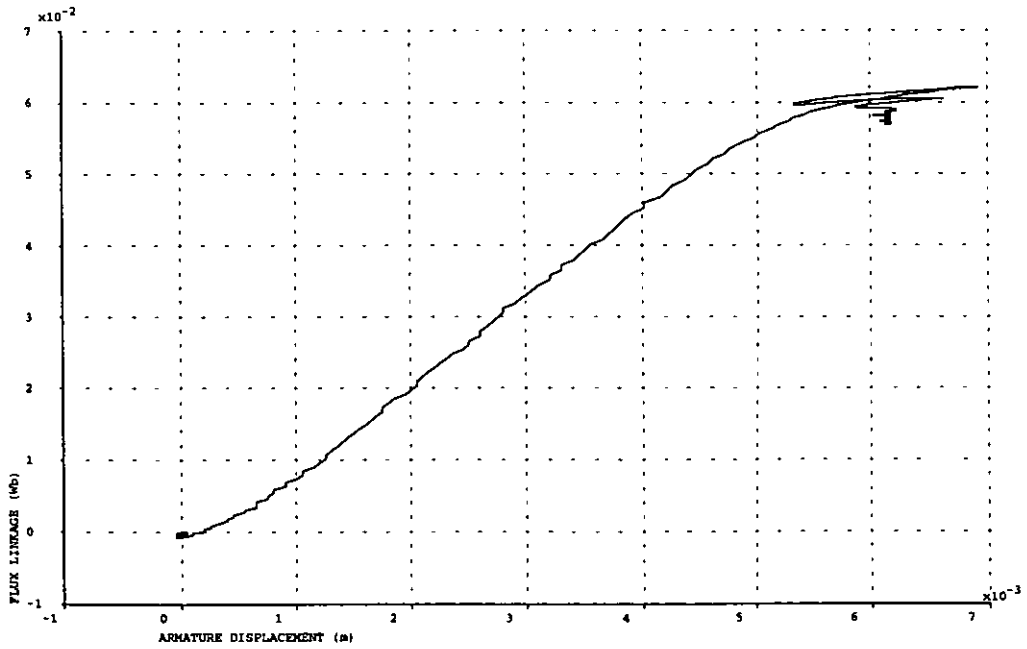


Fig. 7.41 Flux linkage variation with armature displacement derived from experimental results

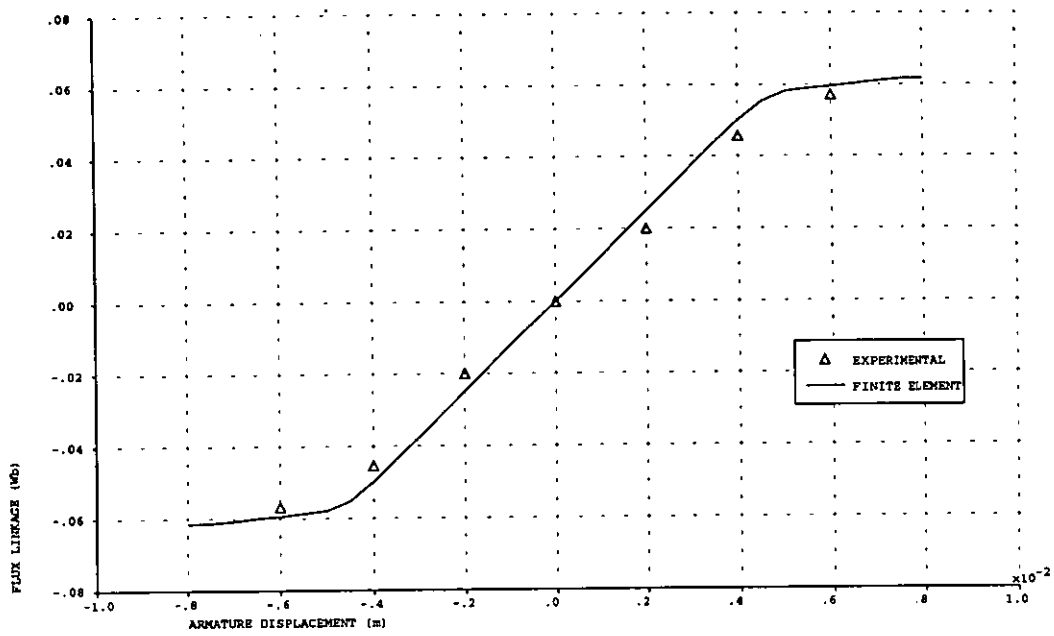


Fig. 7.42 Comparison between experimental and finite element obtained flux linkage characteristic for armature A (armature central position)

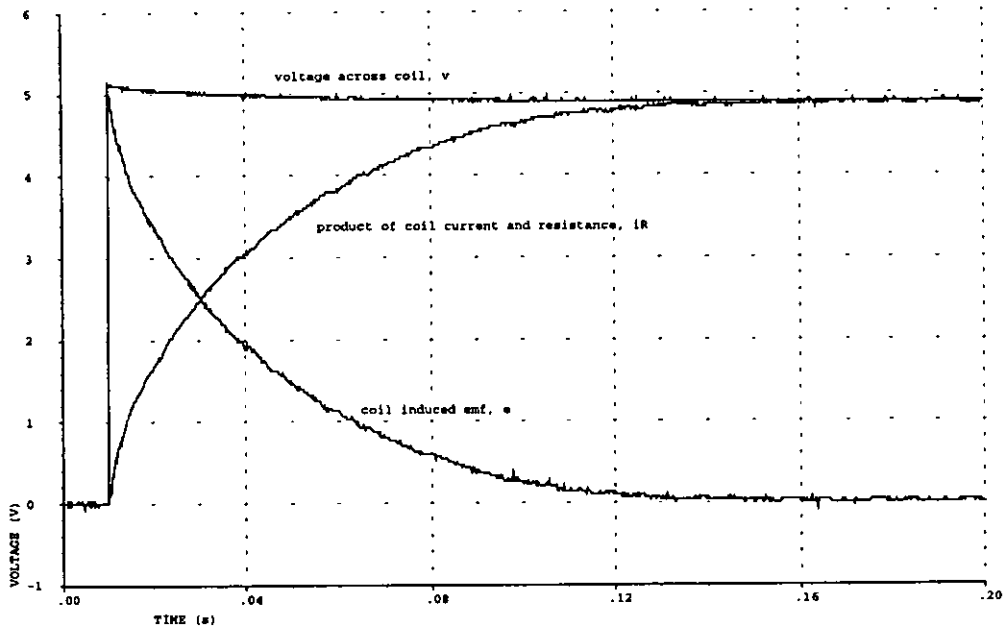


Fig. 7.43 Experimentally obtained voltage waveforms for a current of 0.5 A (armature displaced -4.0 mm from the central position)

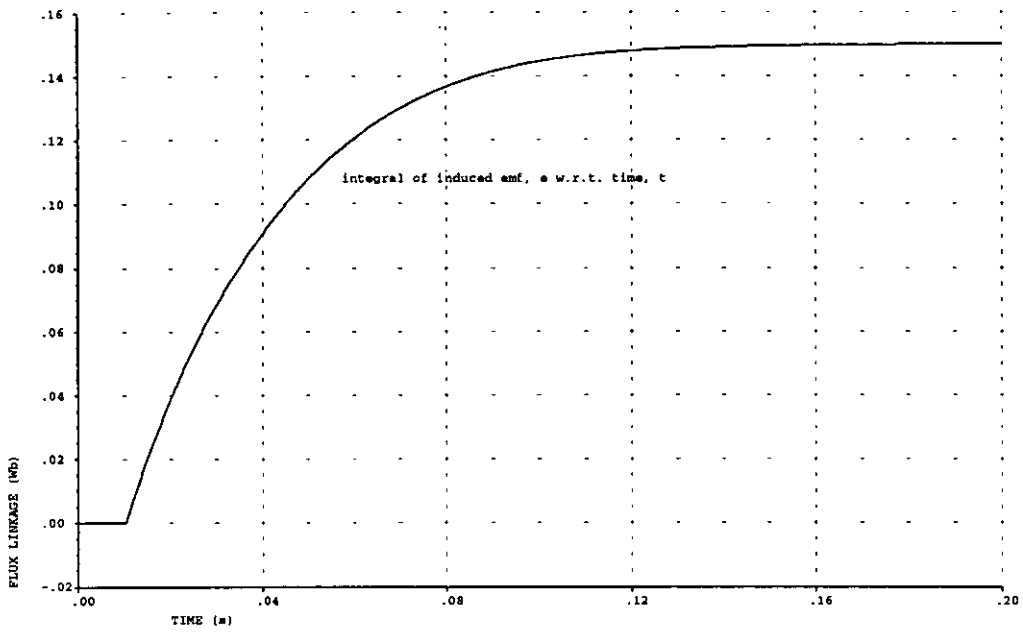


Fig. 7.44 Integral of experimentally obtained induced emf waveform

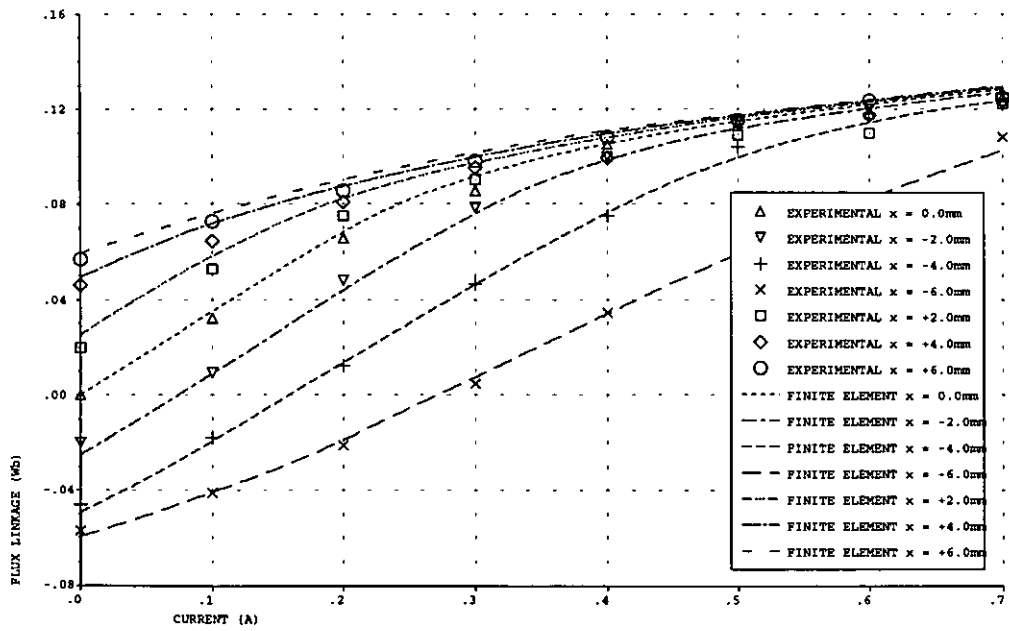


Fig. 7.45 Comparison between experimental and finite element obtained flux linkage characteristics for armature A

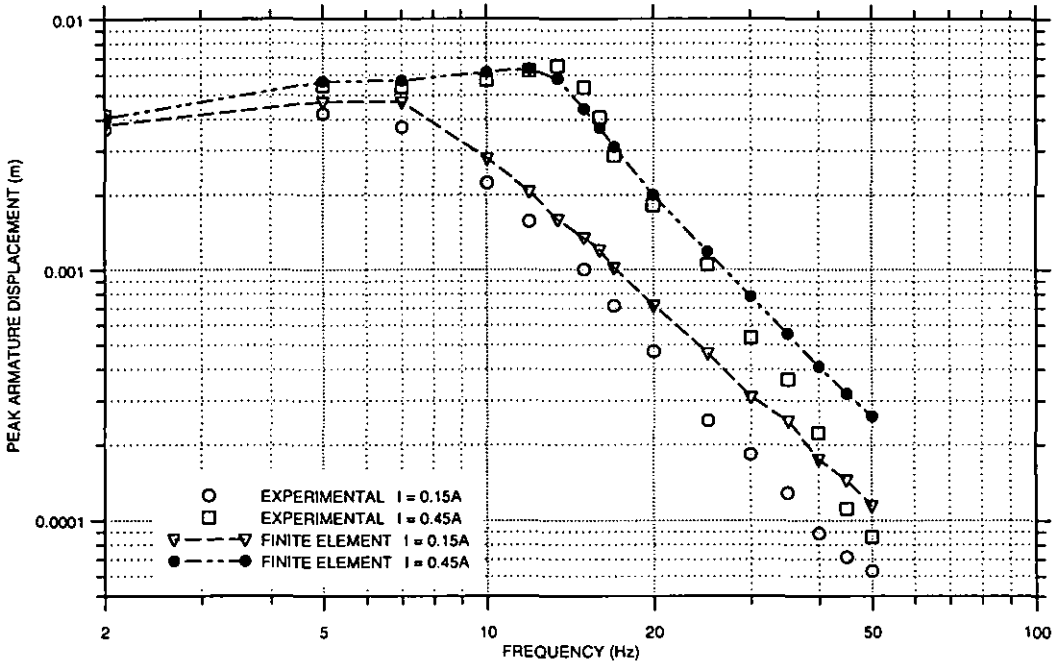


Fig. 7.46(a) Dynamic response characteristics at various peak sinusoidal currents for armature A

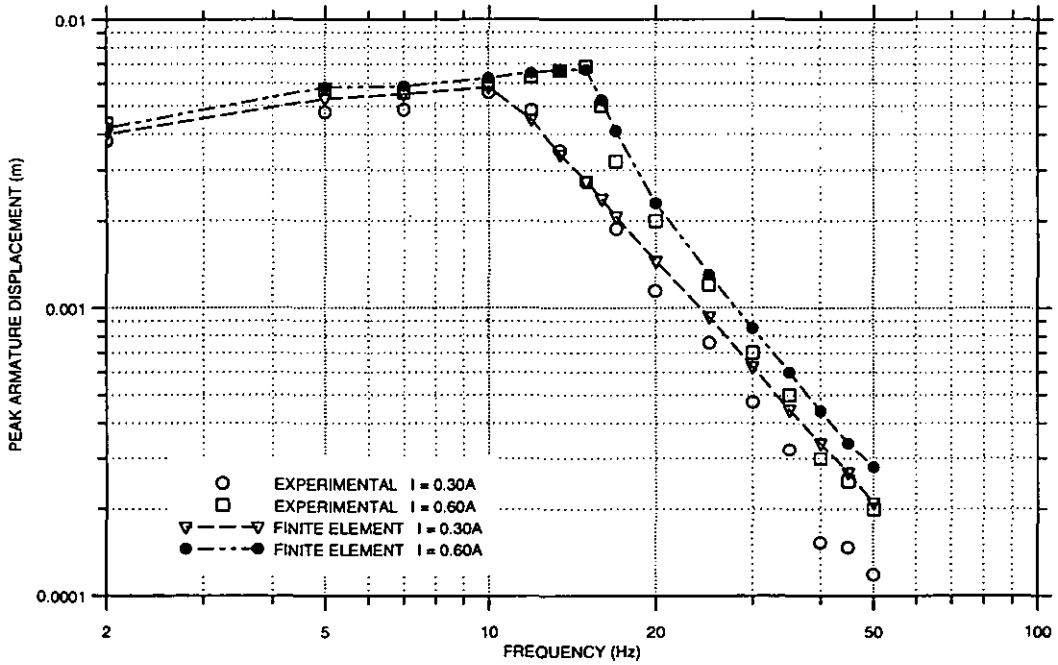
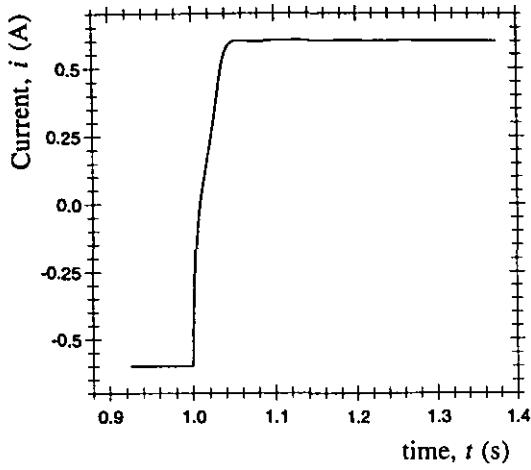
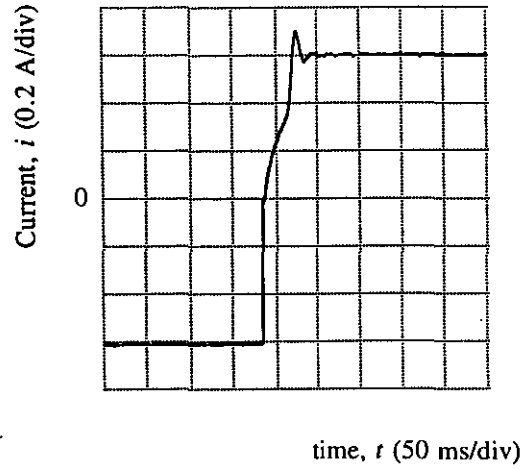


Fig. 7.46(b) Dynamic response characteristics at various peak sinusoidal currents for armature A

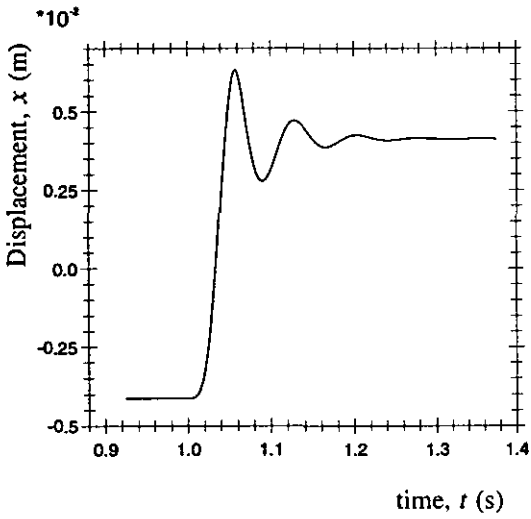




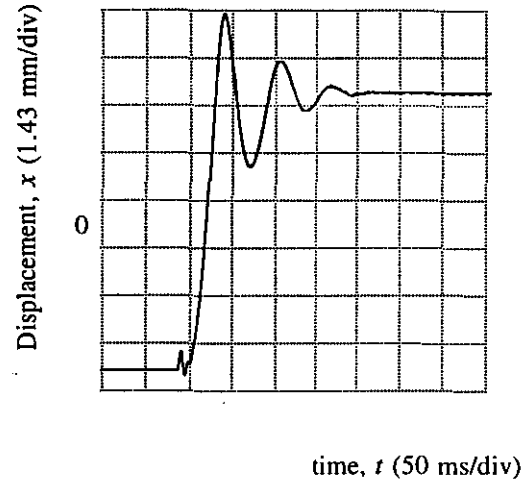
(a) Simulated current response



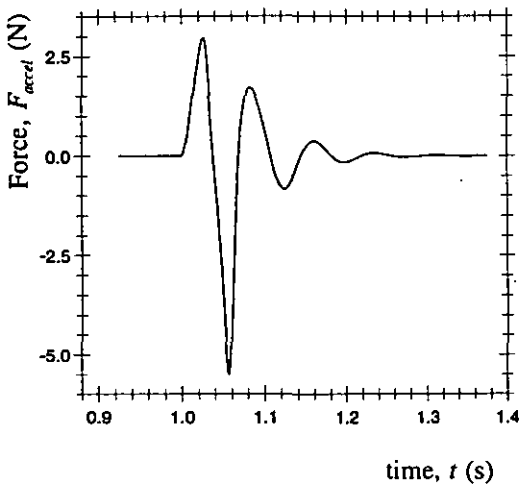
(b) Experimental current response



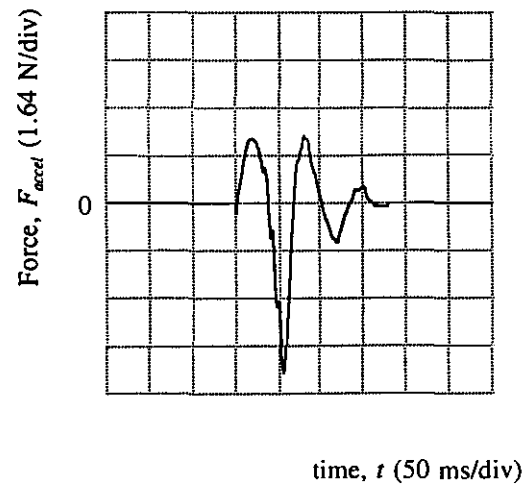
(c) Simulated armature displacement



(d) Experimental armature displacement

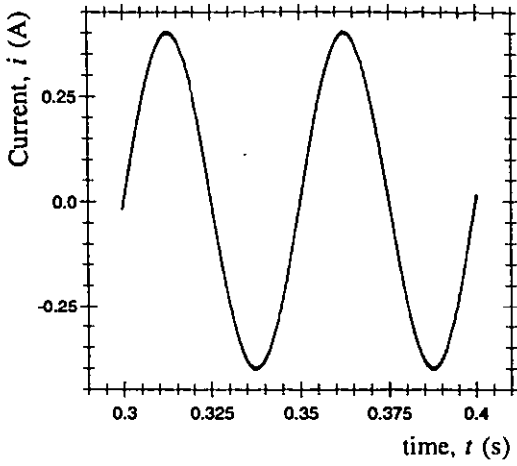


(e) Simulated acceleration force

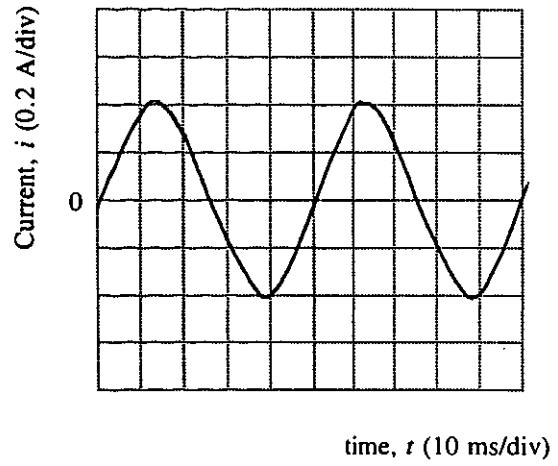


(f) Experimental acceleration force

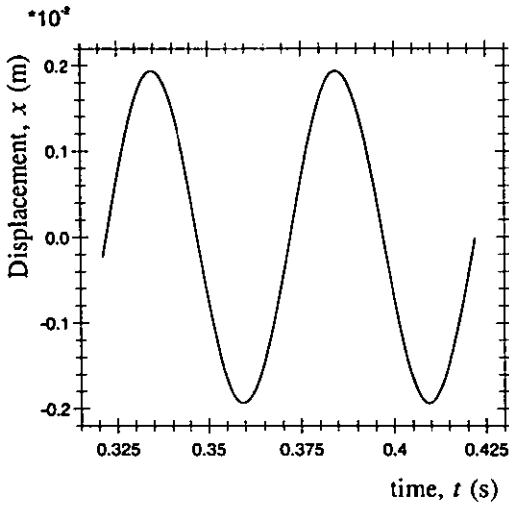
**Fig. 7.47** Simulated and experimental results for a coil voltage reversal of  $\pm 5.87$  V, ( $I = \pm 0.60$  A)



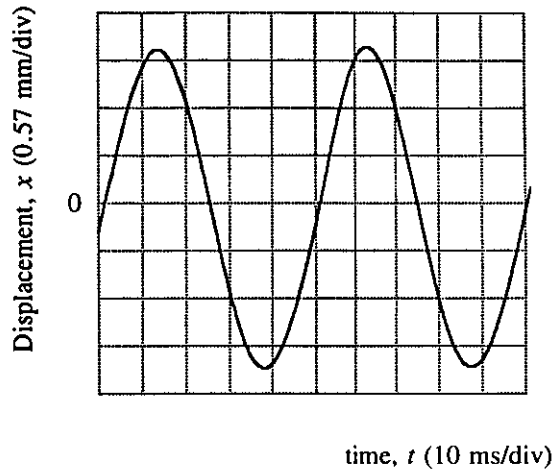
(a) Simulated current waveform



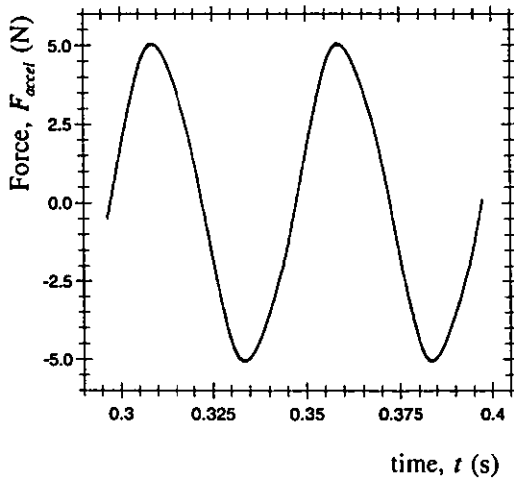
(b) Experimental current waveform



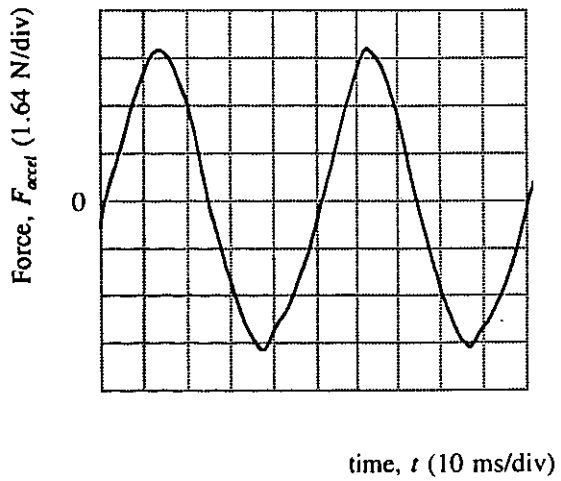
(c) Simulated armature displacement



(d) Experimental armature displacement

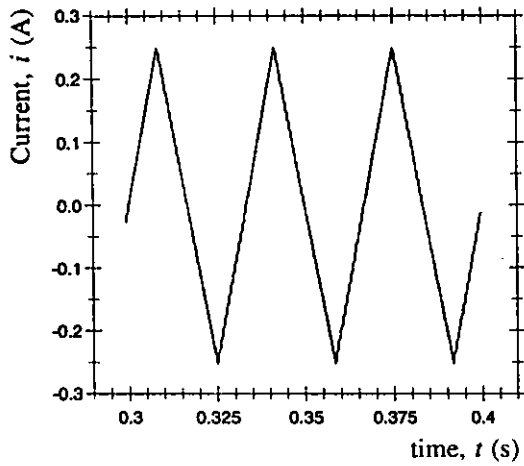


(e) Simulated acceleration force

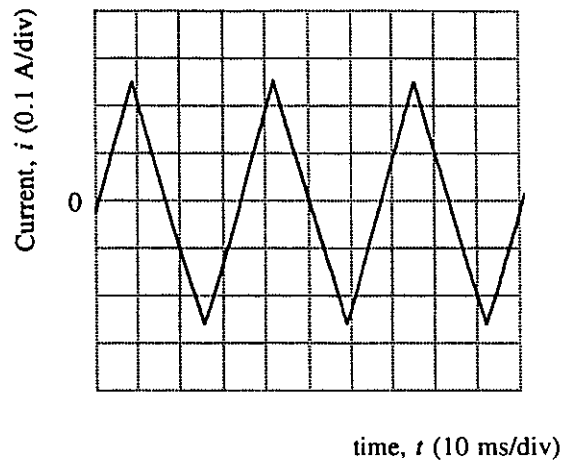


(f) Experimental acceleration force

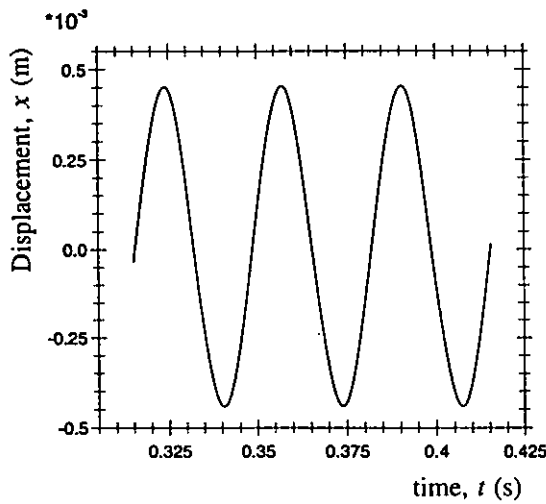
**Fig. 7.48** Simulated and experimental results for a 0.40 A peak sinusoidal 20 Hz coil current



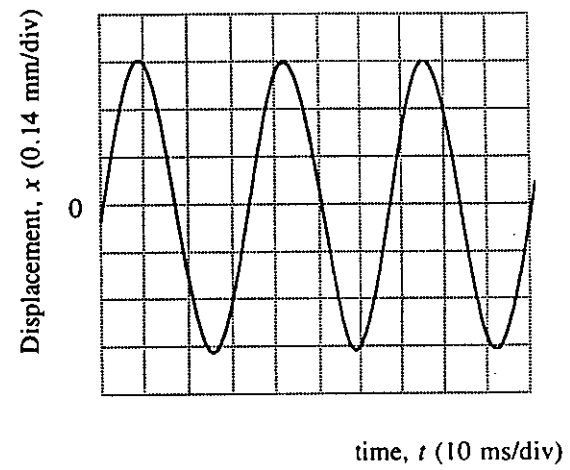
(a) Simulated current waveform



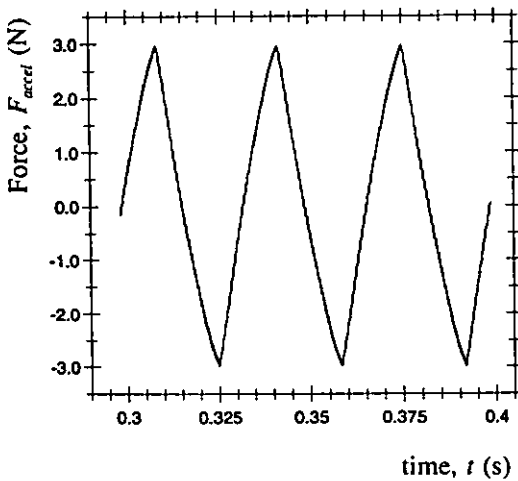
(b) Experimental current waveform



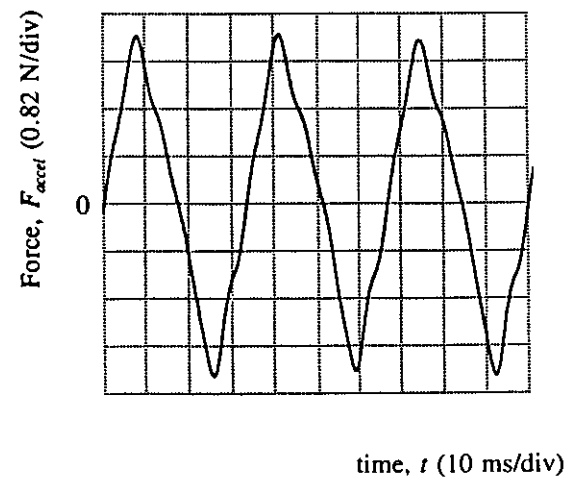
(c) Simulated armature displacement



(d) Experimental armature displacement



(e) Simulated acceleration force



(f) Experimental acceleration force

**Fig. 7.49** Simulated and experimental results for a 0.25 A peak triangular 30 Hz coil current

**RE-FORMATION OF THE LINEAR RELUCTANCE MOTOR II**

This chapter further modifies the magnetic circuit of the motor and considers also the use of alternative magnetic materials. The design employed throughout is that with a 25 mm diameter armature, which has been shown to be superior to the other diameters in terms of stiffness, linearity and peak developed force.

**8.1 FURTHER GEOMETRIC PARAMETER MODIFICATIONS**

A number of modifications to the magnetic circuit are investigated in this section including:

- (i) the possibility of using hollow armatures;
- (ii) the air-gap length;
- (iii) radially magnetized permanent magnets and;
- (iv) the stator yoke pole-shoe length.

The effect of the dimensional changes were investigated at increasing excitation currents up to 0.7 A and over the complete armature stroke length. The following sections describe each geometric parameter change and the influence this has on the performance of the motor.

**8.1.1 Hollow Armatures**

In section 7.1.3 the dynamic response associated with the 25 mm diameter armature design was found to be poor, when compared with the 15 mm diameter design, due to the response being largely influenced by the armature mass. Reducing this mass should improve the frequency response, and also have some effect on the peak force developed and the linearity, due to the decreased cross-section. This idea was investigated by modifying the armature by the introduction of two concentric holes,

to give modification *A* with a 10 mm diameter hole, and modification *B* with a 15 mm diameter hole. The half cross-sections of the two modified armatures are shown in Fig. 8.1, together with the initial arrangement.

The vector equipotential plots of each different arrangement with the coils unexcited and the armatures centred are shown in Fig. 8.2. (Table 7.1 should be consulted for the contour plot information). The armature with a 10 mm diameter hole (modification *A* in Fig. 8.2(a)), leaked three flux contours into the surrounding air, whereas the 15 mm diameter hole armature (modification *B* in Fig. 8.2(b)), leaked four such contours. This is expected since the cross-sectional area of the magnetic circuit has decreased, thereby increasing the flux leakage. Fig. 8.2(b) also shows a small amount of leakage into the hole in the armature, opposite the permanent magnets, suggesting that this region is very heavily saturated. This is clear from Fig. 8.3, which displays the flux density in the motors, where modification *B* is saturated with a flux density of 1.68 T. The modulus of the flux density in the air-gap of the two modified armatures is compared with that of the solid armature in Fig. 8.4, and the flux density is seen to drop with increasing hole diameter. Although, this would decrease the force developed on the armature and degrade the stiffness characteristic, which is undesirable, an improvement should be evident in the dynamic response of the two modified armatures.

Table 8.1 shows the operating points of the magnets and the equal and opposite centralising forces of each model, including the solid armature, with the coils unexcited and the armatures at their central positions. It is expected that both the magnet operating points and centralising forces will decrease with increasing armature hole diameter.

The stiffness characteristics of the motor are shown in Fig. 8.5, and the degradation of the stiffness with increasing hole diameter is clearly seen, although modification *A* is still acceptable. The force characteristics are shown in Figs. 8.6 and 8.7. Modification *A* appears to have lost its linearity, with the force curves not being equi-spaced and parallel, and modification *B* has an unacceptable characteristic which is

Armature Hole Diameter (mm)	Operating Point of Permanent Magnets (T)	Centralising Force (N)
0.00	0.92	$\pm 6.98$
10.0	0.88	$\pm 5.52$
15.0	0.82	$\pm 3.43$

**Table 8.1** Magnet operating points and armature centralising forces

similar in appearance to the 15 mm solid armature design. The force/coil current characteristics when the armature is centralised are shown in Fig. 8.8, where modification *A* develops a larger force per unit of current than does the solid armature design but is seen to be non-linear. Modification *B* saturates at about 0.3 A and is inferior to the other two designs. The worsening linearity with increasing hole diameter is clearly seen in the coil current/armature displacement characteristics of Fig. 8.9, where modification *B* simply acts as a bistable actuator.

An improvement to the dynamic response when using the two modified armatures was expected. The armature masses and viscous damping coefficients, calculated as described in section 6.2.3, are tabulated below in Table 8.2, together with the data from the solid armature.

The dynamic response characteristics given in Fig. 8.10, show that the response of the lightest armature is the most acceptable, with an armature displacement of  $\pm 7.5$  mm at 25 Hz, although, this design is unsuitable due to its poor linearity and stiffness. Modification *A* has a much improved response over the solid armature but an inferior linearity and stiffness. Introducing holes into the armature improves the dynamic characteristics but degrades the linearity and stiffness, and any final design will be a compromise between the three criteria.

Armature Hole Diameter (mm)	Armature Mass (g)	Damping Coefficient (Ns <sup>2</sup> /m)	Motor Mass (g)
0.00	261.96	12.13	640
10.0	214.32	9.922	592
15.0	154.76	7.164	533

**Table 8.2** *Mechanical parameters for each armature arrangement*

To exploit the good dynamic response of armature *B* and produce an acceptable fast bistable motor design, the stiffness must be improved. This was achieved by reducing the centre-section diameter, as discussed in section 7.1.5, and the half cross-section with the radius reduced to 9.40 mm is compared in Fig. 8.11 with the initial centre-section arrangement. Fig. 8.12 compares the improved stiffness characteristic that results, with the equal and opposite centralising forces increased to  $\pm 4.03$  N, with the characteristics of armature *B* and the initial solid armature. Figs. 8.13 and 8.14 show the force/coil current characteristics when the armature is centralised and the coil current/armature displacement characteristics of the various designs now being considered. As expected, both the saturation force and the maximum armature displacement have decreased with the reduced centre-section diameter.

Figs. 8.15(a) and 8.15(b) show an armature with a further reduced centre-section diameter, which produces an adverse affect, with the stiffness or returning force dropping even more, and actually reversing in direction, as seen in Fig 8.16. If the motor of Fig. 8.15(a) is unexcited, the armature has three stable positions; the central position and  $\pm 4.0$  mm from this position. Fig. 8.15(b) would produce similar results, with stable positions at the centre and displacements of  $\pm 5.2$  mm. The extra material added to the armatures at the centre-section, in Figs. 8.15(a) and 8.15(b), was to reduce the saturation in this region. The results of these modifications illustrate the highly undesirable effects that occur if the centre-section air-gap becomes too large.

This section has shown that although introducing holes into the armature improves the dynamic response of the motor, it degrades both the stiffness and the linearity. Reducing the centre-section diameter can improve the stiffness but will also reduce the maximum armature displacement. Too much reduction will of course have a detrimental affect on the stiffness characteristic.

### 8.1.2 Comparison of Hollow and Solid Armatures

In Fig. 8.17, the dynamic response of the 20 mm diameter solid armature is compared with that of the 25 mm diameter hollow armature (10 mm hole diameter). The near identical responses suggest that the velocity and acceleration of both armatures are nearly identical. If they are assumed to be equal, rearranging equation (6.4) gives:

$$F_{accel} = Ma = F_{coil} - k_d v - F_{mag} \quad (8.1)$$

where  $F_{accel}$  is the acceleration force. From equation (8.1):

$$a = \frac{F_{accel}}{M} \quad (8.2)$$

and for the 20 mm diameter solid armature:

$$a_{20} = \frac{F_{20}}{0.162} \quad (8.3)$$

and for the 25 mm diameter hollow armature:

$$a_{25} = \frac{F_{25}}{0.214} \quad (8.4)$$

where  $a_{20}$  and  $a_{25}$  are the acceleration of the 20 mm and 25 mm diameter armatures respectively and,  $F_{20}$  and  $F_{25}$  are the acceleration forces. Equating equations (8.3) and (8.4) gives:

$$F_{25} = \frac{0.214}{0.162} F_{20} \approx 1.32 F_{20} \quad (8.5)$$

The result from equation (8.5) is a ratio of the two armature masses, and shows that the force developed by the 25 mm diameter hollow armature is about 32 % larger than



that of the 20 mm diameter armature. This larger force is shown in the comparison of the force envelopes at 0 A and 0.6 A for the two armature designs in Fig. 8.18. The comparison between coil current/armature displacement characteristics are shown in Fig. 8.19, and the similarities are clear.

### 8.1.3 Air-gap Length

An important geometric parameter that has not so far been investigated is the air-gap length, which has remained fixed at approximately 0.31 mm. Various air-gap lengths were therefore considered, by refining the mesh near the pole-tips and by simply changing the material properties of the refined elements to either iron or air. Fig. 8.20 compares the effects of three different lengths: 0.15 mm, 0.31 mm and 0.46 mm. The shortest of these develops the largest peak force of about 52.5 N and provides an improved stiffness, but the force developed is reduced from  $-1.0$  mm to  $+5.0$  mm. The longest air-gap produces the greatest force at the central position but the stiffness suffers slightly, and so the best compromise is to continue using the 0.31 mm air-gap length. Manufacturing a 0.15 mm air-gap length would also demand extremely high machining tolerances, which may be hard to achieve as Radiometal is a difficult material to machine.

### 8.1.4 Radially Magnetized Permanent Magnets

Axially magnetized permanent magnets have been employed in all the designs so far considered, with the magnetic flux directed radially to the air-gap by means of the end-rings. An alternative design could be to eliminate the end-rings and the axially magnetized magnets and to replace them with radially magnetized magnets. The benefits of this arrangement are given in [92] and, due to the magnetic orientation, the motor is inherently self-shielding, leaking minimal flux. Such a design is shown in Fig. 8.21(b), in which the 25 mm diameter hollow armature design (10 mm diameter armature hole) of Fig. 8.21(a), has been modified. Sufficient space is left between the magnets and the adjacent stator yoke to reduce flux leakage, whilst still keeping the overall length of the motor the same. The volume of the magnets is kept the same,

to enable useful comparisons to be made.

In the vector equipotential plot of Fig. 8.22(a) the coil is unexcited and the armature is centralised, and the reduction of leakage flux in the surrounding air can clearly be seen. However, as expected, considerable flux has leaked across the gap between the magnets and the stator yokes. The flux density plot in Fig. 8.22(b) shows that the cross-sectional area of the stator magnetic circuit near to the magnets needs to be larger, to avoid saturation of the magnetic material. The modulus of the air-gap flux density is shown in Fig. 8.23, together with the design of Fig. 8.21(a), and a significant reduction is seen. Fig. 8.24 compares the force characteristics of this design with those of the axially magnetized magnet motor design for a coil current of zero and 0.6 A. The reduction of the force with the radial design is due to the lower flux density in the air-gap. The stiffness has also suffered, with the centralising forces decreasing to  $\pm 4.56$  N, compared with  $\pm 5.52$  N for the design of Fig. 8.21(a).

It is clear that for this particular motor axial magnets are the better choice, even though, unlike the self-shielding radially magnetized magnet motor design, they produce leakage flux in the surrounding air.

### 8.1.5 Stator Yoke Pole-Shoe Length

This section illustrates the effect that the stator yoke pole-shoe length has on the maximum possible armature displacement. The length considered so far has been 15.0 mm, shown in Fig. 8.25(a). The length expected to produce the smallest armature stroke length is when the end of the pole-shoe coincides with the edge of the centre-section of the armature, as shown in Fig. 8.25(d), where the pole-shoe length is 8.25 mm. Two further lengths were investigated, equi-spaced between the previous two, at 10.50 mm, Fig. 8.25(b), and 12.75 mm, Fig. 8.25(c). The magnetic stiffness characteristics for all four designs are given in Figs. 8.26, where the result of the various pole-shoe lengths on the stiffness curves are seen by the sudden change of force. These abrupt changes occur when the edges of the centre-sections of the armatures coincide with the ends of the pole-shoes.

The force/coil current characteristics when the armature is in the central position are shown in Fig. 8.27, and the coil current/armature displacement characteristics are shown in Fig. 8.28, where the different maximum armature displacements can be seen. It is of interest to note from Fig. 8.28 that, even though the difference between pole-shoe lengths is 2.25 mm, the difference between the maximum armature displacements is only about 1.70 mm.

## 8.2 MAXIMISING THE ARMATURE DISPLACEMENT

The maximum displacement of the armature is governed by the stator yoke pole-shoe and armature centre-section lengths. Table 8.3 compares the maximum displacement of all six armature designs, and shows that the armature displacement is largest when its cross-sectional area is as large as possible.

Armature Diameter (mm)	Maximum Armature Displacement (mm)	Armature Cross-Sectional Area ( $\times 10^{-4} \text{ m}^2$ )	Maximum Armature Flux Density (T)
10.0	3.30	0.692	1.82
15.0	4.25	1.625	1.75
20.0	4.85	2.951	1.66
25.0	5.15	4.670	1.60
25.0 (10.0)	4.85	3.885	1.61
25.0 (15.0)	4.00	2.903	1.68

**Table 8.3** Comparison of each armature for maximum armature displacement

This effect is due to the flux generated by the coil permeating further through a large cross-section armature than through a smaller one, due to the magnetic material in the smaller diameter armatures being more saturated and producing a higher reluctance.

A large cross-section armature will therefore produce a greater distortion of the symmetrical flux distribution in the magnetic circuit when control flux exists, which will cause the armature to move through a larger distance. This is shown for a 10 mm diameter armature design in Table 8.3 when a current of 0.7 A flowing through the coil producing an armature displacement of only 3.30 mm, compared with 5.15 mm in the 25 mm diameter design. The numbers in brackets in the first column denote the armature hole diameters of the hollow armature arrangements and the cross-sectional areas are calculated opposite the permanent magnets and not in the smaller centre-section region.

Unique combinations of stator yoke pole-shoe and armature centre-section lengths exist that will increase the displacement of the armatures in all the designs of Table 8.3. Maximum possible displacement occurs when the edge of the centre-section of the armature, at the end of the motor experiencing an increase in the level of flux, coincides with the edge of the corresponding pole-shoe, creating maximum overlap. Simultaneously, the other edge of the centre-section of the armature, at the end of the motor experiencing a decrease in the level of flux, reaches its limit of travel. The overlap has then become as small as possible and will not reduce more due to the high stiffness force attempting to centre the armature. The study was implemented on the 25 mm diameter hollow armature motor design (10 mm diameter hole). The increase in each pole-shoe length from 15.0 mm to 16.5 mm reduced the gap between each pole-shoe to 4.0 mm, which was still sufficiently large to avoid leakage between the poles. The centre-section length was decreased from 20.5 mm to 16.5 mm and this modified arrangement increased the maximum armature displacement from 4.85 mm to 5.50 mm. However, this increase in the displacement caused a small drop in the force developed and a compromise is needed between the maximum armature displacement and the force developed for any design.

### 8.3 MAGNETIC MATERIAL STUDY

The force developed by the motor depends on the air-gap flux density, which in turn depends on the properties of the magnetic circuit material. An alternative magnetic

material that saturates at a higher level than Radiometal should increase the air-gap flux density, and subsequently increase the force acting on the armature. Radiometal was used initially because it has the highest saturation level of all the nickel-iron alloys as discussed in section 3.2.1, and so an alternative material needed to be used to increase the saturation level. The highest flux density achieved in a magnetic material is about 2.43 T, obtained with Permendur, compared with 2.158 T for pure iron [36].

Permendur is a Cobalt-iron ( $\text{Fe}_2\text{Co}$ ) alloy containing 50 % Cobalt and 50 % iron. The excellent magnetic properties at very high flux densities are exploited in laminations of rotating electrical machinery to raise the flux carrying capacity of the armature or stator teeth [36], and it has recently been used in a cylindrical moving-core linear oscillatory actuator [93], in place of a stainless steel with a 30 % increase in force being reported. A disadvantage of Permendur is its cost, which is higher than Radiometal. The  $BH$  curves of Permendur (Vacoflux 50) [94], Radiometal (Permenorm 5000 S2) [94] and Mumetal in Fig. 8.29 shows clearly the higher saturation level of Permendur of about 2.26 T.

The 25 mm diameter hollow armature (10 mm diameter hole) was used to compare different magnetic materials. Fig. 8.30 shows the force characteristic with Radiometal and Permendur used for both the stator and armature for coil currents of zero and 0.6 A. The stiffness when using Radiometal is superior to that with Permendur, as shown by Fig. 8.30; however at 0.6 A the Permendur force curve is much above that for Radiometal, with a peak force developed of about 54.0 N. In all the designs investigated when using Radiometal, the regions of very high saturation occurred only on the armature, and it was decided therefore to keep the armature material as Permendur but to revert to Radiometal for all the stator components where the flux density is lower. This also helps to keep costs down, by only using the more expensive Permendur material on the armature.

Fig. 8.31 compares the force characteristic for this design with those for the design using only Radiometal for coil currents of zero and 0.6 A. The stiffness when using

the composite material design is clearly a major improvement over that when only Radiometal is used. The stiffness is even superior to the 25 mm diameter solid armature, which had a restoring force of about 8.0 N at 4.0 mm armature displacement compared with about 8.7 N for the composite material design. Figs. 8.32 and 8.33 show the force characteristics of the two new designs (Permendur stator and armature) and (Radiometal stator and Permendur armature) for various coil currents. The composite design also enables linear movement of the armature, whereas the all Permendur design suffers from a non-linear relationship similar to the characteristic obtained from the 20 mm diameter solid armature motor.

The force/coil current characteristics at the armature central position for the two designs are compared with the initial design (Radiometal stator and armature) in Fig. 8.34. Using Permendur for both the armature and the stator produces a force of over 16.0 N with a current of 0.7 A. The characteristic when using the composite material design is slightly lower than the initial design, but has the advantage of being more linear. The linearity of the composite material design is compared in Fig. 8.35, with the two non-linear characteristics of the initial design and the design using only Permendur.

Another magnetic material considered was Mumetal, which saturates at about 0.8 T. Although unlikely to be used in an optimum design, due to this very low saturation level, its use does however lead to a more thorough understanding of the motor operation. Various composite designs were studied to highlight the correct choice of materials for use in the motor. Fig. 8.36 shows the force characteristics when Mumetal is used for the stator, and the armature is modelled with all three materials. The model which uses only Mumetal has an acceptable stiffness, but, when a material with a higher saturation level is used for the armature, the stiffness improves greatly.

The curves with Radiometal and Permendur used for the armature are identical, which show that the armature is not saturated although the stator is. Therefore, to create a design with a high stiffness and good linearity the stator must saturate, not the armature. This agrees with the findings in section 7.1.3, that an armature with the

largest cross-section possible must be used to create a high stiffness and good linearity.

Fig. 8.37 shows the force characteristics when Radiometal is used for the stator and all three different materials for the armature. A high stiffness again exists when the stator saturates and not the armature (Radiometal stator, Permendur armature). The stiffness should therefore be poor when the armature is heavily saturated, and this is shown to be true when analyzing the Radiometal stator, Mumetal armature design. With Permendur used for the stator then, whatever material used for the armature, the stiffness characteristics should be very poor. This is confirmed in Fig. 8.38, where the best stiffness characteristic of the three (Permendur stator, Permendur armature) is still unacceptable.

The best possible design has been shown to use a composite design with a Radiometal stator and a Permendur armature. In terms of linearity and stiffness another good design would have a Mumetal stator and a Radiometal armature, but this arrangement would produce low forces compared to the Radiometal/Permendur combination. Some deterioration of the motor hysteresis would be expected if Permendur was used for both the stator and armature, due to its large hysteresis loop. However, with the design developed above the high stiffness is more than adequate to overcome this problem. Finally, the increased stiffness and good linearity will enable a slightly larger hole to be introduced in the armature which will reduce the armature mass. Coupled with the fact that the density of Permendur ( $8.15 \text{ g/cm}^3$ ) is slightly below that of Radiometal ( $8.25 \text{ g/cm}^3$ ), will considerably improve the dynamic response.

#### 8.4 CONCLUSIONS

In this chapter the magnetic circuit of the motor has been further modified by employing a hollow armature arrangement to improve the dynamic performance. The air-gap length has been varied and a suitable length determined, and the stator yoke pole-shoe length has been studied. The direction of magnetization of the permanent magnets have been investigated. Finally, the choice of magnetic material has been

extensively analyzed and the best possible design has been shown to consist of a composite design using Radiometal for the stator components, and Permendur for the armature. Chapter 9 uses an optimization algorithm on this improved design in order to increase further the performance.



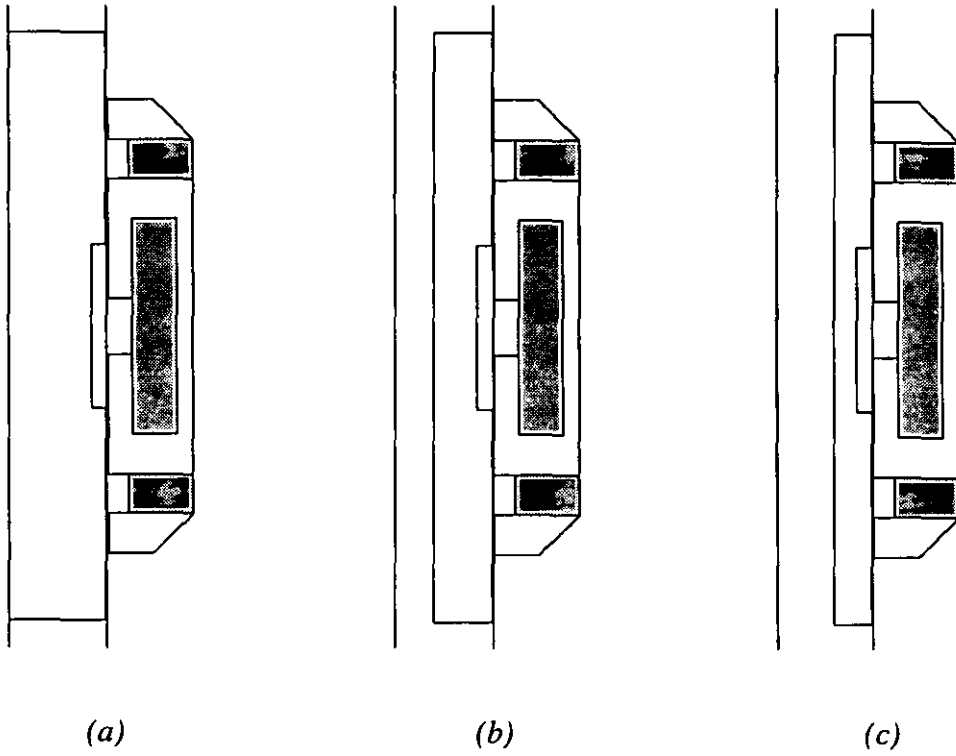


**Fig. 8.1** Half cross-sections of (a) the 25 mm diameter armature motor design and (b) armature modification A (c) armature modification B

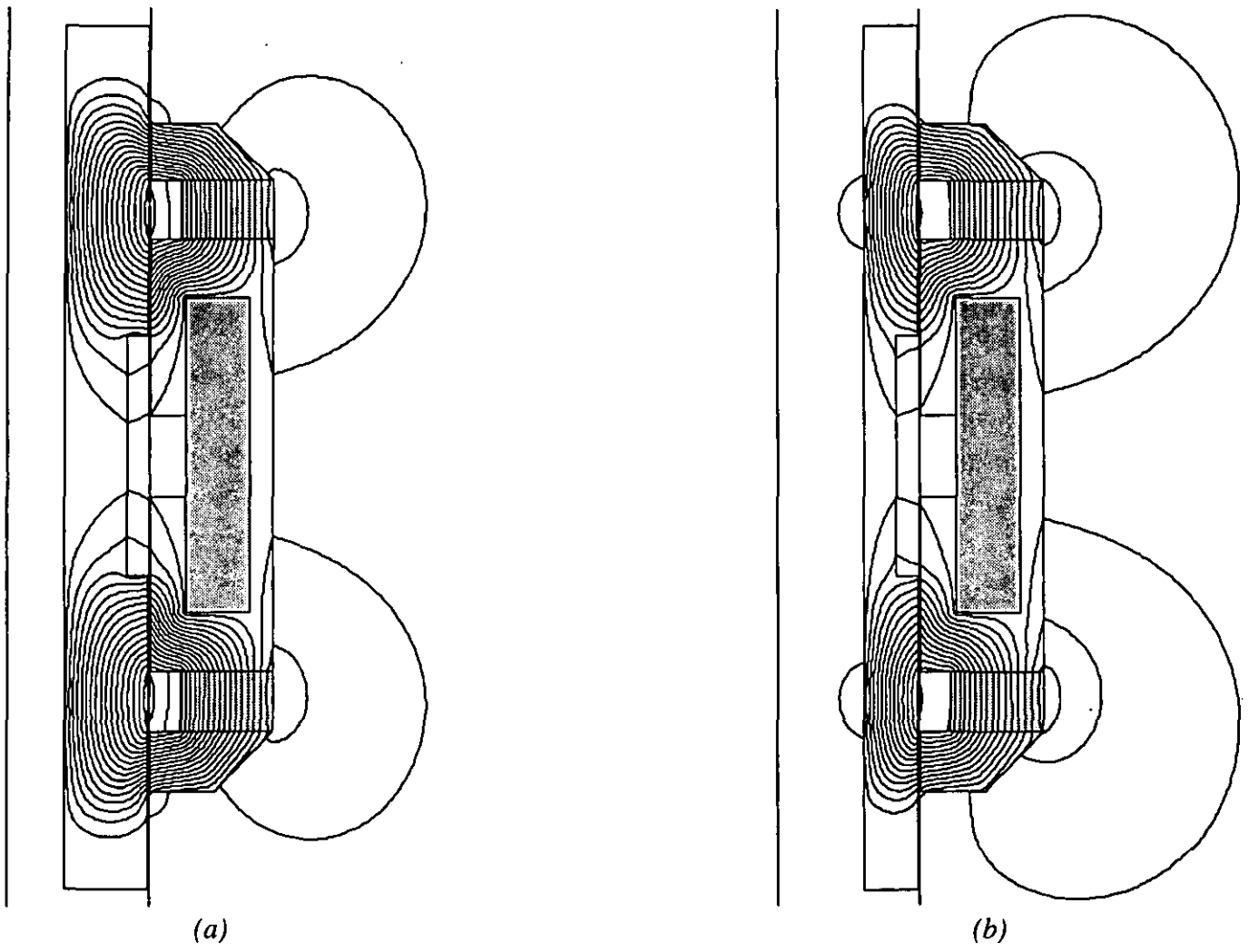


**Fig. 8.2** Magnetic vector equipotential plots (a) armature modification A  
(b) armature modification B

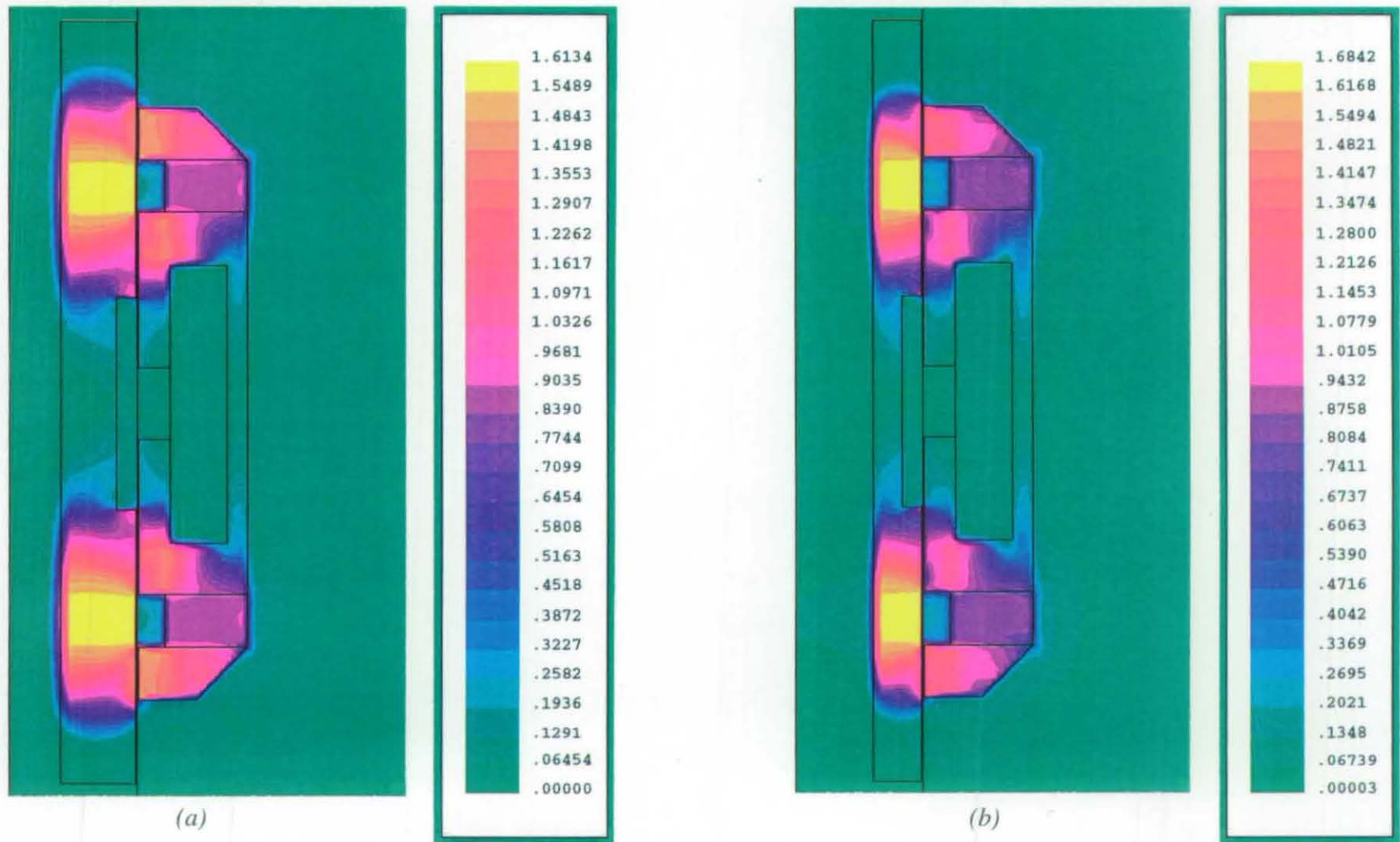


Fig. 8.3 Magnetic flux density plots (a) armature modification A (b) armature modification B

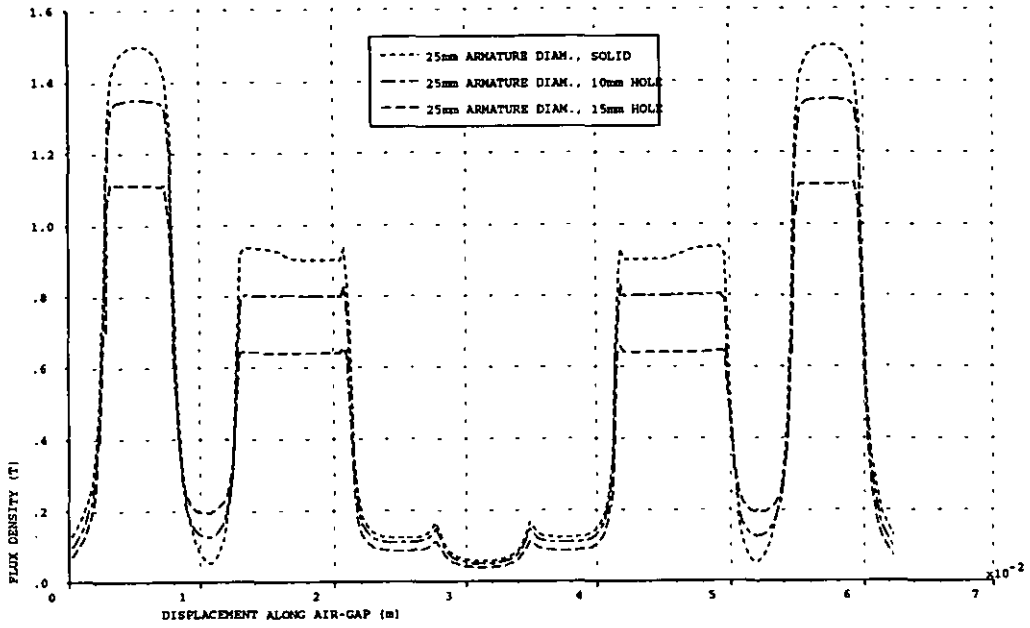


Fig. 8.4 Air-gap flux density for the 25 mm diameter solid armature motor and the two modified armature motor designs

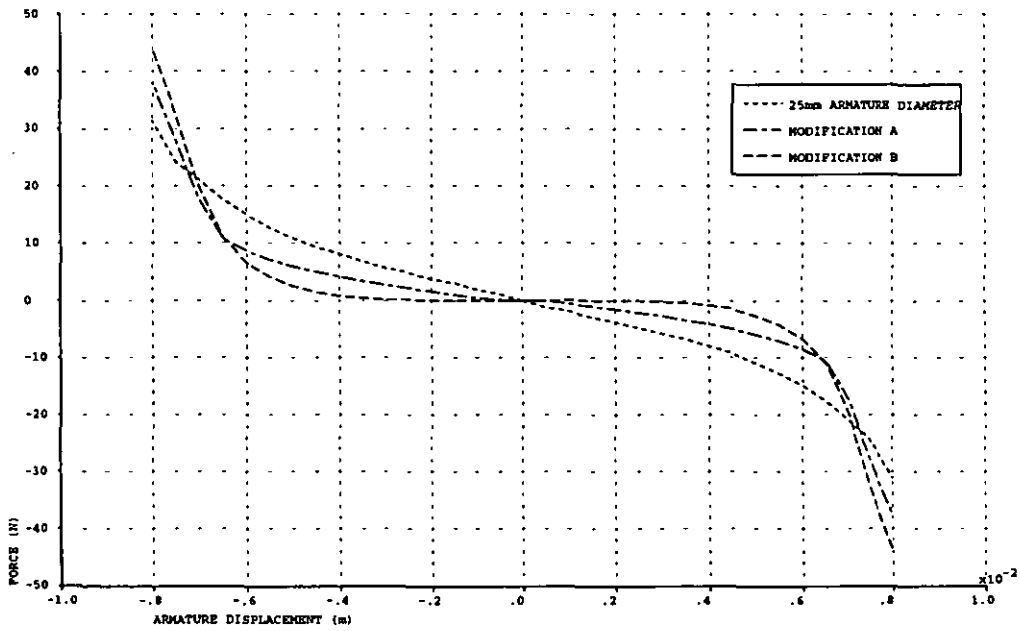


Fig. 8.5 Magnetic stiffness characteristics for the 25 mm diameter solid armature motor and the two modified armature designs

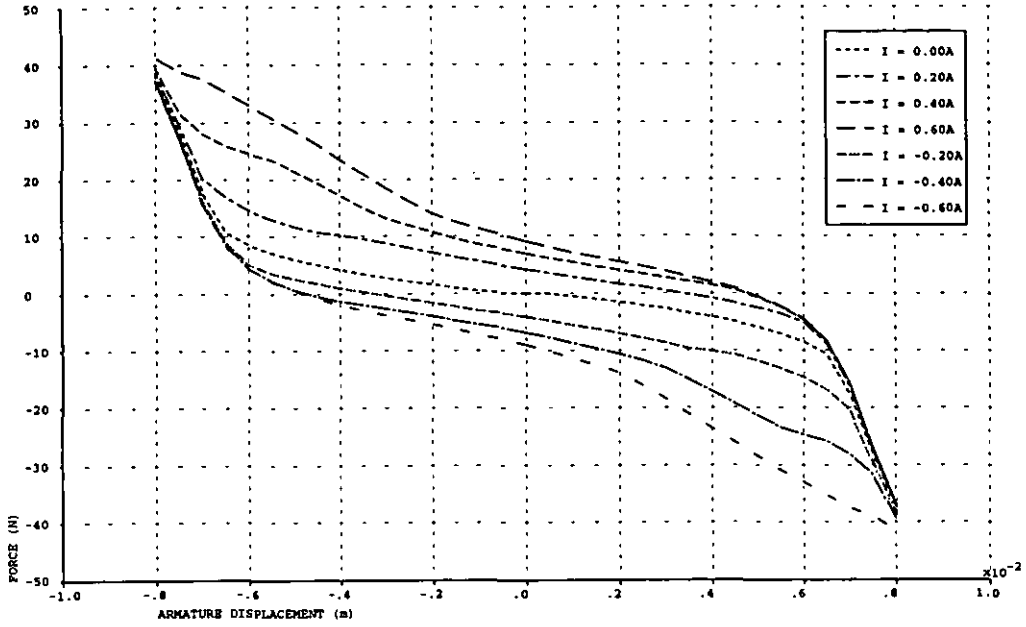


Fig. 8.6 Force characteristic for various coil currents for the 25 mm diameter hollow armature motor (10 mm diameter hole)

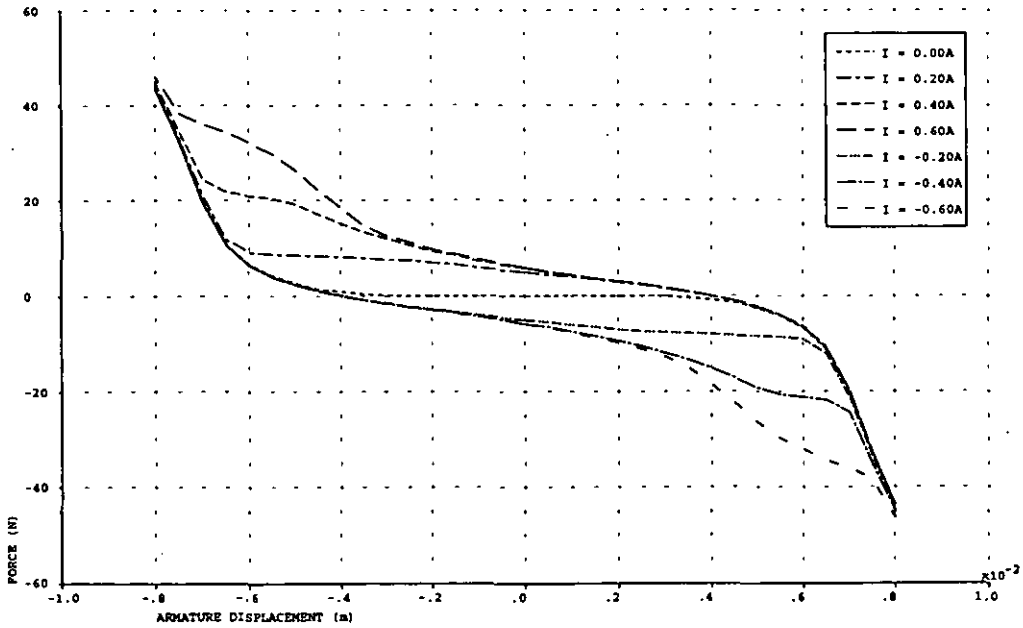


Fig. 8.7 Force characteristic for various coil currents for the 25 mm diameter hollow armature motor (15 mm diameter hole)

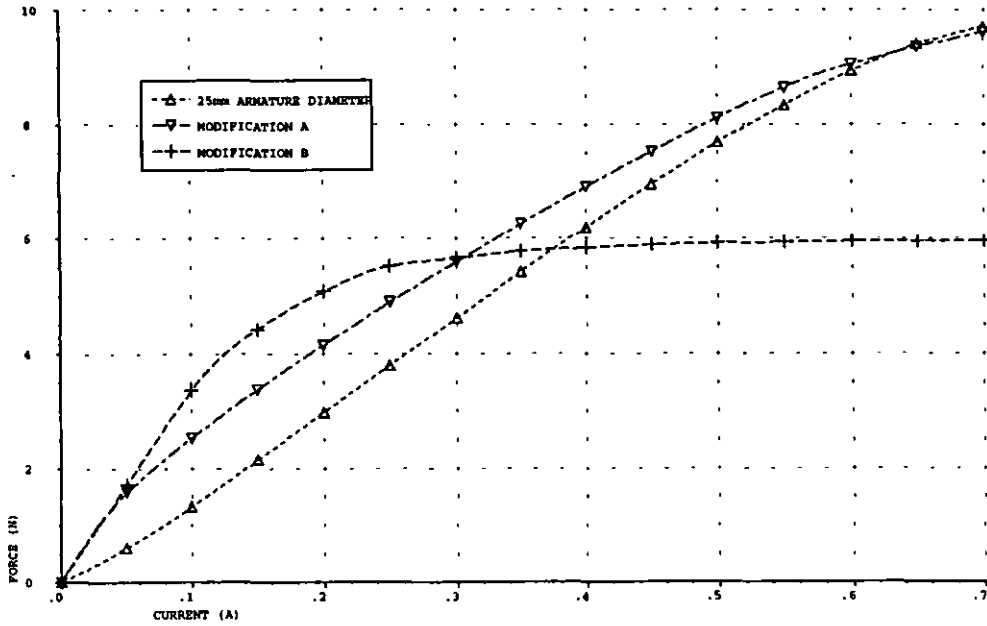


Fig. 8.8 Force/coil current characteristics for the 25 mm diameter solid armature motor and the two modified armature designs (armature central position)

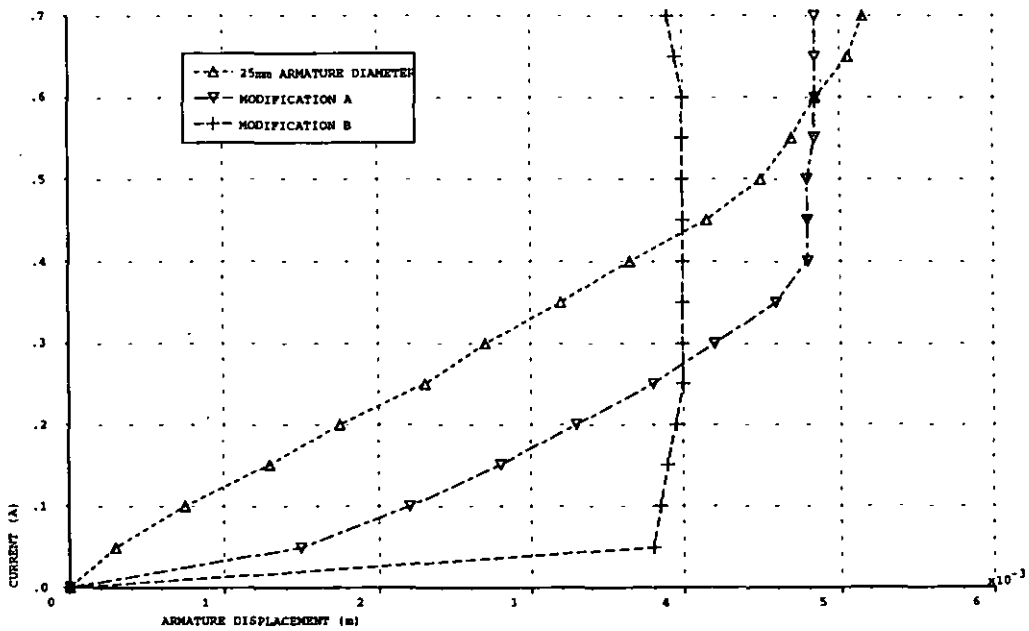


Fig. 8.9 Coil current/armature displacement characteristics for the 25 mm diameter solid armature motor and the two modified armature designs

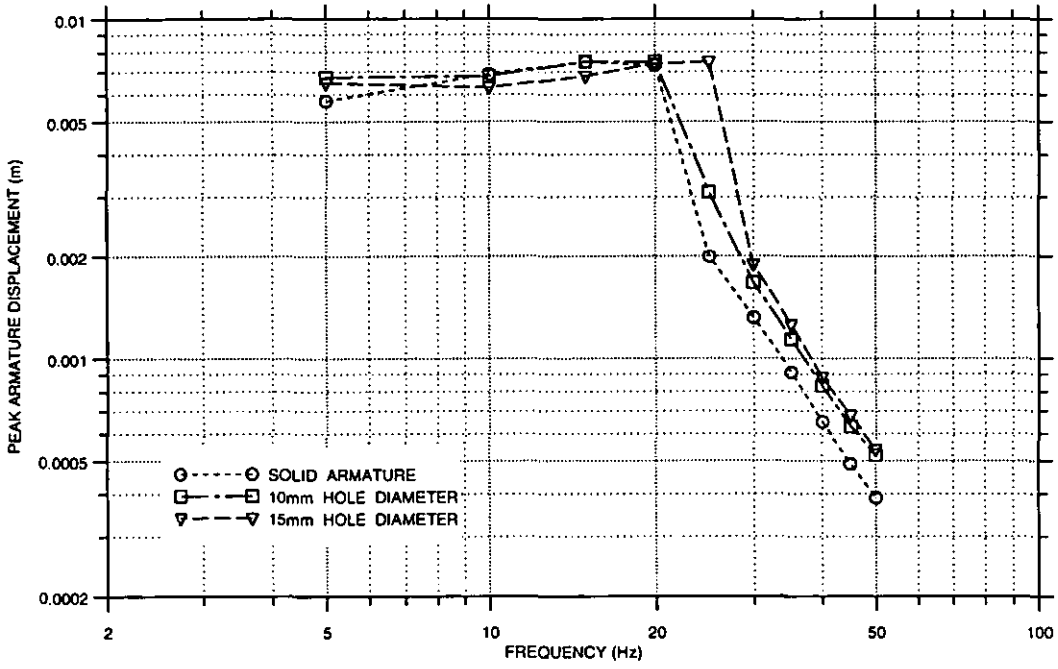


Fig. 8.10 Dynamic response characteristics for the 25 mm diameter solid armature motor and the two modified armature designs

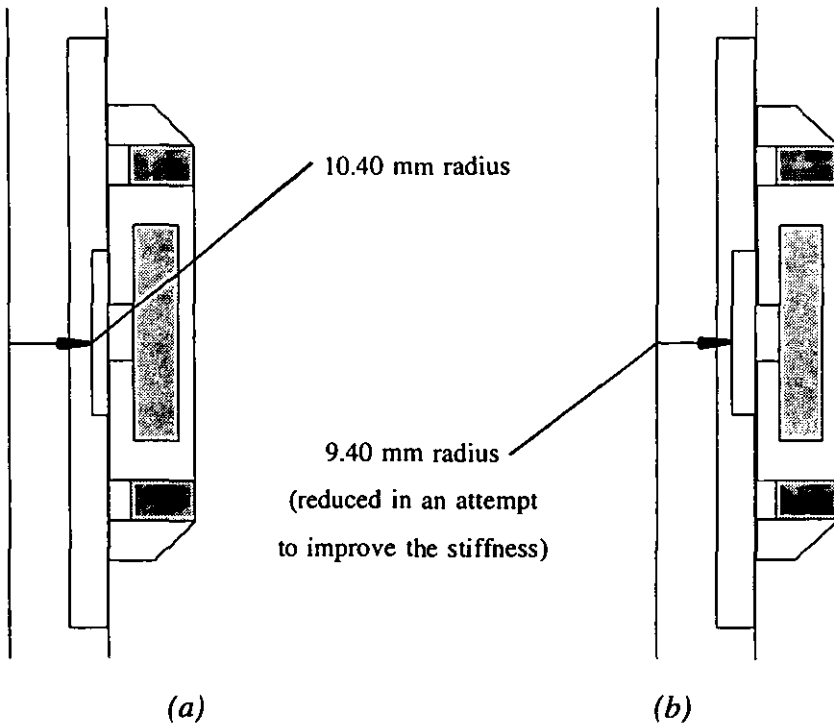


Fig. 8.11 Half cross-sections of (a) armature modification B (b) armature modification C designs

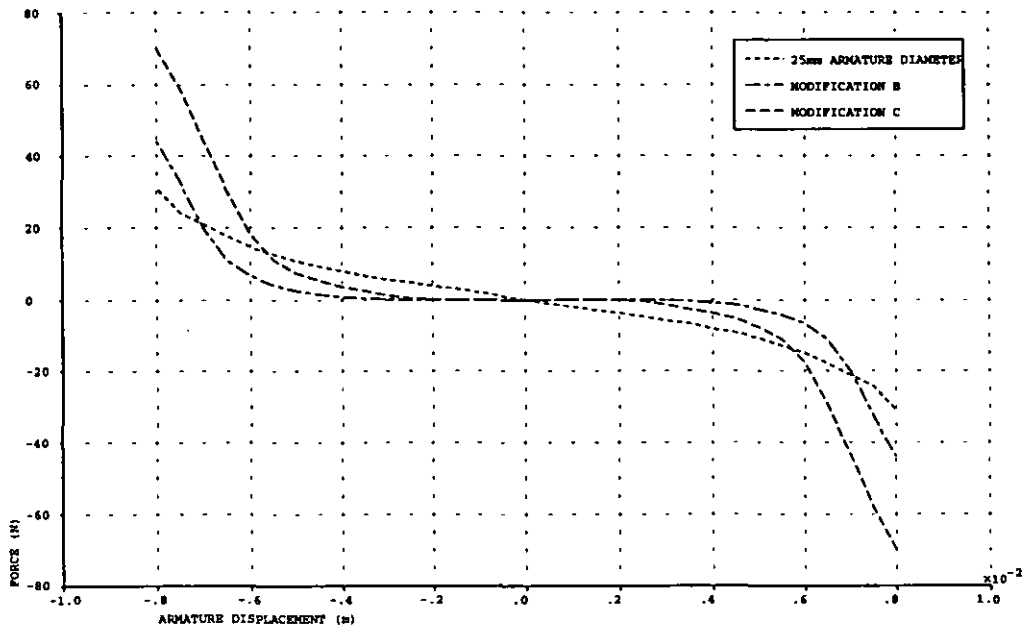


Fig. 8.12 Magnetic stiffness characteristics for armature modification B and armature modification C designs

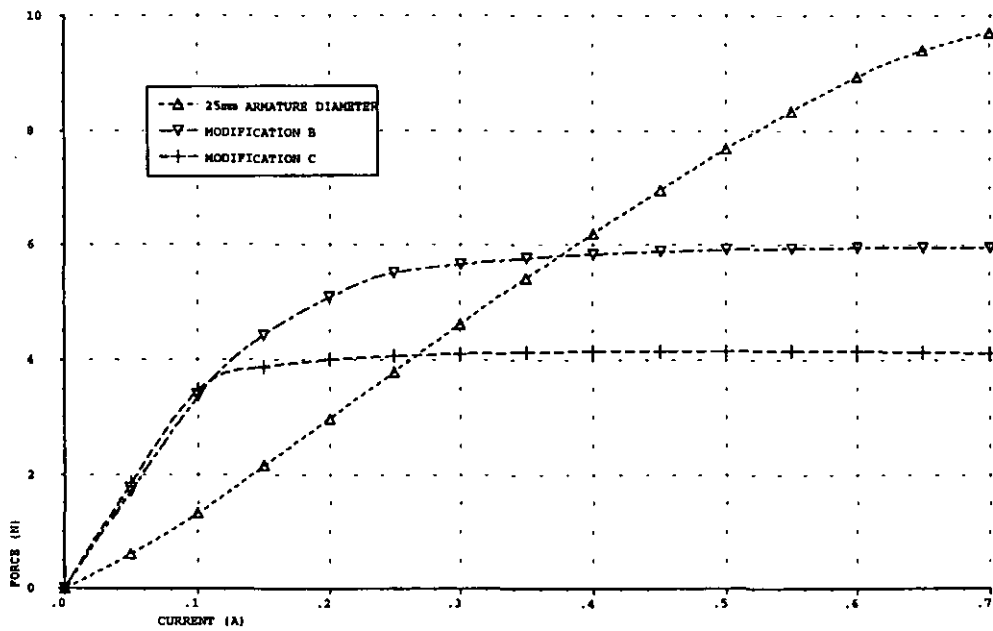


Fig. 8.13 Force/coil current characteristics for armature modification B and armature modification C designs (armature central position)



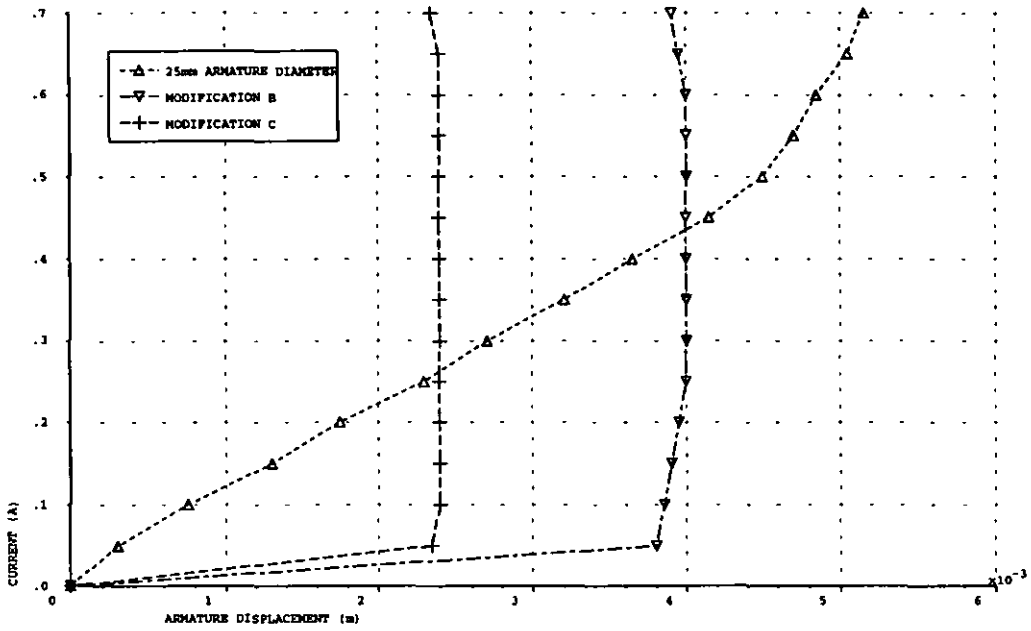


Fig. 8.14 Coil current/armature displacement characteristics for armature modification B and armature modification C designs

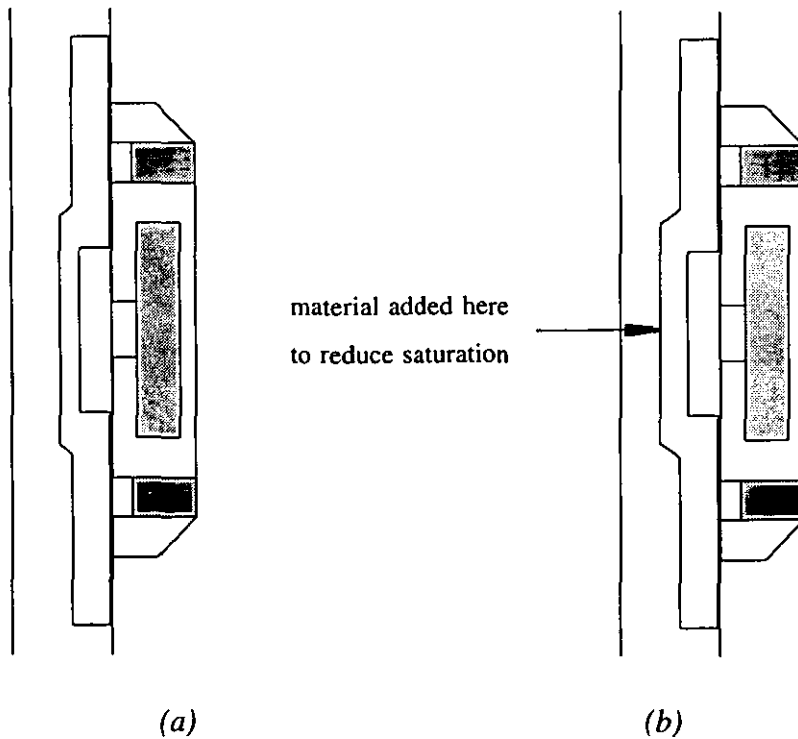


Fig. 8.15 Further reduction of the centre-section diameter

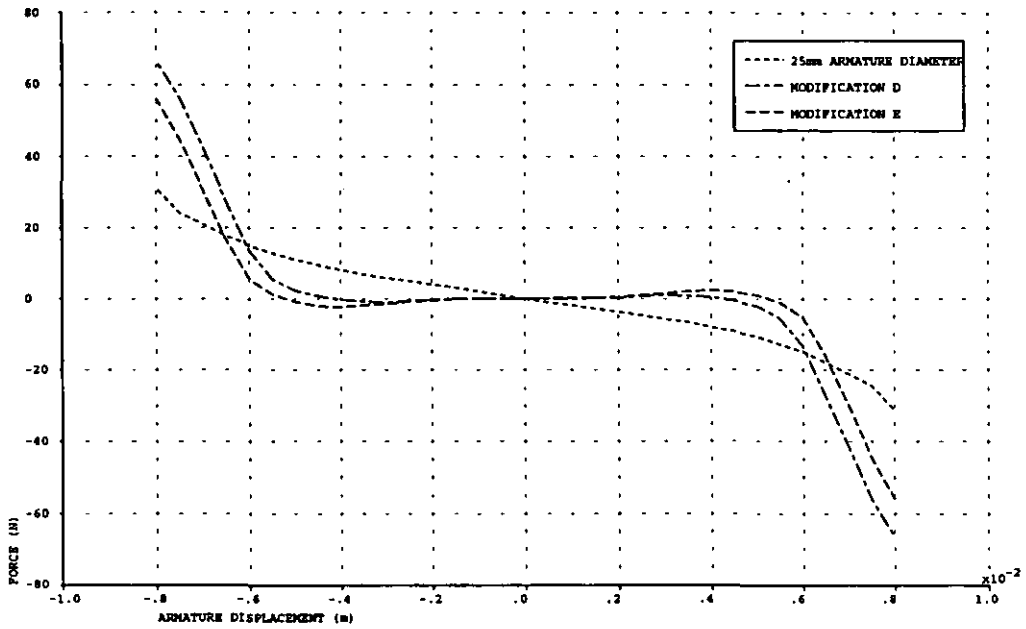


Fig. 8.16 Magnetic stiffness characteristics for armature modification D and armature modification E designs

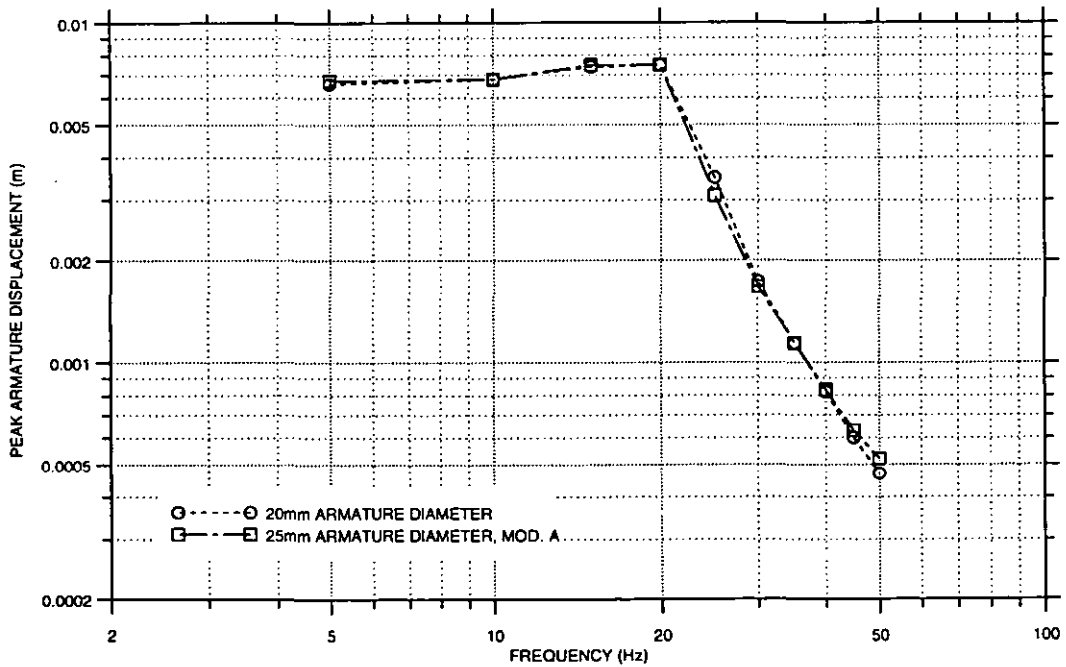


Fig. 8.17 Dynamic response characteristics for the 20 mm diameter solid armature and the 25 mm diameter hollow armature (10 mm diameter hole) motors

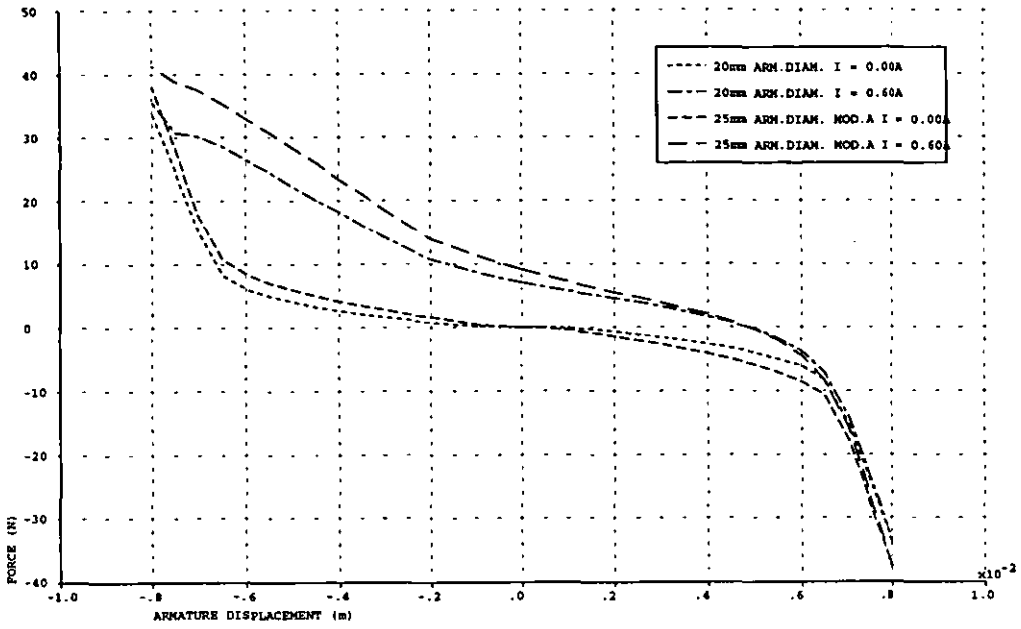


Fig. 8.18 Comparison of force characteristics for the 20 mm diameter solid armature and the 25 mm diameter hollow armature (10 mm diameter hole) designs

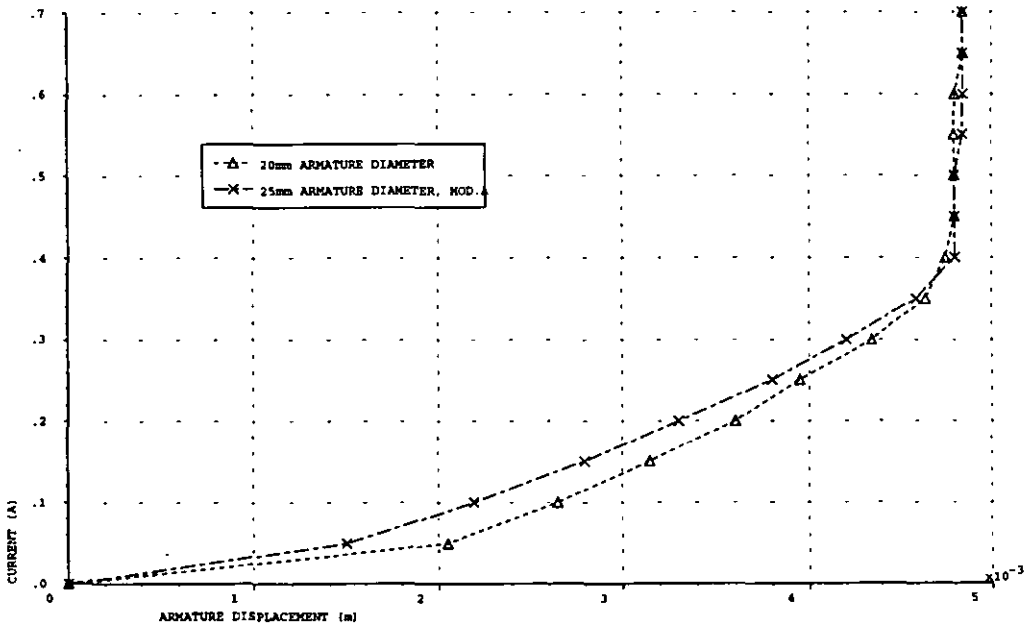


Fig. 8.19 Coil current/armature displacement characteristics for the 20 mm diameter solid armature and the 25 mm diameter hollow armature (10 mm diameter hole) motors

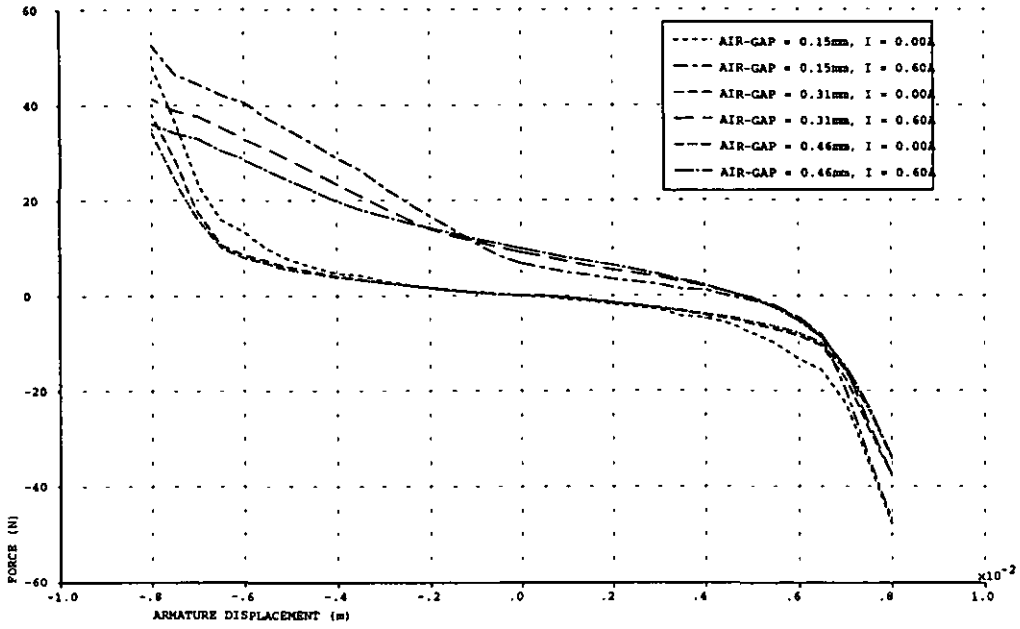


Fig. 8.20 Comparison of force characteristics for the 25 mm diameter hollow armature (10 mm diameter hole) motor design with various air-gap lengths

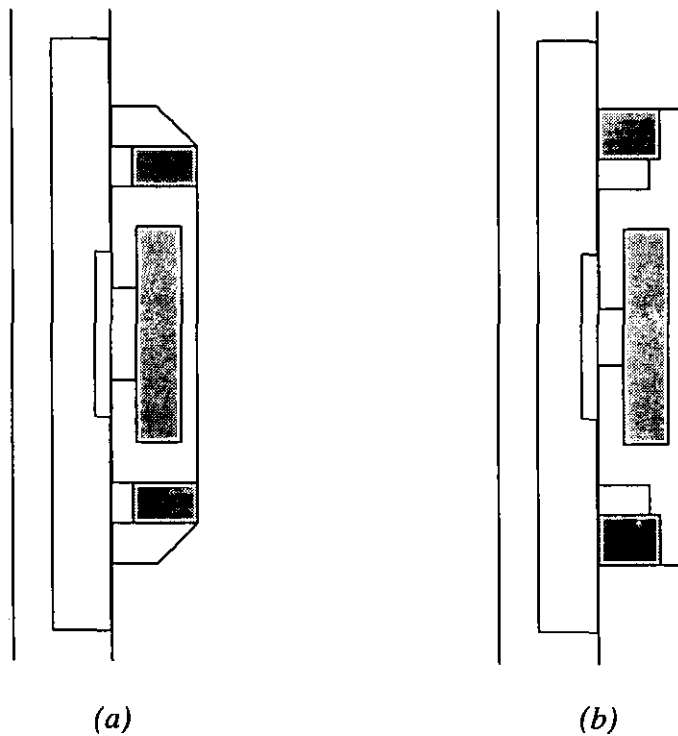
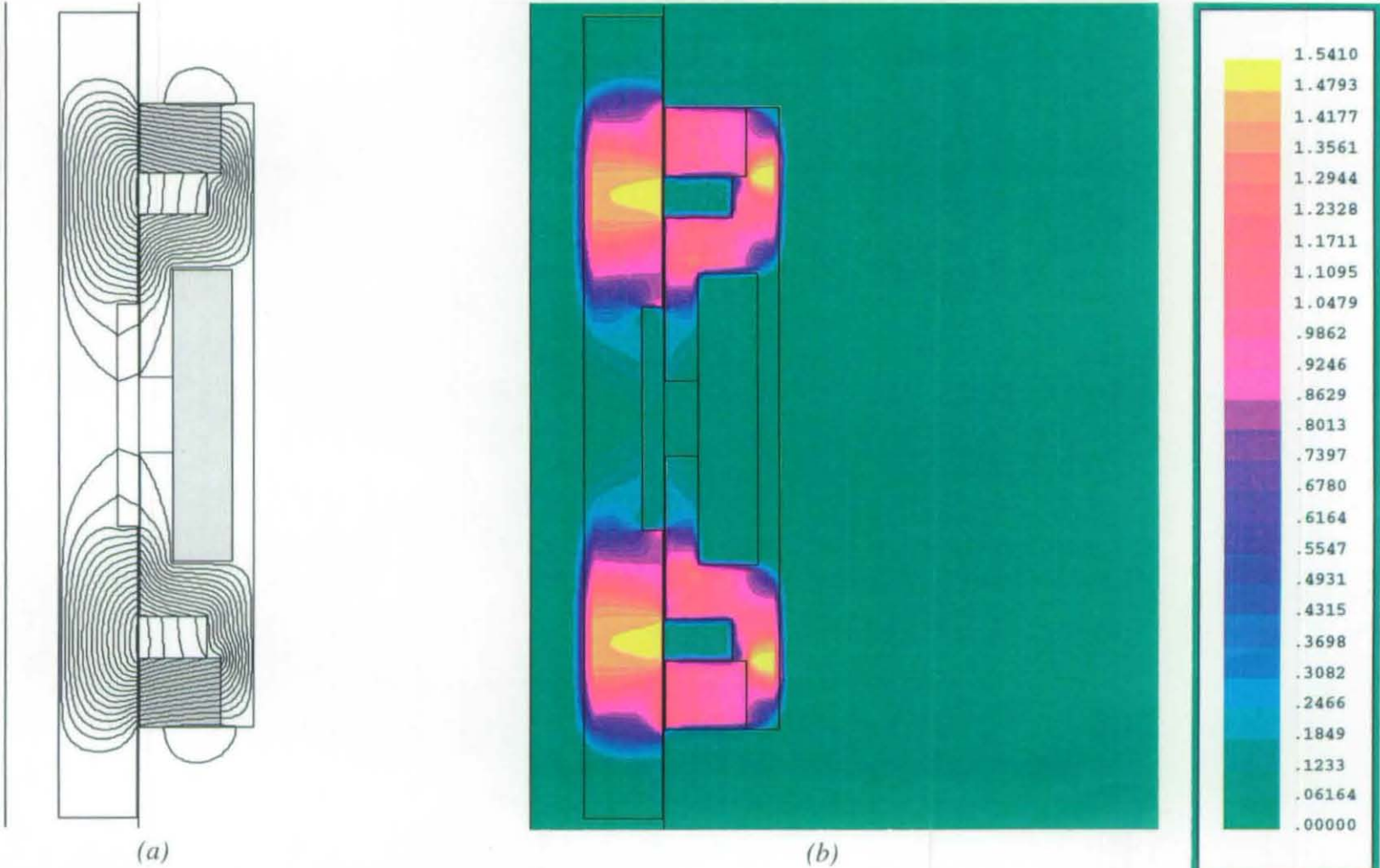


Fig. 8.21 Half cross-sections of 25 mm diameter hollow armature (10 mm diameter hole) motor design with (a) axially and (b) radially magnetized magnets



**Fig. 8.22** (a) Magnetic vector equipotential plot and (b) flux density plot of the 25 mm diameter hollow armature (10 mm diameter hole) motor design with radially magnetized magnets

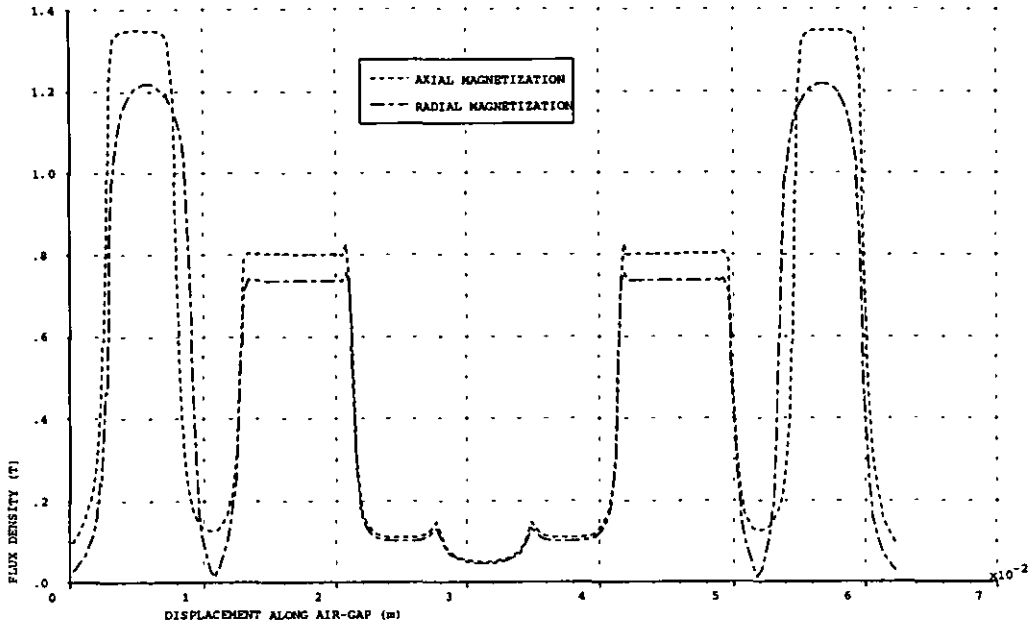


Fig. 8.23 Comparison of air-gap flux densities for the axially and radially magnetized motor designs

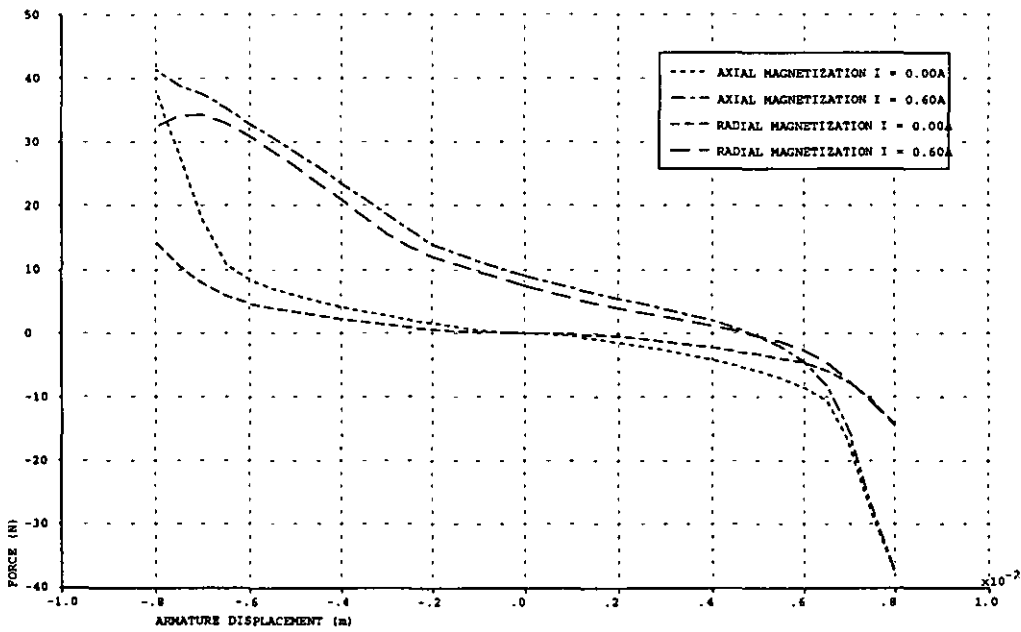


Fig. 8.24 Comparison of force characteristics for the axially and radially magnetized motor designs

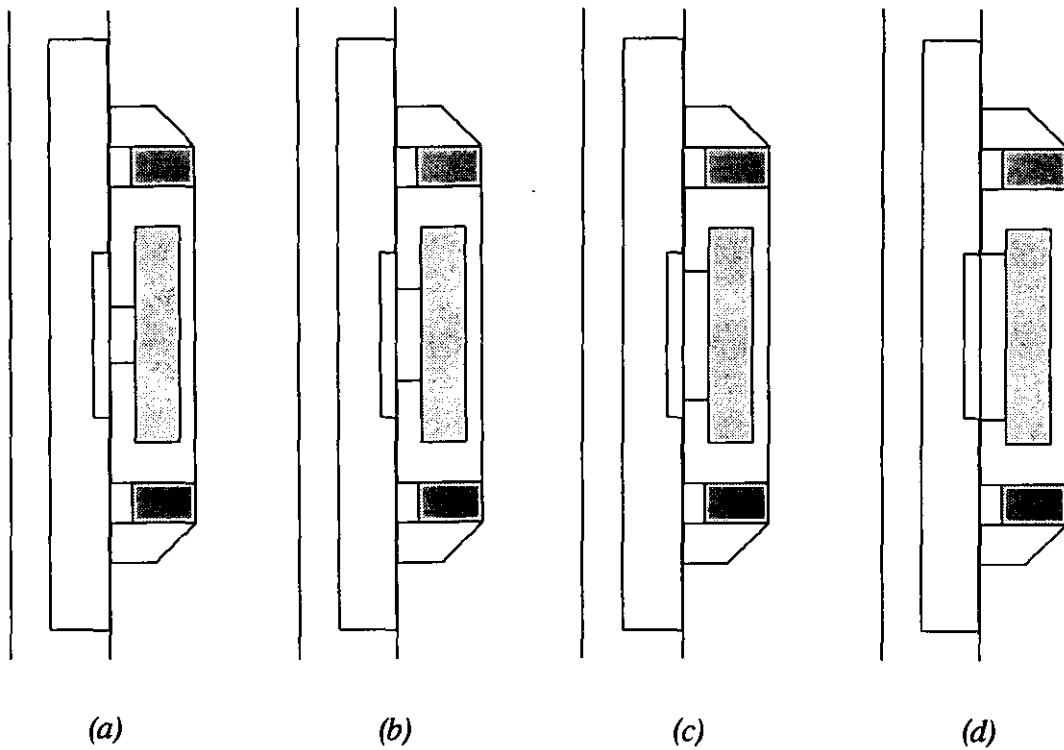


Fig. 8.25 Half cross-sections of (a) the 25 mm diameter hollow armature (10 mm diameter hole) design (b) modification A (c) modification B (d) modification C

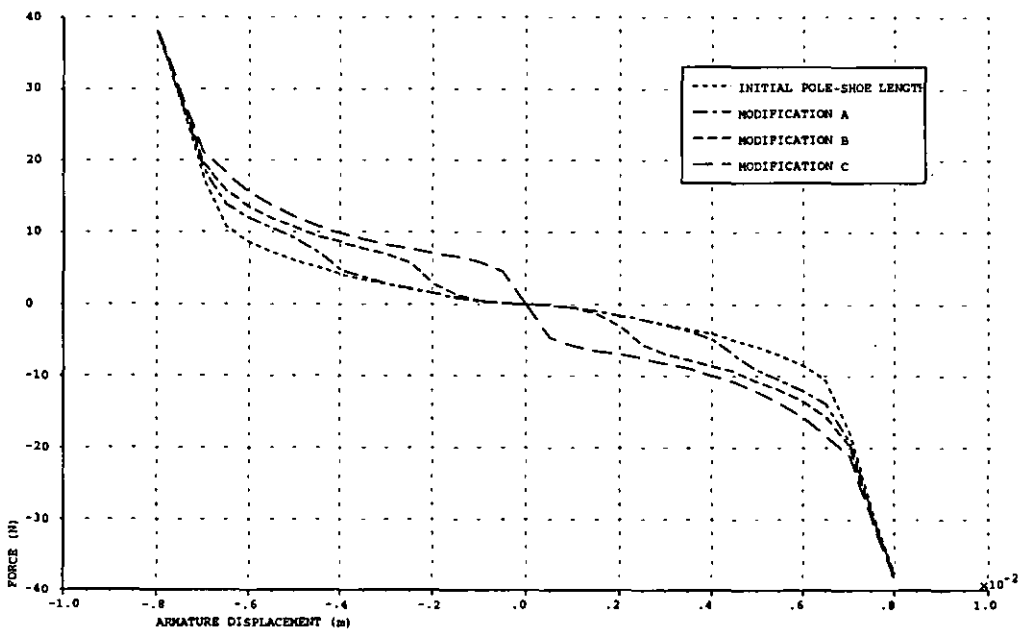


Fig. 8.26 Magnetic stiffness characteristics for the initial pole-shoe length and the three modifications

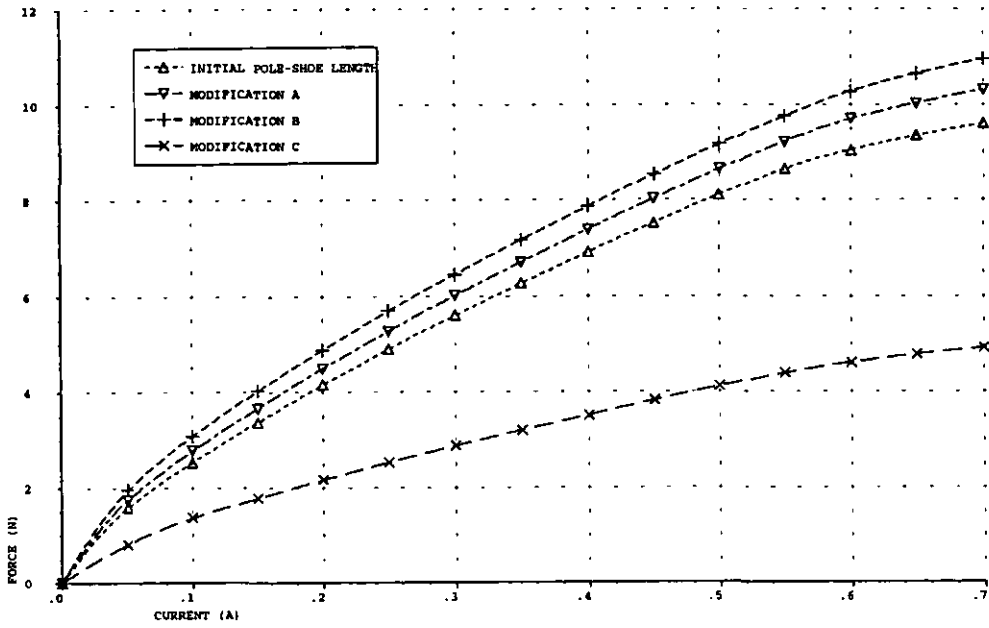


Fig. 8.27 Force/coil current characteristics for the initial pole-shoe length and the three modifications (armature central position)

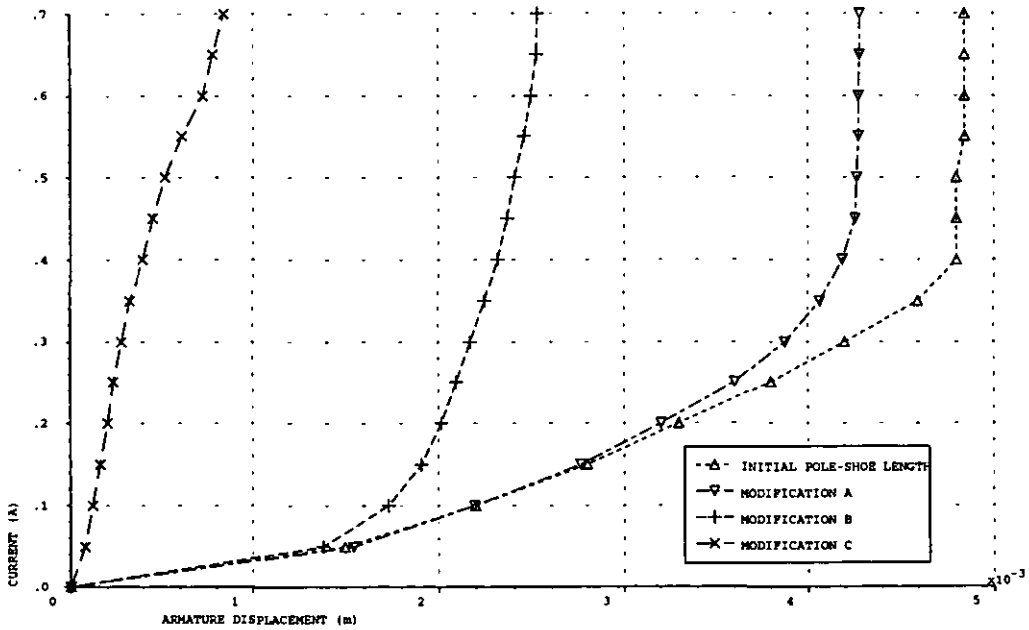


Fig. 8.28 Coil current/armature displacement characteristics for the initial pole-shoe length and the three modifications



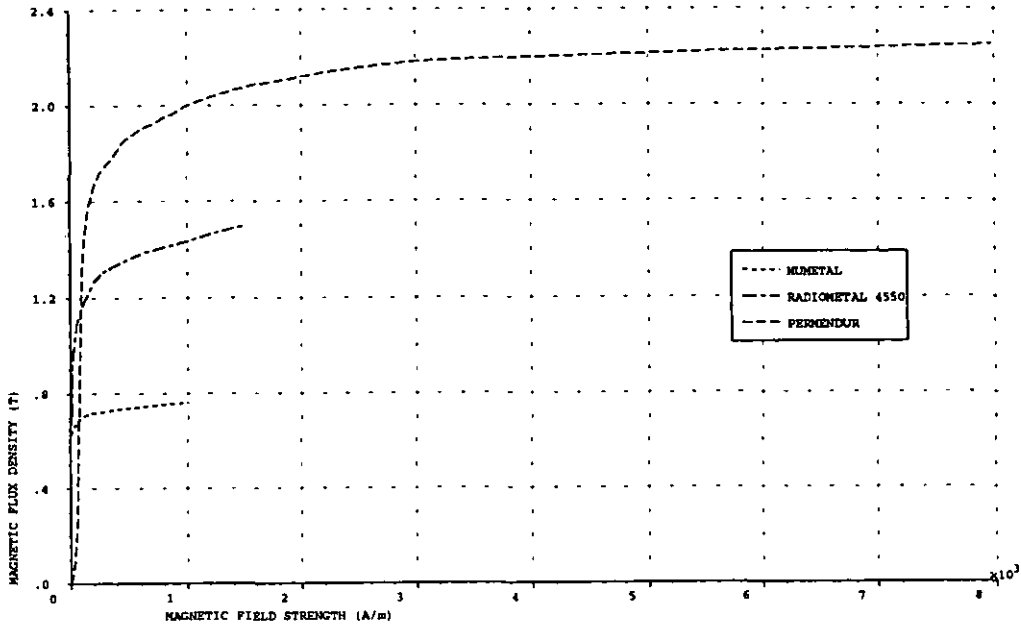


Fig. 8.29 Magnetization curves of Mumetal, Radiometal and Permendur

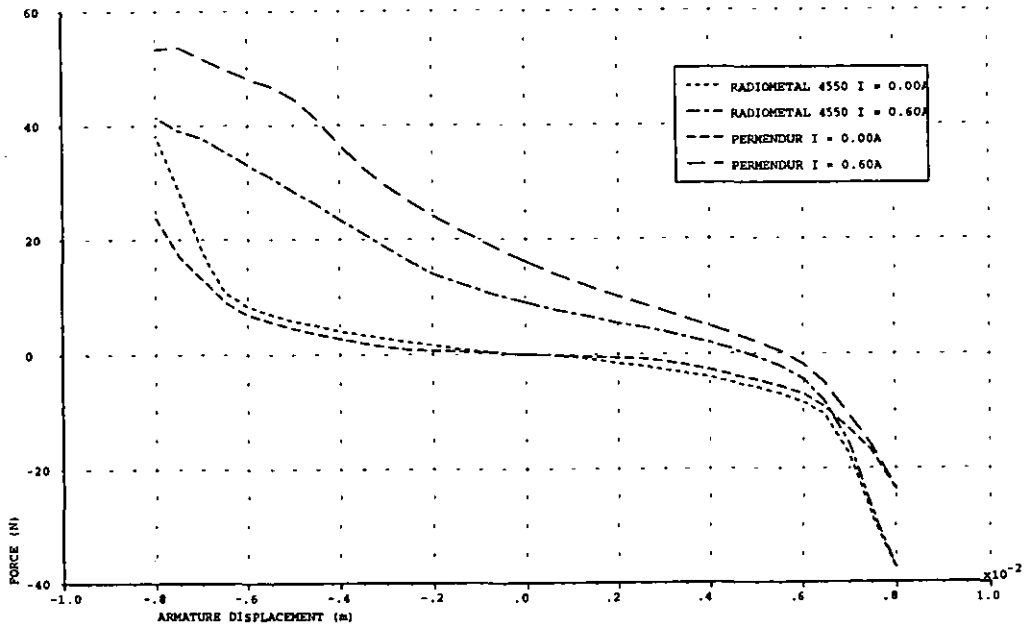
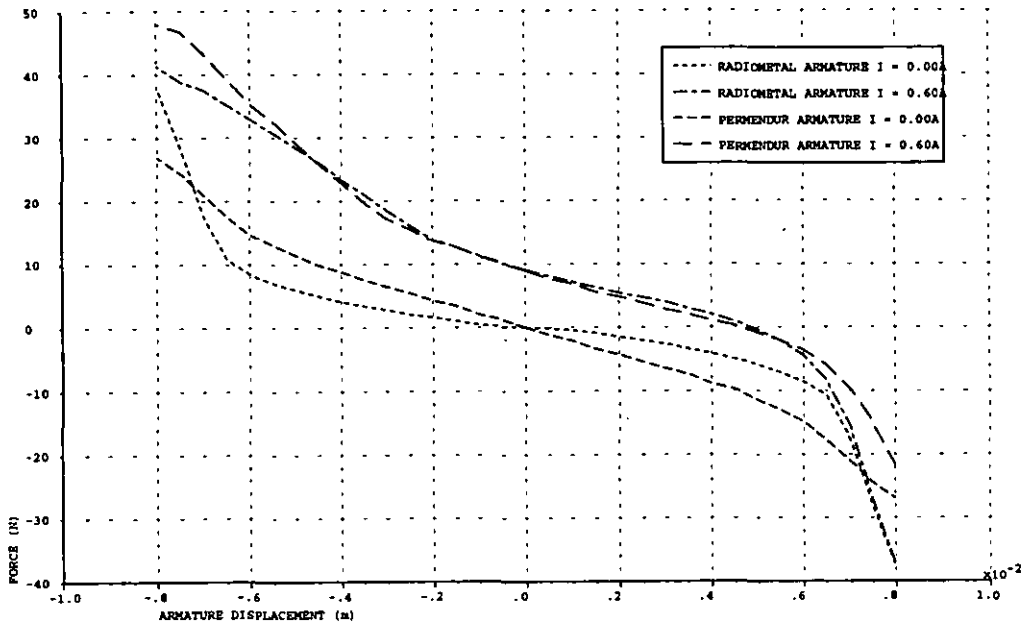
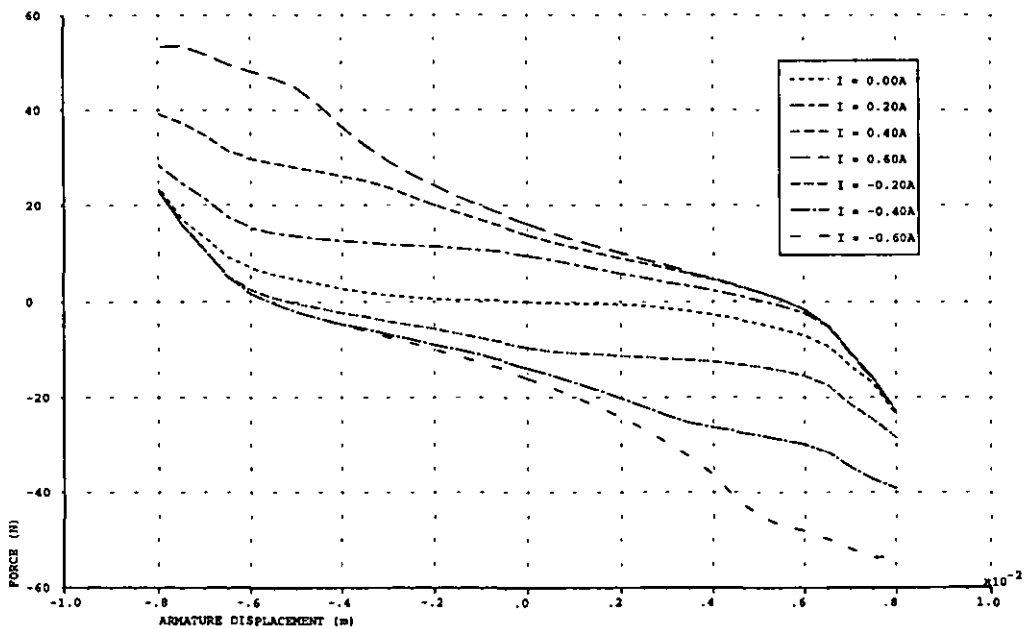


Fig. 8.30 Comparison of force characteristics for the 25 mm diameter hollow armature (10 mm diameter hole) design when using Radiometal and Permendur



**Fig. 8.31** Comparison of force characteristics for the 25 mm diameter hollow armature (10 mm diameter hole) design when using Radiometal stator/armature and Radiometal stator/Permendur armature



**Fig. 8.32** Force characteristics for the 25 mm diameter hollow armature (10 mm diameter hole) design when using Permendur

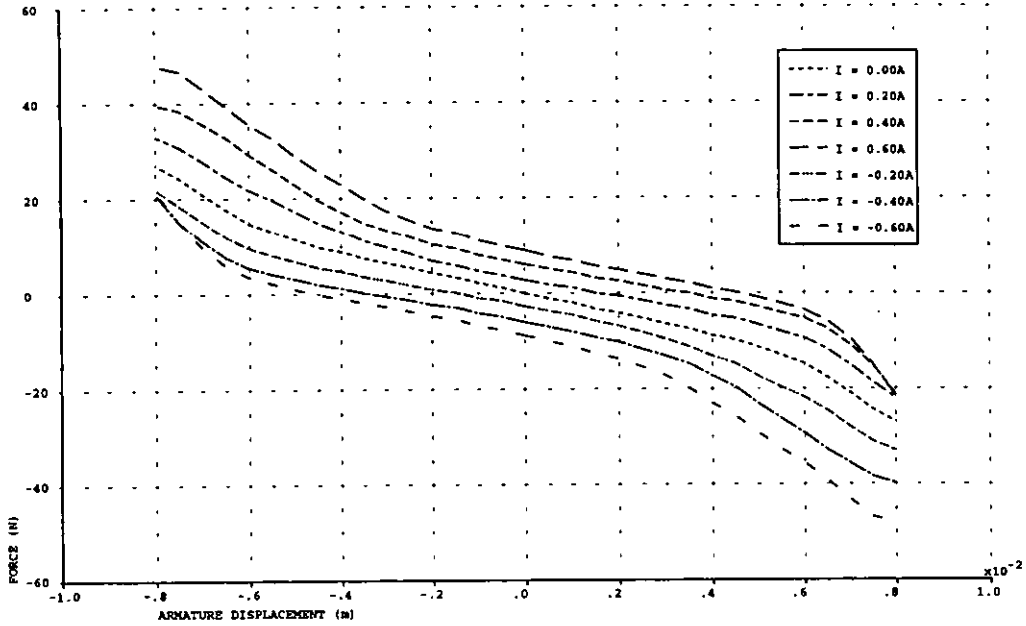


Fig. 8.33 Force characteristics for the 25 mm diameter hollow armature (10 mm diameter hole) design when using Radiometal stator/Permendur armature

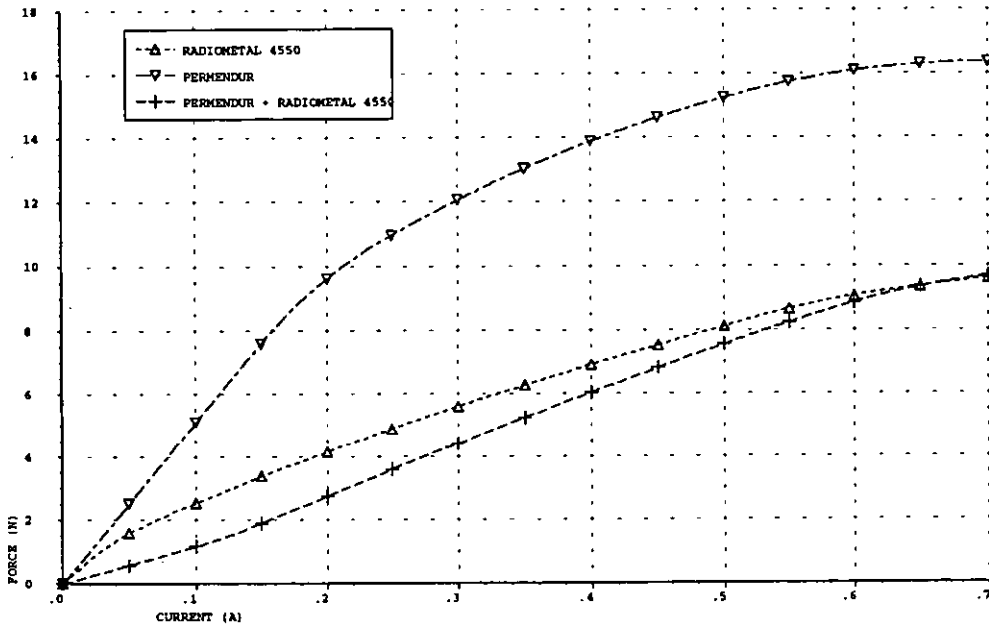


Fig. 8.34 Comparison of force/coil current characteristics for various composite material designs (armature central position)

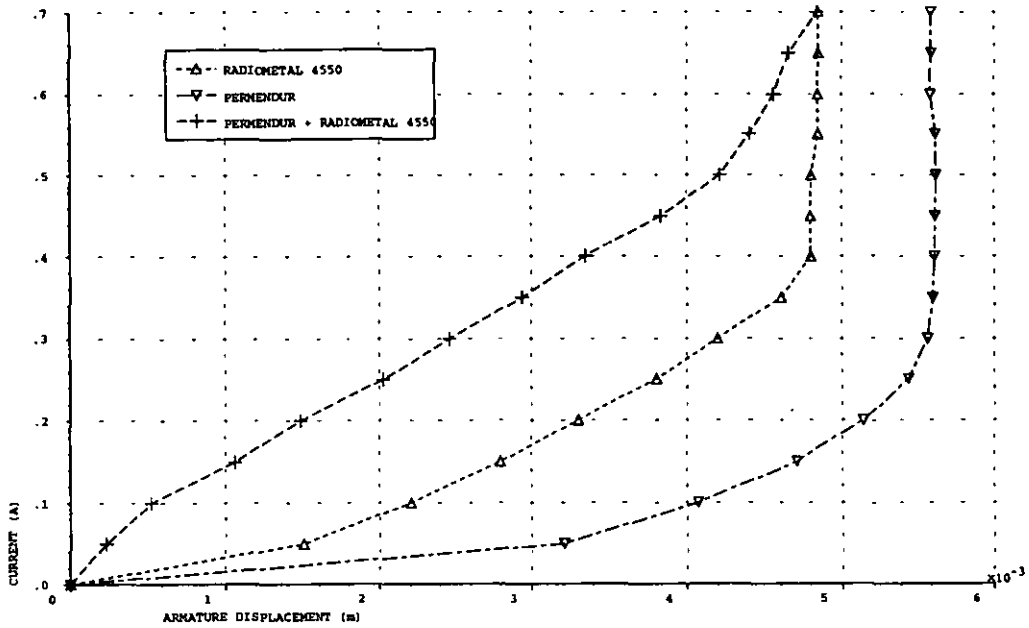


Fig. 8.35 Comparison of coil current/armature displacement characteristics for various composite material designs

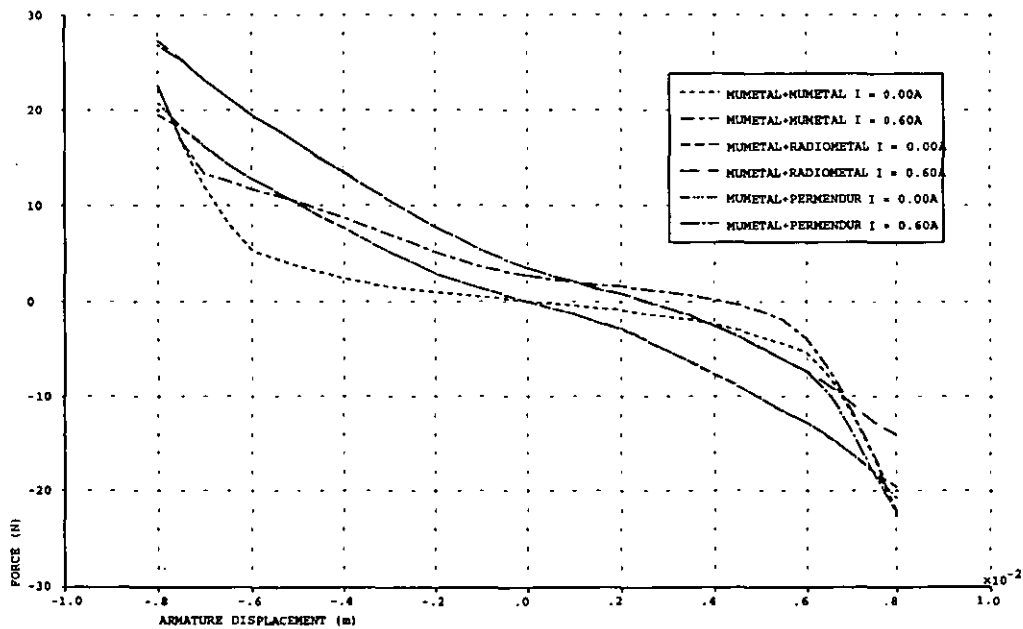


Fig. 8.36 Comparison of force characteristics for the 25 mm diameter hollow armature (10 mm diameter hole) design when using a Mumetal stator and various armature materials

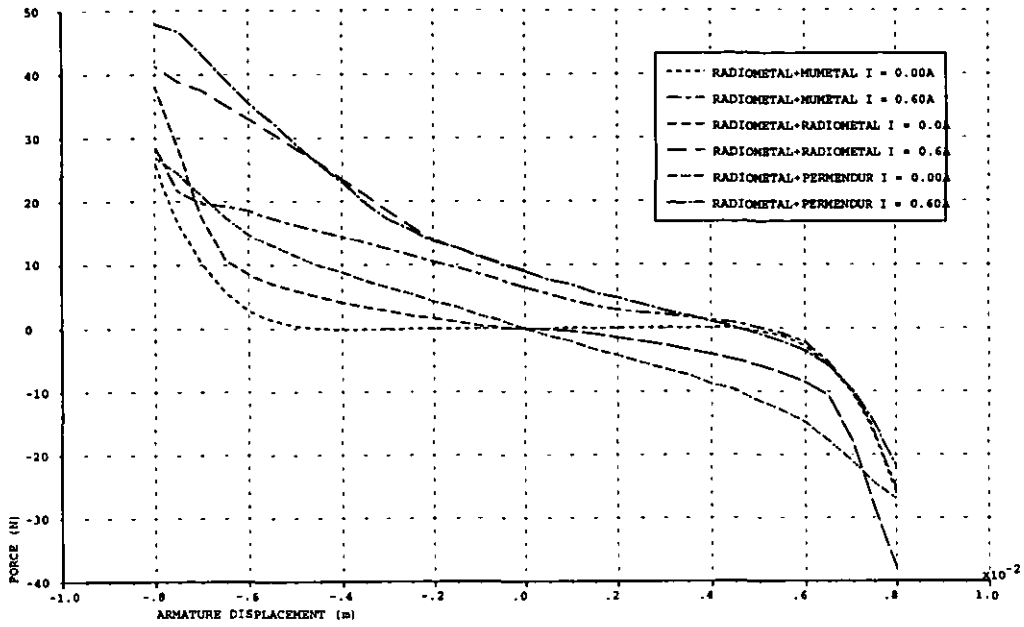


Fig. 8.37 Comparison of force characteristics for the 25 mm diameter hollow armature (10 mm diameter hole) design when using a Radiometal stator and various armature materials

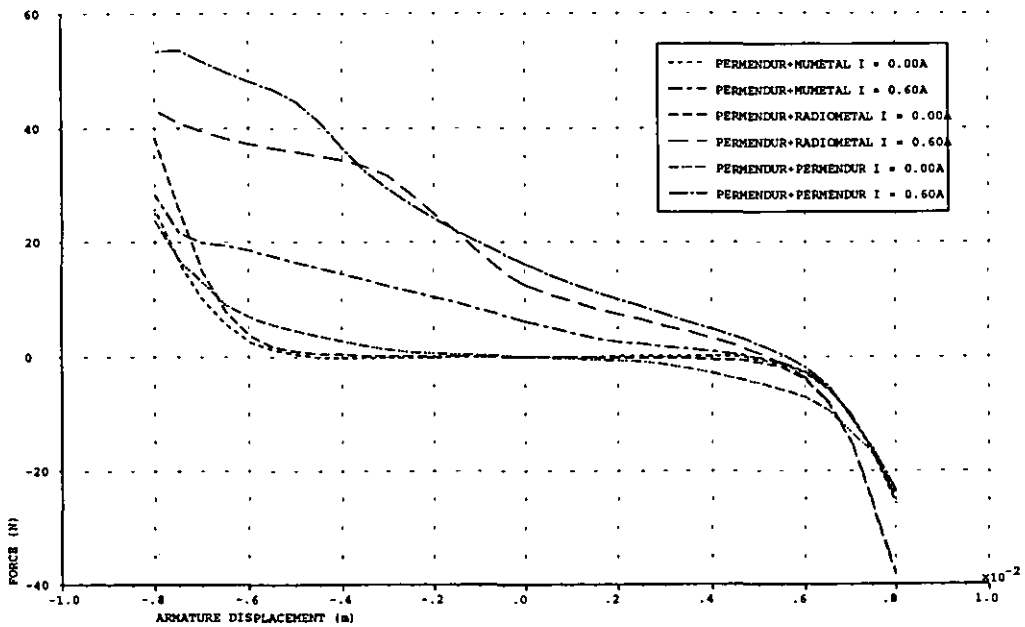


Fig. 8.38 Comparison of force characteristics for the 25 mm diameter hollow armature (10 mm diameter hole) design when using a Permendur stator and various armature materials

## **OPTIMIZATION OF THE LINEAR RELUCTANCE MOTOR**

The objective of the two previous chapters was to improve the design of the linear motor, by making major changes to the magnetic circuit geometry and experimenting with different magnetic materials. This final part of the motor evolution uses an optimization routine to make minor geometrical modifications to this re-formed motor, so as to produce an optimum design.

### **9.1 DETERMINATION OF OPTIMIZATION PROCEDURE**

Optimization algorithms, such as simulated annealing [95, 96] or evolutionary methods [97], are penalty function constrained optimization techniques used to minimise an application specific objective function. Methods such as these are however restricted when attempting to optimize both the static and dynamic performance of a device, and because the dynamic performance of the linear motor is important they were not considered.

An alternative scheme employed recently uses a geometric parameter scanning optimization technique [98], based on an analytical model of the device under development to predict its static characteristics and coupled to an equivalent circuit representation of the mechanical system [92] to determine its dynamic performance. When the leading design parameters have been identified, the method then increments these between pre-specified limits, with designs being produced for many possible parameter combinations. This scheme has been shown to produce good results when an accurate analytical model of the device has been produced, but since the magnetic circuit of the linear motor is moderately to highly saturated the non-linear characteristics of the magnetic materials must be taken into account. This would however excessively complicate a model, because an equivalent non-linear lumped parameter network would have to be developed, using cubic splines to represent the material curves and standard permeance formulae to evaluate the reluctances to allow

accurate evaluation of the air-gap flux density.

A simpler approach to optimization is to identify the leading design parameters, to assign two states to each, and to use an interactive finite element software package such as *MEGA* to obtain designs for each parameter combination that can then be modelled and assessed. This method does not require an analytical model to be produced, but limits the number of design parameters that can be investigated, since a separate finite element model and subsequent post-processing needs to be produced for each parameter combination. The factorial design method described below is based on this approach.

## 9.2 FACTORIAL DESIGN STUDIES

Factorial design studies are widely used in experiments involving several parameters [99, 100], when it is necessary to study the interactive effect of the various parameters on a particular response. They have been used in previous computer-based investigations [101, 102], as an aid to the identification of the sensitivity to parameter changes of a specific response of an electrical system. The most useful design method in the early stages of optimization, when there are likely to be many factors to be investigated, is the  $2^n$  factorial design, where  $n$  is the number of variable parameters.

### 9.2.1 The $2^n$ Factorial

With this method each parameter is set at only two levels. A complete analysis of a motor design then requires  $2^n$  tests and provides the smallest number of tests with which  $n$  parameters can be studied in a complete factorial design, although the use of only two levels assumes that the response is approximately linear over the range of the parameter levels defined. The method consists of determining a general response model that relates the overall response of interest  $y$  to the parameters  $x$  being varied, and then using the calculated responses obtained for each parameter combination to determine the coefficients  $\beta$  in this model. That is, if  $\beta_0$  is the response with nominal parameters and  $x_1, x_2, x_{12}, \dots$  are the variations in these parameters from their nominal

values and  $\beta_1, \beta_2, \beta_{12}, \dots$  are the coefficients of the variation in response due to the varying parameters, then for  $n = 3$  the response  $y$  can be described by:

$$y = \beta_0 + \beta_1 x_1 + \beta_2 x_2 + \beta_3 x_3 + \beta_{12} x_1 x_2 + \beta_{13} x_1 x_3 + \beta_{23} x_2 x_3 + \beta_{123} x_1 x_2 x_3 \quad (9.1)$$

### 9.2.2 Armature Variable Parameters

The responses of interest when optimizing the linear motor are:

- linearity of coil current/armature displacement characteristic;
- maximum armature displacement;
- stiffness characteristic;
- dynamic performance;
- force generated at armature central position;
- force/coil current ratio and;
- force/armature mass ratio.

The last three responses are closely related but will be considered individually. The influential geometric parameters can be divided into two groups, those on the armature and those on the stator, and two separate factorial design studies were therefore undertaken. Before the factorial design study was implemented the length of the stator pole-shoe gap was reduced in the motor design evolved in chapters 7 and 8. A 7 mm gap was considered slightly too large, since it might inhibit the motion of the armature and reduce its maximum displacement.

A number of finite element investigations were performed at pole-shoe gaps of 3, 5 and 7 mm, with the narrow centre-section having lengths of 20.52 mm, as in the improved design, and 16.52 mm. The analysis was carried out at 0.7 A over the complete armature stroke length, and the results are shown in Figs. 9.1 and 9.2 for the two lengths and the various pole-shoe gaps. Little difference is seen in Fig. 9.1 between the different designs with, in each case, the armature moving to a position approximately 4.65 mm from its central position. In Fig. 9.2 the maximum armature



displacement increases from about 4.30 mm for a gap length of 7 mm to about 5.00 mm for a 3 mm gap. A reduction in the pole-shoe gap also causes the generated force to drop slightly, therefore a compromise must be sought. It was therefore decided to fix the gap length at 5 mm (pole-shoe length of 16.5 mm) when implementing the factorial design study.

The characteristics of the improved motor design (with the 16.5 mm long pole-shoes) are shown in Figs. 9.3 to 9.6. The stiffness, coil current/armature displacement characteristic at no load and force/coil current characteristic at the armature central position are all clearly non-linear. The dynamic performance of the motor is compared in Fig. 9.6 with a design geometrically identical but with the armature made from Radiometal, to highlight the effect of the Permendur armature.

### 9.2.3 The Armature Factorial Design Study

The armature dimensions that were altered in the improved design, together with their nominal values, associated variable parameters and unit variations, are shown in Table 9.1.

Factorial design parameter	Armature parameter	Nominal value (mm)	Unit variation
$x_1$	outer radius	12.192	$\pm 5\%$
$x_2$	inner radius	5.000	$\pm 40\%$
$x_3$	centre-section radius	10.407	$\pm 5\%$
$x_4$	centre-section length	20.517	$\pm 25\%$

**Table 9.1** Variation in armature parameters for factorial design study

The outer radius was varied by only  $\pm 5\%$ ; since making the variation larger, i.e.  $\pm 10\%$ , would have increased the armature mass substantially and degraded the dynamic

performance. The lower limit would have produced an outer radius smaller than the upper limit of the narrow centre-section radius (if a variation of about  $\pm 5\%$  was also used for this parameter) thereby distorting the shape of the armature. Hence, a very small variation would be needed for the centre-section radius, of the order of  $\pm 2\%$ , to maintain the narrowing of the armature at the centre-section when this parameter was at its upper limit. Such a small variation would however produce minimal change in motor performance and would be pointless to implement.

The armature inner radius was set at  $\pm 40\%$ , resulting in a 3 mm radius hole at the lower limit of the parameter and a 7 mm radius at the upper limit, the nominal hole radius being 5 mm. A wider variation was not used, as a larger radius hole would reduce appreciably the armature cross-sectional area, resulting in saturation and a non-linear coil current/armature displacement characteristic. A 3 mm radius hole should be sufficient to produce a linear device when using Permendur, with any further reduction in the radius having minimal affect on the linearity but adding to the armature mass.

The unit variation of the centre-section radius was set at  $\pm 5\%$ , for a  $\pm 5\%$  change in the outer radius, and this produced a wide range of armature shapes for the various combinations of both parameters. The centre-section length was varied by  $\pm 40\%$ , to produce again a large variety of armature geometries that would result in a wide range of maximum armature displacements. Fig. 9.7 illustrates the armature parameter changes and the unit variation of each.

The different combinations of parameter limits for which the finite element investigations were performed are specified by the factorial design plan of Table 9.2, where the positive and negative signs indicate for each investigation the upper and lower parameter limit settings defined in Table 9.1. The signs of the interactive effects, (i.e.  $x_{12}$  is the combined or interactive effect of the individual parameters  $x_1$  and  $x_2$ ), are obtained by multiplication of the signs of the individual parameters. The full plan requires  $2^4$  or 16 finite element investigations and Fig. 9.8 shows 4 of the 16 designs modelled, these being designs 6, 7, 10 and 11.

No.	(1)	$x_1$	$x_2$	$x_3$	$x_4$	$x_{12}$	$x_{13}$	$x_{14}$	$x_{23}$	$x_{24}$	$x_{34}$	$x_{123}$	$x_{124}$	$x_{134}$	$x_{234}$	$x_{1234}$
1	+	+	+	+	+	+	+	+	+	+	+	+	+	+	+	+
2	+	-	+	+	+	-	-	-	+	+	+	-	-	-	+	-
3	+	+	-	+	+	-	+	+	-	-	+	-	-	+	-	-
4	+	+	+	-	+	+	-	+	-	+	-	-	+	-	-	-
5	+	+	+	+	-	+	+	-	+	-	-	+	-	-	-	-
6	+	-	-	+	+	+	-	-	-	-	+	+	+	-	-	+
7	+	-	+	-	+	-	+	-	-	+	-	+	-	+	-	+
8	+	-	+	+	-	-	-	+	+	-	-	-	+	+	-	+
9	+	+	-	-	+	-	-	+	+	-	-	+	-	-	+	+
10	+	+	-	+	-	-	+	-	-	+	-	-	+	-	+	+
11	+	+	+	-	-	+	-	-	-	-	+	-	-	+	+	+
12	+	-	-	-	+	+	+	-	+	-	-	-	+	+	+	-
13	+	-	-	+	-	+	-	+	-	+	-	+	-	+	+	-
14	+	+	-	-	-	-	-	-	+	+	+	+	+	+	-	-
15	+	-	+	-	-	-	+	+	-	-	+	+	+	-	+	-
16	+	-	-	-	-	+	+	+	+	+	+	-	-	-	-	+

Table 9.2 Complete factorial design plan for the four armature parameters

9.2.3.1 Analysis of the Response Models

The general response model for the study is:

$$\begin{aligned}
 y = & \beta_0 + \beta_1x_1 + \beta_2x_2 + \beta_3x_3 + \beta_4x_4 + \beta_{12}x_1x_2 + \beta_{13}x_1x_3 + \beta_{14}x_1x_4 \\
 & + \beta_{23}x_2x_3 + \beta_{24}x_2x_4 + \beta_{34}x_3x_4 + \beta_{123}x_1x_2x_3 + \beta_{124}x_1x_2x_4 \\
 & + \beta_{234}x_2x_3x_4 + \beta_{134}x_1x_3x_4 + \beta_{1234}x_1x_2x_3x_4
 \end{aligned}
 \tag{9.2}$$

When analyzing the responses obtained from the factorial design plan a single figure is needed to calculate the coefficients of equation (9.2), and each response of the

motor is therefore represented by a single value taken from the characteristics. Thus the stiffness is regarded as the returning force when the armature is displaced 4.0 mm from its central position and the force generated at the central position of the armature is that for a coil current is 0.70 A. The dynamic performance of each design is represented by the peak armature displacement when a 0.50 A peak sinusoidal current waveform is forced through the coil at a frequency of 30 Hz, obtained using the simulation program of section 6.5. The viscous damping coefficients for the sixteen motor designs were calculated using the mechanical time constant determined in section 6.2.3.

The maximum armature displacement is determined when the coil current is 0.7 A. The armatures are modelled at 0.1 mm increments in armature displacement around the suspected range of zero force. When the force  $F$  reverses in sign from one displacement increment  $x_p$ , with a positive force  $F_p$ , to another incremental displacement  $x_n$ , with a negative force  $F_n$ , the zero force acting on the armature has been detected. The position of the zero force  $x_0$  is determined by linear interpolation as:

$$x_0 = x_p + (x_n - x_p) \left[ \frac{F_p}{F_p + F_n} \right] \quad (9.3)$$

Since the incremental movement is small, the force characteristic can be assumed linear between each increment, which results in an accurate position of the zero force.

The coil/current armature displacement characteristics for each design are determined from 0 to 0.7 A by the same method used to find the maximum armature displacement. The linearity is represented by first fitting a least squared  $y = ax$  function [103] to the coil current/armature displacement characteristics of each of the 16 designs, considering only 90% of the armature movement to eliminate the sharp gradient observed in most of the characteristics at each limit of armature movement. The least squares routine fits a linear function to each characteristic, so as to minimize the sum of the errors between the linear fitted function and the coil current/armature displacement characteristic at every calculated point along this characteristic, that is:

$$\sum_{i=1}^n (y_i - \hat{y}_i)^2 \quad (9.4)$$

where  $y_1, y_2, \dots, y_n$  are the points along the characteristic and  $\hat{y}_1, \hat{y}_2, \dots, \hat{y}_n$  are points fitted by the linear equation. The sample variance  $s^2$  is then calculated from:

$$s^2 = \frac{\sum_{i=1}^n (y_i - \hat{y}_i)^2}{n - 1} \quad (9.5)$$

and the smaller the variance the more linear is the characteristic.

The force/coil current ratio, or motor constant, is calculated, again using the least squared  $y = ax$  function, and is fitted from zero to 0.6 A. At higher currents a number of the gradients of the characteristics start to decrease due to saturation, which would distort the linear function fit. The least squares fit is  $F = k_f I$ , where  $k_f$  is the motor constant, similar to a dc motor. This method can be applied to the characteristics because below 0.6 A, they are nearly linear, and each fit is good with a minimal sample variance. The force/armature mass ratio was obtained by dividing the force developed at the armature central position when using a coil current of 0.7 A by the armature mass.

Calculated values of the seven responses for the 16 motor designs are given in Table 9.3. The characteristics of stiffness, force developed at the central position and the coil current/armature displacement for the 16 designs are shown in Figs. 9.9, 9.10 and 9.11 respectively. The force/current and force/armature mass ratios are shown diagrammatically in Figs. 9.12 and 9.13, and clearly show the superiority of five designs; 1, 4, 7, 9 and 12.

No.	stiffness $F_{max}$ (N)	force @ 0.7 A (N)	max. $x$ (mm)	linearity $\times 10^{-4} s^2$ (A <sup>2</sup> )	dynamic response (mm) pk.	force/ current (N/A)	force/ mass (N/kg)
1	18.39	14.71	2.957	3.375	5.60	21.60	78.17
2	2.950	8.547	4.345	3.864	1.65	14.23	56.43
3	18.39	14.81	3.555	3.725	2.20	21.59	56.09
4	28.74	14.82	2.003	2.077	4.40	24.81	85.17
5	6.602	4.392	4.026	30.34	0.47	5.813	21.98
6	5.996	8.885	5.269	1.564	0.98	13.52	39.12
7	14.08	14.20	3.000	4.579	5.20	24.13	103.5
8	1.409	4.612	5.290	6.733	0.79	7.945	29.69
9	23.03	17.89	3.293	2.331	5.20	25.57	71.68
10	6.793	4.464	3.862	34.40	0.33	5.886	16.20
11	7.767	4.138	2.582	9.063	0.57	6.250	21.63
12	13.41	15.59	4.428	1.129	3.25	22.70	73.23
13	3.577	4.993	5.145	7.064	0.51	7.523	21.61
14	7.898	4.889	3.739	27.02	0.39	6.469	18.31
15	2.659	6.385	4.790	4.570	1.32	11.26	43.49
16	5.630	6.894	4.956	2.262	0.77	10.37	30.99

**Table 9.3** Results for the seven responses

To determine an optimum design, Table 9.4 lists each response and the six best designs for that response. Designs 1, 4, 7, 9, and 12 are consistently high in the order of merit for most responses. The greatest maximum armature displacement obtained from these five designs was 4.428 mm (design 12), and the maximum displacement achieved by the other four was design 9, whose armature moved to a maximum displacement of only 3.293 mm. Table 9.4 highlights the positions of design 12, which is the most linear of the 16 designs, generates the second largest force at the

order of merit	response						
	stiffness $F_{mag}$	force @ 0.7 A	max. $x$	linearity $s^2$	dynamic response	force/ current	force/ mass
1st	4	9	8	12	1	9	7
2nd	9	12	6	6	7	4	4
3rd	1	4	13	4	9	7	1
4th	3	3	16	16	4	12	12
5th	7	1	15	9	12	1	9
6th	12	7	12	1	3	3	2

**Table 9.4** Performance merit of the 16 designs for each response

central position and performs exceptionally well in all the other response tests.

### 9.2.3.2 Analysis of the Coefficients of the Response Models

The magnitude of the coefficients of equation (9.2) can be used to produce a short list of possible optimum designs, because they indicate the significance of each parameter in affecting each response. Parameter limits that improve the performance of each response can be determined by studying the sign of coefficients that are particularly large in magnitude with respect to other coefficients in any one response model. Having found parameter limit settings that improve the responses, the factorial design plan given in Table 9.2 can be used to find the designs with the parameter settings determined.

The coefficients of equation (9.2) for each response were determined from the mean of the 16 calculated values given in Table 9.3, when summed in accordance with the signs in the correct column in the design plan. For example, in determining coefficient  $\beta_0$  the mean of the 16 responses is calculated, since column (1) contains all + signs. However in obtaining  $\beta_1$ , the coefficient relating to variation in the

armature outer diameter, the responses have to be summed taking into account the + and – signs in the  $x_1$  column, that is:

$$\beta_1 = \frac{y_1 - y_2 + y_3 + y_4 + y_5 - y_6 - y_7 - y_8 + y_9 + y_{10} + y_{11} - y_{12} - y_{13} + y_{14} - y_{15} - y_{16}}{16}$$

$$\approx 4.243$$
(9.6)

The coefficients of the seven response models obtained by this method are given in Table 9.5. For each response, the coefficients that have a relatively large magnitude in each response model are highlighted.

In Table 9.5 the stiffness response has coefficients  $\beta_1$  and  $\beta_4$  highlighted, therefore, to produce a large stiffness, parameters  $x_1$  and  $x_4$  in equation (9.2) will need to be at the upper limit (+1) to produce positive products of  $\beta_1 x_1$  and  $\beta_4 x_4$ . Similarly, the force developed at the central position for a current of 0.70 A will be large when parameter  $x_4$  is at its upper limit, thereby creating a large force  $\beta_4 x_4$ . The maximum armature displacement response has coefficient  $\beta_1$  highlighted, so fixing  $x_1$  at its lower limit (–1) will produce a product  $\beta_1 x_1$  of positive sign to maximise the armature displacement.

When attempting to improve the linearity, the sample variance needs to be minimised, and in Table 9.5 the corresponding coefficients  $\beta_1$  and  $\beta_4$  are highlighted. The product  $\beta_1 x_1$  therefore needs to be negative, which requires  $x_1$  to be set at its lower limit since  $\beta_1$  is positive. Similarly,  $x_4$  needs to be set at its upper limit to produce a product  $\beta_4 x_4$  with a negative sign. The dynamic response, force/current ratio and the force/armature mass ratio all have a large  $\beta_4$  coefficient, which requires the parameter  $x_4$  to be set at its upper limit to improve all three responses.

It is clear from the above analysis that for an optimum design  $x_4$  needs to be at its upper limit, which will improve considerably six of the seven responses. Setting  $x_1$  to its lower limit will produce a more linear device that will have a large stroke length but with a slightly reduced stiffness, since  $x_1$  needs to be at its upper limit to improve the



coef.	stiffness $F_{mag}$	force @ 0.7 A	max. $x$ $\times 10^{-4}$	linearity $s^2$ $\times 10^{-4}$	dynamic response $\times 10^{-4}$	force/ current	force/ mass
$\beta_0$	10.46	9.388	39.52	9.006	21.01	14.35	47.95
$\beta_1$	4.243	0.625	-7.004	5.035	2.934	0.394	-1.800
$\beta_2$	-0.133	-0.413	-3.285	-0.931	3.991	0.150	7.049
$\beta_3$	-2.444	-1.213	3.537	2.377	-5.353	-2.091	-8.042
$\beta_4$	5.167	4.292	-3.463	-6.175	14.59	6.664	22.47
$\beta_{12}$	0.806	-0.085	-0.316	-1.896	-0.334	-0.282	-1.466
$\beta_{13}$	0.288	0.791	-0.058	1.542	2.909	1.064	4.998
$\beta_{14}$	2.270	1.250	0.461	-4.989	4.966	1.979	4.159
$\beta_{23}$	-0.543	0.303	1.768	0.626	1.628	-0.017	-0.394
$\beta_{24}$	0.550	-0.199	-2.018	1.574	2.534	0.023	3.340
$\beta_{34}$	-1.748	-0.732	0.716	-2.076	-4.172	-1.193	-4.924
$\beta_{123}$	-0.178	0.155	0.749	1.099	3.566	0.131	1.773
$\beta_{124}$	0.204	-0.094	0.897	1.102	0.309	-0.079	-2.997
$\beta_{134}$	0.159	0.353	-1.154	-1.170	2.116	0.422	2.321
$\beta_{234}$	-0.636	0.202	-0.273	-0.781	2.022	0.023	-0.148
$\beta_{1234}$	-0.071	0.086	-0.514	-0.967	3.284	0.056	0.913

**Table 9.5** Coefficients of the seven response models

stiffness. Designs that have the parameter combinations of  $x_1$  (-1), and  $x_4$  (+1) will therefore be superior to the others, and these designs are 2, 6, 7 and 12.

It can be seen however that designs 2 and 6 do not appear in Table 9.4. This is due to parameter  $x_3$ , (the centre-section radius), being set at its upper limit, which when coupled with  $x_1$ , (the outer radius), set at its lower limit, produces an armature with only a small reduction from the outer radius to the narrow centre-section radius. This

is clearly seen in Table 9.5, where six out of the seven  $\beta_4$  coefficients require  $x_3$  to be at its lower limit to aid the performance, with only the maximum armature displacement response suffering. Design 7 can also be dismissed, because as Table 9.4 shows its maximum armature stroke length is only 3.0 mm and it fails also on linearity. This analysis confirms the earlier statement that design 12 provides the best characteristics of the 16 that were modelled.

Fig. 9.9(b) shows that the stiffness characteristic of design 12 is fairly linear over the whole armature stroke. The force/current characteristic of Fig. 9.10(b), for the armature at its central position, shows a slight non-linearity at small coil excitations, and Fig. 9.11(b) shows that the coil current/armature displacement characteristic is quite linear up to 3.8 mm.

### 9.2.3.3 Variation of Parameter Limit Settings

A method for checking the accuracy of the response model is to obtain the seven responses with all the parameters set at their nominal values, i.e.  $x_1 = x_2 = x_3 = x_4 = 0.0$ , and to compare their values with the finite element results. Table 9.6 compares corresponding results, and shows that the stiffness, force at the central position, force/current ratio and force/armature mass ratio obtained by the two calculations are in good agreement.

method	response						
	stiffness $F_{mag}$ (N)	force @ 0.7 A (N)	max. $x$ (mm)	linearity $\times 10^{-4} s^2$ (A <sup>2</sup> )	dynamic response (mm) pk.	force/ current (N/A)	force/ mass (N/kg)
F.D.S.	10.46	9.388	3.952	9.006	2.10	14.35	47.95
F.E.	9.547	9.331	4.566	6.408	1.47	13.64	43.86

**Table 9.6** Comparison of the seven responses from factorial design study (F.D.S.) and from the finite element (F.E.) investigation

The differences between the factorial design responses and those responses determined from the finite element investigation range from 0.61% (force at central position) to 30.00% (dynamic response). The stiffness error is 8.73%, the maximum armature displacement error is 15.54% and the linearity error is 28.85%. These large errors highlight the problem with a response model in which the parameter variations are assumed to be first order only. This assumption reduces the value of the model as an accurate design tool, although valuable information can be gained from the coefficients of the model in finding a possible optimum design. To produce a response model of some merit an alternative factorial design study, such as  $2^n$  (with mid-points) or  $3^n$  [99, 100] should be used, but both of these require a large increase in the number of finite element investigations required and would be excessively time consuming to implement. The  $3^n$  study would require 81 separate finite element models to be constructed, since  $n = 4$ , which is clearly not practical.

The response models can however be of value and produce useful results when considering responses outside the parameter variation limits, providing the limits are not too large. This is shown in Table 9.7 where parameter  $x_2$ , the armature inner radius, is set to +1.0 (design 7, hole radius = 7.0 mm), -1.0 (design 12, hole radius = 3.0 mm), -1.5 (hole radius = 2.0 mm) and -2.0 (hole radius = 1.0 mm).

param. $x_2$	response						
	stiffness $F_{mag}$ (N)	force @ 0.7 A (N)	max. $x$ (mm)	linearity $\times 10^{-4} s^2$ (A <sup>2</sup> )	dynamic response (mm) pk.	force/ current (N/A)	force/ mass (N/kg)
+1.0	14.08	14.20	3.000	4.579	5.20	24.13	103.5
-1.0	13.41	15.59	4.428	1.129	3.25	22.70	73.23
-1.5	13.25	15.94	4.786	0.267	2.76	22.34	65.67
-2.0	13.08	16.29	5.143	-0.596	2.28	21.99	58.12

**Table 9.7** Seven responses from the factorial design study when parameter  $x_2$  is above the upper limit

Outside the parameter limits the results are acceptable with the exception of the linearity response when  $x_2 = -2.0$ , which is negative and too large, meaning that for this particular response the parameter variation is too large. As the armature hole decreases in size the dynamic response suffers, as expected since the armature mass has increased, and the maximum armature displacement has increased as expected from the findings in section 8.2. Again, as expected, the linearity is improved when  $x_2 = -1.5$ , since the increased cross-sectional area of the armature has reduced the flux density. The force generated at the armature central position has increased as the hole radius is reduced, while the force/armature mass ratio has fallen due to the large increase in armature mass.

#### 9.2.4 The Stator Factorial Design Study

A number of constraints are imposed on the motor, including overall motor length and diameter, and these reduce considerably the number of dimensions that can be varied on the stator. The coil dimensions were kept fixed to keep the maximum current density at approximately  $8.0 \text{ A/mm}^2$  and the copper losses at an acceptable level. Increasing the coil size would also reduce the magnetic circuit dimensions and further increase the flux density which in certain parts of the motor, is already about  $1.2 \text{ T}$ .

To change significantly the permanent magnet dimensions at this stage of the motor development would be pointless, as the design is near optimum with the existing magnet dimensions. Therefore, the magnet length was kept fixed, but the inner radius was varied slightly, to allow for further small improvements. Additionally, to increase the length of the magnets and keep the coil and overall motor length the same would mean reducing the length of the stator yokes and/or end-rings, which must be avoided due to increased iron saturation. The only other dimension that was varied was the pole-shoe length since, when studying the cross-section of design 12, the ends of the pole-shoes appear to be redundant even when the armature has its maximum displacement. Table 9.8 shows the variations that were investigated.

Factorial design parameter	Stator parameter	Nominal value (mm)	Unit variation
$x_1$	pole-shoe length	13.677	$\pm 17\%$
$x_2$	magnet inner radius	15.000	$\pm 6.6\%$

**Table 9.8** Variation in stator parameters for factorial design study

The magnet inner radius variation of  $\pm 6.6\%$  resulted in a lower limit radius of 14.0 mm and an upper limit of 16.0 mm. Setting the existing pole-shoe length to the upper limit of its variation and the lower limit such that with the armature at its central position the edge of the armature (where the narrow centre-section starts) is at the middle of the pole-shoe, created a parameter variation of  $\pm 17\%$ . Fig. 9.14 illustrates the stator parameter changes and the unit variation of each.

The different combinations of the parameter limits for which the finite element investigations were performed are given in Table 9.9.

No.	(1)	$x_1$	$x_2$	$x_{12}$
12.1	+	+	+	+
12.2	+	-	+	-
12.3	+	+	-	-
12.4	+	-	-	+

**Table 9.9** Complete factorial design plan for the two stator parameters

Positive and negative signs indicate the upper and lower parameter limit settings. The full plan requires only  $2^2$  or 4 finite element investigations and Fig. 9.15 shows 2 of the 4 designs modelled, (12.1 and 12.4).

### 9.2.4.1 Analysis of the Response Models

The general response model for the study is:

$$y = \beta_0 + \beta_1 x_1 + \beta_2 x_2 + \beta_{12} x_1 x_2 \quad (9.7)$$

and all seven responses for the four designs were calculated. Identical methods to those described in section 9.2.3.1 were used and the results are given in Table 9.10.

It is clear from Table 9.10 that the designs with the shorter pole-shoes (12.2 and 12.4) have a number of advantages over the longer pole-shoe designs (12.1 and 12.3). The stiffness, force developed at the central position, dynamic response, force/current ratio and force/armature mass ratio are all better than for the two longer pole-shoe designs. The only disadvantage is that the maximum armature displacements are about 0.2 mm smaller.

No.	stiffness $F_{mag}$ (N)	force @ 0.7 A (N)	max. $x$ (mm)	linearity $\times 10^{-6} s^2$ (A <sup>2</sup> )	dynamic response (mm) pk.	force/ current (N/A)	force/ mass (N/kg)
12.1	10.03	14.17	4.929	1.269	2.92	22.02	66.54
12.2	12.09	17.78	4.707	2.098	4.37	26.82	83.49
12.3	16.06	17.50	4.029	5.190	4.05	24.78	82.21
12.4	18.70	22.54	3.874	7.073	5.40	31.66	105.9

**Table 9.10** Results for the four responses

Figs. 9.16 and 9.17 show the stiffness and the force/current characteristics of designs 12.2 (magnet inner radius = 16.0 mm) and 12.4 (magnet inner radius = 14.0 mm). From Fig. 9.17, the characteristic below 0.30 A of design 12.2 appears to be convex whereas that of design 12.4 appears to be concave. An optimum design clearly exists between the two, where the force/current characteristic is linear, which is confirmed by the coil current/armature displacement characteristics of Fig. 9.18.

The problem now exists of determining the linearity of each coil current/armature displacement characteristic. The armature factorial design study produced good results, but Fig. 9.18 highlights that it is clearly not now appropriate since each design appears to be quite linear between 0.10 A and 0.30 A, although below 0.10 A both are non-linear. Problems arise when a least squared  $y = ax$  function is fitted to these characteristics, because the function will not fit the best straight line through the linear part of each characteristic since the origin of each curve will affect the fit. A better method to represent the curves is to fit a  $y = ax + b$  function to the results, when the linear portion of each characteristic will be fitted well and the origin ignored. The objective of the optimization is then to minimise the constant  $b$  in the equation. Table 9.11 gives the constants for the four designs.

Design No.	constant $b$ $\times 10^{-2}$ (A)	Design No.	constant $b$ $\times 10^{-2}$ (A)
12.1	-2.106	12.3	4.509
12.2	-4.090	12.4	2.737

**Table 9.11** Constant  $b$  for the four responses

#### 9.2.4.2 Analysis of the Coefficients of the Response Models

Table 9.12 gives the coefficients of equation (9.7) for the seven responses, with the sample variance replaced by the more appropriate constant  $b$ . It is clear from the table that to increase the performance of five of the responses, (the stiffness, force developed at the armature central position, dynamic response, force/current ratio and force/armature mass ratio), it is necessary to set both parameters at the lower limits which results in the products  $\beta_1 x_1$  and  $\beta_2 x_2$  improving the performance. As discussed previously, the only response that benefits from both parameters being set at their upper limits is the maximum armature displacement. Design 12.4 ( $x_1 = x_2 = -1.0$ ) appears to produce the best performance with an optimum clearly existing between 12.2 and 12.4 (see Figs. 9.17 and 9.18).

coef.	stiffness $F_{mag}$	force @ 0.7 A	max. $x$ $\times 10^{-4}$	linearity const. $b$ $\times 10^{-3}$	dynamic response $\times 10^{-4}$	force/ current	force/ mass
$\beta_0$	14.22	18.00	43.85	2.627	41.85	26.32	84.53
$\beta_1$	-1.175	-2.162	0.942	9.389	-7.000	-2.920	-10.16
$\beta_2$	-3.159	-2.026	4.333	-33.60	-5.400	-1.897	-9.514
$\beta_{12}$	0.147	0.357	1.679	0.529	-0.250	0.521	1.679

**Table 9.12** Coefficients of the seven response models

### 9.2.5 Determining the Optimum Design

The optimum design can be determined by rearranging equation (9.7) for  $x_2$  and substituting  $x_1 = -1.0$  (common to both design 12.2 and 12.4) and  $y = 0$ . This effectively sets the constant  $b$  to zero and gives:

$$x_2 = \left[ \frac{y - \beta_0 - \beta_1 x_1}{\beta_2 + \beta_{12} x_1} \right] \quad (9.8)$$

where the coefficients  $\beta_0$ ,  $\beta_1$ ,  $\beta_2$  and  $\beta_{12}$  are given in Table 9.12. The resulting value of  $-0.198$  means that the optimum design has a magnet inner radius of  $(15.0 - 0.198) = 14.802$  mm. This however assumes that the relationship between the magnet inner radius and the constant  $b$  is linear, and assumptions such as this were shown in section 9.2.3.3 to be inaccurate for other responses. The magnet inner radius was therefore set to 15.00 mm when determining the optimum design. A finite element analysis undertaken with a magnet inner radius of 15.00 mm (design 12.5) produced a constant  $b$  of  $+6.608 \times 10^{-3}$ . A further analysis with an inner radius of 15.50 mm (design 12.6) gave a value for  $b$  of  $-8.864 \times 10^{-3}$ . A curve fitted to the four constants obtained for inner radii of 14.00, 15.00, 15.50 and 16.00 mm, is shown in Fig. 9.19, and an inner radius of about 15.25 mm (design 12.7) was determined at that which would make  $b = 0$ , i.e. a linear design. Fig. 9.19 also highlights the inadequacy of modelling the relationship as a linear function.



Figs. 9.20, 9.21 and 9.22 compare the stiffness, force/current and coil current/armature displacement characteristics for design 12.2 (inner radius = 16.00 mm), design 12.4 (inner radius = 14.00 mm) and the optimum design 12.7 (inner radius = 15.25 mm). The force/current characteristic for the optimum design is linear up to maximum excitation and the coil current/armature displacement characteristic when the motor is unloaded is quite linear up to approximately 3.7 mm. The stiffness is however slightly non-linear.

### 9.3 OPTIMUM DESIGN

The stator and armature dimensions of the optimum design are shown in Figs. 9.23(a) and (b). The following section compares the optimized design with the improved design (before the factorial design study) and the original prototype.

#### 9.3.1 Comparison of Optimized, Improved and Original Designs

Fig. 9.24 illustrates the high air-gap flux density of the optimized and improved designs compared with the original prototype, where for the optimum design the increase is about 0.7 T under the stator end-rings and 0.85 T under the stator pole-shoes. The improved stiffness characteristic, seen in Fig. 9.25, would then easily overcome a substantial amount of bearing friction to return the armature to its central position. Fig. 9.26 shows the force/current characteristic with the armature in its central position. The excellent linearity of the optimized design is evident as is the large increase in gradient over the improved design. The very poor result from the original design again highlights the hazard of armature saturation. The large increase in both stiffness and force/current characteristics in the optimum design is a consequence of the smaller pole-shoes and pole-face overlap. The coil current/armature displacement characteristics of the three designs on no-load given in Fig. 9.27 confirm the linearity of the optimized design up to about 3.7 mm and show the bistable action of the original design.

Fig. 9.28 shows the dynamic response for the three designs and illustrates that at frequencies above 25 Hz the optimum design is clearly better. The peak coil current in the original and improved designs was 0.6 A over the whole frequency range, whereas for the optimized design it had to be reduced to 0.2 A at about 20 Hz, (see Fig. 9.29), to prevent the increased armature displacement damaging the motor. This frequency is clearly the natural self-resonant frequency  $f_r$  of the motor which is clearly the most effective frequency at which to operate [104]. Where the input power to maintain the motion of the armature is minimal. At this frequency the applied coil force  $F_{coil}$  is equal to the damping force:

$$F_{coil} = k_d \frac{dx}{dt} \quad (9.9)$$

Therefore from equation (6.3) the inertial force is equal to the magnetic restoring spring force:

$$M \frac{d^2x}{dt^2} = F_{mag} = k_s x \quad (9.10)$$

The coil is excited with a sinusoidal excitation current so the armature displacement  $x$  will be approximately sinusoidal. Substituting  $x = \sin 2\pi f_r t$  into equation (9.10) and rearranging gives:

$$f_r = \frac{1}{2\pi} \sqrt{\frac{k_s}{M}} = 21.3 \text{ Hz} \quad (9.11)$$

where the stiffness  $k_s$  was estimated from Fig. 9.25 as 3.8 N/mm. This theoretical resonant frequency compares well with the simulated frequency of 20 Hz.

Table 9.13 presents a comparison between the three designs, to highlight the dramatic increase in the force/volume ratio ( $F/V_m$ ) and the force/armature mass ( $F/M$ ) ratio that has been achieved.

Ratio	Design		
	Optimum	Improved	Original
$F/V_m (\times 10^{-6} \text{ N/mm}^3)$	206.73	98.51	9.633
$F/M (\text{N/kg})$	91.98	43.86	13.29

**Table 9.13** Comparison of the three designs (force calculated at 0.7 A)

The corresponding characteristics shown in Fig. 9.30 are similar to the ideal characteristic shown previously in Fig. 2.5, and the armature only saturates at high coil excitations where the curves are no longer equidistant and parallel. The figure also shows two load lines, one with a load stiffness of 20 N/mm (typical gas spring rate of Stirling cycle cryogenic coolers), which reduces the maximum armature movement to about 0.70 mm for a coil current of 0.6 A. The other load of 5 N/mm reduces the armature displacement to about 1.85 mm at 0.6 A.

The two components of the force/current/armature displacement characteristic of Fig. 9.30 are shown in Fig. 9.31, and are similar to the ideal response of Fig. 7.7, where the coil force components should be equispaced and parallel. Fig. 9.32 shows the magnetic vector equipotential plot and the flux density plot for the optimum design, with no coil excitation and the armature centralised. The highest armature flux density of approximately 1.8 T is well below the saturation level of Permendur. A detailed specification of the optimum design is given in appendix B.

## 9.4 CONCLUSIONS

This chapter has described the optimization of the motor design by using factorial design techniques to identify the geometric parameters most significant in affecting the motor performance. Armature and stator parameter studies were carried out, the static and dynamic performances of the optimum design were compared with those of both the improved design and the original prototype. A detailed specification of the optimum design concluded the work.

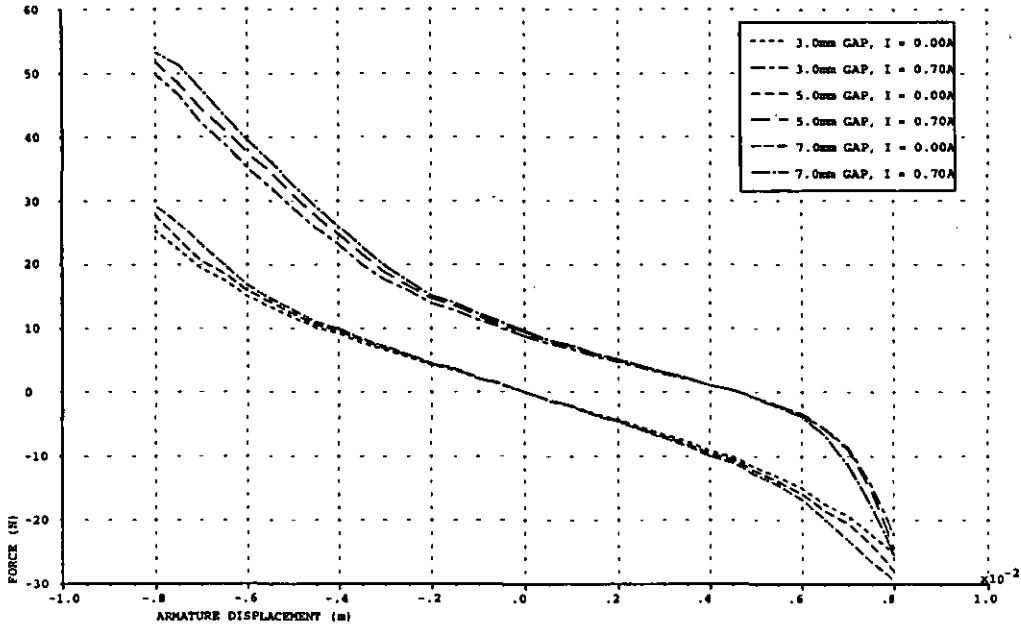


Fig. 9.1 Force characteristics when  $I = 0.0\text{ A}$  and  $0.7\text{ A}$  for an armature centre-section length of  $20.52\text{ mm}$  with various pole-shoe gap lengths

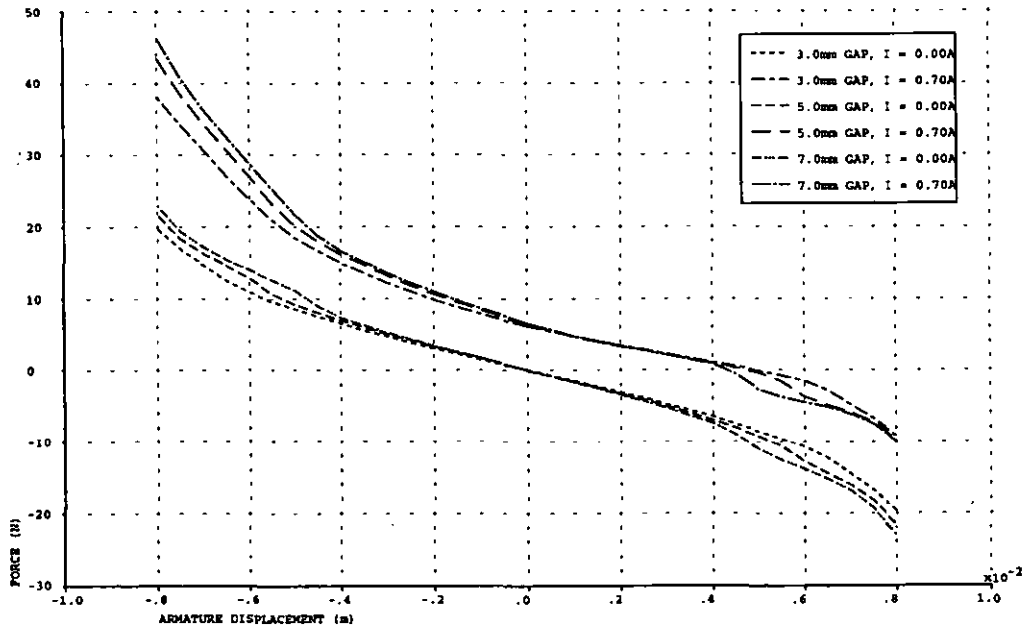


Fig. 9.2 Force characteristics when  $I = 0.0\text{ A}$  and  $0.7\text{ A}$  for an armature centre-section length of  $16.52\text{ mm}$  with various pole-shoe gap lengths

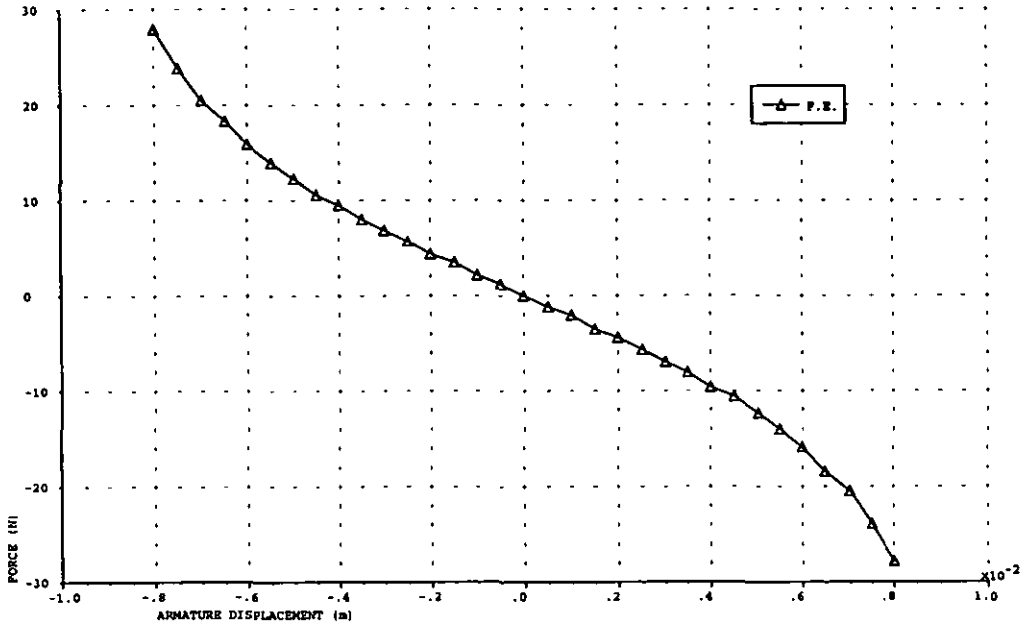


Fig. 9.3 Magnetic stiffness characteristic for the improved motor design

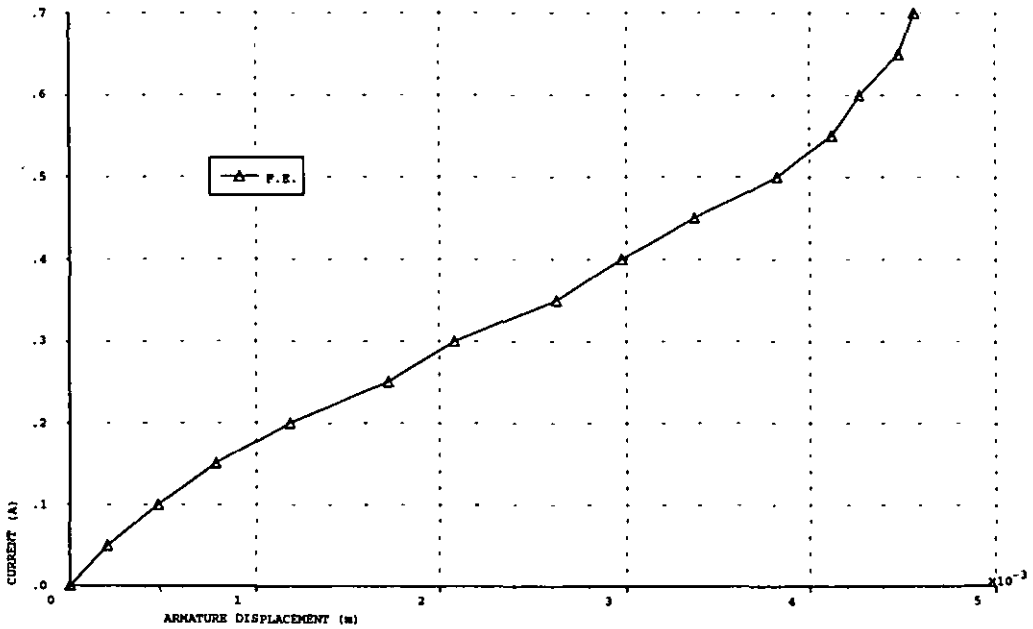


Fig. 9.4 Coil current/armature displacement characteristic for the improved motor design

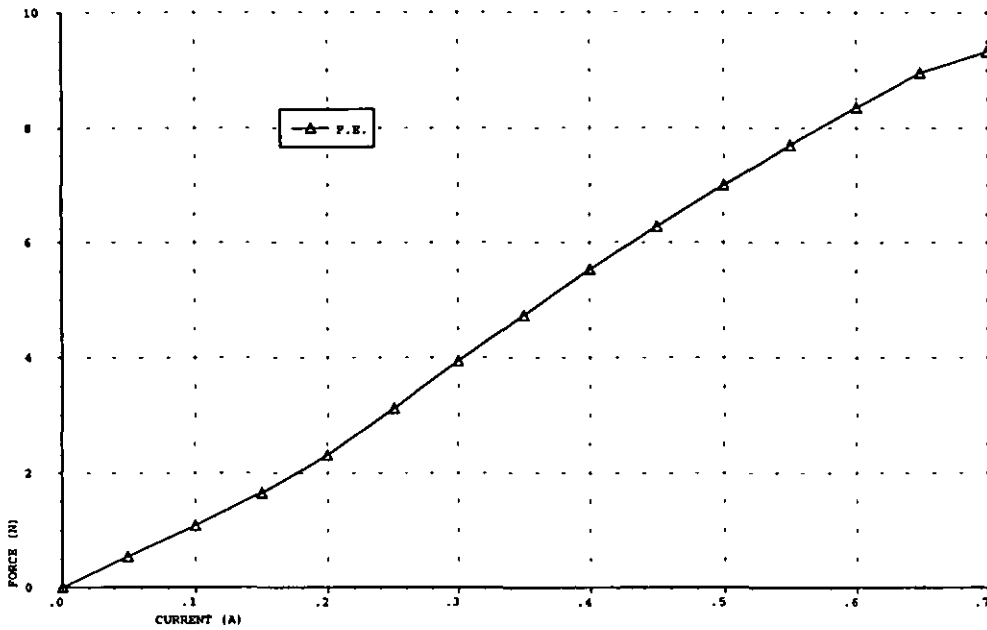


Fig. 9.5 Force/coil current characteristic for the improved motor design (armature central position)

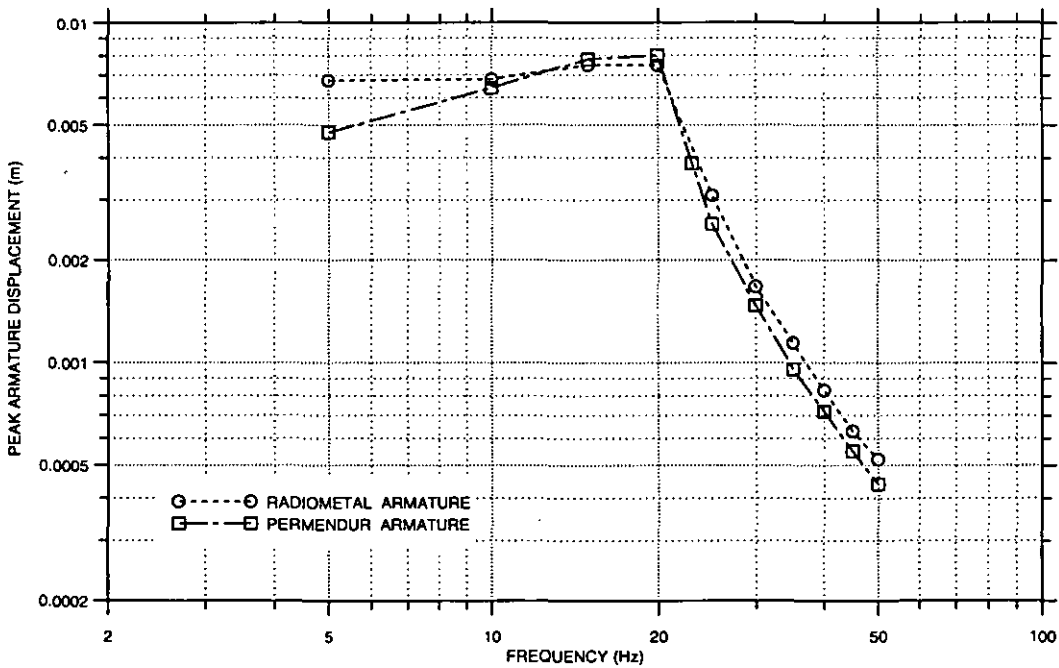
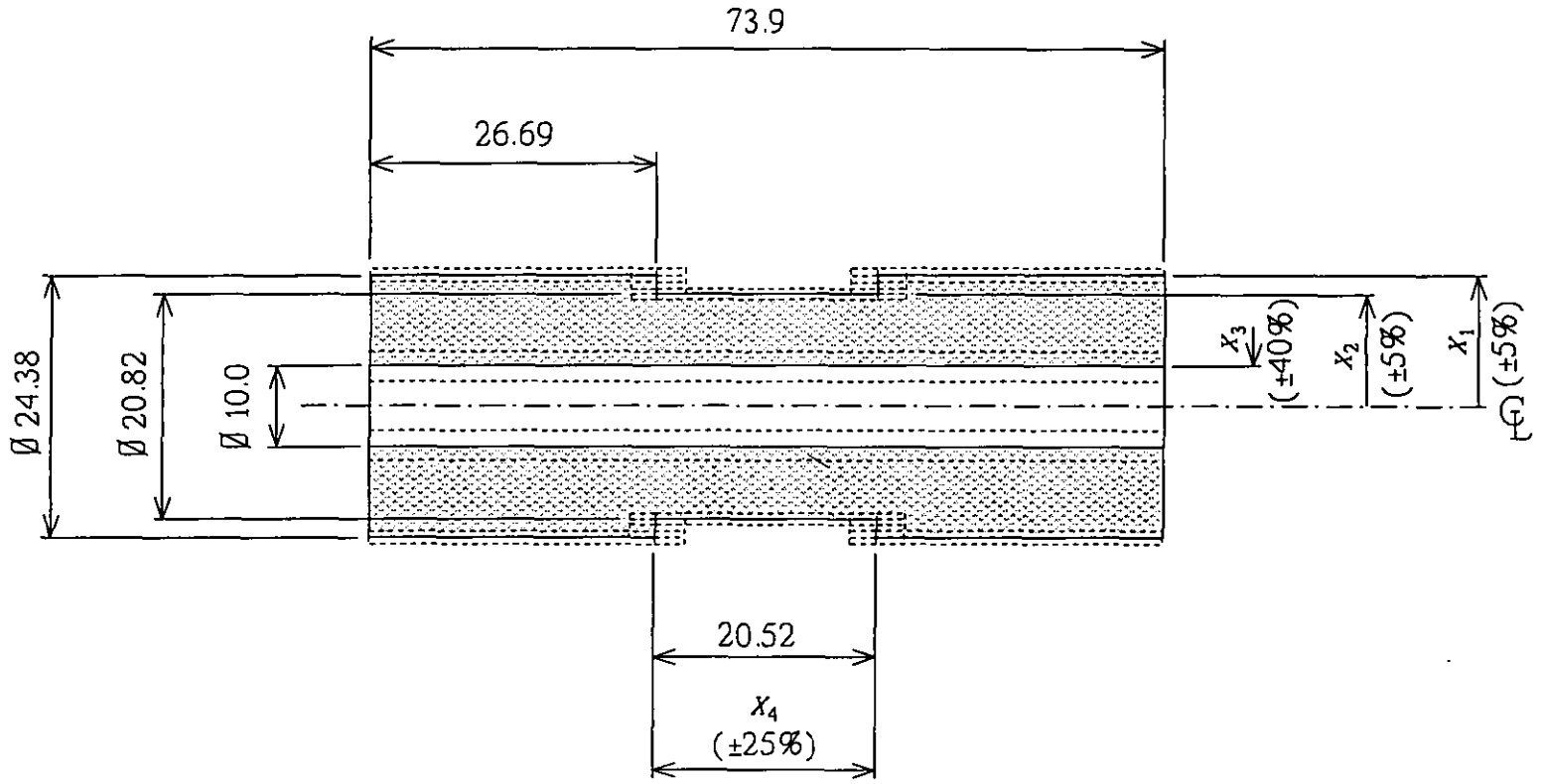


Fig. 9.6 Dynamic response characteristics for the improved motor design when using Radiometal and Permendur armatures



ARMATURE

All Dimensions in mm.

Fig. 9.7 Armature parameter changes and the unit variation of each

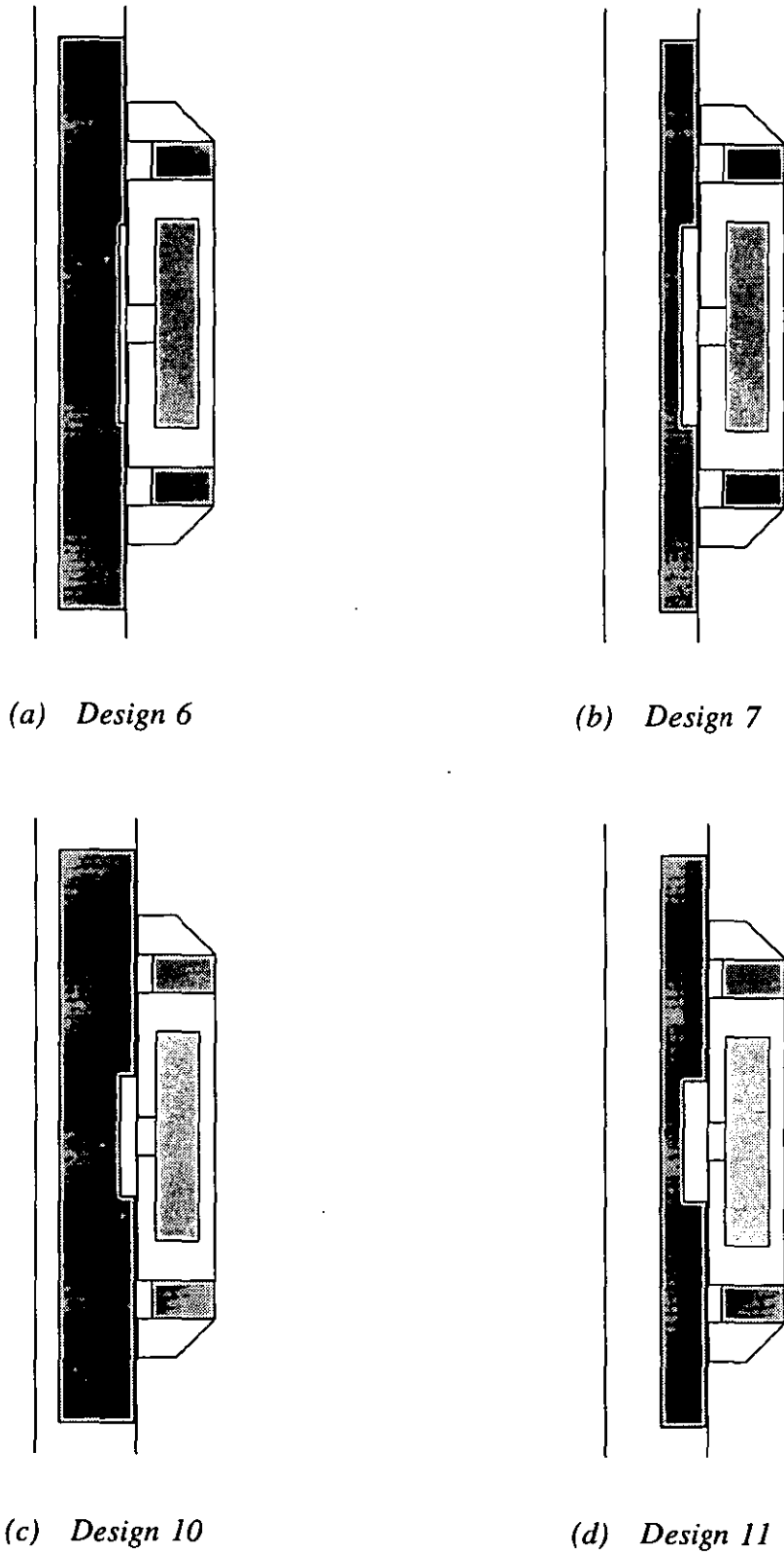


Fig. 9.8 Half cross-sections of 4 of the 16 motor designs



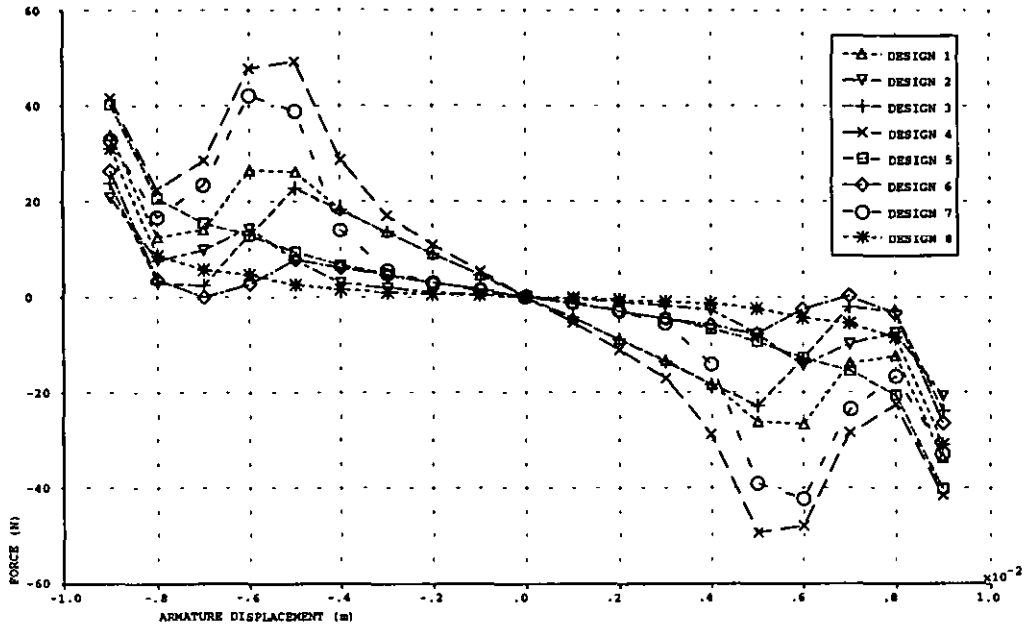


Fig. 9.9(a) Magnetic stiffness characteristics for motor designs 1 to 8

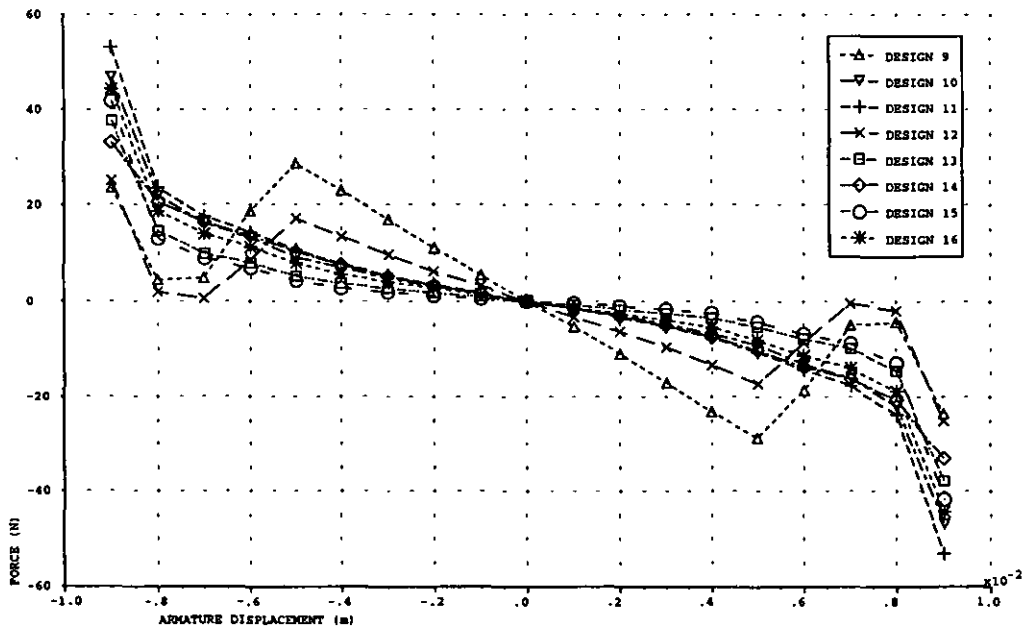


Fig. 9.9(b) Magnetic stiffness characteristics for motor designs 9 to 16

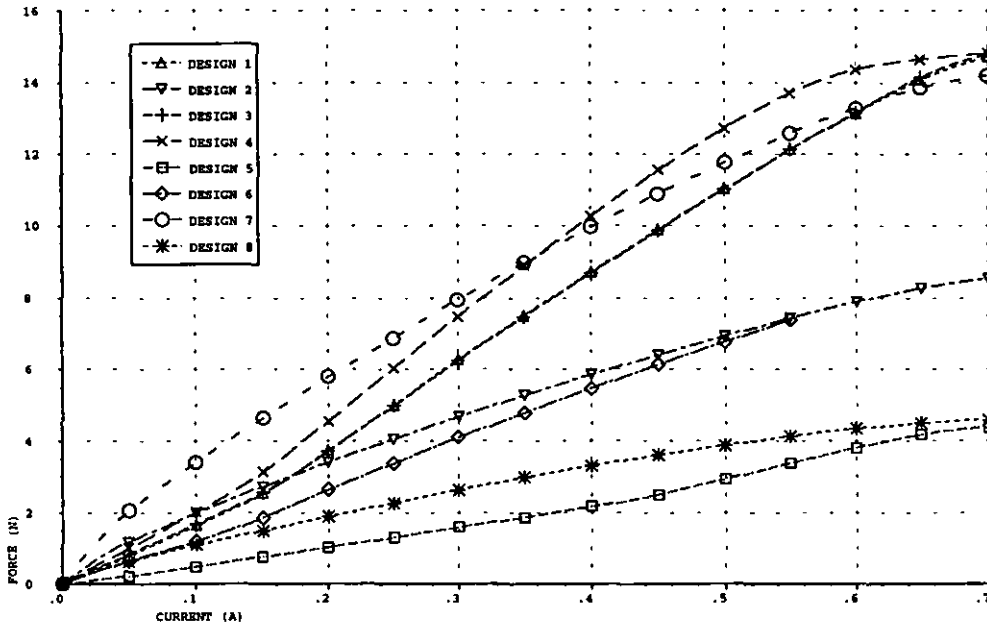


Fig. 9.10(a) Force/coil current characteristics for motor designs 1 to 8 (armature central positions)

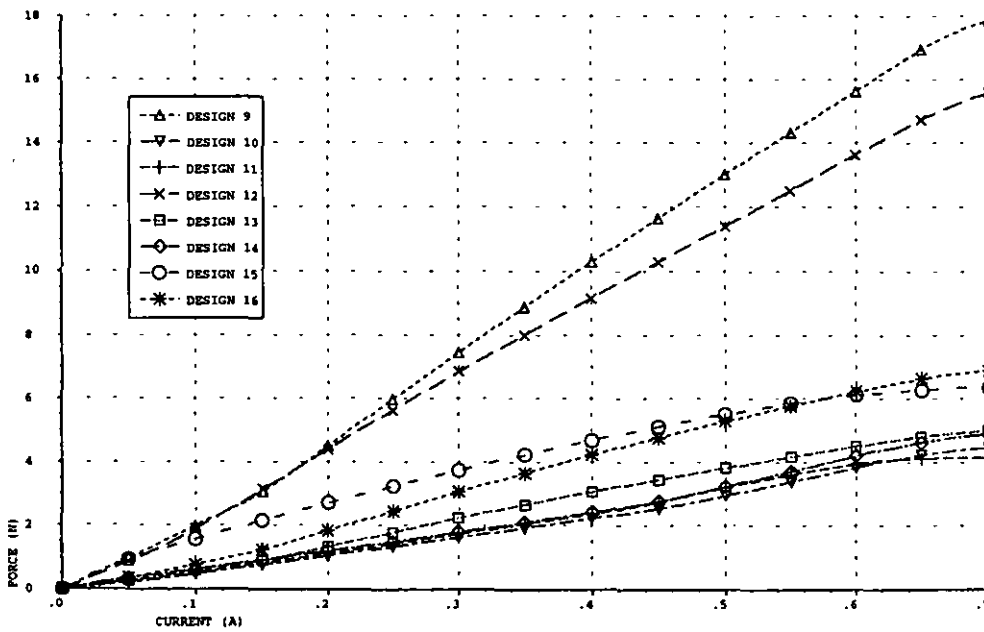


Fig. 9.10(b) Force/coil current characteristics for motor designs 9 to 16 (armature central positions)

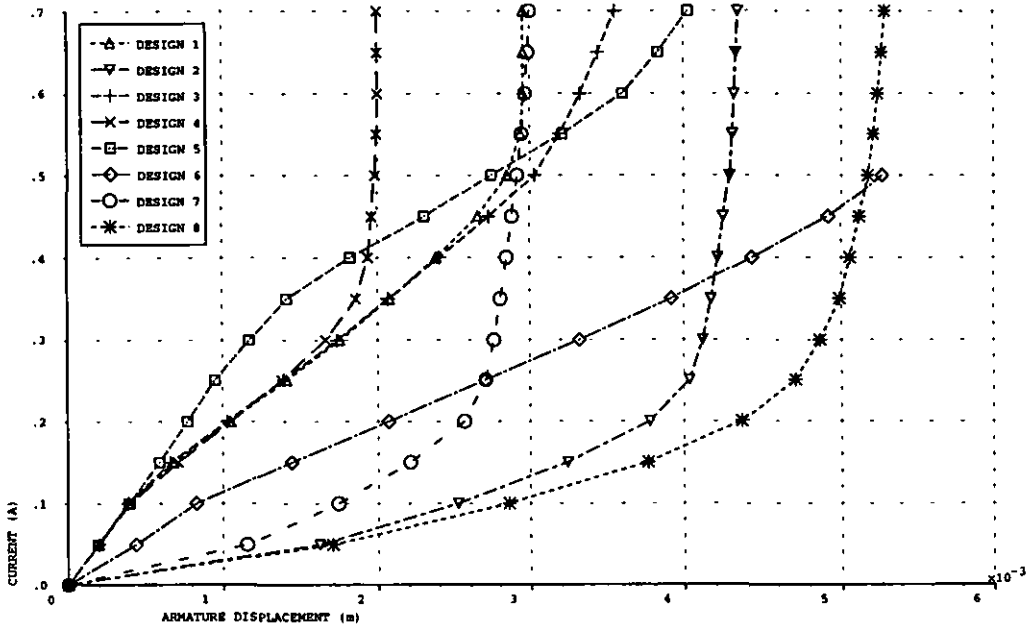


Fig. 9.11(a) Coil current/armature displacement characteristics for motor designs 1 to 8

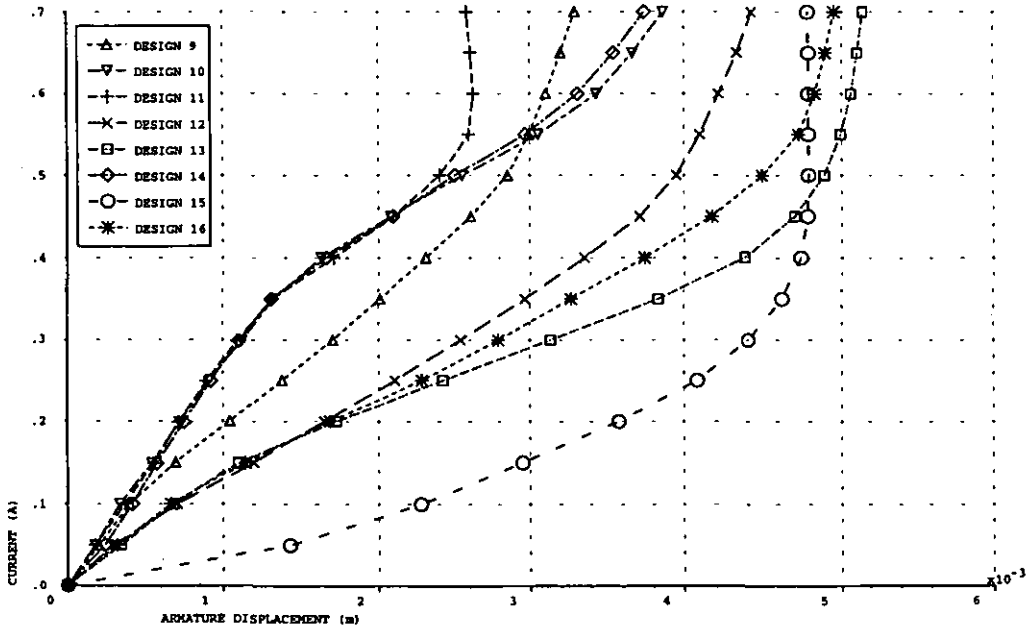


Fig. 9.11(b) Coil current/armature displacement characteristics for motor designs 9 to 16

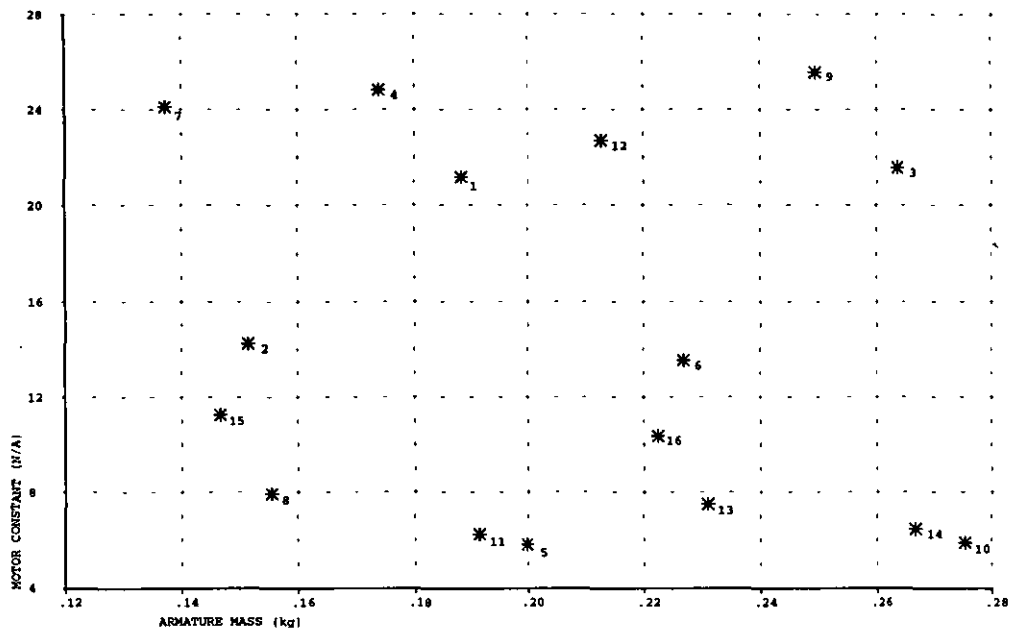


Fig. 9.12 Motor constants compared with the armature mass for the 16 motor designs

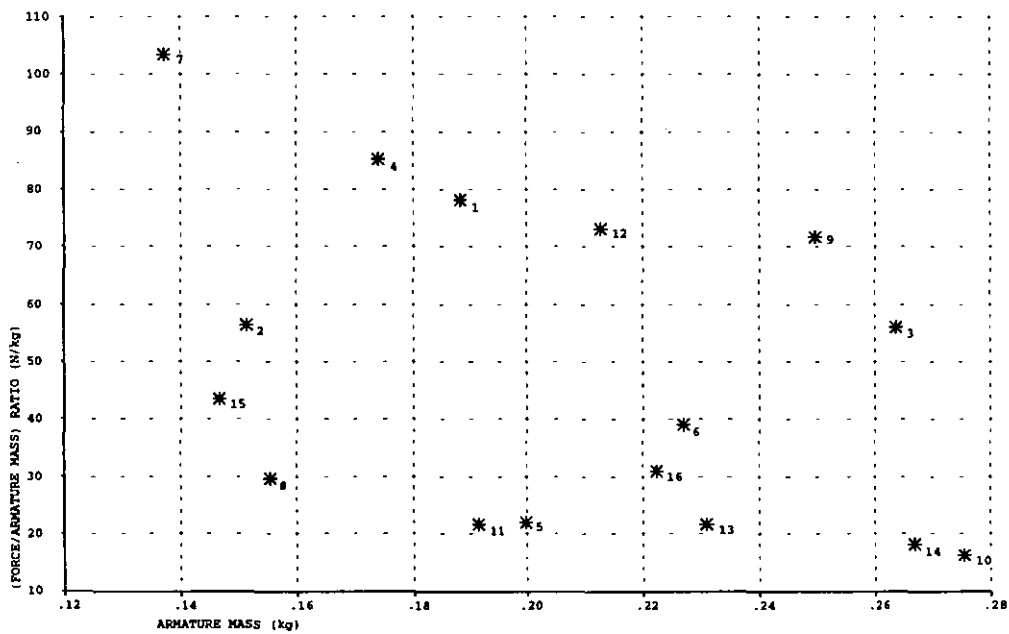
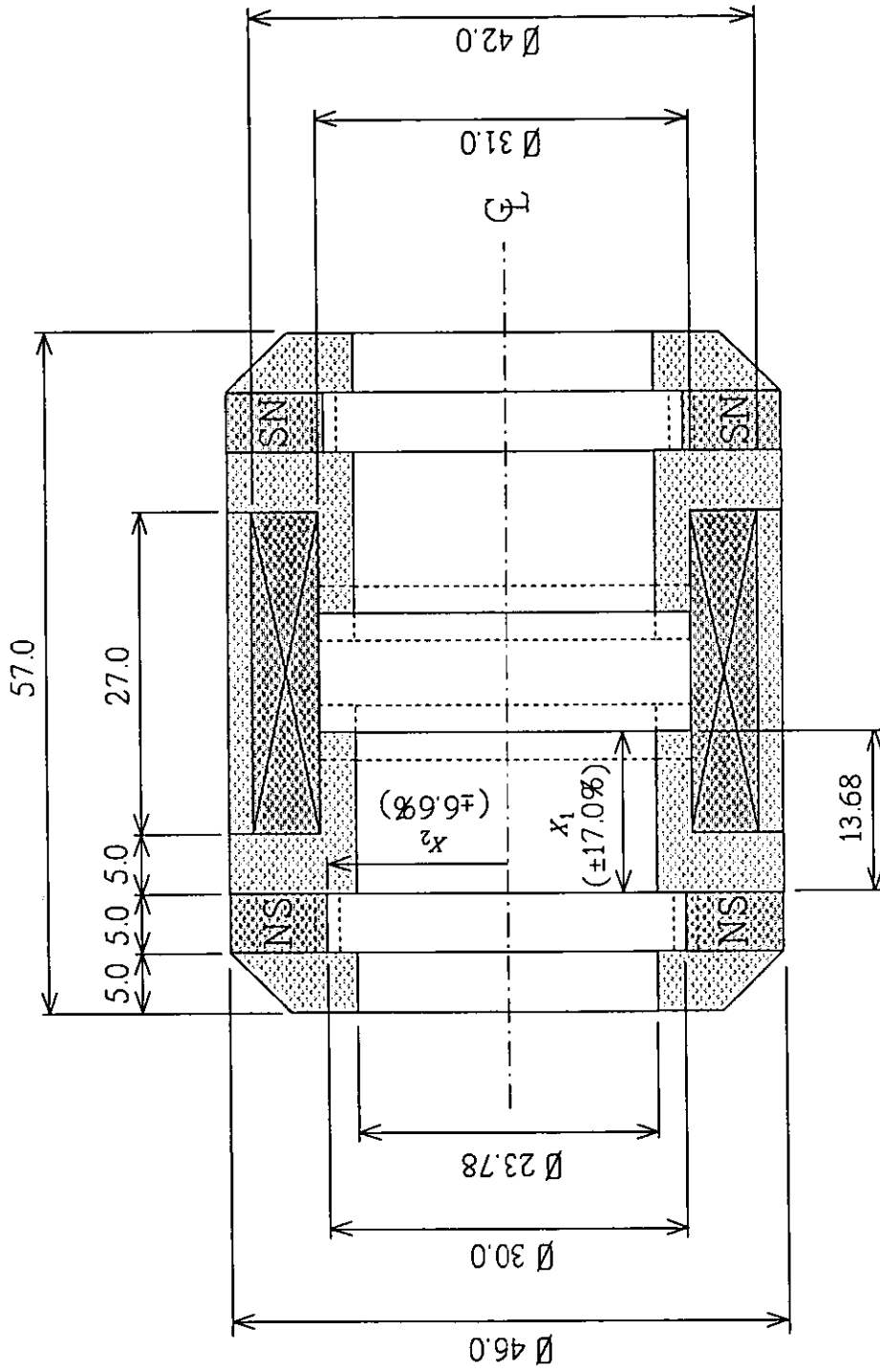


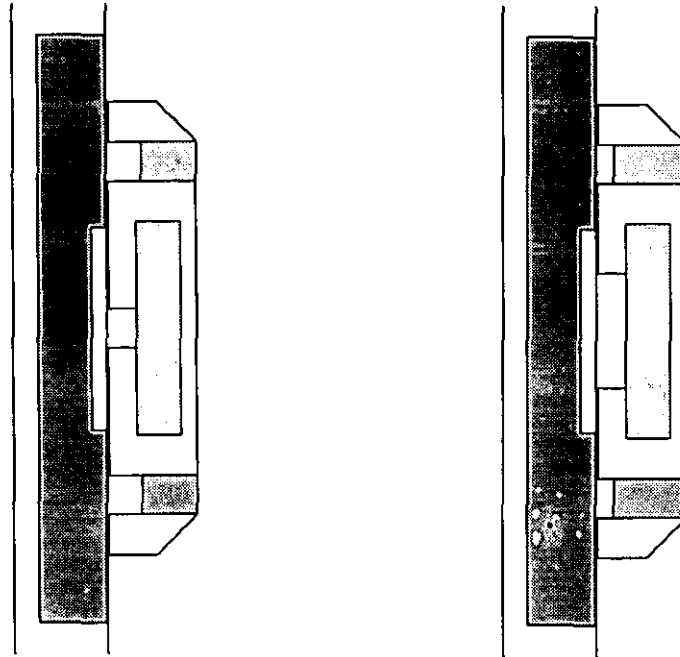
Fig. 9.13 Force/armature mass ratios compared with the armature mass for the 16 motor designs



STATOR

All Dimensions in mm.

Fig. 9.14 Stator parameter changes and the unit variation of each



(c) Design 12.1

(d) Design 12.4

Fig. 9.15 Half cross-sections of 2 of the 4 motor designs

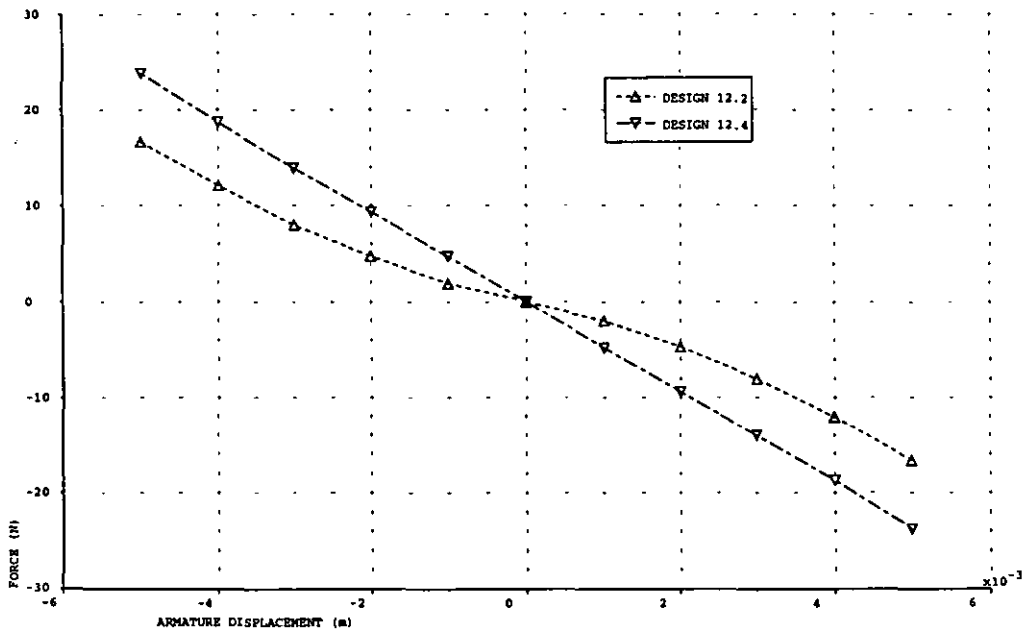


Fig. 9.16 Magnetic stiffness characteristics for designs 12.2 and 12.4

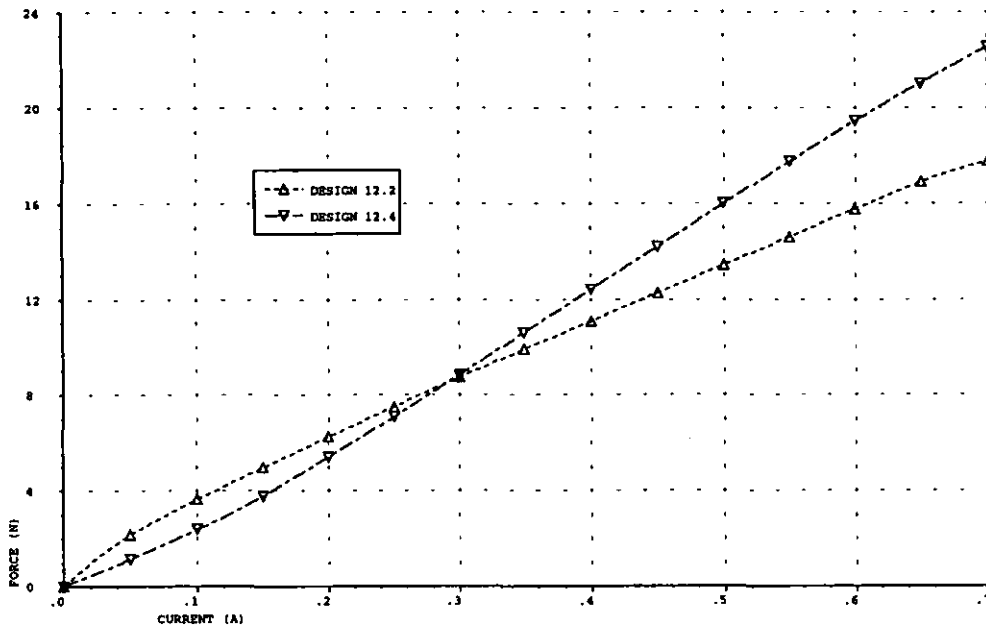


Fig. 9.17 Force/coil current characteristics for designs 12.2 and 12.4 (armature central position)

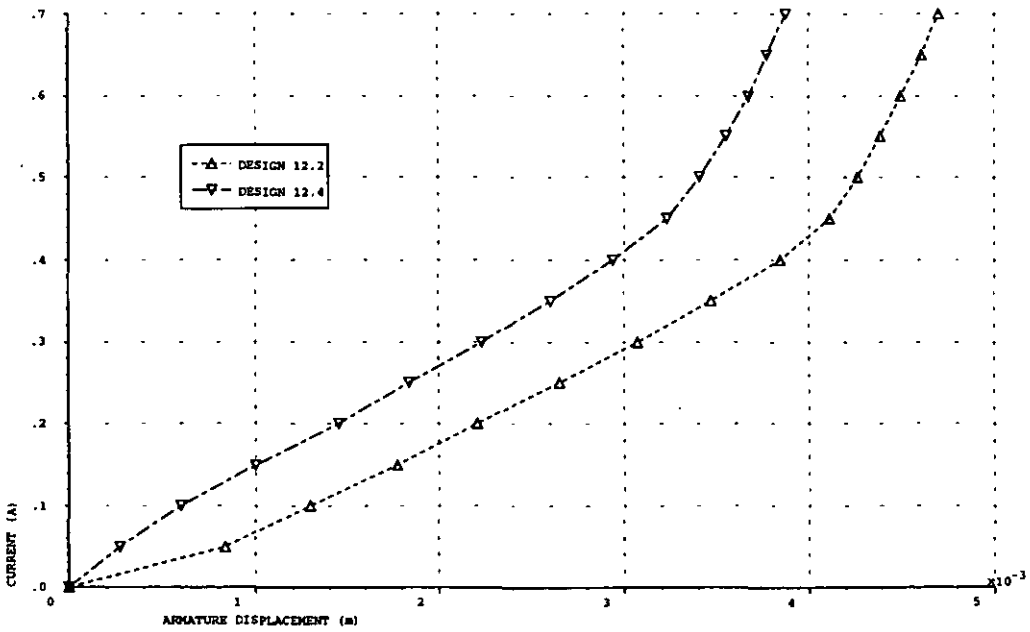


Fig. 9.18 Coil current/armature displacement characteristics for designs 12.2 and 12.4

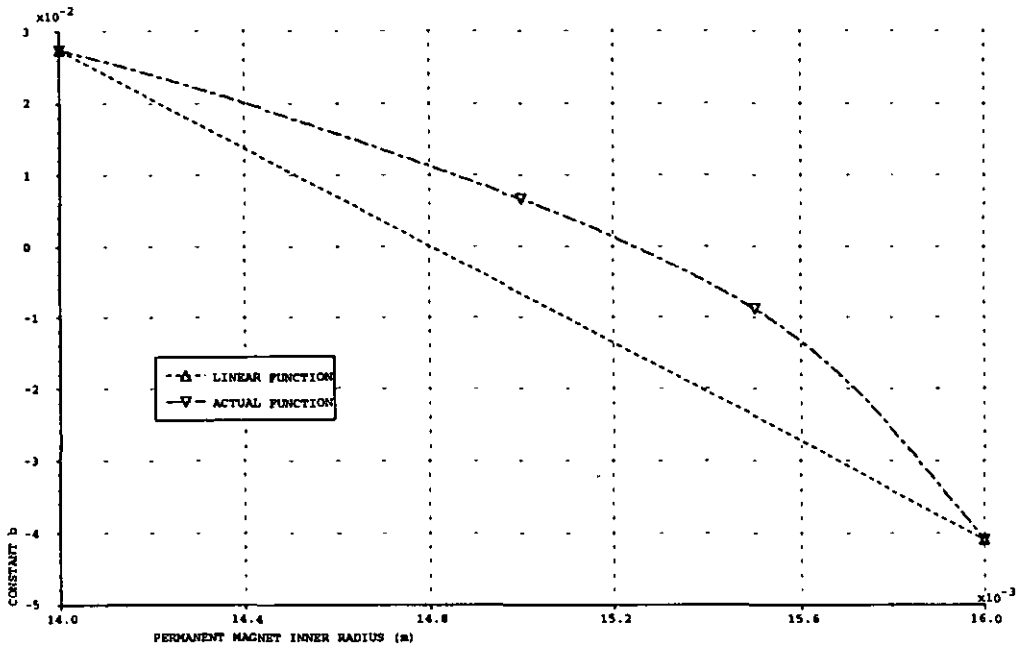


Fig. 9.19 Non-linear constant  $b$  versus permanent magnet inner radius function

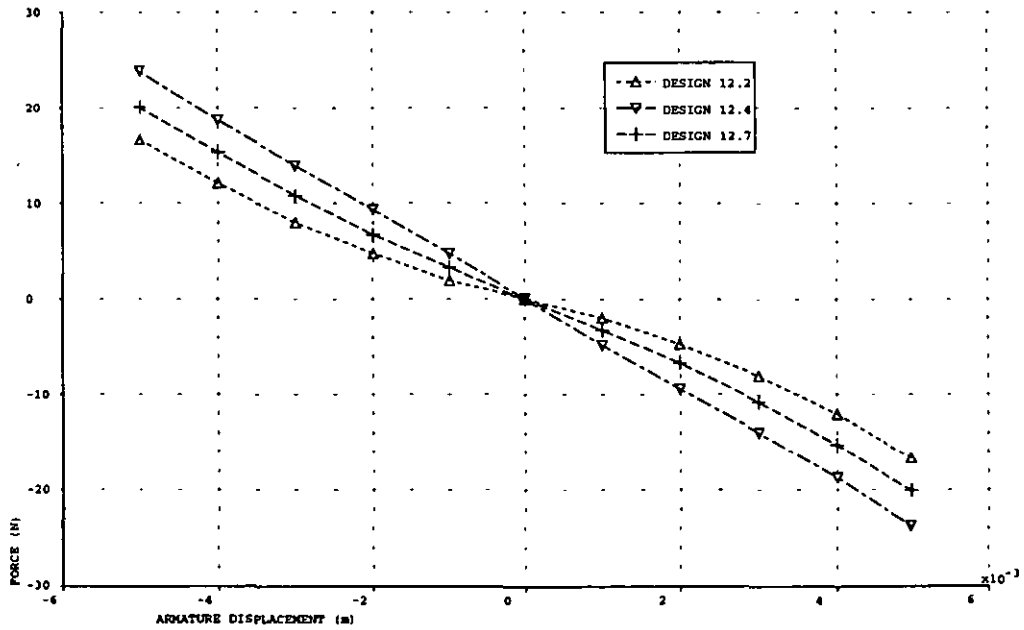


Fig. 9.20 Magnetic stiffness characteristics for designs 12.2, 12.4 and 12.7



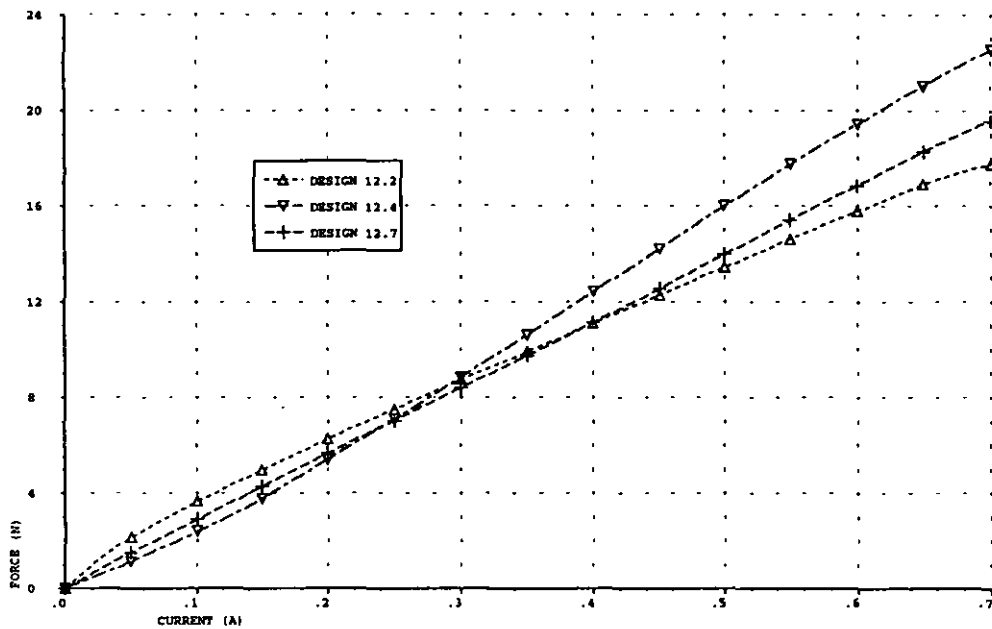


Fig. 9.21 Force/coil current characteristics for designs 12.2, 12.4 and 12.7 (armature central position)

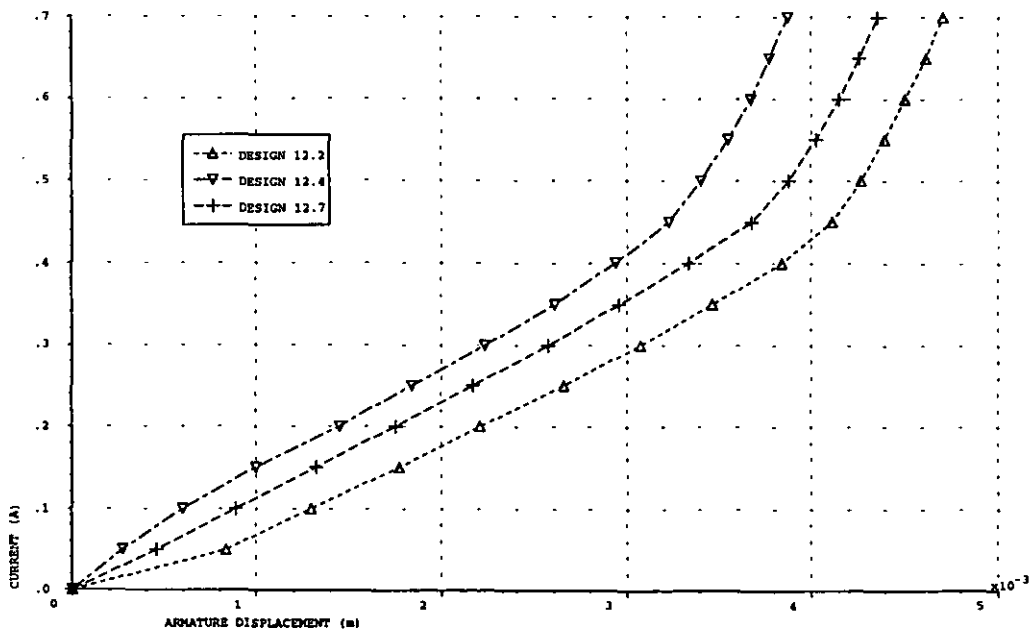
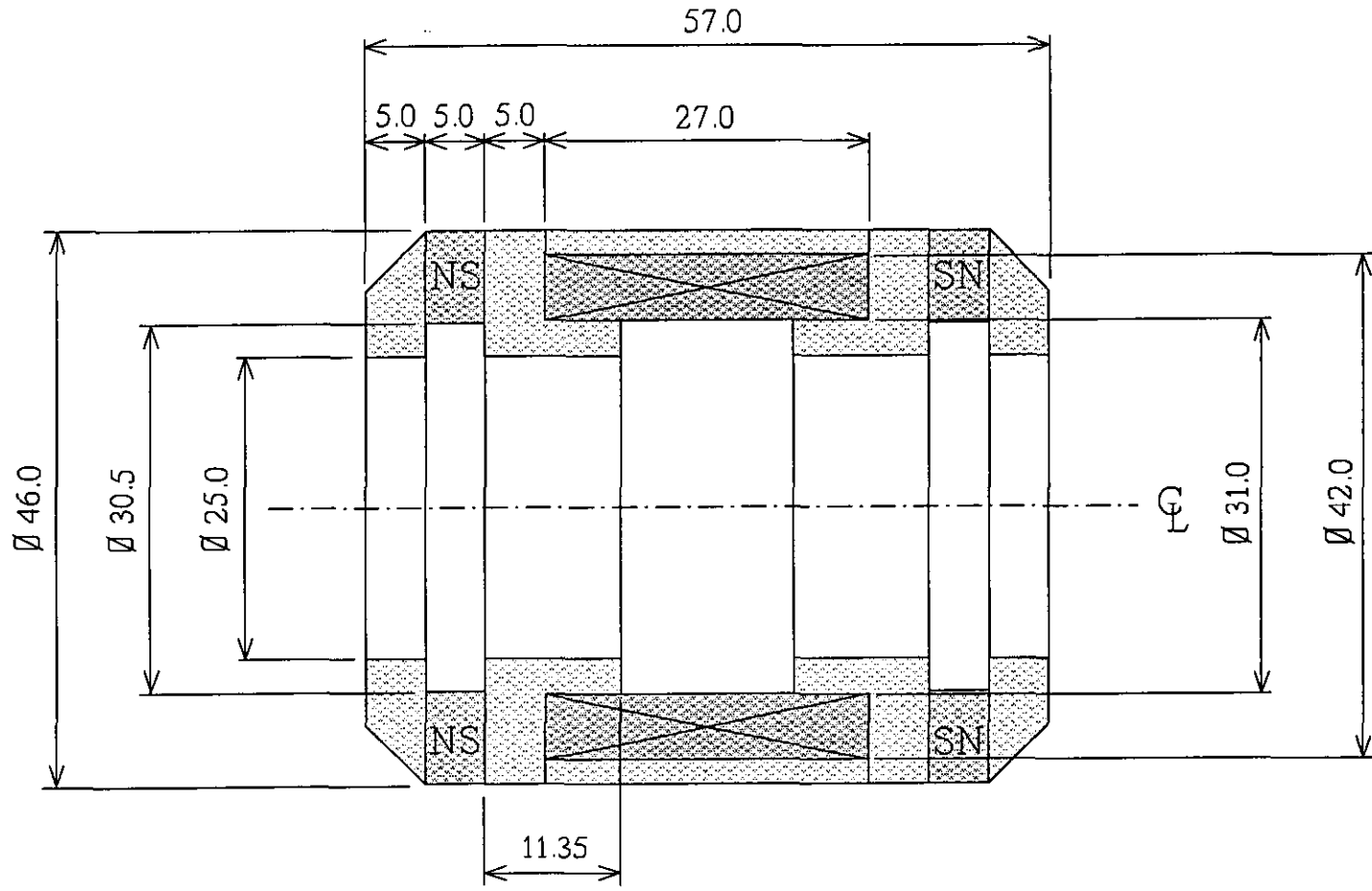


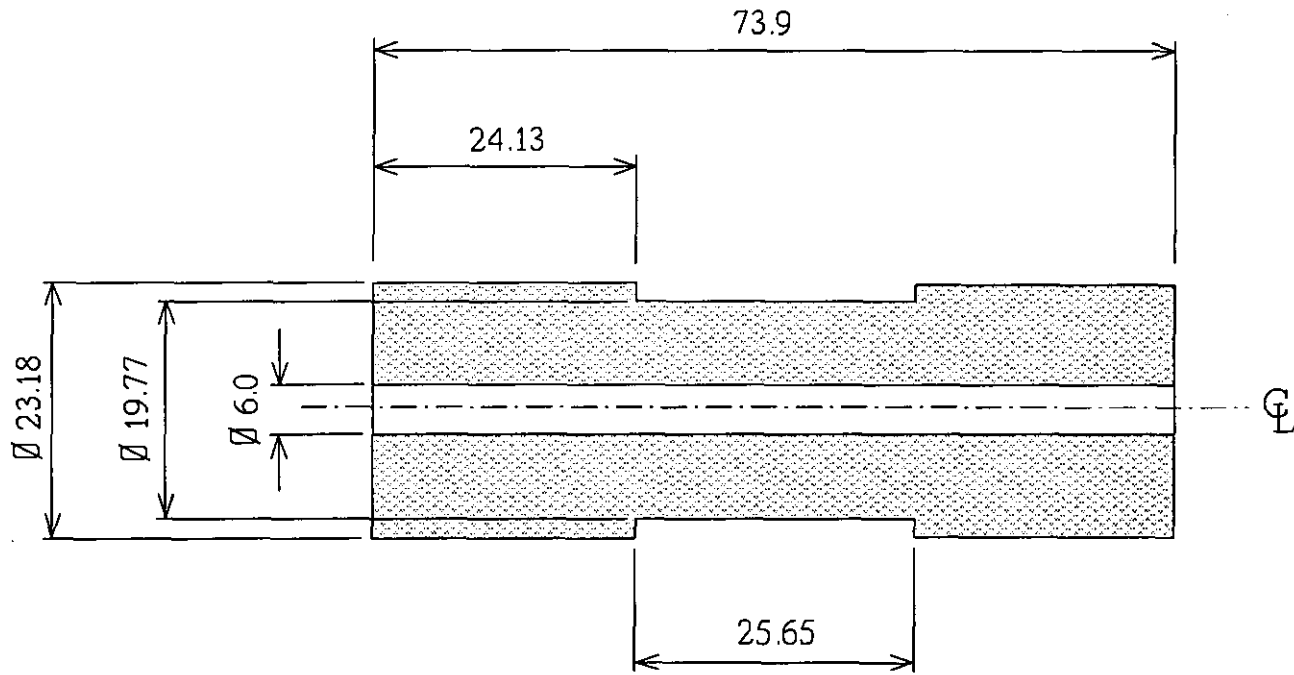
Fig. 9.22 Coil current/armature displacement characteristics for designs 12.2, 12.4 and 12.7



STATOR

All Dimensions in mm.

Fig. 9.23(a) Stator dimensions of the optimum motor design



ARMATURE

All Dimensions in mm.

**Fig. 9.23(b)** Armature dimensions of the optimum motor design

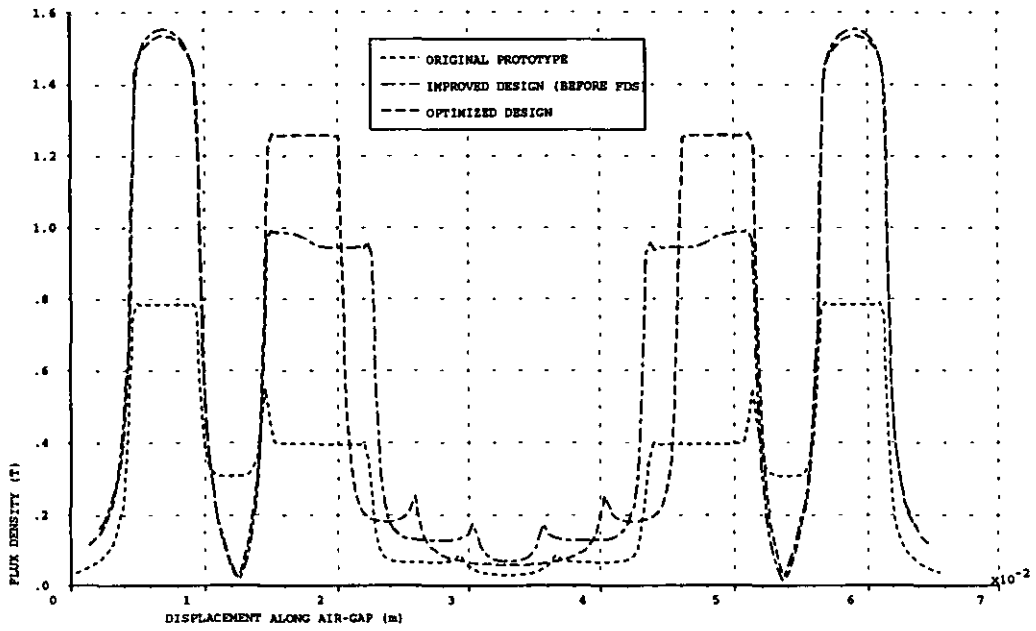


Fig. 9.24 Air-gap flux density for the optimized design, improved design and the original prototype

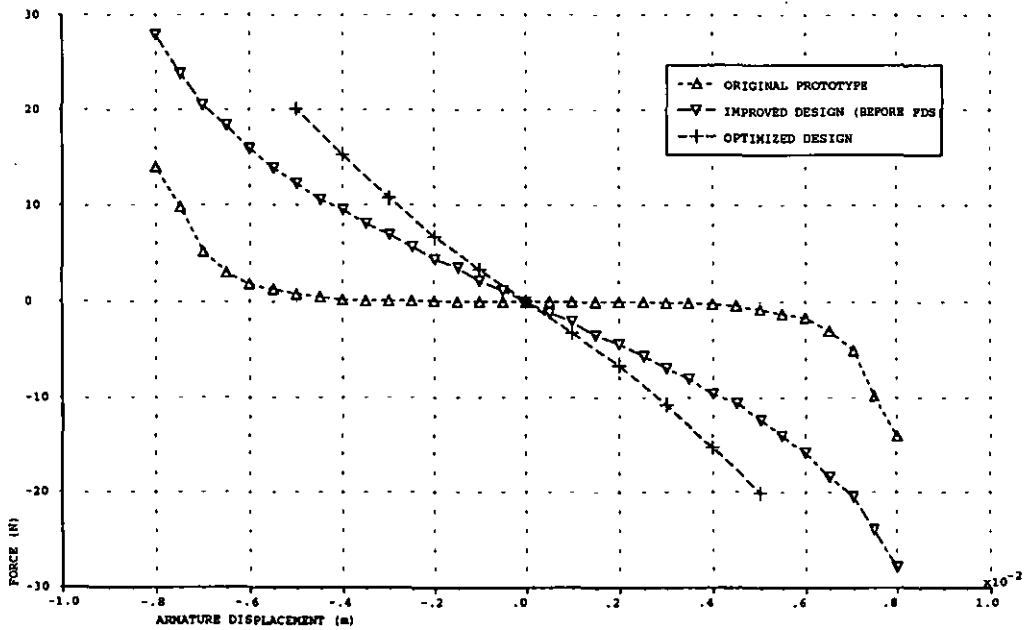


Fig. 9.25 Magnetic stiffness characteristics for the optimized design, improved design and the original prototype

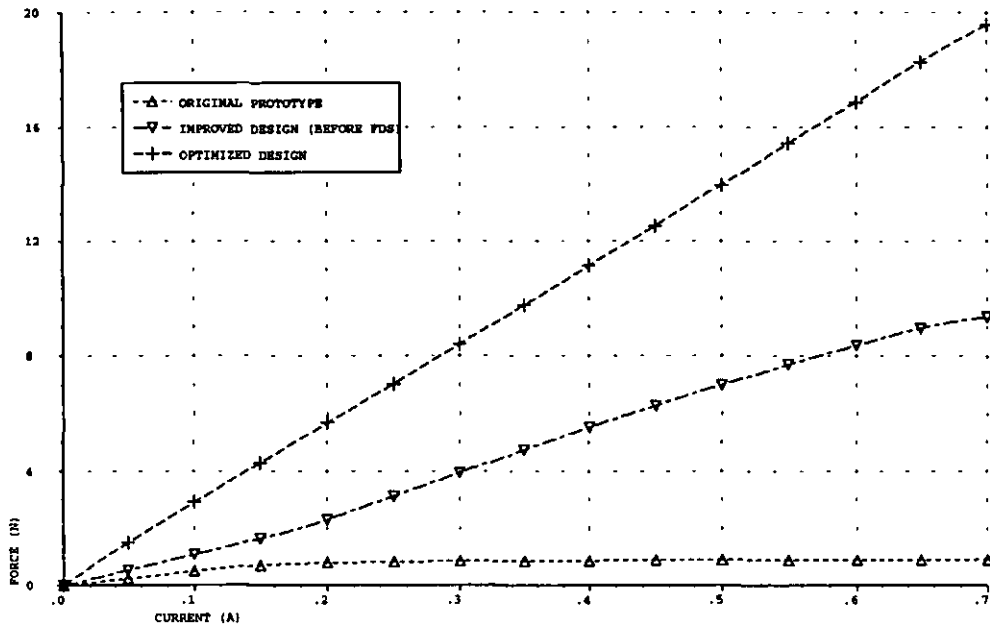


Fig. 9.26 Force/coil current characteristics for the optimized design, improved design and the original prototype (armature central position)

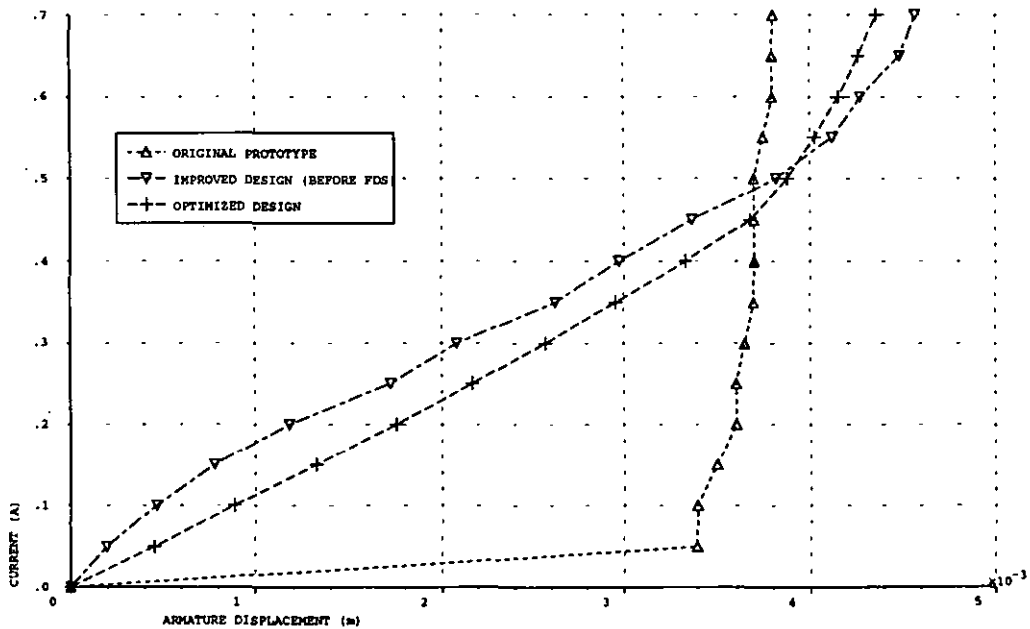


Fig. 9.27 Coil current/armature displacement characteristics for the optimized design, improved design and the original prototype

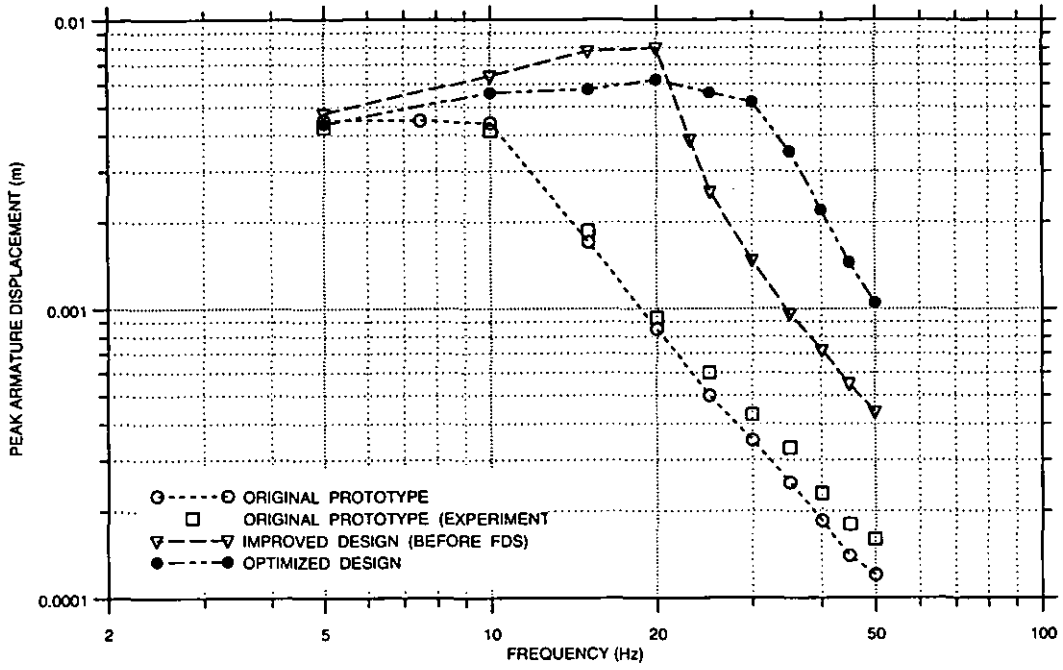


Fig. 9.28 Dynamic response for the optimized design, improved design and the original prototype

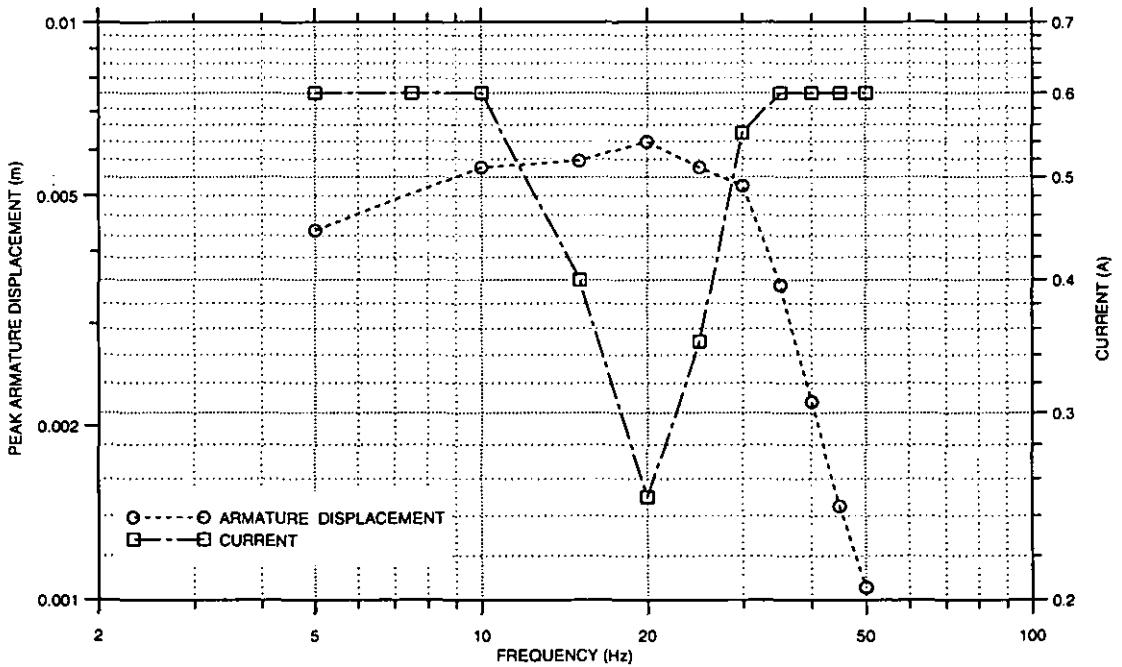


Fig. 9.29 Armature displacement and coil current for the optimized motor design

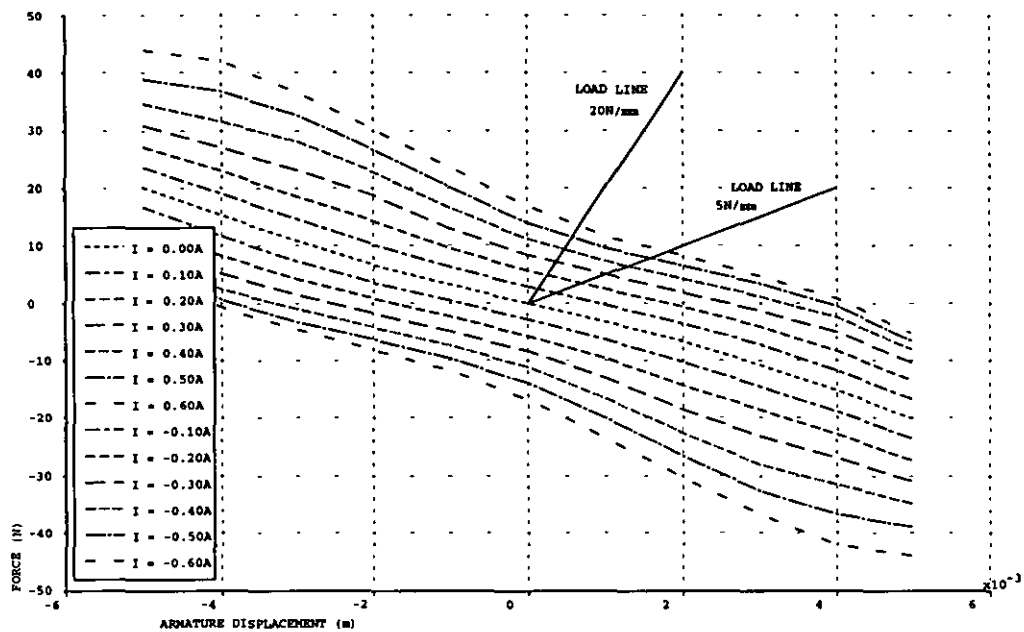


Fig. 9.30 Force/current/armature displacement characteristic for the optimized motor design

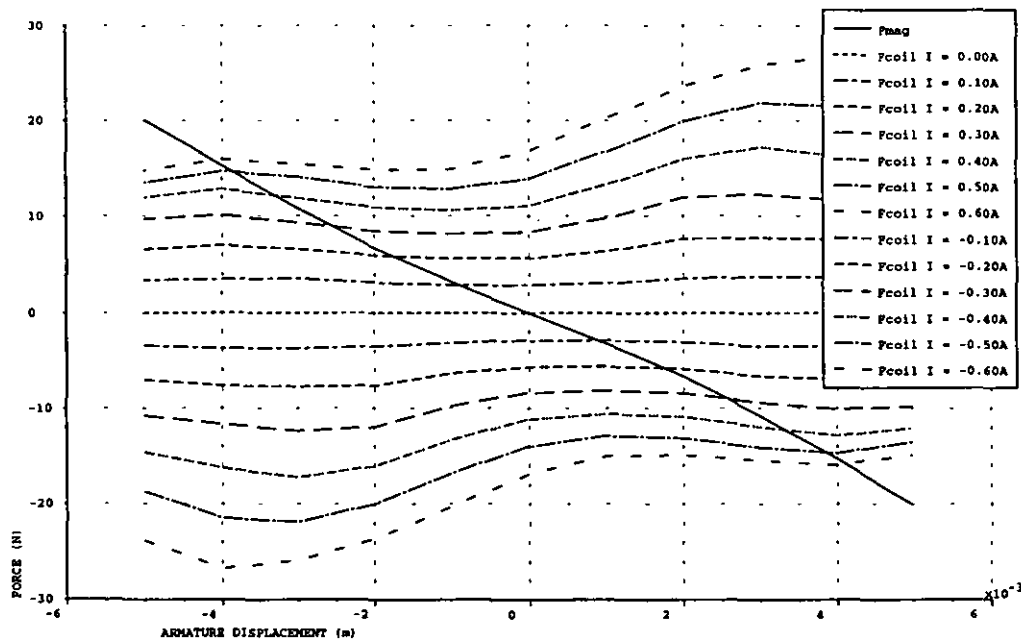
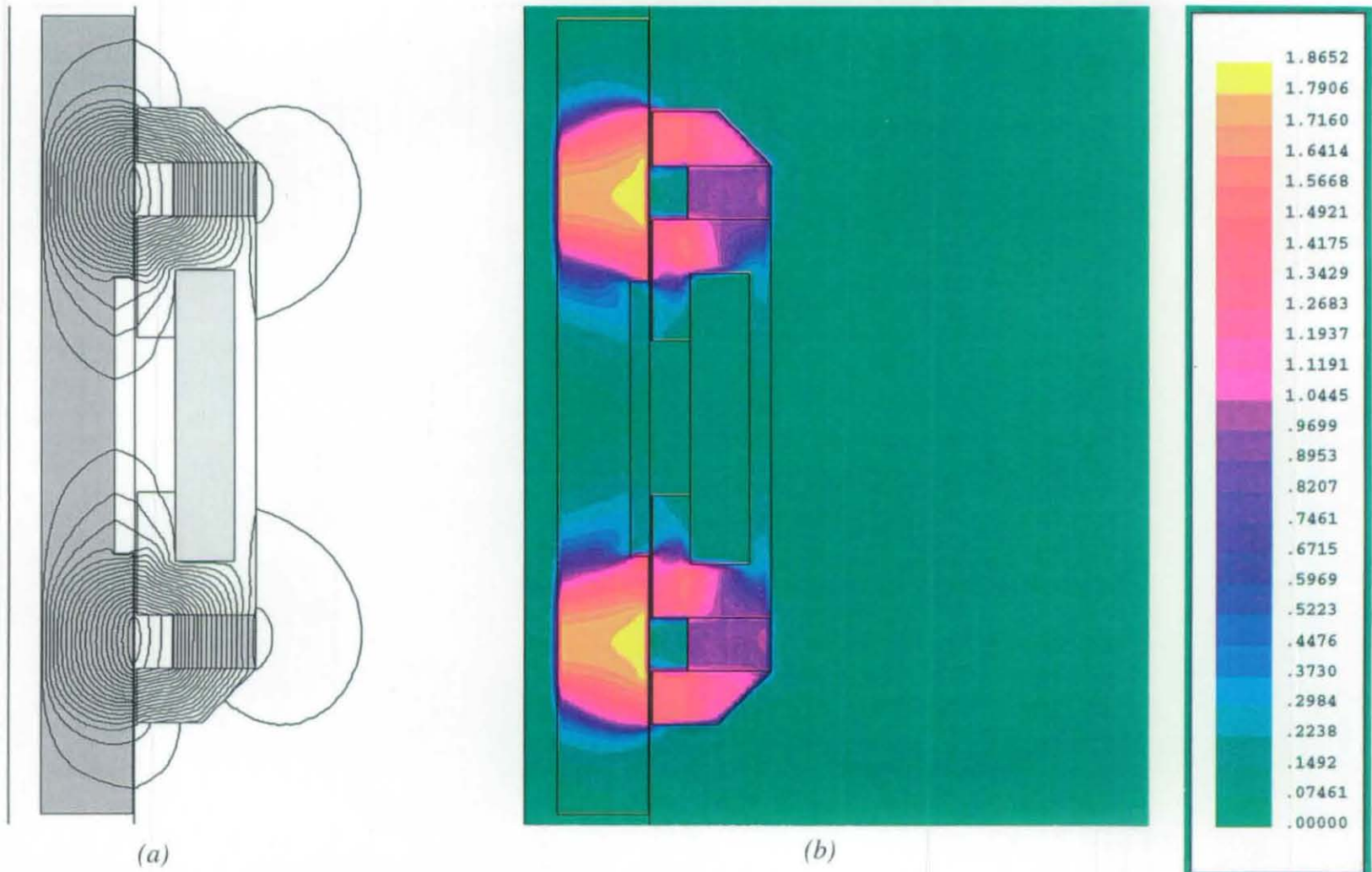


Fig. 9.31 Two force components of the optimized motor design



**Fig. 9.32** (a) Magnetic vector equipotential plot and (b) flux density plot of the optimised motor design



## CONCLUSIONS AND FURTHER WORK

This chapter presents overall conclusions drawn from the work described in the thesis and makes suggestions for its continuation.

### 10.1 Conclusions

The thesis has described the design, analysis and successful optimization of a permanent magnet linear reluctance motor for use in short-stroke reciprocating electro-mechanical systems. It was shown, after a detailed evaluation of a number of candidate designs, that this motor was the most appropriate choice for use in the applications described. In order to satisfy the bi-directional motion requirements, the motor employs a symmetrical magnetic circuit, where a soft-iron armature, positioned on the central axis of two opposing ring magnets, moves when a current is applied to a solenoidal coil situated between the magnets. To obtain a device with the highest possible force/weight ratio within a pre-defined volume, as stated in the initial specification, rare earth magnets were employed. A prototype motor was developed and built to verify the principle of operation and this provided experimental results to aid the theoretical modelling work.

An optimum design was determined as having a linear coil current/armature displacement characteristic (on no-load and loaded), a high force production capability, a large restoring axial force to centre the armature in the absence of any coil current, and a fast dynamic performance. To achieve this it was established that a finite element approach had to be used to study the magnetic field within the motor, due to the complicated magnetic circuit geometry and non-linear materials. The method was shown to accurately predict the static performance of the prototype motor, which suffered from a highly saturated armature causing a non-linear armature movement and low force production.

The mathematical model of the motor and drive system, developed using tensor techniques, was a valuable development tool for predicting the dynamic performance, and was validated by substantial experimental investigations using the prototype motor.

To improve the performance of the prototype motor, various dimensional changes were made to the magnetic circuit, which included:

- (i) re-positioning the permanent magnets;
- (ii) varying the armature diameter and centre-section dimensions;
- (iii) using hollow armatures;
- (iv) varying the air-gap length;
- (v) possibly using radially magnetized permanent magnets and;
- (vi) varying the stator yoke pole-shoe length.

The major change that was made to the magnetic circuit following the above parameter study was to use a large diameter hollow armature. It was shown that although a large diameter solid armature reduced the flux density in the armature and improved the device linearity, it degraded the dynamic response due to the increased armature mass. Employing a hollow armature configuration was shown to improve the dynamic characteristics but had the disadvantage of reducing the linearity. The magnetic materials used in the design were also studied, and an improvement in static performance was observed when using an armature material with a higher saturation level than the stator material. The final design used a Radiometal stator and a Permendur armature to create a near linear armature movement with a high force production capability.

To further improve the performance a factorial design study was carried out on the improved motor design. An armature parameter study (varying the inner and outer diameters, centre-section diameter and length) was implemented, followed by a stator parameter study (varying the stator yoke pole-shoe length and magnet inner diameter). It was established that the major modification resulting from the study that improved

the device performance was the use a longer narrow centre-section on the armature and smaller stator yoke pole-shoes. This alteration reduced the pole-face overlap, and thereby considerably improved the stiffness characteristic. A near linear armature movement and a superior dynamic performance also resulted.

A second prototype motor was designed and built to confirm further the validity and accuracy of the finite element models and the motor and drive system mathematical model.

## 10.2 Further Work

Suggestions for further research are discussed below.

- (a) The optimized motor design could be manufactured and its performance compared with the theoretical results presented in chapter 9. Mechanical aspects of the motor should also be studied, in particular the bearing arrangement. Radially stiff diaphragm springs could be used rather than the existing linear bearings, to reduce the physical size. Accelerated life tests could be carried out to monitor its structural and thermal reliability.
- (b) Recent grades of NdFeB available have typically remanent flux densities of 1.35 T and coercive forces of 1020 kA/m, and using permanent magnets made from this new material would enable a higher force to be generated with an improved stiffness characteristic.
- (c) A digital controller, implemented using either a 16-bit microcontroller or a digital signal processor (DSP), could be designed and developed for use with the optimized motor, to produce a high performance linear drive system with current, speed and position feedback loops capable of micrometre positional accuracy. The whole system could be simulated using the motor and drive system simulation software developed in this work, which already contains both speed and position loops. The position loop contains a PID controller

- that could be tuned using software such as *SIMBOL 3*. Alternatively, *SIMULINK* could be used to model both the motor and drive system.
- (d) The axi-symmetric non-linear magnetostatic finite element analysis solver also developed could be modified and extended to create a transient solver. This could be coupled into the mathematical model of the motor and drive system to simulate more closely the motor dynamics. Post-processing software to compute the force on the armature has already been developed, leaving only the need for a flux linkage computation program. Existing meshes created in *MEGA* could still be used, since the software provides the facility for the mesh information to be exported for use in other programs. A method of overcoming the distortion of the air-gap elements due to armature movement would also have to be addressed.
  - (e) An alternative method for optimizing the motor, which includes producing an accurate analytical model of the motor, could be studied. A non-linear lumped parameter network to evaluate the magnetic circuit reluctances would be needed, to allow accurate calculation of the air-gap flux density for use in the analytical model. Geometric parameters could then be scanned between appropriate limits to determine an optimum design.
  - (f) The axi-symmetric non-linear magnetostatic finite element analysis solver and post-processing software could be combined with the *MATLAB* optimization toolbox to implement various optimization strategies such as simulated annealing.
  - (g) The structural and thermal characteristics of the optimized motor could be studied by employing finite element techniques by using a software package such as *ANSYS* or *COSMOS/M*.

## REFERENCES

---

- [1] Laithwaite, E. R., *Linear Electric Motors*, M & B Monograph TL/EE/1, Mills & Boon Ltd., London, 1971.
- [2] Nasar, S. A. and Boldea, I., *Linear Electric Motors: Theory, Design, and Practical Applications*, Prentice-Hall, Inc., Englewood Cliffs, New Jersey, 1987.
- [3] Nasar, S. A. and Unnewehr, L. E., *Electromechanics and Electric Machines*, Second Edition, John Wiley & Sons, New York, 1983.
- [4] Ezekiel, F. D., "Electromagnetic actuators", *Instruments & Control Systems*, Vol. 40, No. 12, December 1967, pp. 90-96.
- [5] Binnie, J. N., Garitano, R., Pickup, I. E. D. and Tipping, D., "A study of direct drive actuation systems in aircraft", *Proceedings of the International Conference on Electrical Machines*, UMIST, Manchester, UK, 15th-17th September 1992, pp. 175-179.
- [6] Sivadasan, K. K., "A novel magnetic suspension cum linear actuator system for cryo coolers", *IEEE Transactions on Magnetics*, Vol. MAG-30, No. 3, May 1994, pp. 1258-1262.
- [7] "Linear force motor uses no springs", *Eureka (Engineering Materials & Design)*, Innopress Ltd., Kent, UK, Vol. 12, No. 3, March 1992, p.13.
- [8] Henry, J. P. and Dennis, D. S., "Predicting solenoid transient performance", *Sensors & Actuators: 1987*, International Congress and Exposition, Detroit, Michigan, February 23rd-27th, 1987, pp. 93-99.
- [9] Eastham, J. F., "Novel synchronous machines: linear and disc", *IEE Proceedings*, Vol. 137, Pt. B, No. 1, January 1990, pp. 49-58.

- [10] Akmese, R. and Eastham, J. F., "Dynamic performance of a brushless dc tubular drive system", *IEEE Transactions on Magnetics*, Vol. **MAG-25**, No. 5, September 1989, pp. 3269-3271.
  
- [11] Cathey, J. J., Topmiller, D. A. and Nasar, S. A., "A tubular self-synchronous motor for artificial heart pump drive", *IEEE Transactions on Biomedical Engineering*, Vol. **BME-33**, No. 3, March 1986, pp. 315-319.
  
- [12] Green, C. W. and Paul, R. J. A., "Application of dc linear machines as short-stroke and static actuators", *Proceedings of the IEE*, Vol. **116**, No. 4, April 1969, pp. 599-604.
  
- [13] Green, C. W. and Paul, R. J. A., "Performance of dc linear machines based on an assessment of flux distribution", *Proceedings of the IEE*, Vol. **118**, No. 10, October 1971, pp. 1413-1420.
  
- [14] Hirata, K., Kagami, Y., Yanosaka, M., Ishihara, Y. and Todaka, T., "Thrust calculation of linear pulse motors using combined technique employing the finite element method and the permeance analysis method", *IEEE Transactions on Magnetics*, Vol. **MAG-28**, No. 2, March 1992, pp. 1394-1397.
  
- [15] Cho, Y., Lee, J. and Koo, D., "The analysis of the static thrust of a hybrid type double-sided linear pulse motor", *IEEE Transactions on Magnetics*, Vol. **MAG-31**, No. 3, May 1995, pp. 2084-2087.
  
- [16] Takeda, Y., Sanada, M., Morimoto, S., Hirasu, T. and Taniguchi, K., "Cylindrical linear pulse motor with interior permanent magnet mover", *IEEE Transactions on Industry Applications*, Vol. **IA-30**, No. 1, January/February 1994, pp. 141-145.

- 
- [17] Yamada, H., Hamajima, T., Xiang, S. and Nishizawa, N., "Six-phase cylindrical linear pulse motor as linear oscillatory actuator", *IEEE Transactions on Magnetics*, Vol. **MAG-23**, No. 5, September 1987, pp. 2841-2843.
- [18] Khan, S. H. and Ivanov, A. A., "An analytical method for the calculation of static characteristics of linear step motors for control rod drives in nuclear reactors", *IEEE Transactions on Magnetics*, Vol. **MAG-31**, No. 3, May 1995, pp. 2324-2331.
- [19] Matt, D., Goyet, R., Lucidarme, J. and Rioux, C., "Longitudinal-field multi-air-gap linear reluctance actuator", *Electric Machines and Power Systems*, Vol. **13**, 1987, pp. 299-313.
- [20] Iwabuchi, N., Kawahara, A., Kume, T., Kabashima, T. and Nagasaka, N., "A novel high-torque reluctance motor with rare-earth magnet", *IEEE Transactions on Industry Applications*, Vol. **IA-30**, No. 3, May/June 1994, pp. 609-614.
- [21] Mhango, L. M. C. and Perryman, R., "An overview of impact of NdFeB magnets on brushless dc machines for future aerospace low power drives", *Proceedings of the 30th Universities Power Engineering Conference*, University of Greenwich, London, UK, 5th-7th September 1995, pp. 645-649.
- [22] Evans, S. A., Kettleborough, J. G. and Smith, I. R., "Design and analysis of a permanent magnet linear actuator", *Proceedings of the 7th International Power Electronics & Motion Control Conference*, Budapest, Hungary, 2nd-4th September 1996, Vol. **3**, pp. 266-270.
- [23] Ebihara, D. and Watada, M., "Development of a single-winding linear oscillatory actuator", *IEEE Transactions on Magnetics*, Vol. **MAG-28**, No. 5, September 1992, pp. 3020-3032.
- [24] Roters, H. C., *Electromagnetic Devices*, John Wiley & Sons, New York, 1941.

- [25] Kano, Y., Maeda, K. and Basak, A., "Analysis and reformation of characteristic of linear electromagnetic solenoid", *IEEE Transactions on Magnetics*, Vol. **MAG-29**, No. 6, November 1993, pp. 2929-2931.
  
- [26] Lequesne, B. P., "Finite element analysis of a constant-force solenoid for fluid flow control", *IEEE Transactions on Industry Applications*, Vol. **IA-24**, No. 4, July/August 1988, pp. 574-581.
  
- [27] Lequesne, B. P., "Fast-acting, long-stroke solenoids with two springs", *IEEE Transactions on Industry Applications*, Vol. **IA-26**, No. 5, September/October 1990, pp. 848-856.
  
- [28] Lequesne, B. P., "Design and optimization of two-spring linear actuators", *Proceedings of the International Conference on Electrical Machines*, Paris, France, 5th-8th September 1994, pp. 30-35.
  
- [29] Lequesne, B. P., "Fast-acting long-stroke bistable solenoids with moving permanent magnets", *IEEE Transactions on Industry Applications*, Vol. **IA-26**, No. 3, May/June 1990, pp. 401-407.
  
- [30] Dawson, C. and Bolton, H. R., "Performance prediction of a wide-angle limited-motion rotary actuator", *Proceedings of the IEE*, Vol. **125**, No. 9, September 1978, pp. 895-898.
  
- [31] Laws, A. E., "An electro-mechanical transducer with permanent magnet polarisation", Technical Note No. G.W.202, Royal Aircraft Establishment, Farnborough, UK, July 1952.
  
- [32] Bolton, H. R. and Shakweh, Y., "Performance prediction of Laws's relay actuator", *IEE Proceedings*, Vol. **137**, Pt. B, No. 1, January 1990, pp. 1-13.



- 
- [33] Dawson, C. and Bolton, H. R., "Limited motion rotary actuators of the toroidal-stator, permanent-magnet rotor type", *IEE Proceedings*, Vol. 129, Pt. B, No. 4, July 1982, pp. 190-198.
- [34] Macfarlane, J., "Torque motor for quantity production", *The Engineer*, 15th May 1964, pp. 866-868.
- [35] Lequesne, B. P., "Permanent magnet linear motors for short strokes", *Conference Record of the IEEE Industry Applications Society Annual Meeting*, Vol. 1, 4th-9th October 1992, Houston, Texas, pp. 162-170.
- [36] Brailsford, F., *Magnetic Materials*, Third Edition, Methuen's Monographs on Physical Subjects, Methuen & Co. Ltd., London, 1960.
- [37] McCaig, M. and Clegg, A. G., *Permanent Magnets in Theory and Practice*, Second Edition, Pentech Press Ltd., London, 1987.
- [38] Marik, H. J. and Schlenk, K., "Cobalt-samarium, A new generation permanent magnet material", *Powder Metallurgy International*, Vol. 9, No. 3, 1977, pp. 142-144.
- [39] Tenaud, P., Vial, F. and Sagawa, M., "Improved corrosion and temperature behaviour of modified NdFeB magnets", *IEEE Transactions on Magnetics*, Vol. MAG-26, No. 5, September 1990, pp. 1930-1932.
- [40] Mitchell, P., "Corrosion protection of NdFeB magnets", *IEEE Transactions on Magnetics*, Vol. MAG-26, No. 5, September 1990, pp. 1933-1935.
- [41] Willman, C. J. and Narasimhan, K. S. V. L., "Corrosion characteristics of RE-Fe-B permanent magnets", *Journal of Applied Physics*, Vol. 61, No. 8, 15th April 1987, pp. 3766-3768.

- [42] Taylor, J. S. and Coles, J. R., "Measurements and characteristics of magnetic materials for use in electromagnetic devices", *Proceedings of the International Conference on Electrical Machines*, UMIST, Manchester, UK, 15th-17th September 1992, pp. 1172-1176.
  
- [43] Man, H. H., Man, H. C. and Leung, L. K., "Corrosion protection of NdFeB magnets by surface coatings - Part 1: salt spray test", *Journal of Magnetism and Magnetic Materials*, Vol. **152**, 1996, pp. 40-46.
  
- [44] Man, H. H., Man, H. C. and Leung, L. K., "Corrosion protection of NdFeB magnets by surface coatings - Part 2: electrochemical behaviour in various solutions", *Journal of Magnetism and Magnetic Materials*, Vol. **152**, 1996, pp. 47-53.
  
- [45] Hoole, S. R. H., *Computer-Aided Analysis and Design of Electromagnetic Devices*, Elsevier, New York, 1989.
  
- [46] Lowther, D. A. and Silvester, P. P., *Computer-Aided Design in Magnetics*, Springer-Verlag, New York, 1986.
  
- [47] Silvester, P. P. and Ferrari, R. L., *Finite Elements for Electrical Engineers*, Second Edition, Cambridge University Press, Cambridge, 1990.
  
- [48] Silvester, P. P. and Chari, M. V. K., "Finite element solution of saturable magnetic field problems", *IEEE Transactions on Power Apparatus and Systems*, Vol. **PAS-89**, No. 7, September/October 1970, pp. 1642-1651.
  
- [49] Chari, M. V. K. and Silvester, P. P., "Finite element analysis of magnetically saturated dc machines", *IEEE Transactions on Power Apparatus and Systems*, Vol. **PAS-90**, No. 5, September/October 1971, pp. 2362-2372.

- 
- [50] Chari, M. V. K. and Silvester, P. P., "Analysis of turboalternator magnetic fields by finite elements", *IEEE Transactions on Power Apparatus and Systems*, Vol. **PAS-90**, No. 2, March/April 1971, pp. 454-464.
- [51] Johnk, C. T. A., *Engineering Electromagnetic Fields and Waves*, Second Edition, John Wiley & Sons, New York, 1988.
- [52] Silvester, P., *Modern Electromagnetic Fields*, Prentice-Hall, Inc., Englewood Cliffs, New Jersey, 1968.
- [53] *MEGA: Electromagnetic Finite Element Analysis Software User Manual*, Version 5.21, University of Bath, UK, 15th April 1993.
- [54] *MEGA: Electromagnetic Finite Element Analysis Software Commands Manual*, Version 5.21, University of Bath, UK, 2nd August 1993.
- [55] Hoole, S. R. H. and Hoole, N. R. G., "Reluctivity characteristics in nonlinear finite element analysis of magnetostatic fields", *IEEE Transactions on Magnetics*, Vol. **MAG-22**, No. 5, September 1986, pp. 1352-1353.
- [56] Brauer, J. R., "Simple Equations for the magnetization and reluctivity curves of steel", *IEEE Transactions on Magnetics*, Vol. **MAG-11**, No. 1, January 1975, p. 81.
- [57] Macfadyen, W. K., Simpson, R. R. S., Slater, R. D. and Wood, W. S., "Representation of magnetisation curves by exponential series", *Proceedings of the IEE*, Vol. **120**, No. 8, August 1973, pp. 902-904.
- [58] Widger, G. F. T., "Representation of magnetisation curves over extensive range by rational-fraction approximation", *Proceedings of the IEE*, Vol. **116**, No. 1, January 1969, pp. 156-160.

- 
- [59] Trutt, F. C., Erdelyi, E. A. and Hopkins, R. E., "Representation of the magnetization characteristic of dc machines for computer use", *IEEE Transactions on Power Apparatus and Systems*, Vol. **PAS-87**, No. 3, March 1968, pp. 665-669.
- [60] Brauer, J. R., Larkin, L. A. and Overbye, V. D., "Finite element modelling of permanent magnet devices", *Journal of Applied Physics*, Vol. **55**, No. 6, 15th March 1984, pp. 2183-2185.
- [61] Fouad, F. A., Nehl, T. W. and Demerdash, N. A., "Permanent magnet modelling for use in vector potential finite element analysis in electrical machinery", *IEEE Transactions on Magnetics*, Vol. **MAG-17**, No. 6, November 1981, pp. 3002-3004.
- [62] Rodger, D., Lai, H. C. and Leonard, P. J., "Coupled elements for problems involving movement", *IEEE Transactions on Magnetics*, Vol. **MAG-26**, No. 2, March 1990, pp. 548-550.
- [63] Allen, N., Lai, H. C., Leonard, P. J. and Rodger, D., "External circuit, movement, and periodicity considerations in the design of electrical machines using finite elements", *Proceedings of the 7th International Conference on Electrical Machines and Drives*, IEE Conference Publication No. 412, University of Durham, UK, 11th-13th September 1995, pp. 126-130.
- [64] Coulomb, J. L., Meunier G. and Sabonnadiere, J. C., "An original stationary method using local jacobian derivative for direct finite element computation of electromagnetic force, torque and stiffness", *Journal of Magnetism and Magnetic Materials*, Vol. **26**, 1982, pp. 337-339.
- [65] Coulomb, J. L., and Meunier, G., "Finite element implementation of virtual work principle for magnetic or electric force and torque computation", *IEEE Transactions on Magnetics*, Vol. **MAG-20**, No. 5, 1984, pp. 1894-1896.

- 
- [66] Coulomb, J. L., "A methodology for the determination of global electro-mechanical quantities from a finite element analysis and its application to the evaluation of magnetic forces, torques and stiffness", *IEEE Transactions on Magnetics*, Vol. **MAG-19**, No. 6, November 1983, pp. 2514-2519.
- [67] Marinescu, M. and Marinescu, N., "Numerical computation of torques in permanent magnet motors by Maxwell stresses and energy method", *IEEE Transactions on Magnetics*, Vol. **MAG-24**, No. 1, January 1988, pp. 463-466.
- [68] Henneberger, G., Sattler, Ph. K. and Shen, D., "Force calculation with analytical accuracy in the finite element based computational magnetostatics", *IEEE Transactions on Magnetics*, Vol. **MAG-27**, No. 5, September 1991, pp. 4254-4257.
- [69] Mizia, J., Adamiak, K., Eastham, A. R. and Dawson, G. E., "Finite element force calculation: comparison of methods for electric machines", *IEEE Transactions on Magnetics*, Vol. **MAG-24**, No. 1, January 1988, pp. 447-450.
- [70] McFee, S. and Lowther, D. A., "Towards accurate and consistent force calculation in finite element based computational magnetostatics", *IEEE Transactions on Magnetics*, Vol. **MAG-23**, No. 5, September 1987, pp. 3771-3773.
- [71] Prescott, J. C. and El-Kharashi, A. K., "A method of measuring self-inductances applicable to large electrical machines", *Proceedings of the IEE*, Vol. **106**, Part A, April 1959, pp. 169-173.
- [72] Jones, C. V., "An analysis of commutation for the unified-machine theory", *Proceedings of the IEE*, Vol. **105**, Part C, April 1958, pp. 476-488.
- [73] Jones, C. V., *The Unified Theory of Electrical Machines*, Butterworths & Co. Ltd., London, 1967.

- 
- [74] Mohan, N., Robbins, W. P., Undeland, T. M., Nilssen, R. and Mo, O., "Simulation of power electronic and motion control systems - An overview", *Proceedings of the IEEE*, Vol. **82**, No. 8, August 1994, pp. 1287-1302.
- [75] Phillips, N. W., Bolton, H. R., Lewis, J. D., Pollock, C. and Barnes, M., "Simulation of switched reluctance drive system using a commercially available simulation package", *Proceedings of the 7th International Conference on Electrical Machines and Drives*, IEE Conference Publication No. 412, University of Durham, UK, 11th-13th September 1995, pp. 257-260.
- [76] Abrahamsen, J. G., Ennemark, P. and Jensen, F., "A novel electromagnetic model of a linear reluctance actuator", *Proceedings of the International Conference on Electrical Machines*, Paris, France, 5th-8th September 1994, pp. 101-106.
- [77] Erping, L. and McEwan, P. M., "Analysis of a circuit breaker solenoid actuator system using decoupled CAD-FE-Integral technique", *IEEE Transactions on Magnetics*, Vol. **MAG-28**, No. 2, March 1992, pp. 1279-1282.
- [78] Wang, S. M., Miyano, T. and Hubbard, M., "Electromagnetic field analysis and dynamic simulation of a two-valve solenoid actuator", *IEEE Transactions on Magnetics*, Vol. **MAG-29**, No. 2, March 1993, pp. 1741-1746.
- [79] Gerald, C. F. and Wheatley, P. O., *Applied Numerical Analysis*, Fourth Edition, Addison-Wesley Publishing Co., Wokingham, UK, 1989.
- [80] Ellis, T. M. R., *FORTRAN 77 Programming: With an Introduction to the Fortran 90 Standard*, Second Edition, Addison-Wesley Publishers Co., Wokingham, UK, 1990.
- [81] Mohan, N., Undeland, T. M. and Robbins, W. P., *Power Electronics: Converters, Applications and Design*, John Wiley & Sons, New York, 1995.

- 
- [82] Kron, G., *Tensors for Circuits*, Second Edition, Dover Publications, Inc., New York, 1959.
- [83] Happ, H. H., *Diakoptics and Networks*, Academic Press, New York, 1971.
- [84] Gregory, K., Kettleborough, J. G., Fitton, C. R., Smith, I. R. and Fanthome, B. A., "Simulation of parallel-connected brushless dc generators", *Proceedings of the 3rd IASTED Symposium on Modelling Identification and Control*, Innsbruck, Austria, February 1984.
- [85] Kettleborough, J. G., Gregory, K. and Fanthome, B. A., "Simulation of a synchronous generator with mixed ac and dc loading" *Proceedings of the 19th Universities Power Engineering Conference*, University of Dundee, Scotland, April 1984.
- [86] Kettleborough, J. G., Smith, I. R. and Fanthome, B. A., "Simulation of a transformer/rectifier unit for aircraft power-supply systems", *IEE Proceedings*, Vol. 129, Pt. B, No. 6, November 1982, pp. 323-329.
- [87] Pawlak, A. M. and Nehl, T. W., "Transient finite element modelling of solenoid actuators: The coupled power electronics, mechanical, and magnetic field problem", *IEEE Transactions on Magnetics*, Vol. MAG-24, No. 1, January 1988, pp. 270-273.
- [88] Gregory, K., "The rapid numerical solution of transient problems in small-scale electrical power systems", *Loughborough University of Technology Ph.D. Thesis*, Loughborough, UK, January 1994.
- [89] Hughes, E., *Electrical Technology*, Seventh Edition, Revised by McKenzie Smith, I., Longman, Harlow, UK, 1995.

- 
- [90] Lee, P. W., Pollock, C. and Jolliffe, C. M., "Measurement of flux linkage in the hybrid stepping motor drive", *Power Electronics and Variable-Speed Drives*, IEE Conference Publication No. 399, 26th-28th October 1994, pp. 131-136.
- [91] Smith, D. S. and Howe, D., "Simulation of the dynamic performance of non-linear electro-mechanical systems", *Proceedings of the 2nd International Conference on Computation in Electromagnetics*, IEE Conference Publication No. 384, Nottingham, UK, 12th-14th April 1994, pp. 24-27.
- [92] Clark, R. E., Smith, D. S., Mellor, P. H. and Howe, D., "Design optimisation of moving-magnet actuators for reciprocating electro-mechanical systems", *IEEE Transactions on Magnetics*, Vol. **MAG-31**, No. 6, November 1995, pp. 3746-3748.
- [93] Yamaguchi, M., Nagumo, M., Iio, M., Yamada, H., Mizuno, T. and Suzuki, H., "Static thrust analysis of a cylindrical moving-core linear oscillatory actuator", *Electrical Engineering in Japan*, Vol. **113**, No. 6, 1993, pp. 132-140.
- [94] Boll, R. (Editor), *Soft Magnetic Materials: Fundamentals, Alloys, Properties, Products, Applications; The Vacuumschelze Handbook*, Vacuumschelze GmbH, Heyden & Sons Ltd., London, 1979.
- [95] Simkin, J. and Trowbridge, C. W., "Optimization problems in electromagnetics", *IEEE Transactions on Magnetics*, Vol. **MAG-27**, No. 5, September 1991, pp. 4016-4019.
- [96] Cheng, Y. B. and Sykulski, J. K., "CAD and optimization of electromechanical actuators", *Proceedings of the International Conference on Electrical Machines*, Paris, France, 5th-8th September 1994, pp. 187-192.



- 
- [97] Preis, K., Biro, O., Friedrich, M., Gottvald, A. and Magele, C., "Comparison of different optimization strategies in the design of electromagnetic devices", *IEEE Transactions on Magnetics*, Vol. **MAG-27**, No. 5, September 1991, pp. 4154-4157.
- [98] Widdowson, G. P., Howe, D. and Evison, P. R., "Computer-aided optimization of rare-earth permanent magnet actuators", *Proceedings of the International Conference on Computation in Electromagnetics*, IEE Conference Publication No. 350, London, UK, 25th-27th November 1991, pp. 93-96.
- [99] Atkinson, A. C. and Donev, A. N., *Optimum Experimental Designs*, Oxford Statistical Science Series, Oxford Science Publications, Clarendon Press, Oxford, UK, 1992.
- [100] Montgomery, D. C., *Design and Analysis of Experiments*, Third Edition, John Wiley & Sons, Inc., New York, 1991.
- [101] Kettleborough, J. G., Smith, I. R. and Fanthome, B. A., "Simulation of a dedicated aircraft generator supplying a heavy rectified load", *IEE Proceedings*, Vol. **130**, Pt. B, No. 6, November 1983, pp. 431-435.
- [102] Smith, I. R. and Hamill, B., "Effect of parameter variations on induction-motor transients", *Proceedings of the IEE*, Vol. **120**, No. 12, December 1973, pp. 1489-1492.
- [103] Vardeman, S. B., *Statistics for Engineering Problem Solving*, PWS Foundations in Engineering Series, PWS Publishing Company, Boston, 1994.
- [104] Walker, G., *Miniature Refrigerators for Cryogenic Sensors and Cold Electronics*, Monographs on Cryogenics No. 6, Oxford Science Publications, Clarendon Press, Oxford, UK, 1989.

## BIBLIOGRAPHY

---

- [1] Sykulski, J. K. (Editor), *Computational Magnetics*, Chapman & Hall, London, 1995.
- [2] Silvester, P. P. (Editor), *Software Applications in Electrical Engineering*, Computational Mechanics Publications, Southampton, UK, 1993, pp. 263-270.
- [3] Chari, M. V. K. and Silvester, P. P. (Editors), *Finite Elements in Electrical and Magnetic Field Problems*, John Wiley & Sons, New York, 1980.
- [4] Parker, R. J., *Advances in Permanent Magnetism*, John Wiley & Sons, New York, 1990.
- [5] Strnat, K. J., "Modern permanent magnets for applications in electro-technology", *Proceedings of the IEEE*, Vol. 78, No. 6, June 1990, pp. 923-946.
- [6] Fish, G. E., "Soft magnetic materials", *Proceedings of the IEEE*, Vol. 78, No. 6, June 1990, pp. 947-972.
- [7] Lavers, J. D., "Electromagnetic field computation in power engineering", *IEEE Transactions on Magnetism*, Vol. MAG-29, No. 6, November 1993, pp. 2347-2352.
- [8] Chari, M. V. K., Bedrosian, G., D'Angelo, J. and Konrad, A., "Finite element applications in electrical engineering", *IEEE Transactions on Magnetism*, Vol. MAG-29, No. 2, March 1993, pp. 1306-1314.
- [9] Konrad, A., "Electromagnetic devices and the application of computational techniques in their design", *IEEE Transactions on Magnetism*, Vol. MAG-21, No. 6, November 1985, pp. 2382-2387.

**INITIAL SPECIFICATION OF THE LINEAR MOTOR**

A general specification of the linear motor on no-load is stated below.

Uni-stable, bi-directional operation

Stroke length	$\pm 0.50$ mm up to $\pm 5.0$ mm
Dynamic response (bandwidth)	$\pm 1.00$ mm at 50 Hz
Force (at the central position of the armature at rated current)	as large as possible (typically 15 N)
Maximum force	as large as possible (typically 60 N)
Maximum drive rating	1.0 A
Maximum weight (excluding housing)	1.0 kg
Maximum dimensions (excluding housing):	
length	60.0 mm
outer diameter	50.0 mm

**SPECIFICATION OF THE OPTIMUM LINEAR MOTOR**

Below is a detailed specification of the optimum design on no-load.

**Mechanical**

Overall device mass <sup>1</sup>	623 g
Armature mass	213 g
Overall device diameter <sup>1</sup>	46.0 mm
Overall device length <sup>1</sup>	57.0 mm
Permanent magnet volume	2 × 4.66 cm <sup>3</sup>
Stiffness	3.8 N/mm
Force <sup>2</sup>	19.58 N
Peak force	49.44 N
Operating range	dc (±4.36 mm) – 50 Hz (±1.05 mm)
Resonant frequency	21 Hz (±6.20 mm)
Motor constant	28.03 N/A
Force/volume ratio <sup>2</sup>	0.2067 × 10 <sup>-3</sup> N/mm <sup>3</sup>
Force/armature mass ratio <sup>2</sup>	91.98 N/kg

**Electrical**

Maximum coil current	0.70 A dc
Coil turns	825
Coil resistance	13.4 Ω
Coil inductance <sup>3</sup>	17.52 mH

---

<sup>1</sup> not including motor housing and linear bearings

<sup>2</sup> when armature is centralised and the coil current is 0.70 A

<sup>3</sup> measured in free space, not in motor

**Magnetic Materials**

Permanent magnets

NdFeB (VACODYM 351 WZ)

Stator components

Radiometal (RADIOMETAL 4550)

Armature

Permendur (VACOFLUX 50)

